

# Electromagnetic processes of nuclear excitation: from direct photoabsorption to free electron and muon capture

Présentée le 21 juin 2023

Faculté des sciences de base  
Laboratoire pour la microscopie et la diffusion d'électrons  
Programme doctoral en physique

pour l'obtention du grade de Docteur ès Sciences

par

**Simone GARGIULO**

Acceptée sur proposition du jury

Prof. O. Yazyev, président du jury  
Prof. F. Carbone, directeur de thèse  
Dr C. J. Chiara, rapporteur  
Prof. L. E. Marcucci, rapporteuse  
Prof. P. Ricci, rapporteur





Sometimes it is the people no one can imagine anything of  
who do the things no one can imagine.  
— Alan Turing

To my parents,  
whose endless efforts and altruism have made my accomplishments possible,  
and to all those who have shaped who I am today.  
I am deeply grateful for your encouragement, support, and patience  
as I followed my dream of becoming a scientist.

# Acknowledgements

To create freedom for oneself and also a sacred No to duty: for that, my brothers, the lion is required. To take the right to new values – that is the most terrible taking for a carrying and reverent spirit. [...] The child is innocence and forgetting, a new beginning, a game, a wheel rolling out of itself, a first movement, a sacred yes-saying.

Three metamorphoses of the spirit I named for you: how the spirit became a camel, and the camel a lion, and finally the lion a child.

— Friedrich Nietzsche, *Thus Spoke Zarathustra*

This has been a fantastic journey! Let's be clear, it has been challenging and full of uncertainties, and the contentment does not certainly come from having completed it. I am grateful as I have learned a bit more about myself and the world that surrounds me – hopefully undergone a metamorphosis of the spirit. Nonetheless, the path toward the spirit of a child – taking the right for oneself to create new values – is only at the beginning.

I slowly realized, over the years, how vital the care and attention my parents had during my childhood was. The certainty of always having them by my side has been the anchor and security that allowed me to devote myself to the pursuit of my passions. To them goes my greatest gratitude; for the years they spent chasing after me and making me a better person. I thank them for the warm, bonded family they have given to me and my siblings. I thank my sister Sara and my brother Costantino. Growing up together has been surely one of the best parts of my life, which I look back on with nostalgia. Thanks for your patience and comprehension.

I have been gifted to have met you, Mary Joy; as I can behave as Ivan Karamazov only because you are my Alëša. Gentleness, care, love, and *joy* are the characteristics that find immense richness in you. Thank you for being the exceptional person you are! Thanks for the way you understand me and make me feel accepted. Thank you for being my strongest supporter under all circumstances. Thank you for showing me, through your kind example, how to improve in the various traits that are lacking in me. These

## Acknowledgements

---

years would not have been the same without you. “If I am really able to care for the sticky little leaves I shall only love them, remembering you”. *Te voglj ben overamente*.

I am thankful to my grandmother Rosa and those who are no longer here: nonno Costantino and nonna Pina. Thank you for your teachings and your love. I know you are proud of me. I keep the memories of my wonderful childhood spent with you as the most precious baggage.

These years have been emotionally challenging for several reasons, and now I can't help but think of you Josef. You would surely have made some jokes today. I am thankful to have met you, but unfortunately, not for long enough. I thank Enzo, Antonio, and Ciccio, who have always been present over the years. I also want to thank the people I met during my previous CERN experience: Daniele, Luca, Leanne, and Francesca. Although we have lost our daily routine together, it feels as if all this time has never passed.

I am grateful to have met Fabrizio Carbone along my academic and life path, as this has been a pivotal point that changed everything. He gave me the incredible opportunity to become a scientist (and a physicist) and realize my potential. He was not only a scientific PI for me but a person with whom I could openly discuss any concern about life. I thank him for his tireless support, the freedom he gave me, extensive and stimulating discussions, and for believing in me more than I do. Thank you for the atmosphere you created in the group, which allowed me to be creative and meet amazing people. Thank you for giving me so much!

I am thankful to Ross Koningstein at Google Inc. for enthusiastically supporting and funding this research project. All this would not have happened without his vision.

I have also been blessed to have found someone like Ivan Madan on this journey. I am grateful and indebted to you for the endless conversations and discussions. Thank you for your untiring perseverance in advising me on the best path to ultimately “become who I am”. The time spent together has been precious. Thank you for setting up a creative environment in which our ideas could flourish. I will keep with me the indelible memory of the day I won an outdoor chess game against you in downtown Lausanne. Thank you for being your *typical* self and the outstanding person you really are. Thank you for all you have taught me as a scientist and as a person; I owe you a lot. I hope that 30 years from now, we can still share these memories while drinking a pleasant coffee in Naples, discussing how our spirits have finally evolved and how we set a new beginning.

I am thankful for having met you, Siham. You have often lightened my days simply with a hug or a laugh. You have always been available in these four years (do you remember that day in the hospital with Paolo?), and I want to thank you warmly. Spending all these years together was a lot of fun. I have missed you very much since you left EPFL. I realize only now how much my daily routine and joy were also connected to you.

I want to thank Francesco for all the nice time we spent together, for the discussions, and for pushing me to try hiking. I still remember your arguments against the Swiss website that listed the route as being of the highest difficulty while you claimed it was entry-level. When I think of you, I associate you irretrievably with Barberousse or the

## Acknowledgements

---

bicycle ride home on a winter night and, of course, with food.

I also want to thank Gianmaria. Even if briefly, it was nice to share time together. Your daily 8 p.m. call before dinner has been a source of entertainment for years. These phone calls reminded me of the typical phone call between Assunta and Salvatore that all Neapolitans know. It has been essential to have you along this path.

I will be forever grateful to my beautiful ‘Italian office’: Paolo, Francesco, Veronica, and Benoît (clearly an Italian name). Meeting all of us together was almost a planetary alignment. I doubt that I will ever have such a fun and cohesive working environment in the future. It was an excellent time spent together. I’ll need pages to even start to share a single episode about every one of you: *Cooosa? WoW! Let’s Barantize the data! Cra Cra! Assurdo! Lausanne is like San Francisco! Who is going to reimburse my time?*. Paolo, you have entertained me so much over the years; I can’t even imagine what it would have been like without you in the office (yes, maybe a little quieter). You and Siham have been my perfect accomplices in pranks and jokes, brightening these years with colors. Thank you, Ben, for your constant availability, help, and joy. Lately, our office has been furtherly enriched by a newcomer from Bergamo (and now I know you are reading this with his voice). This marked a new point of reference for enjoyment but, above all, for stimulating discussions. I want to thank Hui-Yuan for simply being himself and for the way he was always welcoming with a smile or a hug. I will never forget your ability to stand in line for literally any activity during the conferences. I want to thank also Lukas, Alexey, and Tom for the nice time we spent together and for our interesting discussions.

I want to thank also all the scientists with whom I had the opportunity to collaborate, especially Javier García de Abajo, Ido Kaminer, Adriana Pállfy, Yuanbin Wu, Vincenzo Grillo, and Eduardo Dias.

I want to warmly thank the committee for their extensive feedback on this work and the stimulating discussions during the defense. It was a memorable day that I will remember with affection.

I also want to thank Chris Chiara and Jeff Carroll for the countless discussions and for having shared their knowledge on the field and on the NEEC process since day one. I want to thank them for the level of detail in their comments and explanations and the long emails of correspondence. All of this has been as a Rosetta Stone that helped me in the comprehension of the nuclear processes when I was learning to crawl in my research activity.

I am grateful to have met Amedeo Capozzoli at the University of Naples because, after all, he was the one that inflamed my critical thinking during my studies. Meeting him definitely changed my academic path, and I have held over these years, with affection, his priceless pearls of wisdom.

Grazie a voi tutti. Grazie per ciò che siete stati e la ricchezza che mi avete donato.

Lausanne, 26 May 2023

Simone Gargiulo.

«‘O core nun tene padrone, quiet nun se fira ‘e stà.»



Post Tenebras LUMES

*A year seems long to you and it passes quickly;  
when it has passed, it goes far away;  
another one goes by, and when it is gone  
it also runs along with the one before,  
and together five more, twenty, thirty.  
they leave through the air above the clouds.  
And from there, you feel like an uproar,  
which is always the same  
for as long as the world has been above this Earth.  
As if it were the village band playing in the middle of the alley and walking away.  
It enters your ears when it is passing, and you no longer hear it when it has passed.  
But one thing you are left with: do you know what you are left with?  
You are left with the memory of a tune.  
Like it was a lost music of a forgotten dream,  
that seemed alive to you, clearer than a crystal inside the dream.  
And you can't tell it when you wake up even to yourself,  
so much is made up of nothing.*

— Eduardo De Filippo, *Ncopp' a sta Terra*.

# Preface

Recent technological advances allowed for the manipulation of matter at the ultrafast time-scale, offering unprecedented possibilities in the investigation of out-of-equilibrium phenomena. In this thesis, the possibility to apply these methods to control nuclear phenomena is addressed both theoretically and experimentally. When a free electron is captured by an ion having a vacancy in one of its deep core-levels, if the energy of the electron plus the binding energy of the capturing orbital matches one of the atom's nuclear excitations, an isomeric transition can be induced. In this thesis, it has been shown theoretically that if the capturing ion's electronic structure is out of equilibrium, the cross section of such effect can be enhanced. In a separate work, it has also been shown that it is possible to further enhance such a cross section if the wavefunction of the free-electron is engineered prior to the capture to better match the energy-momentum conservation of a specific orbital. Building on these ideas, a new effect is also proposed by exploiting the possibility for any neutral ions to capture muons in one of their naturally empty muonic orbitals, potentially yielding nuclear excitations at much higher energies, in the order of MeV. These results offer a new perspective on the possibility to use modern tools to control the nuclear properties of matter. To implement these ideas, a new instrument has been developed and described in this thesis, aiming at measuring the fluorescence of excited nuclei upon a pulsed excitation. Currently, it is commonly assumed that a laser-driven plasma can be used to generate X-rays to directly photoexcite a nuclear transition. This thesis reports an extensive experimental campaign aiming at reproducing and benchmarking this effect, and shows that the process reported in the literature cannot be ascribed to a nuclear transition. Furthermore, an extensive modeling of the data is provided, offering a quantitative perspective of the excitation probabilities of nuclei in a laser-driven plasma scenario.

Overall, this thesis reports both theoretical and experimental original research aimed at discussing the feasibility and perspective of the ultrafast manipulation of nuclei. These results have perspective implications for discovering novel nuclear energy harvesting or storing methods, but also for nuclear waste management and fundamental nuclear physics.

*Lausanne, 26 May 2023*

Fabrizio Carbone



# Abstract

In the vast expanse of the Universe and on our planet, nuclei exist in a state of excitement. These nuclei, known as nuclear isomers, possess unique properties that make them play a crucial role in diverse domains of physics. In nucleosynthesis, the process by which new atomic nuclei are formed inside stars, isomers can influence the rates of nuclear reactions, leading to variations in the production and abundance of elements we see around us. Additionally, some isomers hold potential applications in nuclear technologies, including the energy sector. These excited nuclear states can persist for varying periods, from fractions of a second to billions of years and beyond, before decaying to their ground state. If harnessed, feeding and depleting these isomers could represent a clean and high-density way to store and release energy on demand. The quest for efficient dynamical population control of nuclear isomer has long captivated the imagination of physicists, yet this elusive goal remains beyond our grasp.

In this dissertation, I examine the potential of employing nuclear excitation mechanisms as viable tools for achieving such manipulation. Three processes of nuclear excitations from both theoretical and experimental perspectives are explored: direct photoabsorption, nuclear excitation by electron capture (NEEC), and nuclear excitation by free muon capture (NE $\mu$ C).

This thesis begins by delving into the historical framework of nuclear excitation by electron capture (NEEC), a process that was proposed in 1976 and is yet to be comprehended. A recently claimed observation has sparked new interest in nuclear excitation processes as a way to release the energy trapped in isomers. However, the irreconcilability between the first observation, the theoretical framework, and the recent repetition of the experiment reveals that there is still much to learn.

Regardless of the specific process being examined, the primary goal is to increase the likelihood of their occurrence. One such possibility involves NEEC taking place in excited ions, where the screening effect of other electrons provides nearly resonant orbitals where capture can occur. This process was initially proposed to mitigate the discrepancy between the experimental finding and the theoretical prediction. In this new setting, three orders of magnitude increase in the NEEC cross-sections for  $^{73}\text{Ge}$  is found



theoretically. Another approach enabling the manipulation of the NEEC cross-section involves engineering the electron wavefunction that undergoes capture. This technique not only demonstrates an increased occurrence of NEEC but also highlights the potential to alter the shell where the highest capture takes place.

The second mechanism,  $NE_{\mu}C$ , occurs in exotic muonic atoms. The process is introduced as a counterpart to NEEC, with the electron being replaced by a muon. It follows a presentation of the framework within which this process has emerged and how it changes the paradigm in comparison to NEEC. Owing to the increased proximity of muons to the nucleus, this process has been found to exhibit cross-sections that are several orders of magnitude higher than NEEC for excitations in the MeV range. By examining the unique properties of  $NE_{\mu}C$ , insights into the process and its potential applications are provided, including muon-induced fission.

Lastly, nuclear excitations are studied in the context of a laser-generated plasma scenario, where nuclei might be excited through the resonant absorption of a photon, together with other competing processes. The design and implementation of a tabletop setup for generating keV-hot plasma upon femtosecond laser irradiation are presented. The experimental work has been conducted on a  $^{181}\text{Ta}$  target using a time-dependent X-ray spectroscopic technique. The absence of a clear decay signal raises the question of whether the excitation of the  $^{181m}\text{Ta}$  isomer has ever been observed in this context.

This dissertation aims to deepen the understanding of nuclear excitation mechanisms, emphasizing their complexities and potential for both further fundamental research and practical applications. Throughout the chapters, ideas for future studies that could expand the boundaries of the discussed physics are debated.

**Keywords:** nuclear isomers, nuclear excitations, direct photoexcitation, nuclear excitation by electron capture (NEEC), nuclear excitation by free muon capture ( $NE_{\mu}C$ ), vortex beams, energy storage, isomer depletion.

# Résumé

Dans l'immensité de l'Univers et sur notre planète, il existe des noyaux atomique dans un état d'excitation. Ces noyaux, appelés isomères nucléaires, possèdent des propriétés uniques qui leurs confèrent un rôle crucial dans divers domaines de la physique. Dans la nucléosynthèse, le processus par lequel de nouveaux noyaux atomiques se forment à l'intérieur des étoiles, les isomères peuvent influencer les taux de réactions nucléaires, entraînant des variations dans la production et l'abondance des éléments que nous observons autour de nous. De plus, certains isomères ont des applications potentielles dans les technologies nucléaires, y compris le secteur de l'énergie. Ces états nucléaires excités peuvent persister pendant des durées variables, allant de fractions de seconde à des milliards d'années et au-delà, avant de passer à leur état fondamental. Si maîtrisés, l'alimentation et la déplétion de ces isomères pourraient représenter un moyen propre et à haute densité de stocker et de libérer de l'énergie à la demande. La quête d'un contrôle dynamique efficace de la population des isomères nucléaires a longtemps captivé l'imagination des physiciens, mais cet objectif reste encore hors de notre portée.

Dans cette thèse, j'examine le potentiel des mécanismes d'excitation nucléaire comme outil viable pour atteindre un tel contrôle. Trois processus d'excitations nucléaires sont explorés, tant d'un point de vue théorique qu'expérimental : l'absorption directe de photons, l'excitation nucléaire par capture d'électron (NEEC) et l'excitation nucléaire par capture de muons libres ( $NE\mu C$ ).

Cette thèse commence par explorer le cadre historique de l'excitation nucléaire par capture d'électron (NEEC), un processus qui a été proposé en 1976 et qui est encore loin d'être compris. Une observation récemment revendiquée a suscité un nouvel intérêt pour les processus d'excitation nucléaire comme moyen de libérer l'énergie emprisonnée dans les isomères. Cependant, l'incompatibilité entre cette observation, le cadre théorique et la la récente réitération de l'expérience révèle qu'il reste encore beaucoup à apprendre.

Quel que soit le processus spécifique examiné, l'objectif principal est d'augmenter la probabilité de leur apparition. L'une des possibilités suppose que la NEEC se produise dans des ions excités où l'effet d'écran des autres électrons génère des orbitales presque résonantes où la capture est plus efficace. Ce processus a été initialement suggéré comme

un moyen d'atténuer les divergences entre les résultats expérimentaux et les prédictions théoriques. Dans ce nouveau cadre, une augmentation de trois ordres de grandeur des sections efficaces de la NEEC pour le  $^{73}\text{Ge}$  est trouvée théoriquement. Une autre approche pour manipuler la section efficace de la NEEC consiste à concevoir la fonction d'onde de l'électron capturé. Cette technique démontre non seulement une augmentation de l'occurrence de NEEC (jusqu'à six ordres de grandeur) mais met également en évidence le potentiel de modifier la couche atomique où le taux de capture le plus élevé se produit.

Le deuxième mécanisme,  $\text{NE}\mu\text{C}$ , se produit dans des atomes muoniques. Le processus est introduit comme un homologue de NEEC, l'électron étant remplacé par un muon. Ensuite, je présenterai le cadre dans lequel ce processus a émergé et comment il change le paradigme par rapport à la NEEC. En raison de la proximité des muons avec le noyau, ce processus présente des sections efficaces supérieures de plusieurs ordres de grandeur à celles de la NEEC pour des excitations de l'ordre de MeV. L'analyse des propriétés uniques de la  $\text{NE}\mu\text{C}$  permet de mieux comprendre le processus et ses applications potentielles, y compris la fission induite par les muons.

Enfin, les excitations nucléaires sont étudiées dans un scénario expérimental où un plasma est généré par un laser. Dans ce cas, les noyaux pourraient être excités par l'absorption résonnante d'un photon. La conception et la mise en œuvre d'un dispositif pour générer un plasma avec des températures de l'ordre du keV par interaction avec un laser femtoseconde sont présentées. Des mesures expérimentales des émissions de rayon-X en fonction du temps sur un échantillon de  $^{181}\text{Ta}$  en utilisant une technique spectroscopique. L'absence manifeste d'un signal de décroissance nucléaire soulève la question de savoir si l'excitation de l'isomère  $^{181\text{m}}\text{Ta}$  a déjà été observée dans ce contexte.

Cette thèse vise à approfondir la compréhension des mécanismes d'excitation nucléaire, en mettant l'accent sur leurs complexités et leur potentiel pour la recherche fondamentale et les applications pratiques. Tout au long des chapitres, des idées pour de futures études pouvant repousser les limites de ces phénomènes physiques sont proposées.

**Mots clés:** isomères nucléaires, excitations nucléaires, photoexcitation directe, excitation nucléaire par capture d'électron (NEEC), excitation nucléaire par capture de muon libre ( $\text{NE}\mu\text{C}$ ), faisceaux vortex, stockage d'énergie, déplétion d'isomères.

# Sinossi

Nella vasta distesa dell'Universo e sul nostro pianeta, esistono nuclei in uno stato di eccitazione. Questi nuclei, noti come isomeri, possiedono proprietà uniche che li rendono cruciali in diversi ambiti della fisica. Nella nucleosintesi, il processo attraverso il quale nuovi nuclei atomici si formano all'interno delle stelle, gli isomeri possono influenzare la frequenza delle reazioni nucleari, influenzando la produzione e l'abbondanza degli elementi che vediamo intorno a noi. Inoltre, alcuni isomeri possono trovare applicazione nelle tecnologie nucleari, incluso il settore energetico. Questi stati nucleari eccitati possono persistere per periodi variabili, da frazioni di secondo a miliardi di anni e oltre, prima di passare al loro stato fondamentale. Se padroneggiati, l'alimentazione e lo svuotamento di questi isomeri potrebbero rappresentare un metodo pulito e ad alta densità per poter immagazzinare e rilasciare energia a piacimento. La ricerca di un controllo efficiente e dinamico della popolazione degli isomeri nucleari ha a lungo affascinato l'immaginazione dei fisici, ma al momento questo obiettivo rimane al di fuori della nostra portata.

In questa dissertazione, esploro la possibilità di utilizzare i meccanismi di eccitazione nucleare come valido strumento per il raggiungimento di tale manipolazione. Tre processi di eccitazione nucleare vengono studiati sia da un punto di vista teorico che sperimentale: fotoassorbimento diretto, eccitazione nucleare per cattura di elettroni (NEEC) ed eccitazione nucleare per cattura di muoni liberi (NE $\mu$ C).

Questa tesi propone un approfondimento del quadro storico dell'eccitazione nucleare per cattura di elettroni (NEEC), un processo che è stato proposto nel 1976 e tuttavia ancora lontano dall'essere compreso. Una recente osservazione sperimentale ha suscitato un rinnovato interesse nei processi di eccitazione nucleare come mezzo per poter rilasciare l'energia intrappolata negli isomeri. Tuttavia, l'irreconciliabilità tra la prima osservazione, il modello teorico e la recente replica dell'esperimento rivela che ci sia ancora molto da imparare.

Indipendentemente dai processi in esame, l'obiettivo principale è quello di aumentare la probabilità che si verifichino. Una prima possibilità consiste nell'avere NEEC in ioni eccitati, dove l'effetto schermante degli altri elettroni fornisce orbitali quasi risonanti, nei quali possa verificarsi la cattura in maniera più efficiente. Questo processo è stato

inizialmente proposto con l'obiettivo di mitigare la discrepanza tra i risultati sperimentali e le previsioni teoriche. In questo nuovo contesto, si riscontra dal punto di vista teorico un aumento di tre ordini di grandezza nelle sezioni d'urto del NEEC per  $^{73}\text{Ge}$ . Un altro approccio per manipolare la sezione d'urto del NEEC consiste nel modificare la funzione d'onda dell'elettrone che subisce la cattura. Questa tecnica non solo dimostra un aumento della probabilità con la quale NEEC possa verificarsi (fino a sei ordini di grandezza), ma mette anche in evidenza la possibilità di poter scegliere dall'esterno l'orbitale in cui la cattura più efficiente si verifichi.

Il secondo meccanismo,  $\text{NE}\mu\text{C}$ , ha luogo invece in atomi muonici. Il processo viene introdotto come semplice controparte del NEEC, dove l'elettrone viene sostituito da un muone. Segue poi una presentazione del contesto nel quale questo processo è emerso e come esso offra un cambio di paradigma rispetto al NEEC. Grazie alla maggiore vicinanza dei muoni al nucleo, questo processo presenta sezioni d'urto di svariati ordini di grandezza superiori al NEEC, consentendo inoltre eccitazioni nell'ordine del MeV. Tramite l'analisi delle proprietà uniche del  $\text{NE}\mu\text{C}$ , il processo stesso e le sue potenziali applicazioni, tra cui la fissione indotta dalla cattura di muoni, vengono approfondite.

Infine, le eccitazioni nucleari vengono studiate in uno scenario sperimentale dove un plasma viene generato dall'interazione con un laser. Qui i nuclei potrebbero essere eccitati attraverso l'assorbimento risonante di un fotone. Viene presentata la progettazione e l'implementazione di un setup volto alla generazione di un plasma con temperature del keV mediante l'interazione con un laser a femtosecondo. Le misure sperimentali di emissione di raggi-X sono state condotte su un campione di  $^{181}\text{Ta}$  utilizzando una tecnica spettroscopica tempo dipendente. La mancata osservazione di un segnale di decadimento nucleare inequivocabile solleva la domanda se l'eccitazione dell'isomero  $^{181\text{m}}\text{Ta}$  sia mai stata osservata in questo contesto.

Questa tesi ha come obiettivo l'approfondimento della comprensione dei meccanismi di eccitazione nucleare, enfatizzando le loro complessità e potenzialità sia per ulteriori ricerche fondamentali che per applicazioni pratiche. Nel corso dei vari capitoli, vengono discusse idee per studi futuri che potrebbero ampliare i confini della fisica trattata.

**Parole chiave:** isomeri nucleari, eccitazioni nucleari, fotoeccitazione diretta, eccitazione nucleare per cattura di elettroni (NEEC), eccitazione nucleare per cattura di muoni liberi ( $\text{NE}\mu\text{C}$ ), fasci vorticosi, immagazzinamento di energia, esaurimento degli isomeri.



# Contents

<b>Acknowledgements</b>	<b>i</b>
<b>Preface</b>	<b>v</b>
<b>Abstract (English/Français/Italiano)</b>	<b>vii</b>
<b>List of figures</b>	<b>xv</b>
<b>List of tables</b>	<b>xix</b>
<b>Introduction</b>	<b>1</b>
<b>1 Nuclear Isomers</b>	<b>9</b>
1.1 Classification and nature of Isomers . . . . .	19
1.1.1 Spin Traps . . . . .	20
1.1.2 K-Isomers . . . . .	22
1.1.3 Shape Isomers . . . . .	25
1.2 Essence and significance of nuclear isomers as long duration energy storage solution . . . . .	29
<b>2 Nuclear Excitation by Electron Capture</b>	<b>39</b>
2.1 From the origins to the present day: a recipe for the future . . . . .	39
2.2 Nuclear Excitation by Electron Capture in Excited Ions . . . . .	52
2.3 Supplemental Material: Nuclear Excitation by Electron Capture in Excited Ions . . . . .	58
2.4 Dynamical Control of Nuclear Isomer Depletion via Electron Vortex Beams	69
2.5 Supplemental Material: Dynamical Control of Nuclear Isomer Depletion via Electron Vortex Beams . . . . .	75
<b>3 Nuclear Excitation by Free Muon Capture</b>	<b>81</b>
3.1 Why muons? . . . . .	81
3.2 Nuclear Excitation by Free Muon Capture . . . . .	88
3.3 Supplemental Material: Nuclear Excitation by Free Muon Capture . . . . .	95

<b>4 Nuclear excitations in optical-laser generated plasma</b>	<b>101</b>
4.1 Search of suitable isotopes . . . . .	105
4.2 Design of the experimental setup . . . . .	107
4.3 Alignment procedure . . . . .	109
4.4 Plasma hydrodynamic model: properties and evolution of the optical-laser generated plasma . . . . .	112
4.5 Experimental prototyping . . . . .	120
4.6 Experimental results . . . . .	128
 <b>Beyond Dichotomies: Reflections and Takeaways</b>	 <b>137</b>
 <b>Addendum: Charge Dynamics Electron Microscopy</b>	 <b>141</b>
Nanoscale Imaging of Femtosecond Plasma Dynamics . . . . .	146
 <b>A Appendix</b>	 <b>155</b>
A.1 $I=0^{+-}$ isomeric states . . . . .	155
A.2 $0 \rightarrow 0$ E0 isomeric transitions . . . . .	156
A.3 Recoupling coefficients for NEEC–EXI . . . . .	158
A.3.1 $\mathbf{N}_{\text{ele}} = \mathbf{0} \rightarrow \mathbf{N}_{\text{ele}} = \mathbf{1}$ . . . . .	158
A.3.2 $\mathbf{N}_{\text{ele}} = \mathbf{1} \rightarrow \mathbf{N}_{\text{ele}} = \mathbf{2}$ . . . . .	158
A.3.3 $\mathbf{N}_{\text{ele}} = \mathbf{2} \rightarrow \mathbf{N}_{\text{ele}} = \mathbf{3}$ . . . . .	158
A.3.4 $\mathbf{N}_{\text{ele}} = \mathbf{3} \rightarrow \mathbf{N}_{\text{ele}} = \mathbf{4}$ . . . . .	162
A.4 Additional Figures . . . . .	170
 <b>Bibliography</b>	 <b>175</b>
 <b>Curriculum Vitae</b>	 <b>191</b>



# List of Figures

I.1	Global greenhouse gas emissions by sector. . . . .	3
I.2	Global electricity production by source. . . . .	4
1.1	Pattern of disintegration at the beginning of the uranium radioactive series with the isomeric pair $UX_2$ and $UZ$ . . . . .	9
1.2	Isomeric chart . . . . .	10
1.3	Histogram of the isomer half-lives . . . . .	11
1.4	Scatter plot of the distribution of isomers along the nuclear chart . . . . .	11
1.5	Excitation energies and half-lives of isomers on the nuclear chart . . . . .	12
1.6	Nuclear shell model and intruder orbitals. . . . .	13
1.7	Classification of nuclear isomers. . . . .	19
1.8	Isomeric islands in odd-A nuclei. . . . .	21
1.9	Definition of the K quantum number. . . . .	23
1.10	Appearance of K-isomers in the energy level schemes of $^{178}\text{Hf}$ and $^{180}\text{Hf}$ . . . . .	24
1.11	Nuclear deformations and time evolution of vibrational modes for low-order multipoles. . . . .	26
1.12	Nuclear shapes for quadrupolar deformations. . . . .	27
1.13	Fission barrier and nuclear deformations. . . . .	28
1.14	Partial level scheme of $^{180}\text{Ta}$ and identification of pathways for isomer depletion. . . . .	30
1.15	Desirable energy level scheme for the isomer depletion. . . . .	31
1.16	Feynman diagrams for several nuclear deexcitation processes. . . . .	33
1.17	Energy diagrams for several mechanisms of nuclear excitation. . . . .	34
2.1	The process of nuclear excitation by electron capture. . . . .	39
2.2	Feynman diagrams for the two processes of inverse internal electron conversion and NEEC. . . . .	41
2.3	The isomer depletion of $^{93\text{m}}\text{Mo}$ as evidence of the process of nuclear excitation by electron capture. . . . .	43
2.4	The nuclear excitation by electron capture in excited ions. . . . .	44
2.5	The cross-section shapes for the NEEC process differ depending on whether the electrons involved in the capture are initially bound in a target medium or free . . . . .	45



## LIST OF FIGURES


2.6	Reinvestigation of the isomer depletion occurring in $^{93}\text{Mo}$ at RIBLL. . . .	47
2.7	Nuclear excitation by vortex electron capture. . . . .	49
2.8	Isomer depletion of $^{152\text{m}}\text{Eu}$ through vortex electron beams. . . . .	50
3.1	The process of nuclear excitation by free muon capture ( $\text{NE}\mu\text{C}$ ) . . . . .	81
3.2	Energy diagrams for the NEEC and $\text{NE}\mu\text{C}$ processes. . . . .	82
3.3	Half-life and energy map of the nuclear levels identified for the $\text{NE}\mu\text{C}$ process. . . . .	84
3.4	Overview of the muon-induced fission processes. . . . .	85
3.5	Possible reaction pattern to study rare decay modes through monopole transitions. . . . .	87
4.1	Tantalum and tungsten deexcitation in laser-generated plasma experiment. . . . .	102
4.2	Competition between direct photoexcitation and NEEC in optical-laser generated plasma. . . . .	103
4.3	Temporal discrimination between plasma radiation and delayed nuclear decay. . . . .	104
4.4	Research of suitable isotopes for nuclear excitation in optical-laser gener- ated plasma. . . . .	105
4.5	Research of suitable isotopes for nuclear excitation in optical-laser gener- ated plasma. . . . .	106
4.6	3D CAD of the experimental setup designed at EPFL. . . . .	108
4.7	Pictures of the experimental setup implemented at EPFL. . . . .	109
4.8	Alignment procedures to be performed before the laser-plasma experiment. . . . .	110
4.9	Observing the movements of planar and cylindrical samples via the align- ment camera. . . . .	111
4.10	Plasma hydrodynamic model applied to the case of $^{181}\text{Ta}$ interacting with a femtosecond laser. . . . .	117
4.11	Isomer photoexcitation rate as a function of the plasma temperature. . . . .	119
4.12	Experimentally measured plasma radiation as a function of energy and time . . . . .	121
4.13	Pictures showing film deposition on some of the components of the experi- mental setup. . . . .	122
4.14	Surfaces of the W cylindrical sample acquired through 3D optical pro- filometer. . . . .	123
4.15	Widths and depths of the grooves left by laser ablation on the W sample. . . . .	124
4.16	Optical-laser generated plasma: time series acquisitions with the Tantalum sample. . . . .	125
4.17	Optical-laser generated plasma: time series acquisitions with the Tungsten sample. . . . .	125
4.18	Count dispersion among different time series. . . . .	126
4.19	Comparing the time-dependent signals measured with the Tantalum and Tungsten samples. . . . .	127

## LIST OF FIGURES

---

4.21	Optical-laser generated plasma experiment: total number of events over time. . . . .	129
4.22	Optical-laser generated plasma experiment: 2D energy-time map. . . . .	130
4.23	Optical-laser generated plasma experiment: taking a closer look at the prompt and delayed signals . . . . .	132
4.24	Optical-laser generated plasma experiment: spectra of the prompt and delayed signals . . . . .	133
BD.1	Navigating the Unknown. . . . .	138
A.1	Parent and child electronic configurations for $\mathbf{N}_{\text{ele}} = \mathbf{3} \rightarrow \mathbf{N}_{\text{ele}} = \mathbf{4}$ . . . . .	159
A.2	Histograms illustrating the detected event distribution as a function of pixel number, both before and after removing outlier pixels. . . . .	170
A.3	Optical-laser generated plasma experiment: 2D energy-time map. . . . .	171
A.4	Detection efficiency of the AdvaPIX TPX3. . . . .	171
A.5	Comparison of bremsstrahlung and TDE photon flux models. . . . .	172
A.7	The ultrafast transmission electron microscope (UTEM). . . . .	174





# List of Tables

1.1	Transition rates $W$ ( $s^{-1}$ ) and Weisskopf's estimates of the reduced transition probabilities $B_W(\lambda L)$ for the electric ( $e^2 \cdot fm^{2L}$ ) and magnetic ( $\mu_N^2 \cdot fm^{2L-2}$ ) multipoles. . . . .	17
1.2	Parity-favored and parity-unfavored transitions. . . . .	18
4.1	Characteristics of the laser pulse. . . . .	112
4.2	Application of the plasma hydrodynamic model to our experimental conditions in case of a $^{181}\text{Ta}$ sample. . . . .	116
4.3	Number of excited nuclei, deexcitations, and photons in plasma, considering the TDE case. . . . .	120
4.4	Number of excited nuclei, deexcitations, and photons in plasma, considering bremsstrahlung as the origin of the photons gas. . . . .	120
A.1	Isomer states with $0^+ -$ total nuclear angular momentum. . . . .	155
A.2	Isomeric E0 transitions towards a $I = 0$ ground state. . . . .	156





# Introduction

From the inception of human society, the mastery of energy has played a significant role in our evolutionary journey. Beginning with the simple act of gathering around hearths, we discovered the value of group cooperation for survival. This fundamental principle has laid the foundation for our system of values and societal organization, along with our search for meaning [1]. To this day, we continue to fight to uncover the underlying laws that would enable us to comprehend our own nature. Simultaneously, we have managed to transcend this struggle, distilling – as revelations between dreams and consciousness – the attributes that have proven advantageous to our *progress*. The expansion of human civilization has been closely linked to our capacity to harness and control resources. For millennia, human and animal labor have been the only propellants to power our activities; here, the capacity to control and manipulate the elements around us has proven essential in shaping the development of our society. Over the last hundred years, various energy sources and technological advancements have enhanced our abilities beyond measure, pushing the extraordinary progress witnessed in modern times. Many of our greatest achievements began through the efforts of individuals who were able to convert natural resources into energy and propel humanity to new heights on the evolutionary ladder. However, this very capability that has driven our progress also bears a significant impact on our planet, and it may pose a substantial threat to our survival in the coming centuries.

As we become consumed by our daily concerns and challenges, we often lose sight of the bigger picture. In 2008, James Hansen, former director of the NASA Goddard Institute for Space Studies, along with his co-authors, posed the critical question: “Where should humanity aim?” [2]. Paleoclimatic evidence suggests that in order to maintain the Holocene climate, to which both humans and the biosphere have adapted, atmospheric CO<sub>2</sub> should be kept below the line of 350 ppm. However, even with reduced emissions or phasing out coal by 2050, CO<sub>2</sub> concentrations are likely to remain above this safety line for centuries to come. While the inertia of oceans and ice sheets provides a buffer that delays climate responses, their reaction is anticipated to be faster than the lifetime of CO<sub>2</sub>.

For decades, resource selection was primarily driven by ease of access and economic factors. This approach has indeed proven effective; following the industrial revolution, the quality of life has significantly improved for billions of individuals worldwide. However,

it has not been without its costs. We are now faced with the challenge of carrying on with our activities without contributing any additional grams of greenhouse gases to the atmosphere. And “our activities” encompass virtually everything, ranging from powering our cities to cultivating our food sources. Environmental impacts and policies will play a crucial role in shaping the processes and approaches we adopt in the coming years. The Paris Agreement [3] mandates that countries outline their climate actions, known as nationally determined contributions (NDCs), and encourages the submission of long-term strategies (LT-LEDS). To limit global warming to  $1.5^{\circ}\text{C}$  by the end of the century,  $\text{CO}_2$  emissions must be reduced by 45% compared to 2010 levels by 2030. In contrast, a 2022 study [4] analyzed the officially submitted data from 196 countries and found that the projected emissions for 2030 are estimated to be 6% to 13% higher than those in 2010. Only by 2050, if long-term strategies are successfully achieved, we can expect greenhouse gas (GHG) emissions to be reduced by 32%-34% compared to 2010 levels. In terms of global mean surface temperature, if NDCs and LT-LEDS are fully implemented on schedule, we may witness a 21st-century median peak of approximately  $2.0^{\circ}\text{C}$  with a 42%-52% probability of exceeding this threshold. Keeping global temperatures below  $1.5^{\circ}\text{C}$  is viewed as the goal for preventing severe climate change and, in extreme cases, reducing the likelihood of a runaway climate instability that could result in an ice-free planet. The differences between a mean global temperature increase of  $1.5^{\circ}\text{C}$  and  $2.0^{\circ}\text{C}$  are substantial [5]. The risks of extreme heatwaves, heavy precipitation, floods, wildfires, sea-level rise, and soil droughts will significantly differ between these two scenarios, as will the proportion of the population exposed to these hazards. In essence, climate change acts as a disaster and poverty generator; the greater the temperature change, the higher the likelihood of adverse outcomes. And these consequences also extend to the health and the food systems.

Energy plays a significant role in the annual release of approximately 50 billion tonnes of  $\text{CO}_2$  equivalents. These are the emissions that are drifting Earth away from the natural balance of the carbon cycle. While electricity is responsible for nearly 30% of these 50 billion, the methods used for producing goods and growing food account for another 50% of the total emissions. Interestingly, during the COVID-19 pandemic, greenhouse gases release experienced only a minor decline. This emphasizes that merely shutting down certain sectors of the economy and transportation, along with their associated economic consequences, is far from sufficient. We often fail to recognize the extent of our dependence on fossil fuels and how deeply ingrained they are in our lives. Virtually everything we do or use has, at some point and in some way, contributed to the release of greenhouse gases – more than we would like to admit and more than we would like to give up. A comprehensive restructuring of each sector is therefore crucial if we aspire to realistically achieve the goal of net-zero emissions. Undoubtedly, this presents an immense challenge, perhaps unlike any we have ever faced before. If we consider the historical inertia of the energy sector in implementing changes, high capital costs often meant that new technologies took decades to be adopted on a large scale and to produce a significant portion of the global energy supply [7].

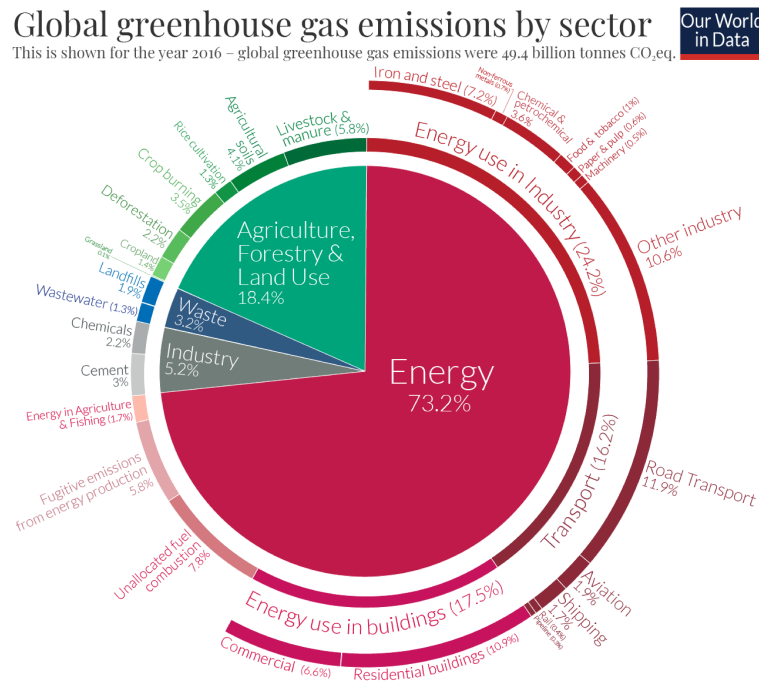


Figure I.1: **Global greenhouse gas emissions by sector.** Retrieved from Ref. [6].

In the meanwhile, we have grown accustomed to the idea of inexpensive, reliable electricity available at the flick of a switch. Today, electricity production relies on coal for approximately 36%, and oil and gas account for roughly 26%. This has been the case since 1985. As global energy demands have increased, the proportion of electricity generated from these sources has remained constant. While wealthier nations are reducing their dependence on fossil fuels, many developing countries are climbing the economic ladder, and coal-fired power plants remain the most affordable and accessible option for them.

Hydropower and other renewable energy sources, which currently constitute 28% of total energy production, along with nuclear power plants (10%), represent the most valuable tools we have at our disposal for generating clean energy. Nevertheless, things start to be complicated when these two alternatives are mentioned together and the conversation might become quite complex. Many suggest we should simply increase our use of renewables to supply the energy the world needs. However, factors such as power density, intermittency, geographic constraints, and seasonality suggest that although we must significantly expand our use of renewable energy sources, these alone cannot provide a complete solution. The intrinsic dependence on specific geographical conditions (e.g., sunny and windy places or the presence of rivers and hills) also complicates the transportation of energy from production sites to consumption areas across countries, as most of the transmission grid has not been designed with this in mind [9]. In a 2018 study, researchers examined 1000 scenarios and found that the most cost-effective and arguably most feasible approach to achieving zero emissions in the United States consistently involves a source of clean and continuously available power [10]. Nuclear



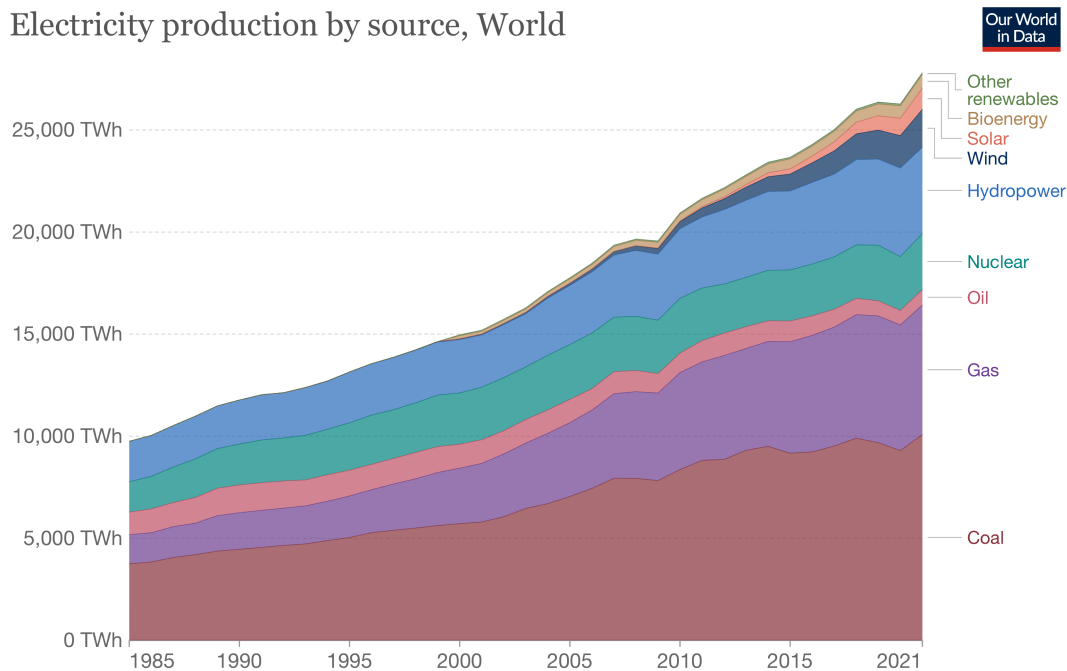


Figure I.2: **Global electricity production by source.** Retrieved from Ref. [8].

power plants could provide this, especially considering that by 2050 we might need to produce three times more electricity than we do today. Bill Gates summarized nuclear power as follows: «*it is the only carbon-free energy source that can reliably deliver power day and night, through every season, almost anywhere on Earth, that has been proven to work on a large scale*» [9]. Additionally, it has one of the lowest CO<sub>2</sub> emissions per kilowatt-hour generated. However, its drawbacks are evident and public opinion has been quite hesitant to encourage its use, even though coal has been significantly more dangerous to human health. Yet, it must be said that over the last decades «*instead of innovating the sector, we just stopped trying to advance the field*» [9], accepting the obsolescence of the technology used therein.

As we increase our share of renewables in the coming years, it becomes increasingly important to focus on solving the challenges of intermittency and periods of over and undergeneration. Certainly, one might argue that intermittency issues can be addressed by storing all the necessary energy in batteries. While this may be true to some extent, grid-scale batteries introduce an additional cost on top of what we already pay for energy production. It is essential to recognize that economics plays a pivotal role in the adoption of green technologies [11], as financial feasibility represents «*L'Amor che move il sole e l'altre stelle*»<sup>1</sup> [12]. Choosing a green technology over a conventional one often incurs in a premium cost, known as the “green premium”. In a narrow-margin economy, a green premium that raises the price of a commodity by 20% can significantly impact a

<sup>1</sup>Literally: *the Love which moves the sun and the other stars.*

## Introduction

---

company's viability. The goal is to drive innovation in zero-carbon technologies globally, eventually minimizing the impact of green premiums. Unfortunately, existing energy storage solutions have not yet achieved the required economic viability or performance level to act as reliable alternatives. Although economic feasibility is crucial, it may not be sufficient to accelerate change at the necessary pace. This highlights the need for a truly disruptive technology capable of reversing climate change [13–15].

It is not an overstatement to say that every aspect concerning the things we do, even those we may not yet be aware of, requires a reevaluation. Our society was not built around the zero-net emissions pledge but rather around economic forcing. Despite the high inertia, building a global consensus and being equipped with effective policies can bring the goal within closer reach. As Bill Gates emphasizes in his book, “we already have some of the tools we need, and as for those we don't yet have, [...] we can invent them, deploy them, and, if we act fast enough, avoid a climate catastrophe” [9]. Echoing Turing's words, it is crucial to consider that, as we face an unprecedented challenge, we must pursue ideas that have never been explored before.

---

At this point, readers may wonder about the connection between climate change, the need for an energy revolution, and this thesis. Admittedly, it would be difficult for any single thesis to comprehensively address the multitude of challenges previously discussed. My aim in presenting this introduction was to establish a broader context before delving into the hundreds of details of the specific topics discussed in the subsequent chapters. In writing this thesis, my goal was to portray concepts not as an aseptic collection of knowledge but as instruments that have assisted me in asking deeper and more relevant questions or simply ignited curiosity. As I have learned, the framework and tools that shape our thinking are often more valuable than the individual thoughts themselves. I acknowledge that I may not have completely fulfilled my desire, but the process has been an incredibly valuable exercise.

The connection between energy breakthroughs and this thesis lies in the exploration of nuclear isomers and the development of methods to excite and control their decay. Similar to electrons moving between atomic shells, releasing photons, or transferring energy to other bound electrons, nuclei can undergo comparable processes, albeit generally on a different energy scale. These excited states have been found to persist for a time comparable to a human lifetime and, in one case, even exceeding the age of the Universe. For decades, their high power density and potential absence of leakage have made isomers ideal candidates for clean, high-density, and long-lasting nuclear batteries. However, despite numerous efforts, controlling their decay and excitation remains elusive. This has prompted investigations into processes that could lead to the feeding and depletion of these states, which could be eventually controlled by an external switch.

In **Chapter 1**, I will present nuclear isomers starting from their discovery that happened in 1921. In this chapter, I followed the overall structure common to many topical reviews and to the book titled “Nuclear Isomers: A Primer” [16]. While doing so, I

tried to condense all the concepts learned from several books that have been instrumental in this journey. With the hope of having written a harmonious and organic text, this may serve as a starting point for various branching paths that can be explored through the cited literature.

In the subsequent chapters, I discuss three mechanisms of nuclear excitation that might be used to feed or deplete isomers. These mechanisms include the capture of a free particle (electron or muon) or the absorption of a photon. In **Chapter 2**, I provide a historical review of the nuclear excitation by electron capture (NEEC) process, along with two of our publications on the subject. In **Chapter 3**, the process of nuclear excitation by free muon capture (NE $\mu$ C) is introduced as the muonic counterpart of the NEEC process, accompanied by our publication on the topic. In **Chapter 4**, I discuss the experiment I had the opportunity to design and implement at EPFL to study nuclear excitations in neutral plasma generated by a femtosecond laser pulse. This includes a theoretical analysis of the experimental conditions and the study of the direct photoexcitation process, as well as a discussion of the experimental results.

The aim is lacking; 'why?' finds no answer.  
— Friedrich Nietzsche



# 1 Nuclear Isomers

It has been nearly 100 years since Otto Hahn, while searching for the precursor of actinium, realized that the newly discovered radioactive product UZ, was not only isotopic with the previously identified UX<sub>2</sub>, but also shared with it the same mass number [17–20].

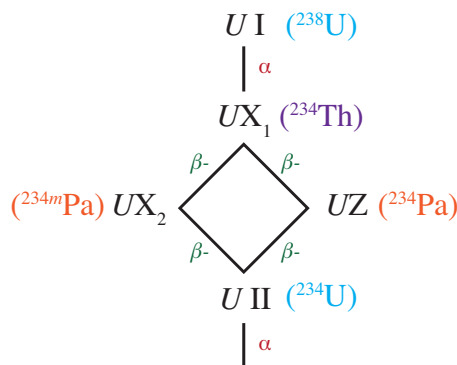


Figure 1.1: **First discovered isomer pair.** Pattern of disintegration at the beginning of the uranium radioactive series with the isomeric pair UX<sub>2</sub> and UZ and modern identifications. The figure is redrawn from the original, published in Ref. [17].

UX<sub>2</sub> and UZ, later identified with <sup>234m</sup>Pa and <sup>234</sup>Pa as shown in Fig. 1.1, represent the first example of isomeric pair states. The word “isomer” was associated with excited nuclear states only in 1934 [21], in analogy to the chemical counterpart, interpreted as physical re-arrangement of the basic constituents: atoms for molecules and nucleons in the case of nuclei.

The definition of what could be accurately referred to as an isomer, particularly concerning the lifetime of the excited nuclear state, has changed over time [16, 20]. To facilitate the temporal and spatial isolation of nuclear excited states from the prompt radiation arising from production processes, experimental half-lives ranging from picoseconds to nanoseconds were required, depending on the particular decay product under observation. Lifetime measurements were initially limited by electronics and the

definition of isomer followed the technological evolution hand in hand. In 1997, the first version of the nuclear database NUBASE considered isomers as those excited states with half-lives longer than 1 ms [22]. Later on, in 2003 [23], the same database adopted the threshold of 100 ns, although there is no fundamental reason not to extend the definition also to shorter-living excited states. The most recent evaluation of such database (2020) lists 3340 nuclides and 1938 isomeric states having a half-life  $T_{1/2} \geq 100$  ns [24]. If a lower limit is considered for the definition of isomer ( $T_{1/2} \geq 10$  ns), as proposed by the Atlas of Nuclear Isomers [25], the number of identified excited states becomes 2623 as of November 2022. The occurrence of isomers with  $T_{1/2} \geq 10$  ns across the whole nuclear chart is presented in Fig. 1.2, using data extracted from the LiveChart of Nuclides [26]. The total number of retrieved isomers is 2367, which is slightly lower than the number reported by the Atlas [25], which uses multiple databases.

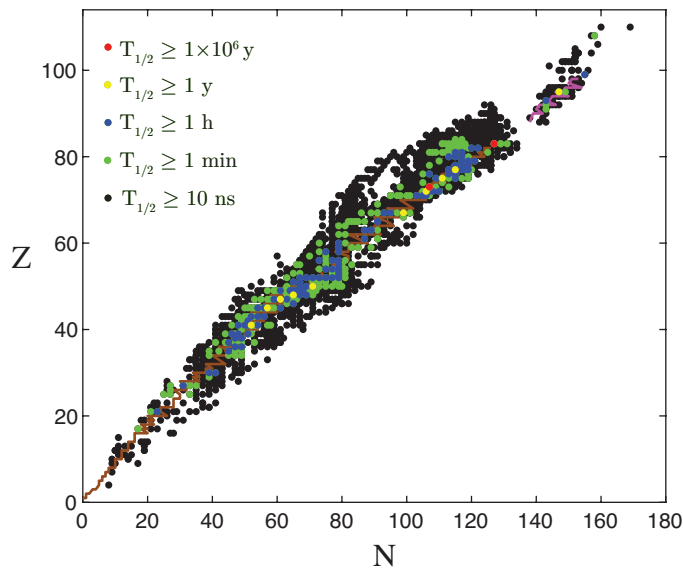


Figure 1.2: **Isomeric states as a function of the neutron and proton numbers along the whole nuclear chart.** Half-lives are split into five categories, distinguished by different colors. The line of beta-stability is composed of two parts: stable nuclei in brown and  $\beta$ -stable nuclei with half-lives higher than 100 years in magenta.

Fig. 1.3 reveals that the quasi-totality (2091) of the nuclear excited states have a lifetime smaller than 1 min, and the number of levels rapidly declines as the timescale increases, which is expected. Of the total number of states, only 99 isomers have a lifetime longer than one hour, and merely two isomers have a lifetime that exceeds one million years. Notably, isomers with longer lifetimes are predominantly situated in the vicinity of the line of  $\beta$ -stability. Although isomers can be found throughout the nuclear chart, from the lightest isomer represented by  $^{12}\text{Be}$  to the heaviest isomer given by  $^{279}\text{Ds}$ , it is evident that they tend to accumulate in proximity to the proton and neutron magic numbers, as depicted in Fig. 1.4. In addition, also the energy landscape offers a broad spectrum of

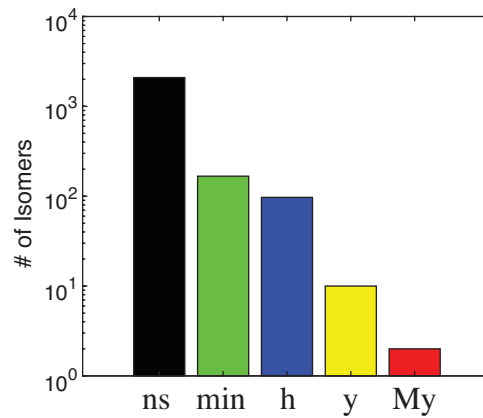


Figure 1.3: **Histogram of the isomer half-lives.** Color code follows the one shown in Fig. 1.2. The label “ns” includes all the isomer in the interval 10 ns–1 min, the label “min” those in the interval 1 min–1 h and so on.

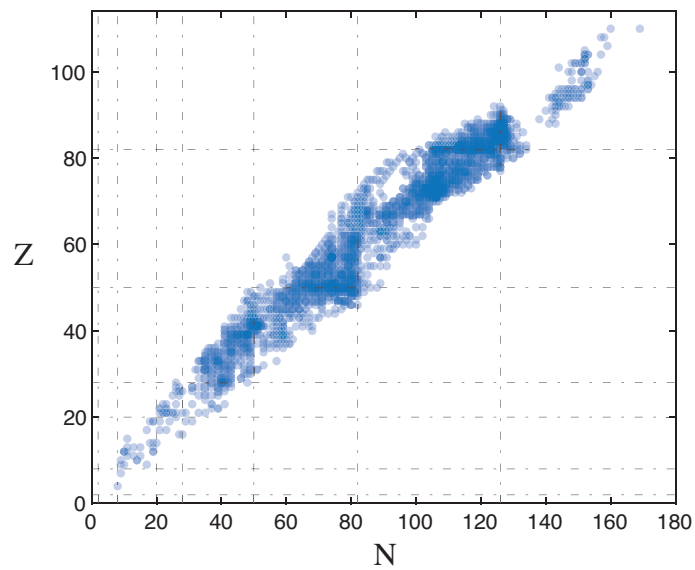


Figure 1.4: **Scatter plot of the distribution of isomers along the nuclear chart.** The dashed vertical and horizontal lines represent the neutron and proton magic numbers, respectively. The markers are rendered with a transparency of 75%; hence, darker markers indicate a higher density of plotted points.



possibilities. Isomers are found to exist across a range of energies, from the low-lying 8 eV state of  $^{229\text{m}}\text{Th}$  and the 76 eV state of  $^{235\text{m}}\text{U}$  to the 13.67 MeV energy level of  $^{208\text{m}}\text{Pb}$ . Fig. 1.5 shows a 3D scatter plot that provides an overview of the energy and half-life distribution of isomers as a function of proton and neutron numbers. Moreover, the lateral panels incorporate information on the nuclear total angular momentum  $I$ .

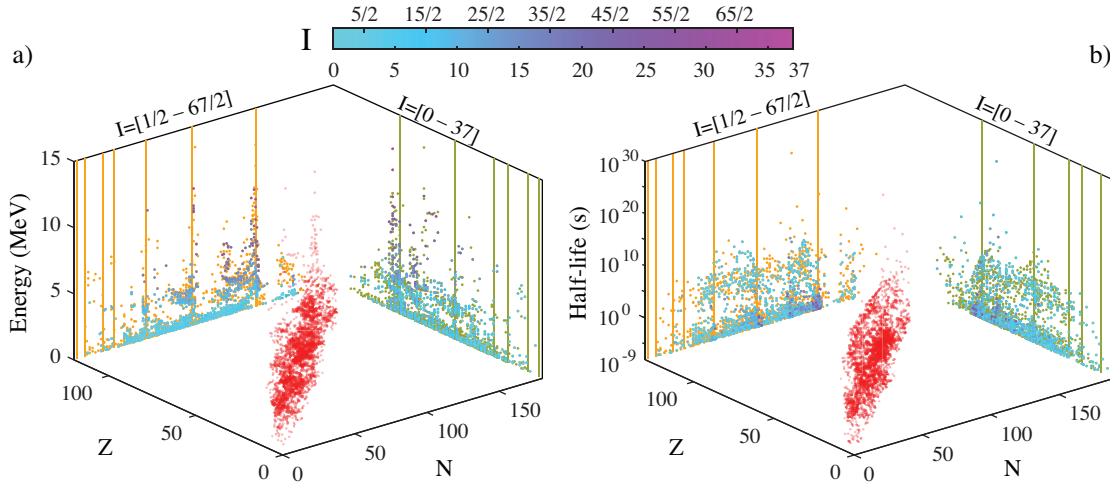


Figure 1.5: **Excitation energies and half-lives of isomers on the nuclear chart.** Occurrence of isomers on the nuclear chart with respect to the energy of excitation (a) and half-life (b). Red markers are rendered with 75% transparency, while projections on the side panels are fully opaque. The vertical orange and green lines correspond to neutron and proton magic numbers, respectively. The lateral panels are color-coded as follows: i) all isomers are represented by orange (projection on the neutron axis) or green markers (projection on the proton axis); ii) lateral panels involving the neutron axis display the total angular momentum  $I$  of half-integer spin nuclei following the dedicated colormap; iii) lateral panels involving the proton axis display the total angular momentum  $I$  of integer spin nuclei. The default color (orange or green) has been retained for isomers for which  $I$  was not defined. In cases of multiple  $I$  assignments, the minimum value has been chosen.

The tendency of high-energy states to congregate in proximity to the magic numbers is a result of the shell structure effects. As it was initially described in 1949 [27], a strong correlation exists between the appearance of isomers in odd- $A$  nuclei and the occupancy of intruder orbitals [28, 29]. This tendency gives rise to the formation of the so-called “islands of isomerism”. As the magic numbers are approached, the energy levels associated with two consecutive harmonic oscillator shells, with principal quantum numbers  $N$  and  $N-1$ , begin to compete in energy, as illustrated in Fig. 1.6. This competition leads to the formation of nuclear shells composed of levels having all the same parity (principal quantum number  $N-1$ ), with the addition of the level of highest spin of the immediately higher harmonic oscillator shell (principal quantum number  $N$ ), which has the opposite parity. This unique nature of high spin difference and opposite parity makes intruder orbitals play a significant role in the emergence of isomerism. Moreover, the energy levels

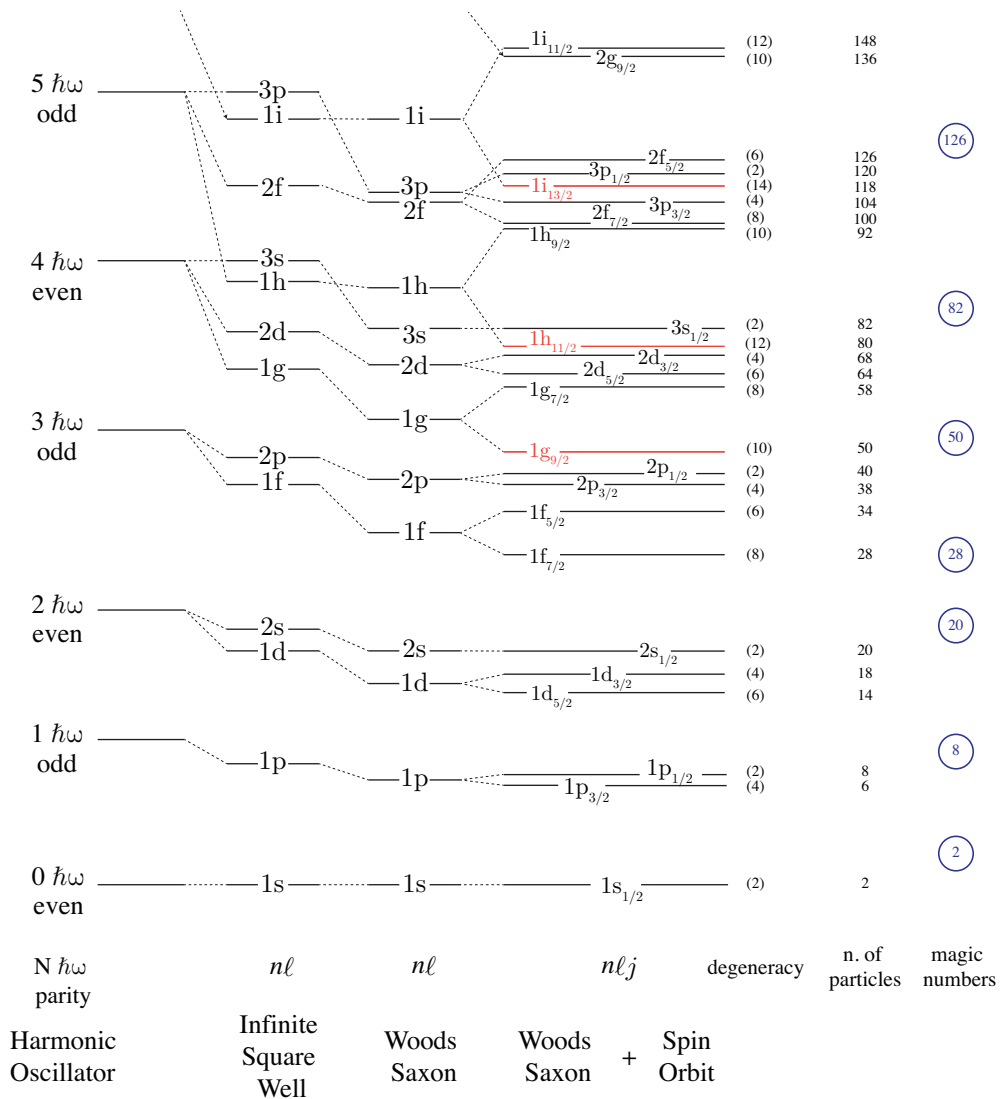


Figure 1.6: **Nuclear shell model and intruder orbitals.** Schematic energy levels of the nuclear shell model in case of harmonic oscillator potential, infinite square-well, Woods-Saxon potential [30] and Woods-Saxon plus spin-orbit coupling. Levels of degeneracy and magic numbers are displayed on the right. Intruder orbitals, highlighted in orange, exhibit opposite parity in comparison to the other members of the nuclear shell, being pushed below the magic gaps by the spin-orbit coupling. The figure is redrawn and adapted from Ref. [31].

at which these isomers lie tend to increase close to the magic numbers, as illustrated in Fig. 1.5a. The three-dimensional plots presented in Fig. 1.5 also offer a comprehensive view of the distribution of the total angular momentum I, commonly referred to as nuclear spin, across the entire nuclear chart. Extremely high-I isomers are observed again in correspondence with the magic number and are characterized by energies on the order

of several MeV. For half-integer spin nuclei, the highest value reported is  $(67/2^-)$  for the excited state at 10.28 MeV of  $^{151}\text{Er}$  with a half-life  $T_{1/2} = 0.42 \mu\text{s}$ . Overall  $^{212}\text{Rn}$  has the highest spin state isomer  $(37^-)$  at 12.21 MeV and  $T_{1/2} = 17 \text{ ns}$ . As evidenced from Fig. 1.5b, these high-I nuclei generally have a lifetime up to a fraction of ms, as for the case of  $^{179}\text{Re}$  with a  $T_{1/2} = 0.46 \text{ ms}$  and spin-parity  $I^\pi = (47/2, 49/2^-)$  at 5.41 MeV. In spite of their high spin values, the limited half-life of these high-I nuclear levels can be attributed to their high energies. As these levels are in the MeV region, it is highly probable for the isomer to have several underlying levels with similar spins that are connected by low-order multipolar  $\gamma$ -transitions. On the other hand, the lowest possible value for the angular momentum is 0. Thirty-five special cases of  $I = 0$  spin isomers can be identified from the LiveChart database, which have been reported in Appendix A.1. Among these, 18 cases lead to the lowest possible multipolar transition (E0) towards a  $0^+$  ground state in even-even nuclei (reported in Appendix A.2). Moving to the other extreme of the half-life distribution depicted in Fig. 1.5b, there is  $^{180m}\text{Ta}$  with  $T_{1/2} \geq 4.5 \times 10^{16} \text{ y}$ , which is Earth's only naturally occurring isomer and nature's rarest primordial nuclide [32]. Compared to the high-I states described earlier, the 77.2 keV isomer of  $^{180m}\text{Ta}$  has a distinct behavior. With a spin of  $9^-$  and relatively low energy, this isomer only has two lower-lying states: the  $1^+$  ground state and the  $2^+$  excited state. Thus only a transition involving a significant change in the nuclear spin could enable its decay. As will become clear later, these transitions are highly forbidden.

In addition to all the possible decay modes available to nuclei, such as  $\alpha$ -decay,  $\beta$ -decay, proton decay, and spontaneous fission, isomers can decay electromagnetically either by  $\gamma$ -emission, internal conversion (IC), and internal  $e^+e^-$  pair production [33, 34]. These processes ( $\gamma$ , IC and  $e^+e^-$ ) are generally referred to as isomeric transitions (IT) and are unavailable decay modes for the ground state. The appearance of isomers in nuclei is itself a manifestation of a mechanism that inhibits or hinders the transition of the nucleus to lower-lying states. This hindrance is often quantified using the Weisskopf hindrance factor, defined as [35]:

$$F_W = \frac{T_{1/2}^\gamma(\text{experimental})}{T_{1/2}^W(\text{theoretical})}, \quad (1.1)$$

where  $T_{1/2}^\gamma$  is the partial  $\gamma$ -decay half-life and  $T_{1/2}^W$  is the theoretical partial  $\gamma$ -decay half-life obtained using Weisskopf single-particle estimates [36, 37]. The probability of absorbing or emitting a photon of type  $\lambda$  (electric or magnetic) with energy  $E_\gamma = \hbar ck = \hbar\omega$  and angular momentum quantum numbers  $L$  and  $m$ , as a result of a transition between two nuclear states represented by their wavefunctions  $\Psi_i$  (initial) and  $\Psi_f$  (final), can be expressed as [38, 39]:

$$W_{\text{fi}}(\lambda, Lkm) = \frac{8\pi(L+1)}{\hbar L ((2L+1)!!)^2} \left( \frac{E_\gamma}{\hbar c} \right)^{2L+1} \left| \langle \Psi_f | \hat{\mathcal{M}}(\lambda, Lkm) | \Psi_i \rangle \right|^2, \quad (1.2)$$

where  $\hat{\mathfrak{M}}(\lambda, Lkm)$  is the multipole transition operator. Generally, measurements do not distinguish between different orientations  $m$  of the angular momentum  $L$ , thus one has to average on the initial orientations  $m_i$  of  $I_i$  and sum over all final states  $m_f$

$$W_{\text{fi}}(\lambda, L) = \frac{1}{2I_i + 1} \sum_{m_i, m_f} W_{\text{fi}}(\lambda, kLm). \quad (1.3)$$

Using the Wigner-Eckart theorem, it occurs the definition of reduced matrix elements [40]:

$$\begin{aligned} \langle I_f m_f, \Psi_f | \hat{\mathfrak{M}}(\lambda, Lkm) | I_i m_i, \Psi_i \rangle &= (-1)^{I_f - m_f} \times \\ &\times \begin{pmatrix} I_f & L & I_i \\ -m_f & m & m_i \end{pmatrix} \langle I_f, \Psi_f || \hat{\mathfrak{M}}(\lambda, L) || I_i, \Psi_i \rangle. \end{aligned} \quad (1.4)$$

The sum over  $m_i$  and  $m_f$  can be performed taking advantage of the invariance under even permutation and the orthogonality conditions of the 3-j Wigner symbols [40]:

$$\sum_{m_i, m_f} \begin{pmatrix} I_i & I_f & L \\ m_i & -m_f & m \end{pmatrix}^2 = \frac{1}{2L + 1} (2L + 1) = 1, \quad (1.5)$$

since there are only  $(2L+1)$  value pairs  $(m_i, m_f)$  that satisfy the condition  $m_i - m_f + m = 0$  for which the Wigner 3-j symbol is not zero. Therefore, the probability (transition rate) of radiative nuclear transition between initial and final states can be expressed as:

$$W_{\text{fi}}(\lambda, L) = \frac{8\pi(L+1)}{\hbar L((2L+1)!!)^2} \left( \frac{E_\gamma}{\hbar c} \right)^{2L+1} B(\lambda L, I_i \rightarrow I_f). \quad (1.6)$$

$B(\lambda L, I_i \rightarrow I_f)$  is called “reduced transition probability” and can be defined in terms of the reduced matrix element of the electromagnetic multipole operator for an electric or magnetic transition:

$$B(\lambda L, I_i \rightarrow I_f) = \frac{1}{2I_i + 1} \left| \langle I_f, \Psi_f || \hat{\mathfrak{M}}(\lambda, L) || I_i, \Psi_i \rangle \right|^2. \quad (1.7)$$

The Wigner 3-j symbol also defines the selection rules for the nuclear transition as follows:

$$|I_i - I_f| \leq L \leq |I_i + I_f| \quad \text{with} \quad L > 0, \quad (1.8)$$

$$m_f - m_i = m. \quad (1.9)$$

Since the computation of the matrix element is ultimately related to the calculation of an integral of the form  $\int \Psi_f^* \hat{\mathfrak{M}} \Psi_i d^3r$ , an overall even-parity is required for the transition not to vanish:

$$\pi_i \pi_{\hat{\mathfrak{M}}_{\lambda L}} \pi_f = 1, \quad (1.10)$$

with  $\pi_{\hat{\mathfrak{M}}_{\lambda L}}$  being the parity of the multipole electric or magnetic radiation

$$\pi_{\hat{\mathfrak{M}}_{EL}} = (-1)^L \quad \text{and} \quad \pi_{\hat{\mathfrak{M}}_{ML}} = (-1)^{L+1}. \quad (1.11)$$

These selection rules imply that transitions of  $E$  and  $M$  types cannot occur with the same multipolarity  $L$  between the same pair of nuclear states. If a parity change is involved between the initial and final states ( $\Delta\pi = \text{yes}$ ), the radiation field must have odd parity, while when no change occurs ( $\Delta\pi = \text{no}$ ), the field must have even parity [41]. Hence, depending on the angular momenta of the states, one can have either E1, M2, E3 or M1, E2, M3, with their relative higher orders. Monopole E0 transitions ( $L = 0$ ) are not allowed to decay via single photon emission since the intrinsic spin of a photon is 1, and the total angular momentum transferred to it by the decay is  $L\hbar$ . Pure E0 decays, which correspond to transitions between  $I = 0$  states possessing the same parity – reported in Table A.2 in the case of isomers – usually proceed through the internal conversion process, in which an orbital electron is ejected from the atom into the continuum. When the excitation energies are greater than or equal to twice the mass of the electron ( $\geq 2m_e = 1022 \text{ keV}$ ), internal pair formation (IPF) becomes significant for E0 transitions. Alternative E0 decay modes involve two-quantum processes, such as pair  $\gamma$ -emission. However, the probabilities of these processes are generally very low, with branching ratios on the order of  $\sim 10^{-4}$  [42, 43].

Calculation of the matrix elements requires knowledge of the nuclear wavefunctions, which is generally the most challenging task. Weisskopf introduced rough estimates in the single-particle picture, where a nuclear excitation is due to a nucleon moving from one orbit to another, leaving the rest unaltered. In the limit of long wavelengths, i.e. the wavelength of the radiation is large with respect to the nuclear radius ( $E_\gamma \ll 197 A^{-1/3} \text{ MeV}$  [38]), it is possible to obtain the following expression for an electric multipole [38]:

$$\begin{aligned} \langle I_f, \Psi_f | \hat{\mathfrak{M}}(E, L) | I_i, \Psi_i \rangle &= \langle I_f, \Psi_f | e r^L Y_L(\theta, \phi) | I_i, \Psi_i \rangle \\ &= e \frac{1 + (-1)^{l_i + l_f + L}}{2} \langle f | r^L | i \rangle \sqrt{\frac{(2I+1)(2I_f+1)(2I_i+1)}{4\pi}} \\ &\times (-1)^{I_f - 1/2} \begin{pmatrix} I_f & I & I_i \\ -1/2 & 0 & 1/2 \end{pmatrix}, \end{aligned} \quad (1.12)$$

where the radial integral  $\langle f | r^L | i \rangle$  is defined as

$$\langle f | r^L | i \rangle = \int_0^\infty R_f(r) r^L R_i(r) r^2 dr, \quad (1.13)$$

with  $R_i(r)$  and  $R_f(r)$  being the radial part of the nuclear wavefunctions. A similar expression can be written for a magnetic multipole. Weisskopf obtained an estimate of the radial integral by replacing  $R_i \sim R_f$  with a constant up to the nuclear radius ( $r \leq R_0$ )

and zero outside:

$$\langle f|r^L|i\rangle = \int_0^\infty R_f(r)r^L R_i(r)r^2 dr \sim \frac{\int_0^{R_0} r^L r^2 dr}{\int_0^{R_0} r^2 dr} = \left(\frac{3}{L+3}\right)R_0^L. \quad (1.14)$$

In this expression, the integral in the denominator has been included for normalization [41]. Furthermore, considering  $I_i = L + 1/2$ ,  $I_f = 1/2$ ,  $l_i = L$  and  $l_f = 0$  [37, 38], the following expressions were obtained for the reduced transition probabilities:

$$\begin{aligned} B_W(EL) &\simeq \frac{(1.2)^{2L}}{4\pi} \left(\frac{3}{L+3}\right)^2 A^{2L/3} e^2 \cdot fm^{2L}, \\ B_W(ML) &\simeq \frac{10}{\pi} (1.2)^{2L-2} \left(\frac{3}{L+3}\right)^2 A^{(2L-2)/3} \mu_N^2 \cdot fm^{2L-2}, \end{aligned} \quad (1.15)$$

where the formula  $R_0 = 1.2A^{1/3}$  fm has been used for the nuclear radius [39, 44]. The reduced transition probability is given in units of  $e^2 \cdot fm^{2L}$  for electric multipoles and in units of  $\mu_N^2 \cdot fm^{2L-2}$  for magnetic multipoles. Finally, Eq. 1.6 can be rewritten for the two types of multipoles as follows [39]:

$$\begin{aligned} W_{\text{fi}}(E, L) &= \alpha \hbar c \frac{8\pi(L+1)}{\hbar L((2L+1)!!)^2} \left(\frac{E_\gamma}{\hbar c}\right)^{2L+1} B(EL, I_i \rightarrow I_f), \\ W_{\text{fi}}(M, L) &= \alpha \hbar c \left(\frac{\hbar}{2M_{\text{p}}c}\right)^2 \frac{8\pi(L+1)}{\hbar L((2L+1)!!)^2} \left(\frac{E_\gamma}{\hbar c}\right)^{2L+1} B(ML, I_i \rightarrow I_f), \end{aligned} \quad (1.16)$$

where the Gaussian units relations  $e^2 = \alpha \hbar c$  and  $\mu_N = \frac{e\hbar}{2M_{\text{p}}c}$  have been used to convert the numerical values in SI units. Table 1.1 lists the transition rates and Weisskopf's single-particle estimates of the reduced transition probability for the first four multipole orders.

Table 1.1: **Transition rates  $W$  ( $s^{-1}$ ) and Weisskopf's estimates of the reduced transition probabilities  $B_W(\lambda L)$  for the electric ( $e^2 \cdot fm^{2L}$ ) and magnetic ( $\mu_N^2 \cdot fm^{2L-2}$ ) multipoles.** Energies  $E$  are in units of MeV. For physical constants, the 2018 CODATA recommended values have been used [45].

$L$	Electric		Magnetic	
	$W$ ( $s^{-1}$ )	$B_W(EL)$	$W$ ( $s^{-1}$ )	$B_W(ML)$
1	$1.590 \times 10^{15} E^3 B(E1)$	$6.446 \times 10^{-2} A^{2/3}$	$1.758 \times 10^{13} E^3 B(M1)$	1.790
2	$1.225 \times 10^9 E^5 B(E2)$	$5.940 \times 10^{-2} A^{4/3}$	$1.355 \times 10^7 E^5 B(M2)$	$1.650 A^{2/3}$
3	$5.708 \times 10^2 E^7 B(E3)$	$5.940 \times 10^{-2} A^2$	$6.312 \times 10^0 E^7 B(M3)$	$1.650 A^{4/3}$
4	$1.697 \times 10^{-4} E^9 B(E4)$	$6.285 \times 10^{-2} A^{8/3}$	$1.876 \times 10^{-6} E^9 B(M4)$	$1.746 A^2$

Considering a medium-weight nucleus with  $A = 125$  and a transition energy of  $E = 1$  MeV, electric radiation is about two orders of magnitude more likely than magnetic multipole transition for a given order  $L$ , despite never competing for the same transition due to selection rules. The probability of emission rapidly decreases with higher multipole orders. Within the first ten multipoles, two consecutive electric transitions differ by four to five orders of magnitude, as do two consecutive magnetic transitions. Therefore, a given transition is generally dominated by the two lowest multipole orders  $L$ . The two lowest multipole orders allowed by angular momentum and parity selection rules are reported in Table 1.2. In parity-favored transitions, the electric radiation of order  $L$  competes

Table 1.2: **Parity-favored and parity-unfavored transitions.** The table shows the lowest possible multipoles for electric and magnetic radiations from the initial  $I_i, \pi_i$  to the final nuclear state  $I_f, \pi_f$ . This table is adapted from Ref. [37].

$I_i \neq I_f$		
	Electric	Magnetic
Parity-favored $\pi_i \pi_f = (-1)^{I_i - I_f}$	$L =  I_i - I_f $	$L =  I_i - I_f  + 1$ none if $I_i$ or $I_f = 0$
Parity-unfavored $\pi_i \pi_f = (-1)^{I_i - I_f + 1}$	$L =  I_i - I_f  + 1$ none if $I_i$ or $I_f = 0$	$L =  I_i - I_f $
$I_i = I_f \neq 0$		
	Electric	Magnetic
$\pi_i = \pi_f$	L=2 none if $I_i = I_f = 1/2$	L=1
$\pi_i = -\pi_f$	L=1	L=2 none if $I_i = I_f = 1/2$

with the magnetic radiation of the next higher order ( $L' = L + 1$ ), while the inverse is true in the case of parity-unfavored transitions. The estimates presented in Table 1.1 lead to the following relations:

$$\frac{W_W(EL')}{W_W(EL)} \simeq \frac{W_W(ML')}{W_W(ML)} \simeq 10^{-5}, \quad (1.17)$$

$$\text{parity-favored} \quad \frac{W_W(ML')}{W_W(EL)} = \frac{W_W(ML')}{W_W(ML)} \frac{W_W(ML)}{W_W(EL)} \simeq 10^{-5} 10^{-2} = 10^{-7}, \quad (1.18)$$

$$\text{parity-unfavored} \quad \frac{W_W(EL')}{W_W(ML)} = \frac{W_W(EL')}{W_W(EL)} \frac{W_W(EL)}{W_W(ML)} \simeq 10^{-5} 10^2 = 10^{-3}.$$

In the previous equations,  $W_W(\lambda L)$  represents the transition rate obtained using Weisskopf's single-particle estimates. These estimates predict purely electric radiation in

parity-favored transitions and purely magnetic radiation in parity-unfavored transitions, although with very different relative strengths. While magnetic radiation is much smaller than electric radiation in parity-favored transitions, the electric multipole competes more effectively with the magnetic one in parity-unfavored transitions. Actual transition rates can vary by several orders of magnitude due to the specific nuclear properties and nature of the excitation mode. While parity-favored transitions are experimentally found to be usually purely electric, it is possible to have  $W(EL') \geq W(ML)$  in parity-unfavored transitions, despite Weisskopf's estimates predicting primarily magnetic radiation. Therefore, Weisskopf's estimates are intended to be an orientation tool to unveil the physics behind the transition rather than a proper theoretical estimate of experimental values. A much smaller  $\gamma$ -decay rate than the one predicted by the estimates could indicate a poor overlap between the initial  $\Psi_i$  and final  $\Psi_f$  nuclear wavefunctions, while a larger rate might indicate that more than one single nucleon is responsible for the transition, acting collectively and leading to vibrational or rotational excitation modes [39]. For this reason, Weisskopf's estimates are used as a unit (referred to as W.u.) to express the experimentally measured reduced transition probabilities.

### 1.1 Classification and nature of Isomers

Isomers can be classified into three main categories depending on the specific mechanism hindering their decay, which can occur in any combination: spin isomers in spherical nuclei, K-isomers in axially-deformed nuclei, and shape isomers in nuclei exhibiting shape-coexistence [16, 20]. Fig. 1.7 provides a schematic visualization of the nuclear potential energy as a function of different nuclear variables such as spin, spin projection, and deformation for the three categories of isomers.

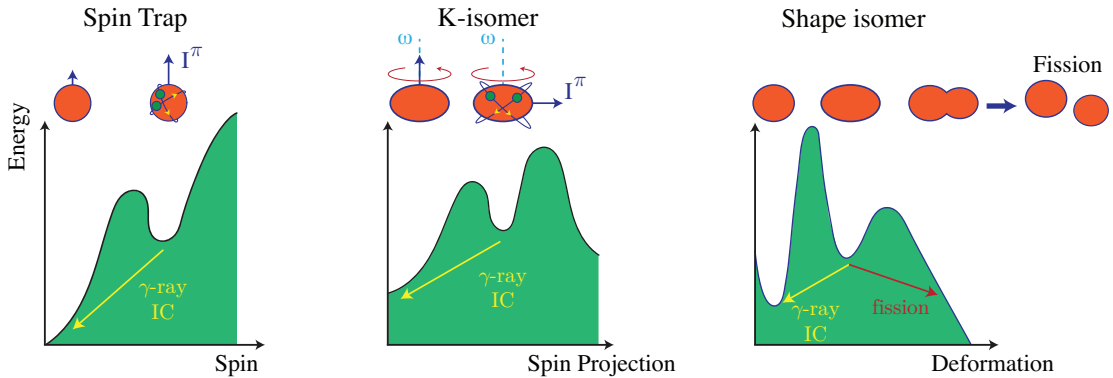


Figure 1.7: **Classification of nuclear isomers.** Nuclear potential energy as a function of spin variation, spin projections, and shape deformation. The blue arrows denote the nuclear spin ( $I^\pi$ ), while  $\omega$  indicates the rotational axis. The figure has been redrawn and adapted from Refs. [46, 47].



### 1.1.1 Spin Traps

The nature of spin traps reflects the findings summarized in Table 1.1, which show a strong suppression of transitions with a significant change in nuclear spin ( $\Delta I$ ) and low energy. These circumstances generally favor the competition of internal conversion for the isomer decay. Neglecting higher-order mechanisms, the total transition probability becomes:

$$W_T = W_\gamma + W_{IC} = W_\gamma(1 + \alpha_{IC}), \quad (1.19)$$

where  $\alpha_{IC}$  is the internal conversion coefficient (ICC). The actual half-life and lifetime of these excited nuclear levels are defined in terms of the total transition probability  $W_T$  as follows [39]:

$$\text{Half-life } T_{1/2} = \frac{\ln 2}{W_T}; \quad \text{Lifetime } \bar{T} = \frac{\int_0^\infty t e^{-W_T t} dt}{\int_0^\infty e^{-W_T t} dt} = \frac{1}{W_T} = \frac{T_{1/2}}{\ln 2}. \quad (1.20)$$

The explanation of isomerism in terms of forbidden  $\gamma$ -transition due to large spin variation was first proposed by Weizsäcker in 1936 [48]. In this vision, isomerism emerges whenever a large  $\Delta I$  exists between a state and all other levels lying below it. It is generally possible to talk about spin traps when the transition involves a  $\Delta I = L \geq 3$ , where Eqs. 1.16 predict a radiative half-life  $T_{1/2}^\gamma \geq 1$  min when  $E \sim 80$  keV.

In this context, Racah [49] and Flowers [50] introduced an additional quantum number, the seniority  $\nu$ , to indicate the number of unpaired nucleons for a given nuclear state. In even-even nuclei, all nucleons are paired, resulting in a seniority of  $\nu = 0$  and a ground state of  $I = 0^+$ . However, in odd-A and odd-odd nuclei, the unpaired nucleons (one for odd-A and two for odd-odd) are expected to determine the properties of the state, such as the angular momentum. Therefore, lower-lying excited states in such nuclei can be interpreted as transitions of odd particles between orbitals of the same shell. The representation of this interpretation can be seen in Fig. 1.7, where spin traps are drawn as two excited nucleons orbiting around a spherically symmetric core.

In odd-A nuclei, isomerism is not expected to occur up to  $Z$  or  $N = 20$ . This is because the maximum angular momentum of the shells is  $5/2$  and the maximum  $\Delta I = 2$ , as seen in Fig. 1.6. When  $20 \leq (Z, N) \leq 38$ , the levels  $f_{7/2}$ ,  $f_{5/2}$ , and  $p_{3/2}$  are being filled with the highest possible multipolar transition still of the order  $L = 2$ . When  $(Z, N) \geq 38$ , the orbitals  $g_{9/2}$  and  $p_{1/2}$  compete for the ground state with a spin difference of  $\Delta I = 4$ , resulting in the emergence of isomeric states. Thus, the nuclear shell model predicts the first “island of isomerism” in the range  $39 \leq (Z, N) \leq 49$  [29, 37]. After shell closure at the magic number 50, competition begins between the intruder orbital  $g_{7/2}$  and the level  $d_{5/2}$ , which are completely filled for  $(Z, N) = 64$ . Since  $\Delta I = 2$ , no long-lived excited states are expected in this range; however, isomerism can emerge just before  $(Z, N) = 64$  due to transitions to the empty higher levels ( $h_{11/2}$  or  $d_{3/2}$ ), which are relatively close in energy. The occurrence of isomers should increase towards the end of the shell due to the energy competition of the  $h_{11/2}$  (intruder),  $s_{1/2}$  and  $d_{3/2}$  orbitals up to shell closure at 82, giving rise to the second “island of isomerism”. In the range  $82 \leq (Z, N) \leq 100$ ,

the lowest energy state is determined by the competition between the  $h_{9/2}$  and  $f_{7/2}$  orbitals, which are connected at most by a quadrupolar transition. Beyond  $(Z, N) = 100$ , competition involves the low-spin orbitals ( $p_{3/2}$ ,  $p_{1/2}$  and  $f_{5/2}$ ) and the intruder orbital  $i_{13/2}$ , leading to the emergence of the third “island of isomerism”. The distribution of isomers, shown in Fig. 1.8, with half-lives  $T_{1/2}$  longer than 60 s and excitation energy  $E$  below 1 MeV (to be fairly below the pairing gap), as a function of the odd nucleon number (either  $Z$  or  $N$ ) reveals the three distinct islands of isomerism. It is worth noting that, as expected, the lowest multipole radiation present is an  $E3$ .

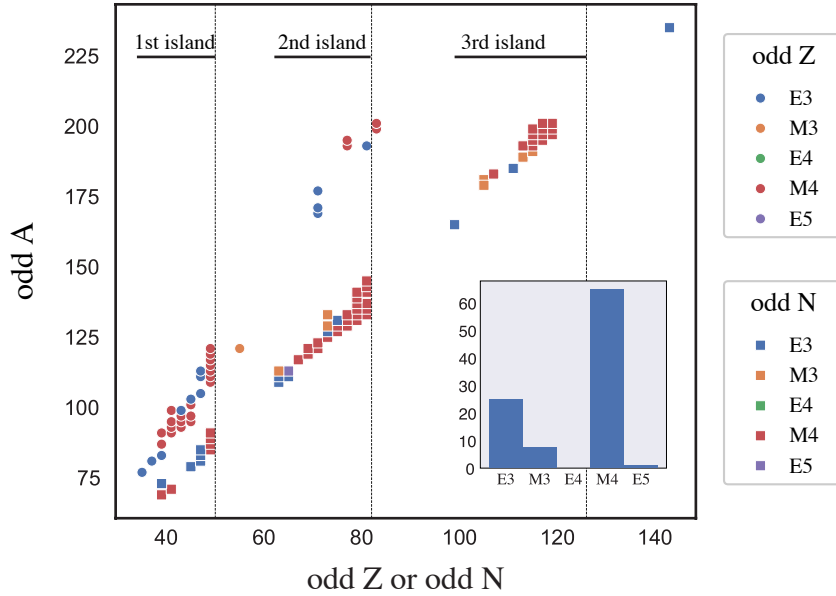


Figure 1.8: **Isomeric islands in odd-A nuclei.** Distribution of isomers occurring in odd-A nuclei with  $T_{1/2} \geq 60$  s and  $E < 1$  MeV plotted as a function of the odd nucleon number ( $Z$  or  $N$ ). The color code of each marker in the plot represents the lowest multipole order radiated by the isomeric level. When multiple transitions are possible (i.e., several decays towards lower-lying levels), the electric multipole has been preferred over the magnetic for the assignment in case of equal order  $L$  (see Eq. 1.18). For the remaining cases, the strongest relative transition was chosen. The inset of the figure shows the histogram of occurrence with respect to the multipolar decays. The vertical dashed lines in the plot represent nuclear magic numbers. The data used to generate this figure were extracted from the LiveChart of Nuclides [26].

In the first island, comprising nuclei with  $39 \leq (Z, N) \leq 49$ ,  $M4$  and  $E3$  are the lowest available transitions, with a certain prevalence of  $M4$  over  $E3$ . This is a result of the competition between the  $p_{1/2}$  orbital with odd parity and the  $g_{9/2}$  orbital with even parity. The decay modes are thus parity-unfavored (see Table 1.2) with parity change and spin change of four, which leads to  $M4$  transitions. However, when an odd number of nucleons occupy the orbitals, other resultant spins – rather than simply  $9/2$  – are also possible due to their coupling. Consequently, the formation of a level with a resultant angular momentum of  $7/2$  is responsible for the appearance of  $E3$  (octupole)

transitions [29]. In the second island, due to the competition between  $d_{3/2}$  (even),  $s_{1/2}$  (even) and  $h_{11/2}$  (odd) orbitals, both  $M4$  and  $E5$  are possible. Additionally, there are special cases where  $E3$  and  $M3$  transitions occur [29]. In the third island a similar situation emerges between  $i_{13/2}$  (even),  $f_{5/2}$  (odd),  $p_{3/2}$  (odd) and  $p_{1/2}$  (odd) orbitals. A spin difference between four and six and a parity change allow for multipoles up to  $M6$ , although none is observed. It is also interesting to note that no  $E4$  transitions are immediately found: this is predicted by the shell model since the levels in competition involve a parity change. Nevertheless, some special cases, such as  $^{179}\text{W}$  and  $^{185}\text{W}$ , exhibit both  $E4$  and a much stronger  $M3$  transition, which cannot be easily assigned using the same logic. Among the three islands, there is a strong predominance of the  $M4$  (65 cases) and  $E3$  (25 cases) transitions. Only one occurrence of a pure  $E5$  transition is observed for  $^{113}\text{Cd}$ , although the primary decay is through  $\beta$ -emission. It is worth mentioning that the  $E5$  was also considered to be the highest order of multipolar decay ever observed in isomers until very recently (March 2023), when an  $E6$  (hexacontatetrapole) 3.04 MeV  $\gamma$ -decay was confirmed in  $^{53\text{m}}\text{Fe}$  [51, 52].

In even-even nuclei ( $\nu = 0$ ), the situation differs from the odd- $A$  case. Here, the excitation of a nucleon requires the breakup of a pair resulting in the creation of a hole below the Fermi level and an unpaired particle, forming what is called a two quasi-particle (2-qp) configuration. As a result, the excitation spectrum of even-even nuclei is expected to lie entirely above the pairing gap, which is of the order of  $2\Delta \sim 12A^{-1/2}$  MeV, except for those states that arise from collective motions [47]. This pairing gap is typically too high to permit the occurrence of long-lived excited states.

Compared to even-even nuclei, odd-odd nuclei already have a 2-qp configuration in their ground state without the need to break a pair. This means that the excitation spectrum of odd-odd nuclei consists of two parts: one below the pairing gap due to the excitation of the two quasi-particles and one above it due to the breaking of an additional pair and the consequent formation of a 4-qp configuration. An interesting observation can be made from Fig. 1.3: the only two isomers with a half-life  $T_{1/2} \geq 1$  My are double-odd spin trap nuclei, namely  $^{180\text{m}}\text{Ta}$  and  $^{210\text{m}}\text{Bi}$ , both lying very close to the line of  $\beta$ -stability, as illustrated in Fig. 1.2.

### 1.1.2 K-Isomers

The second category of isomers depicted in Fig. 1.7, highlights the importance of conserving the direction of the angular momentum with respect to a symmetry axis, rather than its magnitude, during a nuclear transition. This makes already evidently clear that this hindrance mechanism belongs to nuclei that deviate from a spherical shape. In such cases, the solutions of the nuclear wave equations cannot be identified anymore with their  $\ell$  orbital angular momentum, as was done for those derived from the spherical models shown in Fig. 1.6, since  $\ell$  is no longer a “good” quantum number. In a deformed potential, the degeneracy of the single-particle orbit with total angular momentum  $j$  is not given by  $(2j + 1)$ , but rather determined by its projection along the symmetry axis (denoted by  $\Omega$ ). Due to reflection symmetry, the degeneracy is reduced

to two with  $\pm \Omega$  sharing the same energy, while distinct projections result in different energies [41]. These considerations led to the introduction of the  $K$  quantum number in 1955 as the projection of the total angular momentum  $I$  along the symmetry axis of the deformed nucleus [53], as depicted in Fig. 1.9.

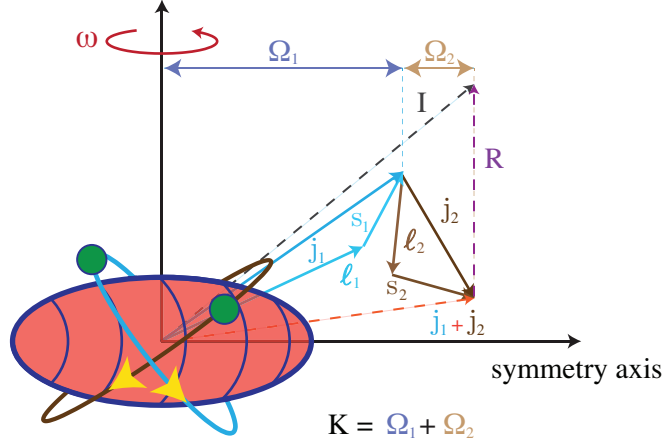


Figure 1.9: **Definition of the  $K$  quantum number as the projection of  $I$  along the symmetry axis of the deformed nucleus.** In the case of a prolate spheroid, which is the most common shape of deformed nuclei, the long axis is the symmetry (deformation) axis, while the short axis is the one around which the collective motion takes place with angular speed  $\omega$ . In this drawing, the total angular momentum  $j$  originates from two unpaired nucleons (2-qp excitation). The nuclear spin is given by  $\mathbf{I} = \mathbf{j} + \mathbf{R}$ , where  $\mathbf{R}$  is the rotational angular momentum. The figure has been redrawn from Ref. [16].

Considering its definition, it would be legitimate to expect transitions to obey the following selection rule, in addition to those in Eq. 1.11:

$$|K_i - K_f| \leq \Delta I \leq L, \quad (1.21)$$

given that a radiation of multipolarity  $L$  cannot change the angular momentum projection by more than  $|L|$ . In Ref. [53], the nuclear motion is divided into intrinsic (which leads to a rearrangement of the internal structure of the nucleus) and rotational (where the internal structure is preserved but rotating at different angular velocities) modes, allowing the wavefunction to be expressed as the product of two independent parts. However, deviations from this model and especially mixing between states do not make Eq. 1.21 a strict selection rule, as those in Eq. 1.11 are. Violation of Eq. 1.21 can act as a retardant for the decay, suggesting that  $K$  is only approximately conserved during the process. Interestingly,  $K$ -forbidden transitions – which violate this selection rule – are more likely to occur as long as they involve small multipole radiations rather than  $K$ -allowed transitions that require a high spin  $\Delta I$  variation. In reason of these considerations, the difference between the multipolarity order  $L$  and  $\Delta K$  is defined as the degree of

forbiddenness:

$$v = \Delta K - L. \quad (1.22)$$

In continuation with the definition of the Weisskopf hindrance factor in Eq. 1.1, which aims to carry information about the multipolarity and energy of the decay, it is possible to define a reduced hindrance factor that also includes the degree of forbiddenness [35]:

$$f_v = (F_W)^{1/v}. \quad (1.23)$$

A historical example of a K-isomer is the case of  $^{180\text{m}}\text{Hf}$ , where the first rotational band was ever observed [54–57]. The isomer in question has  $I^\pi = 8^-$ , excitation energy  $E = 1.14 \text{ MeV}$  and half-life  $T_{1/2} = 5.5 \text{ h}$ , as reported in Fig. 1.10. This state could

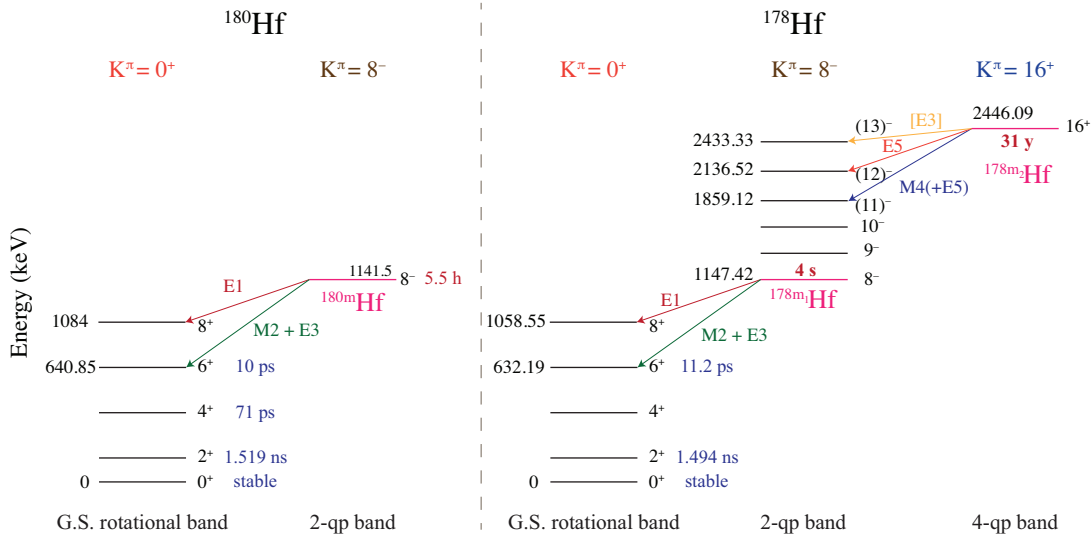


Figure 1.10: **Appearance of K-isomers in the energy level schemes of  $^{180}\text{Hf}$  (left) and  $^{178}\text{Hf}$  (right).** Both isotopes exhibit the characteristic rotational bands of even-even nuclei. Energies,  $I^\pi$ , and half-lives are provided for selected levels of interest. **(left)** The  $^{180\text{m}}\text{Hf}$  isomer is located in the 2-qp band with  $K = 8$ . The two transitions possible from this level,  $E1$  and  $M2 + E3$ , require  $\Delta K = 8 \gg L$ , making them highly forbidden. **(right)** In the case of  $^{178}\text{Hf}$ , the first isomer  $^{178\text{m}_1}\text{Hf}$  is found in the 2-qp  $K^\pi = 8^-$  band, with a half-life of 4 s. The second isomer  $^{178\text{m}_2}\text{Hf}$  is the result of the combination of two 2-qp  $K^\pi = 8^-$  excitations, leading to a 4-qp configuration of  $K^\pi = 16^+$  [57]. Values in round parenthesis are uncertain, while those in square brackets are derived from theory. The data used for this figure were extracted from the ENSDF database [58].

decay towards the lower-lying  $8^+$  or  $6^+$ , through the small radiation multipoles  $E1$  or  $M2 + E3$ , respectively. However, the high value of the hindrance factor  $F_W \sim 10^{16}$  cannot be explained by a simple variation of  $\Delta I$ . These transitions were found to be 7-fold K-forbidden ( $v = 8 - 1 = 7$ ). This is because the lower state of the first rotational band – where the isomer was found – has  $K = 8$ , while the lower-lying states ( $8^+$  and  $6^+$ ) belong to the ground state rotational band and have  $K = 0$ . Thus, the  $E1$  decay requires a

variation of the angular momentum orientation from a situation where there are  $8\hbar$  units of angular momentum along the symmetry axis ( $I^\pi = 8^-, K = 8$ ) to a configuration where the angular momentum is aligned along the rotational axis ( $I^\pi = 8^+, K = 0$ ), which is perpendicular to the axis of symmetry [59], as depicted in Fig. 1.7. Löbner showed that the hindrance factor for K-isomers scales with the degree of forbiddenness and that for a large set of nuclei  $f_v \sim 100$  [35]. This means that the transition rate is generally hindered by a factor of about 100 per degree of forbiddenness, i.e.  $T_{1/2}^\gamma \sim (100)^7 T_{1/2}^W$  in case of  $^{180m}\text{Hf}$ .

Another important example is the case of  $^{178m2}\text{Hf}$ , whose energy level scheme is shown in Fig. 1.10. This isomer is unique for its combination of high energy excitation ( $E = 2.45$  MeV) and very long half-life  $T_{1/2} = 31$  y [60]. The strongest decay pathway (99.9%) from this level is through a 13 keV  $E3$  transition towards the lower-lying  $(13)^-$  state, which is primarily accomplished through internal conversion having a coefficient  $\alpha_{\text{IC}} = 1.47 \times 10^7$  [61]. The appearance of this isomer can be attributed to a mixture of a spin- and K-forbidden transition, involving a spin change  $\Delta I = 3$  and a variation in its orientation  $\Delta K = 8$ , resulting in the degree of forbiddenness  $v = 5$ . It is noteworthy that in the absence of such a large variation in K, the expected half-life of this state would have been only 100 ms [62], emphasizing the significance of the violation of the K-selection rule.

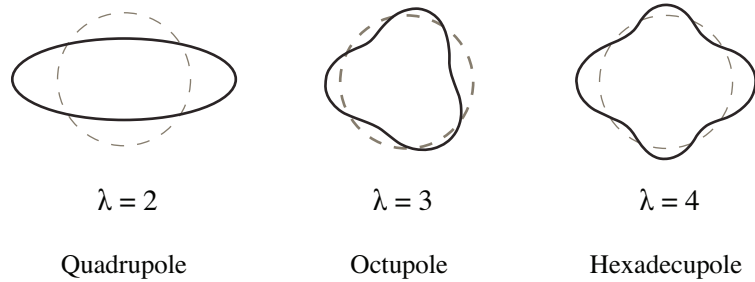
### 1.1.3 Shape Isomers

Shape isomerism arises from the existence of a secondary minimum in the potential energy landscape of the nucleus as a function of its deformations, as illustrated in Fig. 1.7. This results in the requirement of a substantial nuclear shape change for any  $\gamma$ -decay directed back to the ground state, potentially leading to isomerism owing to the poor overlap between the initial and final wavefunctions. According to the liquid drop model (LDM) [63], these deformations can be described by expanding the radius in spherical harmonics [31, 38, 63]:

$$R(\theta, \phi) = R_0 \left( 1 + \alpha_{00} + \sum_{\lambda=1}^{\infty} \sum_{\mu=-\lambda}^{\lambda} \alpha_{\lambda\mu}^* Y_{\lambda\mu}(\theta, \phi) \right), \quad (1.24)$$

where  $\lambda$  is the multipolarity of the nuclear surface. The equation suggests that there are  $2\lambda + 1$  variables associated with each mode of order  $\lambda$ . However, several conditions on symmetry, invariance, and the requirement to have  $R \in \mathbb{R}$  limit the number of independent variables. Generally, any collective motions and dynamical oscillations can be described by letting  $\alpha_{\lambda\mu}$  vary with time. The monopole term ( $\lambda = 0$ )  $\alpha_{00}$  describes the changes in the nuclear volume, and its vibration gives rise to breathing modes. Since nuclear matter is rather stiff, the excitation levels resulting from these oscillations are significantly high in energy, typically around  $\sim 80A^{-1/3}$  MeV [39]. Therefore, assuming the incompressibility of the nuclear fluid,  $\alpha_{00}$  can be considered fixed and expressed in terms of the other deformation parameters. For small deformations, terms with  $\lambda = 1$

## Deformations



## Oscillations

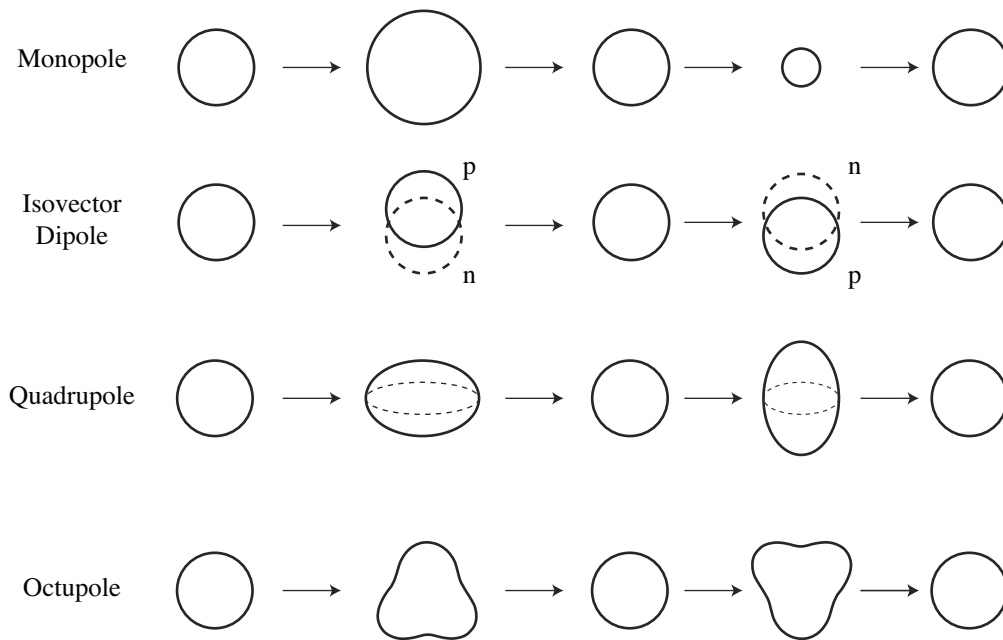


Figure 1.11: **Nuclear deformations and time evolution of vibrational modes for low-order multipoles.** The figure shows the nuclear deformations corresponding to the first three non-trivial multipoles of the surface expansion and the time evolution of the corresponding vibrational modes, including  $\lambda = 0, 1$ . The figure has been redrawn and adapted from Ref. [39].

correspond to a translation of the entire nucleus and an oscillation of the whole system around a fixed point. The isoscalar dipole mode arises when all nucleons move together, while the isovector dipole mode arises when neutrons and protons move out of phase. The latter mode is responsible for the giant dipole resonances (GDR) [64]. However, since these first two motions are considered trivial in the analysis of deformations, their terms are generally omitted from the sum of Eq. 1.24. The first term considered in the expansion is the quadrupolar order  $\lambda = 2$ . Nuclear shapes and oscillations for some of

the lowest multipolar orders of the expansion in Eq. 1.24 are shown in Fig. 1.11.

For quadrupolar deformations, the initial five  $\alpha_{2\mu}$  coefficients reduce to a set of two new real independent variables  $a_{20}$  and  $a_{22}$  in the nucleus fixed coordinate system, where the coordinates are taken along the nucleus principal axes [31, 63]. In this context, the deformations are conveniently described in the  $(\beta, \gamma)$  space [65, 66], which is defined as follows:

$$\begin{aligned} a_{20} &= \beta \cos \gamma \\ a_{22} &= \frac{1}{\sqrt{2}} \beta \sin \gamma. \end{aligned} \tag{1.25}$$

The values of  $\gamma = [0^\circ, 120^\circ, 240^\circ]$  correspond to a prolate axially symmetric deformation, while  $\gamma = [60^\circ, 180^\circ, 300^\circ]$  yield to an oblate axially symmetric deformation. When  $\gamma$  is not a multiple of  $60^\circ$ , the shape of the nucleus does not exhibit axial symmetry, and it is referred to as “triaxial”. These deformations are illustrated in Figure 1.12. A quadrupolar vibration involves the oscillation of the nuclear shape between these two deformations (prolate and oblate), passing through a spherical equilibrium shape ( $\alpha_{\lambda\mu} = 0$ ), as shown in Figure 1.11. For each  $\lambda$ , these vibrations lead to a harmonic excitation energy spectrum if built on a spherical nucleus (no rotational degrees of freedom), while in deformed nuclei, rotational bands are built on each vibrational state [39].

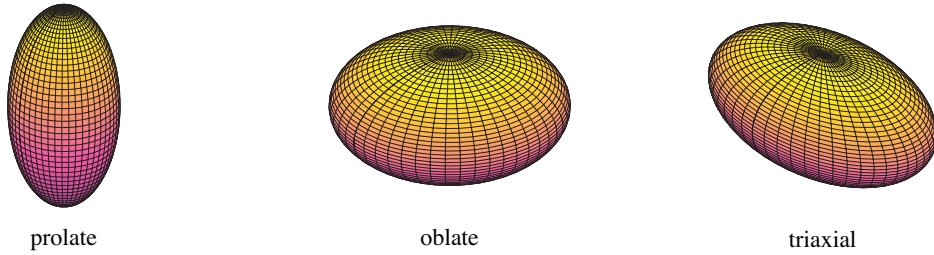


Figure 1.12: Nuclear shapes for quadrupolar deformations.

The discovery of the fission process in 1939 [67, 68] was a significant milestone in nuclear physics, and the use of the liquid drop model (LDM) and its deformations played a crucial role in qualitatively describing the phenomenon. Fission occurs mainly due to the interplay between the Coulomb energy, which repels the protons and pulls them apart, and the surface energy, which tries to keep the nucleus spherical. These two factors constitute the primary contributions to the fission barrier, as depicted in Fig. 1.13. Excitation of the nucleus, as in the case of neutron capture by  $^{235}\text{U}$ , can induce a collective motion and it may become energetically favorable for the nucleus to separate into two overlapping groups of nucleons with a distance  $d$ . The potential energy as a function of this distance presents a saddle point beyond which the fragmentation of the nucleus is inevitable. Furthermore, the inclusion of the shell structure effects leads to a double-humped fission barrier, as shown in Fig. 1.13, with a deeper minimum (I) corresponding to the ground state and the second (II) representative of shape isomerism.



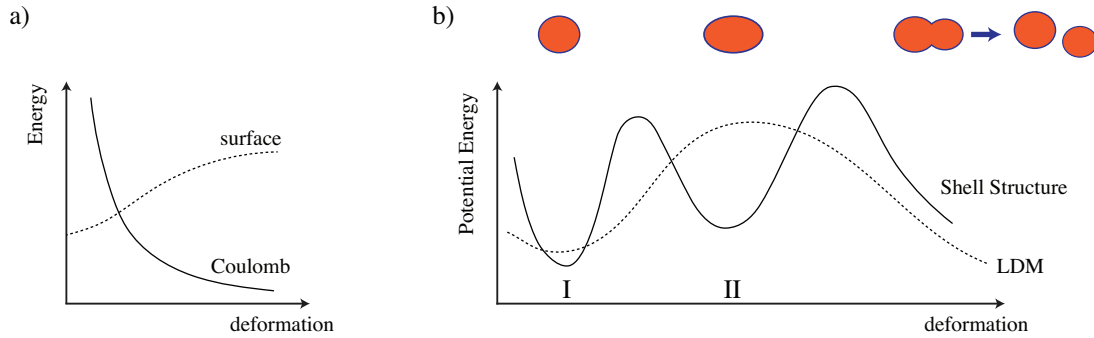


Figure 1.13: **Fission barrier and nuclear deformations.** (a) The competition between the surface energy contribution (dashed curve) and the Coulomb term (solid curve) is shown as a function of the nuclear deformation, seen here as the distance between the two overlapping groups of nucleons. These two contributions primarily constitute the fission barrier illustrated in (b) with a dashed curve (LDM). The inclusion of the shell model effects results in a double-humped barrier with two minima: (I) and (II).

Fission can be distinguished in i) *induced-fission*, where the nucleus overcomes the barrier with sufficient energy (called activation energy), moving from a state of zero or reduced deformation to an unstable configuration; ii) *spontaneous-fission* due to the tunneling of the barrier. The strength of spontaneous fission depends on the shape of the barrier and can occur from both potential minima, which are characterized by very different probabilities. Shape isomers that exhibit spontaneous fission are classified as fission isomers. The first spontaneously fissioning isomer was discovered in  $^{242}\text{Am}$  by Polikanov *et al.* in 1962 [69].  $^{242}\text{Am}$  is known to possess two isomers: the first, denoted as  $^{242\text{m}_1}\text{Am}$ , is located at an excitation energy of 48.60 keV and has a half-life of  $T_{1/2} = 141$  y. This isomer predominantly decays via an  $E4$  multipolar transition to the ground state. The second isomer –  $^{242\text{m}_2}\text{Am}$  – is found at a higher energy of 2.20 MeV, has a significantly shorter half-life of  $T_{1/2} = 14$  ms and decays exclusively (100%) via spontaneous fission. It is worth noting that  $^{242\text{m}_2}\text{Am}$  is also the longest-lived among all the known shape isomers. Currently, 48 cases of fission isomers occur in the actinide region, with  $90 \leq Z \leq 98$  and  $141 \leq N \leq 151$  [16]. The potential energy landscape of some nuclei can also exhibit more than two minima. For example, the nucleus  $^{186}\text{Pb}$  has three different shapes associated with the lowest three states in the excitation spectrum: spherical, oblate, and prolate [70]. This occurrence is referred to as shape coexistence. Other examples of shape isomers are the low-lying  $0^+$  states in even-even nuclei, as in  $^{12}\text{Be}$ ,  $^{72}\text{Ge}$  and  $^{98}\text{Mo}$ .

## 1.2 Essence and significance of nuclear isomers as long duration energy storage solution

The previous classification might have hinted at some crucial features that make isomers attractive for both fundamental research and applications. Their excitation spectrum and the mechanisms behind their emergence provide a valuable probe for investigating nuclear properties related to shell structure and collective motions. Moreover, isomers can have a long half-life, sometimes even surpassing that of the ground state, as seen in  $^{180\text{m}}\text{Ta}$ . In nucleosynthesis, this aspect influences the rates of nuclear reactions, leading to variations in the production and abundance of elements in the Universe [71, 72]. Other important areas of research include gamma-ray lasers [73], nuclear clocks [74], and dark matter detection [75]. Isomers also find practical applications in medical imaging. For instance,  $^{99\text{m}}\text{Tc}$  is widely used for Single Photon Emission Computer Tomography (SPECT), while  $^{34\text{m}}\text{Cl}$  and  $^{52\text{m}}\text{Mn}$  are suitable for Positron Emission Tomography (PET) [76, 77].

In addition, another opportunity appears almost self-evidently when listing the properties of isomers: their ability to store energy over an extended period of time. For decades, isomers have held promise as a more compact ( $10^4$  denser than chemical batteries) and longer-lasting energy storage solution [46, 78–80]. Long-duration energy storage (LDES) solutions have the potential to address the intermittency issues of renewable energy sources, making a cost-effective transition to decarbonized electricity possible [11]. It can be argued that the age of the Universe represents the ultimate long-duration timescale and isomers such as  $^{180\text{m}}\text{Ta}$  – with a half-life  $T_{1/2} \geq 4.5 \times 10^{16}$  y – exceed this limit [32]. The  $E7$  multipolarity, which represents the lowest possible decay mode for the isomeric level at 77.2 keV, has never been observed. This suggests the absence of any form of leaking over its entire existence, a feature of utmost importance for the viability of any potential energy storage technology. Despite the small size of the single energy block stored by isomers compared to fission events ( $\sim 200$  MeV), the amount of energy that can be accumulated in a macroscopic sample can still be significant [46]. For example, one cubic centimeter of natural tantalum can store 82 kJ and up to 690 MJ in a pure  $^{180\text{m}}\text{Ta}$  sample<sup>I</sup>. Another relevant example is represented by  $^{178\text{m}_2}\text{Hf}$ , which exhibits a rare combination of long half-life and high excitation energy. The 2.45 MeV level can store up to 17 GJ in one cubic centimeter of pure  $^{178}\text{Hf}$  with a half-life of 31 y.

Yet ideally, one would like not only to have the absence of leakage during the battery lifespan but also the possibility to release and re-introduce this energy “on-demand”. As the main decay mode of excited nuclear states is through the isomeric transition, the electromagnetic manipulation of the isomer decay assumes particular relevance. However, isomers exist because of a hindrance mechanism that inhibits their decay; hence, it might be necessary to find alternative pathways involving upper-lying levels, to feed or deplete these energy traps. The possibility to induce isomer depletion through direct

---

<sup>I</sup>These quantities only account for the energy stored in the 77 keV isomer.  $^{180}\text{Ta}$  has an unstable ground state with a  $T_{1/2} \simeq 8$  h, thus one could consider this decay as an additional source of energy release.

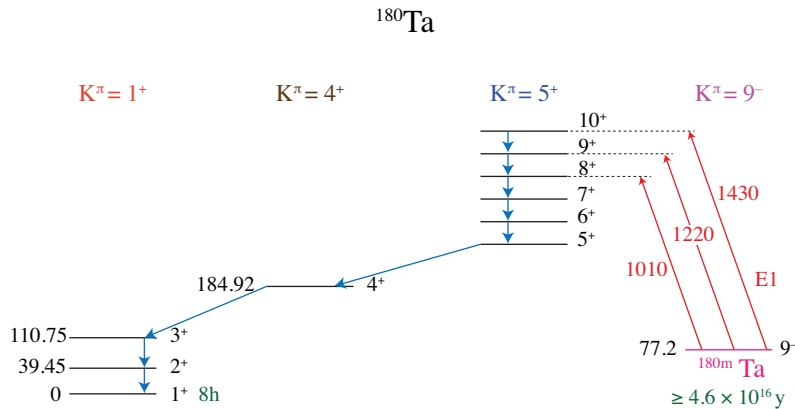


Figure 1.14: **Partial level scheme of  $^{180}\text{Ta}$  and identification of pathways for isomer depletion.** The photoexcitation pathways are indicated with red arrows, along with their photon energy in keV. It should be noted that these E1 transitions are K-forbidden ( $\Delta K = 4$ ). The decay towards the ground state is indicated with blue arrows, while the half-lives of the isomer and the ground state are indicated in green. The figure has been redrawn and adapted from Ref. [81].

photoexcitation, followed by the subsequent decay towards the ground state, has been demonstrated in  $^{180}\text{Ta}$  by connecting the isomer with a set of intermediate levels through a minimum photon energy of  $\sim 1$  MeV [72, 81, 82], as depicted in Fig. 1.14. Belic *et al.* [72] found a total depopulation cross-section of 0.057 b eV for the 1.01 MeV photon, 0.27 b eV for the 1.22 MeV photon, and up to 36 b eV for photons at 2.80 MeV, which are larger than what expected from single-particle estimates [83]. While these transitions appear to bypass the repopulation of the isomer, a back-decay towards the  $9^-$  state – that would be theoretically expected – has not yet been observed, leaving open questions [59, 83] that are further intricate by their potential astrophysical consequences [72, 84, 85]. Regardless of these considerations, the need of  $E \geq 1$  MeV to initiate the isomeric energy release of 77.2 keV makes this process energetically unfavorable for practical applications in nuclear batteries.

A similar photoexcitation pattern was expected to exist for  $^{178\text{m}_2}\text{Hf}$ , but here the situation is much more controversial, and a historical overview can be found in Ref. [86]. The first experiment, published in 1998, claimed the depletion of the  $^{178\text{m}_2}\text{Hf}$  isomer through the absorption of photons with  $E \sim 90$  keV and reported an exceptionally large total cross-section of about  $10^6$  b eV [87]. This result stimulated considerable interest, but subsequent experiments failed to replicate the claimed depletion [88–90] and set an upper limit for the photoexcitation cross-section at  $\sim 2$  b eV, which is more than five orders of magnitude lower than the value reported in Ref. [87]. Direct coupling of the isomeric ( $K = 16^+$ ) and ground state ( $K = 0^+$ ) bands, shown in Fig. 1.10, through low-order multipolar transitions ( $B(\lambda L) \sim 1$  W.u.) has been suggested to be possible, with the minimum energy requirement of 322 keV photons to activate the depletion [80, 91]. Nevertheless, up to date, these transitions have never been tested experimentally.

Besides pure photon absorption, alternative solutions for isomer depletion can be provided by atomic-assisted processes. The fact that the atomic surrounding could play a significant role in the deexcitation of the isomer was shown previously in Eq. 1.19. Most of the time, the lifetime of a state is strongly influenced by the internal conversion channel, where an orbital electron is ejected towards a free continuous state. In highly converted transitions (i.e., those with high values of  $\alpha_{IC}$ ), the half-life of the state can be tremendously increased by stripping away all atomic electrons. Therefore, at least in principle and disregarding any practical considerations, it seems to be always possible to *increase* the half-life. However, the opposite manipulation – i.e., the possibility to *decrease* the lifetime at will – remains an extreme challenge with ambitious applications opening up in case of success [92]. Since innermost shells contribute the most to the  $\alpha_{IC}$ , one possibility for decreasing the lifetime could be the manipulation of the orbital electron wavefunctions via fullerene cages, as similarly done for the enhancement of the radioactive decay of  ${}^7\text{Be}$  through electron capture [93]. However, this process is unlikely to cause an abrupt variation in the lifetime. These considerations outline several desirable ingredients for the isomer depletion scheme, illustrated in Fig. 1.15.

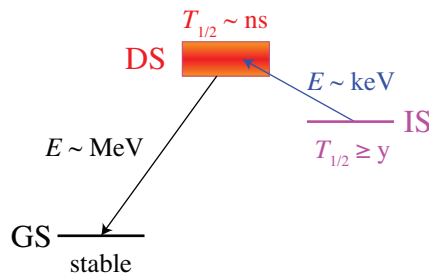


Figure 1.15: **Desirable energy level scheme for the isomer depletion.** IS indicates the isomer, while DS denotes the depletion or intermediate state that facilitates the decay towards the ground state (GS).

The first requirement is the presence of upper-lying levels that allow the decay of the isomer towards the ground state. A stable ground state is preferable if the goal is to achieve “clean” energy storage and avoid radioactive by-products or to have the ability to feed the isomer multiple times after the energy release. The lifetimes of the involved levels are also crucial: ideally, the isomer should last for years, while the depletion state should release the energy on a much faster timescale. To be energetically convenient, the energy required to activate the depletion should be significantly smaller than the energy released by the isomer. The list of mechanisms that could enable the transition between the isomeric and depletion state is extensive.

Generally, these mechanisms can be categorized as resonant photoexcitation, which involves the absorption of real photons [94], atomically assisted excitations, Coulomb excitation through inelastic scattering with charged particles, which involves the exchange of virtual photons [95], and inelastic neutron acceleration [96–98]. While Table 1.1 indicates that dipolar transitions are preferred for resonant photoexcitation, atomically

assisted and Coulomb excitation processes may be more efficient for higher multiplicities. Historically, among others, two mechanisms involving atomic electrons have been extensively discussed: nuclear excitation by electron capture (NEEC) [99, 100] and nuclear excitation by electron transition (NEET) [101]. These mechanisms are intimately intermingled with the internal conversion process, as they are their time reversal (more properly, bound internal conversion is the inverse of NEET [102, 103]). Both mechanisms, NEEC and NEET, require an electronic transition to excite the nucleus. If the transition is between a continuum and a bound state, the process is called NEEC, while if it occurs between two bound orbitals, the process is referred to as NEET. NEET has been invoked as responsible for the high depletion of  $^{178\text{m}_2}\text{Hf}$  observed in Ref. [87], but theoretical analysis reported lower cross-sections that were unable to explain the result [104–106]. While NEET is considered a well-established phenomenon, experimentally observed in  $^{197}\text{Au}$  [107], the nature and the observation of the NEEC process is currently an active area of research, as it will be explained in detail in the next chapter. Examples of third-order processes include: (i) inverse electron bridge (IEB), where the nucleus is excited following the photon absorption by an atomic electron and the consequent transition of this electron to a level coherent with the conservation of energy [108–111]; and the (ii) nuclear excitation by two-photon electron transition (NETP), where the nucleus is excited by the virtual photon of a two-photon-decay occurring in the electronic shell [112, 113]. Feynman diagrams and corresponding energy schemes depicting these mechanisms of nuclear excitation and deexcitation are shown in Fig. 1.16 and Fig. 1.17, respectively. Increasing in complexity, an example of a fourth-order nuclear decay process is the internal conversion in the field of an electron bridge [114]. More complex mechanisms can be identified if the deexcitation involves more than two nuclear states, as in the case of the fourth-order process called electron-nucleus bridge (ENB) [115].

Having reached this point, it seems that the list could go on for a while, and indeed it might, as there are still more mechanisms to be mentioned, such as double-decay processes [109]. Furthermore, the entire framework could be extended to exotic atoms, where the simplest case involves the replacement of the electron with a muon. Therefore, in muonic atoms, one can define the muonic counterpart of the NEET and NEEC processes, namely nuclear excitation upon muonic cascade [116, 117] and  $\text{NE}\mu\text{C}$  [118], respectively. It is worth mentioning that higher-order does not necessarily imply *tout court* a weaker effect. In fact, in some cases, higher-order decay modes may even become stronger than the first-order decay process. An evident example is provided by the internal conversion, which usually overcomes  $\gamma$ -emission, or by IEB as discussed in Ref. [111].

In the following chapters of this thesis, I mostly focus on the first and second-order electromagnetic mechanisms of nuclear excitation. Chapter 2 provides a detailed presentation of the NEEC process, including an excursus of the ongoing debate surrounding the discrepancy between its experimental observation and theoretical description. This discussion also provides the context in which the study of the NEEC process in excited ions was conceived, with the aim of potentially mitigating this discrepancy. This work

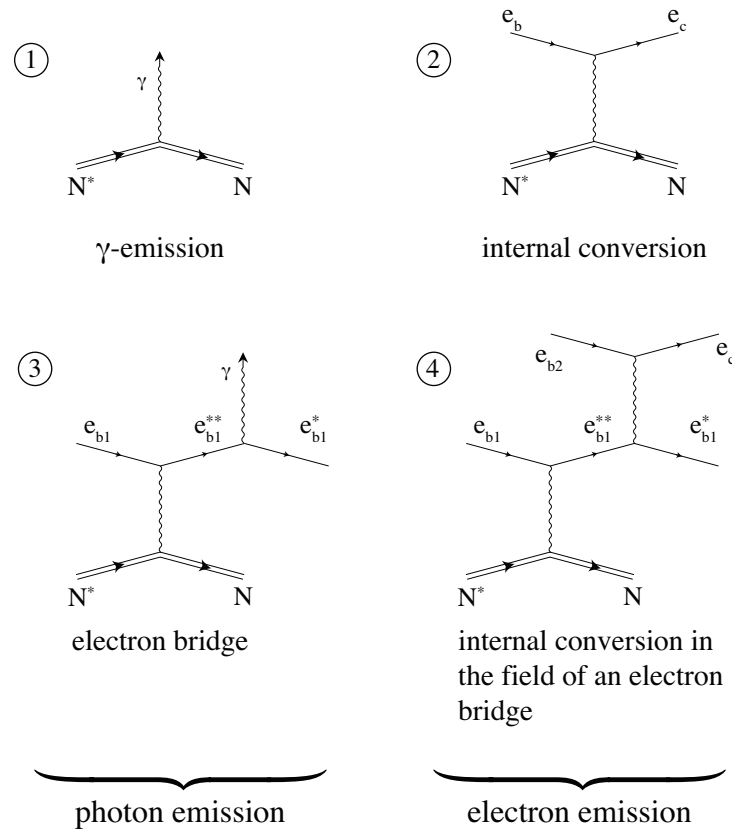


Figure 1.16: **Feynman diagrams for nuclear deexcitation processes of the first-, second-, third-, and fourth-order (in circled numbers).** The nucleus is represented by the double line, while the thin single line represents an electron. Wavy lines with outgoing arrows indicate the emission of real photons, while wavy lines represent the exchange of virtual photons. The asterisk denotes excited states, while the label “b” indicates bound electronic orbitals, and “c” denotes continuum states. This figure has been redrawn and adapted from Refs. [109, 114].

culminated in the publication of Ref. [119]. The potential for dynamically controlling nuclear isomer depletion through the use of NEEC and vortex electron beams will also be examined [120]. Chapter 3 continues with the discussion of the muonic counterpart of the NEEC process, which my colleagues and I have named  $NE\mu C$ , which stands for Nuclear Excitation by Free Muon Capture, as published in Ref. [118]. Chapter 4 presents the experimental setup, which I had the opportunity to design and implement at EPFL, that is aimed at the observation of nuclear excitations in optical laser-generated plasma. This chapter also focuses on the theoretical description of the direct photoexcitation process – initiated by the photons produced by the plasma – and on the discussion of the experimental findings.

At this point, I would like to mention a few directions, though not addressed in this thesis, that could be worth investigating in the future. At the moment, suffice it to say that  $NE\mu C$  enables nuclear excitations with energies on the order of  $\sim$  MeV by providing

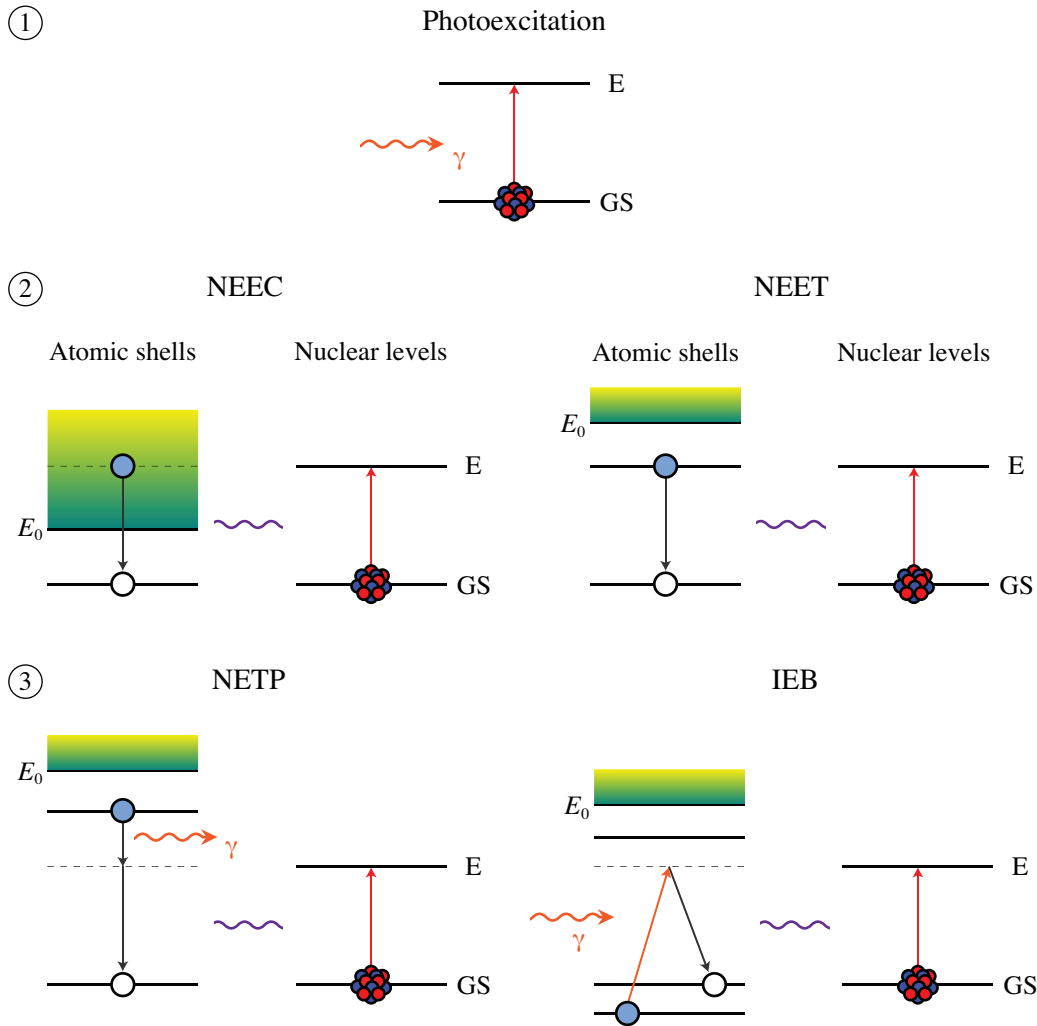


Figure 1.17: **Energy diagrams for several mechanisms of nuclear excitation.** The circled numbers indicate the expansion order in perturbation theory. The vacuum level is denoted by  $E_0$ , while E and GS represent the excited and ground nuclear states, respectively. The orange wavy lines depict real photons, while the purple wavy lines depict the exchange of virtual photons. Virtual states are represented by dashed lines.

slow muons, with energies of tens of keV. In contrast to resonant photon absorption, where the energy of the photon must match the energy of the transition,  $\text{NE}\mu\text{C}$  could offer a more energetically favorable process for isomer depletion or feeding (leaving aside any considerations concerning the muon production). Therefore, it would be interesting to investigate the application of the  $\text{NE}\mu\text{C}$  process to the depletion schemes of  $^{180\text{m}}\text{Ta}$  and  $^{178\text{m}2}\text{Hf}$ , which are shown in Fig. 1.14 and Fig. 1.10, respectively. Another potential application of  $\text{NE}\mu\text{C}$  could involve the exploration of E0 transitions (see Table A.2), which have been left out from the calculations of the NEEC probabilities due to their high excitation levels. Given the higher energies at play with  $\text{NE}\mu\text{C}$ , the excitation of

these  $I^\pi = 0^+$  isomeric states from their ground state becomes more feasible, offering valuable insights into the study of rarer decay processes [20]. Even the more standard process of direct photoexcitation appears to still have room for improvement. While the possibility of nuclear excitation by vortex photon beams was proposed in Ref. [121], to my knowledge, there has been no experimental or theoretical investigation of this process. This presents an opportunity to explore high-order multipolar transitions, which – contrary to Table 1.1 – could be made more favorable by manipulating the orbital angular momentum carried by the photons, as similarly shown for NEEC in Ref. [120].

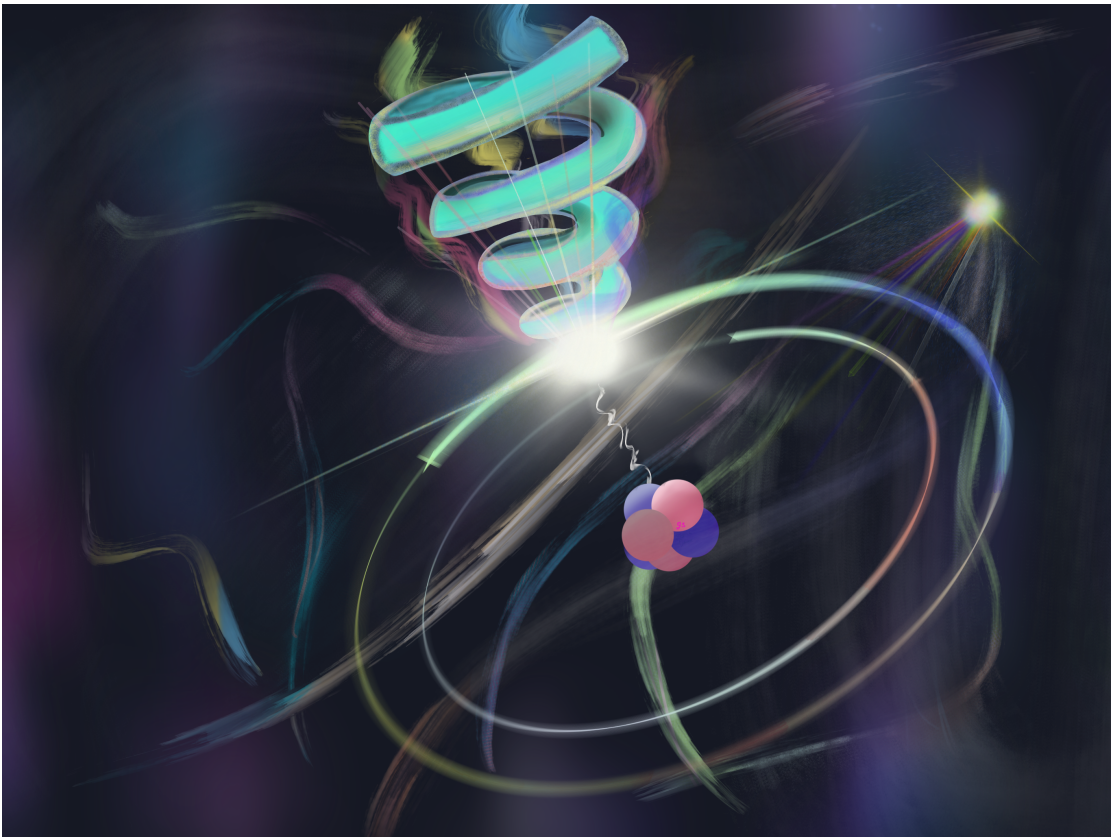
In conclusion, much work has yet to be done in order to achieve, if possible, the desired control on the isomer lifetime: one viable path could be to deepen the understanding of atomically-assisted nuclear excitations, mixed perhaps with other interactions. The manipulation of the wavefunction of the particles involved in the process seems to be one such ingredient. In fact, in recent years, vortex beams have shown great potential in nuclear and particle physics, offering new possibilities for the control of the decay modes [120, 122–126].





It is truly the nature of man to be free and to wish to be so, yet his character is such that he instinctively follows the tendencies that his training gives him. Let us, therefore, admit that all those things to which he is trained and accustomed seem natural to man and that only that is truly native to him which he receives with his primitive, untrained individuality. Thus custom becomes the first reason for voluntary servitude. Men are like handsome race horses who first bite the bit and later like it, and rearing under the saddle a while soon learn to enjoy displaying their harness and prance proudly beneath their trappings.

— Étienne de La Boétie, *Discours de la servitude volontaire*



Nuclear excitation due to the capture of a vortex electron.  
Simone Gargiulo

## 2 Nuclear Excitation by Electron Capture

### 2.1 From the origins to the present day: a recipe for the future

In 1976, Goldanskii and Namiot proposed the possibility of inducing a nuclear excitation through the inverse process of internal electron conversion (IIEC) [99, 100]. Being simply its time reversal, IIEC is a resonant mechanism involving the excitation of the nucleus via the capture of a free electron in an empty shell, provided that the sum of the energy of the free electron  $E_r$  and the binding energy  $E_b$  of the orbital matches the nuclear transition ( $E_n$ ), as shown in Fig. 2.1. With rough estimations, the authors calculated a probability

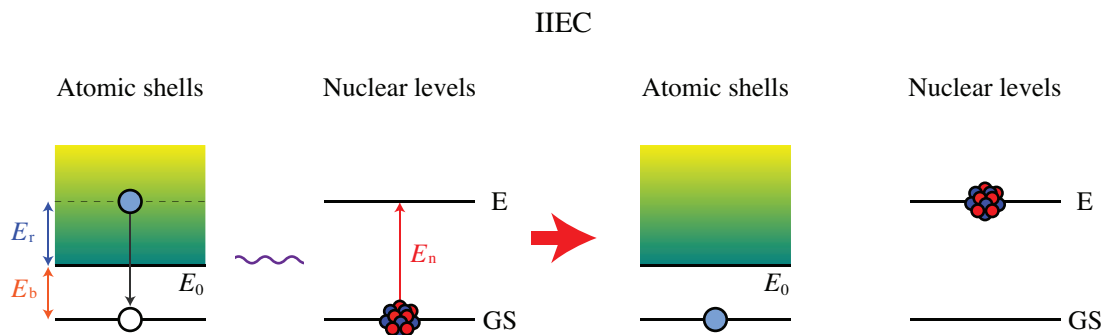


Figure 2.1: **The process of nuclear excitation by electron capture.** The inverse process of internal electron conversion (IIEC) or, as lately called, nuclear excitation by electron capture (NEEC). Here, a free electron is captured from the continuum in an empty orbital, resonantly exciting the nucleus by exchanging a virtual photon. The excited nucleus (on the right) can either decay by internal conversion or emit a  $\gamma$ -ray.

of excitation for the IIEC process of  $P_{\text{exc}} \sim 10^{-14}$  in  $^{235}\text{U}$  laser-generated plasma, which was accompanied by a very large resonance cross-section of  $10^7$  b at  $E \sim 5$  eV. These values correspond to a rate of  $\lambda \sim 10^{-5} \text{ s}^{-1}$  and an expected number of  $N \sim 1000$  excited nuclei per laser pulse for a plasma temperature comparable to the nuclear transition energy  $T \sim E_n = 76$  eV. However, the validity of this estimate for the cross-section was

considered dubious as it did not take into account the nuclear properties [127].

In 1978, Doolen [128, 129] calculated the nuclear deexcitation rate in  $^{237}\text{U}$  and  $^{238}\text{U}$ . In thermal equilibrium, the rate at which a nuclear level is populated must equal the rate at which it decays. In this way, he obtained the excitation rate for different temperatures and compression factors. He estimated the excitation rate for different processes – including IIEC – and predicted a value of  $\lambda^{\text{IIEC}} \sim 10^{-10} - 10^{-8} \text{ s}^{-1}$  for the first excited level of  $^{237}\text{U}$  at  $E = 11.39 \text{ keV}$ , assuming a plasma temperature of several keV.

One year later, Izawa and Yamanaka conducted an experiment in a laser-plasma scenario that bore similarities to the one proposed by Goldanskii and Namiot. This experiment resulted in the observation of the first isomeric level of  $^{235}\text{U}$  at an energy of 76 eV and half-life of  $T_{1/2} = 26 \text{ min}$ . The authors attributed the excitation mechanism leading to the formation of the isomer to the nuclear excitation by electron transition (NEET) process [130]. However, in 1981, Goldanskii and Namiot pointed out that – according to their estimates – the IIEC probability exceeded that of NEET by three orders of magnitude in the experimental conditions of Ref. [130]. Thus, they interpreted Izawa and Yamanaka’s observed excitation as due to IIEC [131].

In 1989, Cue *et al.* proposed the very same IIEC process, which this time did not involve the capture of purely *free* electrons, but rather electrons that were *bound* to atoms or a solid (target material). They named this mechanism nuclear excitation by (target) electron capture (NEEC) [132, 133]. As a consequence of the initial binding state of the captured electrons, the NEEC resonance shape is no longer represented by a Lorentzian function. Instead, it is dominated by the Compton profile of the target electrons, as it will be clear from Fig. 2.5. Cue *et al.* also drew a connection between NEEC and other known atomic processes that only involved atomic electrons. The most important is the resonant charge transfer and excitation process (RTE), which describes the radiationless capture of a bound target electron into an inner shell of the projectile while simultaneously exciting a projectile electron from a bound state to another level [134–136]. The latter process differs from NEEC in the excitation part: in NEEC it is the nucleus that is excited from one discrete state to another and not an electron as in RTE. Following this logic, the authors provided an order of magnitude estimate for the NEEC cross-section by scaling that of the RTE process. The resulting values are substantially lower than those previously reported by Goldanskii and Namiot and fall in the range  $\sim 10^{-3} \text{ b}$  to  $10^{-2} \text{ b}$  for several isomers, except for  $^{235}\text{U}$ , which was not included in the study. Despite the apparent distinction<sup>I</sup> between the original definitions of the NEEC and IIEC processes, also Cue *et al.* identified NEEC as the inverse of internal conversion and the two acronyms began to be used interchangeably<sup>II</sup> in the following years.

In 1991, 12 years after the experiment performed by Izawa and Yamanaka, Arutyunyan

<sup>I</sup>Cue *et al.* were not aware of the process proposed by Goldanskii and Namiot at the time Ref. [132] was written. However, they later became aware of the earlier proposal, as stated in Ref. [133].

<sup>II</sup>Sometimes, the acronym IIC is used in the literature to refer to the inverse process of internal conversion.

*et al.* endeavored to duplicate the same outcomes; however, they failed to observe any excitation of the  $^{235}\text{U}$  isomer in a similar laser-plasma scenario [137]. Nevertheless, Arutyunyan *et al.* were able to successfully detect the  $T_{1/2} \sim 26$  min isomer decay by exposing the uranium target to a relativistic electron beam. Regardless of the excitation mechanism, this led them to estimate the excitation cross-section to be between  $10^{-8}$  b and  $10^{-7}$  b. These values were two to three orders of magnitude smaller than those reported in the laser-plasma scenario of Ref. [130], and the unresolved discrepancy remained controversial.

In 1999, Harston and Chemin presented a theoretical overview of the nuclear excitation mechanisms occurring in a plasma environment, which included NEEC [127]. Here, the NEEC cross-section was determined using the principle of detailed balance and the matrix element calculated for its inverse process, i.e. the internal conversion (IC). The excitation rates obtained were on the order of  $\lambda \sim 10^{-11} \text{ s}^{-1}$  for  $^{235}\text{U}$  for plasma temperature between 20 eV–100 eV. Furthermore, in contrast to the estimates reported by Goldanskii and Namiot in Ref. [131], their findings showed that the probability of NEEC to occur in  $^{235}\text{U}$  for a plasma temperature of  $\sim 100$  eV was substantially lower than that of NEET.

In 2003, Mukoyama attempted to clarify the distinction between IIEC and NEEC [138]. In this work, the author introduced a new nomenclature in which the nuclear excitation resulting from the capture of a *free* electron was referred to as NEFEC, while that resulting from a *bound* electron was called NETEC (with the ‘T’ abbreviating the word ‘target’), as depicted in Fig. 2.2. Despite Mukoyama’s efforts, this terminology has not been formally adopted afterward, and the acronym NEEC continued to be used interchangeably to describe both processes.

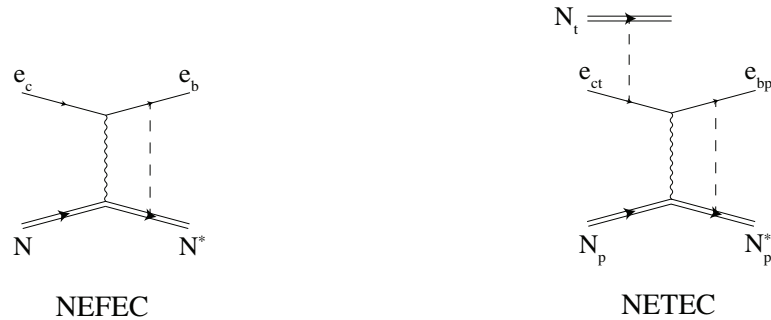


Figure 2.2: **Feynman diagrams for the IIEC (NEFEC) and NEEC (NETEC) as proposed by Mukoyama.** The diagrams depict the nucleus as a double line, the electron as a thin single line, and the exchange of virtual photons as wavy lines. Dashed lines represent an electron in a bound state, while the asterisk indicates excited states. The labels ‘p’ and ‘t’ refer to the projectile and target, respectively. The labels ‘c’ and ‘b’ stand for continuum and bound, respectively.

In 2006, Pálffy *et al.* presented a more sophisticated theoretical framework for NEEC by using a Feshbach projection operator formalism to derive its cross-section. The reported

integrated cross-section values for several isomeric transitions ranged from  $10^{-5}$  b eV up to 1 b eV [139, 140]. The theory was subsequently applied to the isomer depletion scheme of Fig. 1.15, predicting NEEC as the most efficient excitation mechanism for  $^{242\text{m}}\text{Am}$ , with a higher cross-section than a previous crude estimate [141], and stronger than direct photoexcitation for  $^{93\text{m}}\text{Mo}$ ,  $^{178\text{m}}\text{Hf}$ , and  $^{235\text{m}}\text{U}$ .

Although various scenarios have been proposed to observe NEEC experimentally over the years, such as axial channeling [142, 143], electron beam ion traps [139], laser-generated and hot dense plasma [127, 144, 145], and reaction recoil (beam-based) setups [146, 147], the observation of the phenomenon remained elusive for over four decades since its initial proposal.

It was not until 2018 that the first experimental observation of the NEEC process was made in a beam-based scenario on  $^{93}\text{Mo}$  [148]. The excitation spectrum of  $^{93}\text{Mo}$  includes some of the ingredients that are essential for the isomer depletion scheme depicted in Fig. 1.15, namely: an isomeric state with the energy of 2.425 MeV and half-life  $T_{1/2} = 6.85$  h; an upper-lying level located only 4.85 keV away from the isomer, which is an ideal target for depletion, with a half-life of  $T_{1/2} = 3.5$  ns; and a ground state with a half-life of  $T_{1/2} = 4 \times 10^3$  y. In the experiment described in Ref. [148] and illustrated in Fig. 2.3,  $^{93}\text{Mo}$  ions were produced through a fusion-evaporation reaction between a 840 MeV  $^{90}\text{Zr}$  beam and a  $^7\text{Li}$  target. This reaction initially populates the energy levels of the  $^{93}\text{Mo}$  reaction products (“recoils”) that lie above the isomeric state. The subsequent decay of these high energy states may eventually feed the isomer while the ions cross the vacuum gap between the production ( $^7\text{Li}$ ) and stopping ( $^{\text{nat}}\text{C}$ ) targets. During the passage of the recoils through the stopping target, electrons are initially stripped off, leading to highly charged states in the  $^{93\text{m}}\text{Mo}$  ions. Later, these electrons recombine back as the recoiling ions are decelerated through collisions with the target atoms. Provided that the energy of these ions is sufficiently high before approaching the stopping medium, the resonance conditions for NEEC (both for energy and charge states) are met as they cross the thick Carbon layer, as depicted in Fig. 2.3a. In this scenario, a prompt coincidence between the  $\gamma$  that feeds the isomer at 2.425 MeV and the sequence of  $\gamma$ -rays with energies of 268 keV, 685 keV, and 1.478 MeV emitted by the stopped nuclei – highlighted in different colors in the level scheme of Fig. 2.3b – would serve as the signature of the isomer depletion through a process other than its natural decay with  $T_{1/2} = 6.85$  h. As an additional validation, in the absence of depletion, the characteristic 268 keV transition would not appear in the measured spectrum. Chiara *et al.* observed a depletion of the isomer with a probability of  $P_{\text{exc}} \sim 10^{-2}$ , and attributed the excitation between the isomeric and depletion states to the NEEC process. This interpretation was driven by the fact that other known processes, such as Coulomb excitation and above-barrier inelastic scattering, which could have played a role in this scenario, have probabilities on the order of  $P_{\text{exc}} \sim 10^{-6}$ , which are too low to explain the observed phenomenon.

In the same year, further theoretical investigations into the depletion of  $^{93\text{m}}\text{Mo}$  considered NEEC occurring in an optical laser-generated plasma. These studies detailed





is nine orders of magnitude smaller than the experimental value determined in Ref. [148], and significantly smaller than those resulting from other non-resonant processes.

This significant discrepancy highlighted the necessity of gaining a more comprehensive understanding of the experimental and theoretical frameworks, exploring perhaps aspects that might have been disregarded up to that moment. At the time, it was customary to study NEEC occurring in ground-state electronic configurations, referred to as ground-state assumption (GSA). However, one possible mitigation for the discrepancy between the predicted and experimental excitation probabilities is that NEEC may have taken place in highly excited electronic configurations. In light of these circumstances, in 2020<sup>III</sup>, we proposed a study of the NEEC process occurring in a nucleus with electrons populating atomic orbitals in all possible combinations, as shown in Fig. 2.4, a situation that we identified with the acronym NEEC–EXI [119].

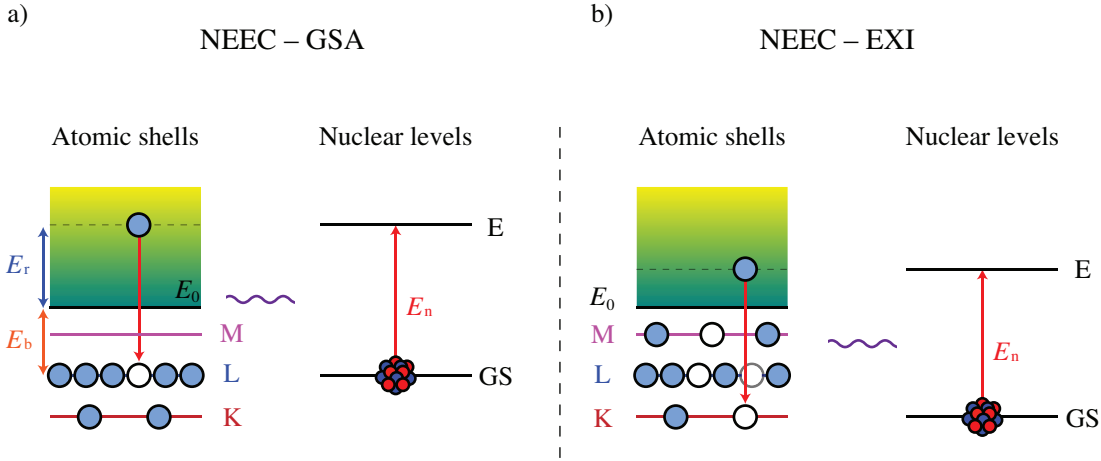


Figure 2.4: **The nuclear excitation by electron capture in excited ions.** In (a), the NEEC process occurs in an ion with its atomic shells in the ground state (NEEC–GSA), while in panel (b), the NEEC process occurs in an ion in an excited electronic state. The inclusion of excited electronic states in the NEEC theory can uncover previously neglected capture channels.

The selection of  $^{73}\text{Ge}$  was strategic to clearly demonstrate the potential of NEEC–EXI. This nucleus exhibits a peculiar feature: four electrons filling its orbitals provide sufficient screening to lower the binding energy of the K-shell ( $E_b^K$ ) below the energy of the isomeric level, which is located at  $E_n = 13.28$  keV. Previously, the ground-state assumption precluded NEEC from occurring as a result of the electron capture in the K-shell. However, by removing this hypothesis, our approach revealed the emergence of new capture channels with cross-sections increased by up to three orders of magnitude. This enhancement can be understood as follows. By filling the orbitals with electrons, we are passing from a condition in which  $E_n < E_b^K$  for  $q = Z$  – i.e., a bare nucleus for which NEEC in the K-shell is not possible – to a condition where  $E_n > E_b^K$  in case of four

<sup>III</sup>Although the preprint was made available on arXiv in 2020, it was not officially published until 2022.

electrons filling the orbitals (i.e.,  $q = Z - 4$ ). The inclusion of excited electronic states in the latter configuration enables NEEC from the capture of electrons in the K-shell and provides orbitals that are nearly resonant with the nuclear transition ( $E_b^K \sim E_n$ ). Since NEEC is a resonant process (i.e.,  $\sigma_{\text{NEEC}} \propto 1/(E_n - E_b^K)$ ), this circumstance leads to a significant increase in its cross-section.

In 2021, a study by Rzadkiewicz *et al.* [155] highlighted that the theoretical analysis of the experiment performed at Argonne should have accounted for the fact that the electrons involved in the NEEC process were initially bound in a target medium, rather than purely free as initially assumed by Wu *et al.* in Ref. [154]. This distinction corresponds to the one previously pointed out by Mukoyama [138] between NEFEC and NETEC, as illustrated in Fig. 2.2. By including the Compton profile of the target electrons in the theoretical analysis, NEEC resonances (here referred to as NEEC–RT to draw a connection to the RTE process) were broadened, resulting in contributions across the entire energy landscape of the projectile ions. This is in contrast to Ref. [154], where resonances appeared at specific discrete energies. Fig. 2.5 shows the different cross-section shapes for these two cases.

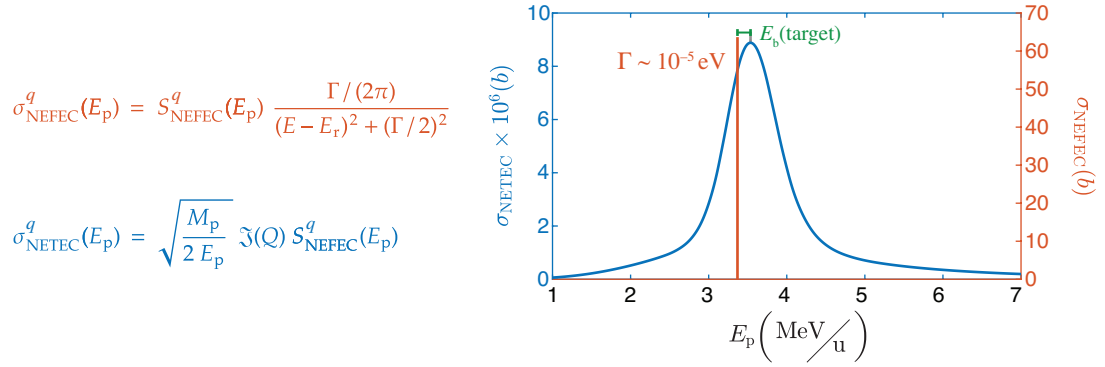


Figure 2.5: **The cross-section shapes for the NEEC process differ depending on whether the electrons involved in the capture are initially bound in a target medium or free.** The cross-sections for the NEEC process involving the capture of *free* (NEFEC, in red) or *bound* target electrons (NETEC, in blue) exhibit distinct differences in their shapes as a function of the energy of the projectile ions ( $E_p$ ). NEFEC cross-section has a Lorentzian shape, with a width typically in the range  $\Gamma \sim 10^{-10} - 10^{-5}$  eV, while the NETEC cross-section extends over a much broader energy range, due to the Compton profile of the target electrons  $\mathfrak{J}(Q)$ . The distance between the two peaks is due to the fact that, in NETEC, the captured electron is bound in the target medium. In the figure, this distance is represented by  $E_b(\text{target}) \sim 100$  eV. The NETEC cross-section presented in this figure was calculated for the 4.85 keV transition in  $^{93}\text{Mo}$ , utilizing the Compton profile from Ref. [156] and the model described in Refs. [135, 155]. In this example, the resonance strength  $S_{\text{NEFEC}}$  was chosen to be  $10^{-3}$  b eV.

Although the inclusion of the Compton profile made the capture in L orbitals no longer insignificant and comparable to those of other shells, it only slightly increased the NEEC excitation probability to  $P_{\text{exc}} \sim 7 \times 10^{-11}$ , leaving the discrepancy between theory and

experiment mostly unaltered. This is because the assumption that atoms are in their electronic ground state before the electron capture suppresses the contribution of the L shells at low projectile energies, where they can actually give most of their contribution. Combining the NEEC-EXI with the NEEC-RT in a future model could further enhance the role of L shells and possibly reduce the disagreement between theory and experiment. However, at the moment, it is unclear whether this will allow to bridge the entire gap.

On the experimental side, in 2021, Guo *et al.* [157] commented on the results of Ref. [148] and attributed the large excitation probability measured in the isomer depletion of  $^{93\text{m}}\text{Mo}$  to false events, caused by  $\gamma$ -contamination from chance coincidences and Compton background. They estimated the probability of the 268 keV decay to be populated by deexcitation of higher spin states or other reactions and to be in time coincidence (between 100 ns and 1  $\mu\text{s}$ ) with any other transitions, without being in true relation to them. The upper limit for this chance probability resulted to be  $P_{\text{chance}} \sim 5 \times 10^{-3}$ , which is close to the experimentally measured NEEC probability ( $\sim 10^{-2}$ ). In addition, they argued that an incorrect background subtraction method could have resulted in the measured excitation probability being only an upper limit for the isomer depletion of  $^{93\text{m}}\text{Mo}$ . To address these concerns, Guo *et al.* suggested repeating the measurements with the  $^{93\text{m}}\text{Mo}$  production site several meters away from the stopping target. By doing so, prompt  $\gamma$ -rays due to the production of  $^{93}\text{Mo}$  and relative deexcitations from high spin states would be separated from the  $\gamma$ -transitions due to the isomer depletion.

A response to this comment was given by Chiara *et al.* in the same issue [158]. They followed the same steps as Guo *et al.* to calculate the chance probability but pointed out some differences in the values used for the estimation. By considering a smaller time window of 90 ns and a lower rate of 1.7 kHz for the population of the 268 keV transition from higher states, Chiara *et al.* concluded that  $P_{\text{chance}} \sim 3 \times 10^{-4}$ , which is smaller than the observed depletion. As a side note, it should be mentioned that this value corresponds to the lower end of the range quoted by Guo *et al.* for  $P_{\text{chance}}$ . To validate their calculations, Chiara *et al.* also extracted the chance-coincidence probability from experimental data, which resulted in a comparable value of  $P_{\text{chance}}^{\text{exp}} \sim 8 \times 10^{-4}$ . They also argued that statistical errors arising from these chance coincidences could lower the measured value of  $P_{\text{exc}}$  to  $8.8 \times 10^{-3} - 9.6 \times 10^{-3}$ . In this reply, the authors provided additional details about the background subtraction and discussed the outcomes of their analysis in contrast to the points raised by Guo *et al.*. In addition, Chiara *et al.* investigated the effect of varying the background parameter within a certain range on the calculated value of  $P_{\text{exc}}$ . Their analysis revealed only a minor change of approximately 9% in the final value of the excitation probability. Therefore, in their opinion, the experimental case is robust and NEEC cannot be excluded as the mechanism responsible for the observed isomer depletion.

In 2022, Guo *et al.* [159] attempted to reproduce the beam-based experiment on  $^{93\text{m}}\text{Mo}$  at the Radioactive Ion Beam Line in Lanzhou (RIBLL) [160], shown in Fig. 2.6a. The main focus of this repetition was on the spatial separation between the prompt  $\gamma$ -rays arising from the fusion-evaporation reaction and the deexcitation of high spin

states of  $^{93}\text{Mo}$ , and those – delayed – originating from the isomer depletion. In the experimental setup shown in Fig. 2.6a, the reaction target produces  $^{93}\text{Mo}$  recoils through the reaction  $^{12}\text{C}(^{86}\text{Kr}, 5n)$ , and is located 35 m away from the stopping target consisting of a carbon foil and a plastic detector (PD). NEEC can occur in the stopping target where the detection system is placed. In contrast, the configuration used by Chiara *et al.* [148] (Fig. 2.6b) had both the reaction target and stopping medium placed inside the Gammasphere spectrometer [161]. Therefore, this reinvestigation under low  $\gamma$ -background aimed at a higher sensitivity measurement of the isomer depletion occurring in  $^{93\text{m}}\text{Mo}$ .

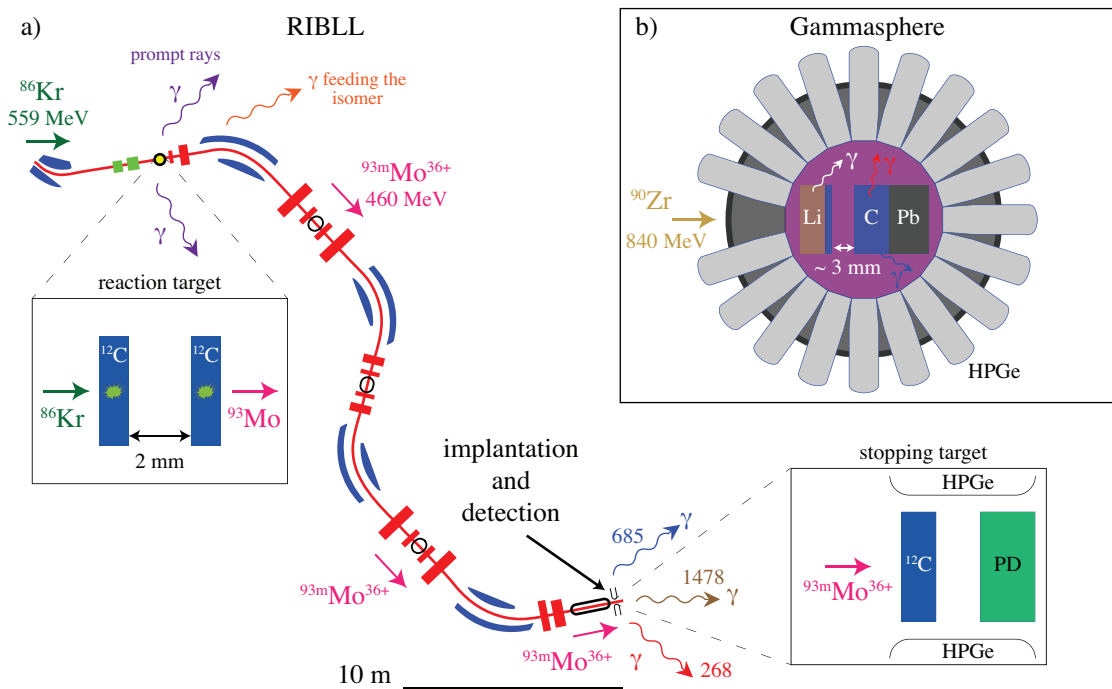


Figure 2.6: **Reinvestigation of the isomer depletion occurring in  $^{93}\text{Mo}$  at RIBLL.** In (a) the Radioactive Ion Beam Line in Lanzhou RIBLL used by Guo *et al.*. Highly charged  $^{93}\text{Mo}^{36+}$  recoils are selected following their production by fusion-evaporation  $^{12}\text{C}(^{86}\text{Kr}, 5n)$  reaction at the primary target. This secondary beam is then delivered to the stopping medium, consisting of a Carbon foil and a plastic detector (PD), located 35 m away from the reaction target. In this configuration, prompt and delayed (originating from the isomer)  $\gamma$ -rays are spatially separated, leading to a low  $\gamma$ -background in the detection system. Implantation events are recorded by the plastic detector (PD), while the  $\gamma$ -transitions are detected by high purity germanium (HPGe) detectors. For comparison, panel (b) shows the configuration used by Chiara *et al.* in the Gammasphere (ANL), where both the primary and secondary targets are surrounded by the detection system.

The  $^{93}\text{Mo}$  recoils are delivered to the stopping medium  $1.14\ \mu\text{s}$  after their production at the reaction target, providing sufficient time for the isomer to be fed. In the case of isomer depletion, a sequence of  $\gamma$ -decays would be detected in coincidence (within a few nanoseconds) with the implantation events recorded in the PD. In the experiment conducted by Guo *et al.*, the 268 keV  $\gamma$ -ray transition was not observed, leading to an

experimental upper limit for the isomer depletion of  $P_{\text{exc}}^{\text{max}} \sim 10^{-5}$ . This upper limit is approximately three orders of magnitude smaller than the value determined by Chiara *et al.* [148]. Theoretical calculations presented for the experimental conditions of Guo *et al.* predicted a probability of isomer depletion due to NEEC of  $P_{\text{exc}} \sim 10^{-12}$ . These calculations included the momentum distribution of the target electrons but once again assumed the electronic shell to be in the ground state prior to the electron capture (NEEC–GSA).

Although the kinetic energies of the  $^{93\text{m}}\text{Mo}$  recoils were different between the two experiments (674 MeV for Chiara *et al.* and 460 MeV for Guo *et al.*), the large discrepancy in the measured  $P_{\text{exc}}$  values seems difficult to explain solely by the different experimental conditions that can be learned from the respective papers. It is worth noting that the different energies in turn affect the average charge states of the ions during the slowdown process in the stopping medium. It is clear that a new attempt with a low  $\gamma$ -background and higher recoil energies is desirable to further investigate the discrepancy in the measured excitation probabilities. On the other hand, exploring other types of experimental scenarios is also necessary to provide a comprehensive test of the theory. While the internal conversion can indirectly prove – due to time reversal – the NEEC theory for the capture of free electrons, an equivalent observation for solid-state targets seems to be lacking.

In 2022, we presented in Ref. [120] (by Wu *et al.*) a novel approach for the enhancement of the NEEC cross-section through the manipulation of the quantum state (i.e., the wavefunction) of the captured electrons. This concept is illustrated in Fig. 2.7. This work represents a significant milestone, in my opinion, as it challenges the conventional vision of nuclear reactions from here on. Traditionally, in most textbooks and literature, the cross-section of such processes is often attributed to the unique properties of the nucleus and the kinematics of the “projectiles”, as probably may have also appeared to the reader from earlier discussions. In the case of NEEC, for instance, the overlap between the wavefunctions of bound and continuum states is a crucial factor in determining the final rate of occurrence. However, since *free* particles are usually treated as plane waves, the NEEC cross-section for a specific orbital and ionization state was previously thought to be entirely determined by the nucleus, almost as if it was an inherent property of nature. In Ref. [120], it was theoretically shown for the first time that the cross-sections of atomically assisted nuclear excitation processes, such as NEEC, may not be solely determined by nuclear properties but can be influenced by engineering the wave function of the electron undergoing capture, as conceptually illustrated in Fig. 2.7. Specifically, nuclear excitation by vortex electron capture was investigated for the isomer depletion schemes of  $^{93\text{m}}\text{Mo}$ , shown in Fig. 2.3, and of  $^{152\text{m}}\text{Eu}$ , shown in Fig. 2.8a. The use of a vortex beam with a topological charge  $m = 5$  for  $^{93\text{m}}\text{Mo}$  leads to a two-orders-of-magnitude increase over the strongest capture channel of the plane wave case. However, an even more intriguing aspect arises for the depletion of  $^{152\text{m}}\text{Eu}$ .

The use of vortices on  $^{152\text{m}}\text{Eu}$  has the striking feature of changing the shell for which the cross-section is strongest, as depicted in Fig. 2.8b. In the case of the plane waves,

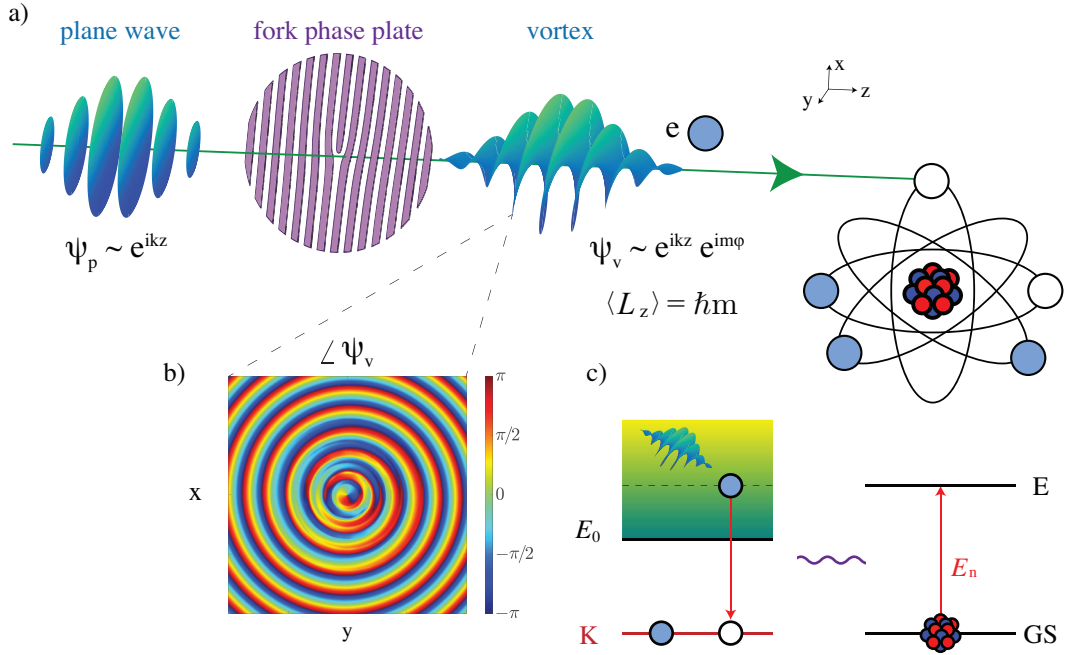


Figure 2.7: **Nuclear excitation by vortex electron capture.** In (a), the electron wavefunction, initially represented as a plane wave  $\psi_p$ , undergoes manipulation through the interaction with a fork phase plate. This imparts a well-defined orbital angular momentum (OAM)  $\hbar m$  to the electrons along the axis of propagation ( $\langle L_z \rangle = \hbar m$ ). In panel (b) is shown an example of the phase ( $\angle \psi_v$ ) that can be imprinted on the electron wavefunction by using phase plates or plasmonic structures, as demonstrated in Refs. [162, 163]. Panel (c) illustrates the energy diagram of the NEEC process with an incoming free electron in a vortex state. The energy-matching conditions still need to be satisfied.

capture in the  $2s_{1/2}$  shell is the most probable. As mentioned earlier, the shell for which the capture and simultaneous nuclear excitation is most efficient is entirely determined by the nucleus, selection rules of the transition, and the overlap between the continuum and bound state wavefunctions (which are again determined by the nucleus and its ionization state). The use of vortex beams breaks this traditional paradigm and reveals that the efficiency of nuclear excitation can depend on specific manipulations of the electron wavefunction. Specifically, a vortex beam with  $m = 3$  externally selects the strongest capture channel to be the  $2p_{1/2}$  orbital (as indicated by the pink arrow labeled ‘plane to vortex’ in Fig. 2.8b). By changing the topological charge to  $m = 5$ , the excitation through the  $2p_{3/2}$  orbital becomes the most efficient channel, as shown by the pink arrow labeled ‘OAM change’. Therefore, the manipulation of the orbital angular momentum (OAM) of the incoming electron beam, which can be achieved on an ultrafast timescale with plasmonic structures [162] or using light phase masks [165, 166], allows for external control over the cross-section of the process. Furthermore, when physical phase plates are employed, as the fork phase plate shown in Fig. 2.7, deflector coils can be utilized to choose the desired vortex topological charge [167]. This newfound ability to control the

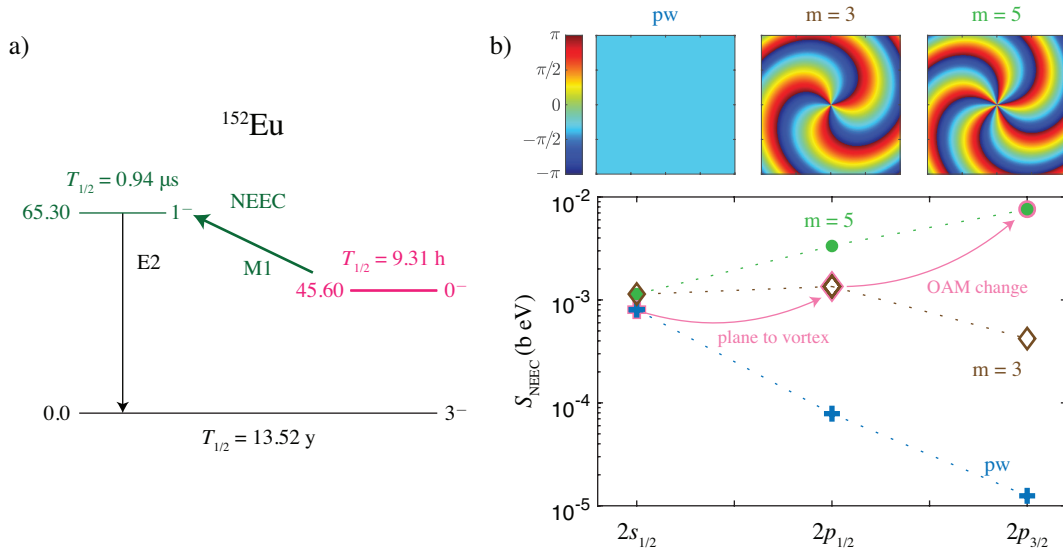


Figure 2.8: **Isomer depletion of  $^{152m}\text{Eu}$  through vortex electron beams.** In (a), the energy level scheme for the isomer depletion of  $^{152m}\text{Eu}$  is shown. The isomeric state is drawn in pink, while the depletion state is in green. The energies are given in keV. In (b), the resonance strengths for NEEC are compared for plane waves (blue) and vortex electron beams with topological charges  $m = 3$  (brown) and  $m = 5$  (green). The phase of the electron wavefunction is shown for the plane wave (PW) and vortex beams (Laguerre-Gaussian solutions [164]) with  $m = 3$  and  $m = 5$ . The markers outlined in pink indicate the strongest capture channel for a given beam solution or topological charge. The pink arrows illustrate the shift of the strongest capture channel towards higher- $\ell$  subshells as we move from plane wave solutions to vortex states.

cross-section through the manipulation of the electron wavefunction brings us closer to realizing the long-sought dream of electromagnetically manipulating the isomer decay. Using NEEC as a testbed, it is clear that applying these concepts to other nuclear excitation mechanisms can lead to unexpected outcomes and perhaps lay the groundwork for incorporating additional aspects to make these processes even more efficient.

From a historical perspective, it is evident that the NEEC process remains a conundrum even almost half a century after its proposition. Recent publications have contributed to improving our understanding of the experimental and theoretical frameworks in which NEEC can occur, incorporating ingredients from the past – that sometimes went lost – and looking towards the future for the implementation and application of the newly developed concepts.

Having reviewed the literature in the preceding pages, it is clear that the superimposition of different acronyms to refer to the same process has led to a perception of chaos (to which I have also partially contributed). My preferred terminology for the process of nuclear excitation by electron capture is NEEC, regardless of whether the capture involves a *free* or *bound* (target) electron. However, I believe it is necessary to specify from time to time the scenario under study in order to avoid confusion. This is

also the approach I took in the next chapter, where the process of nuclear excitation by free muon capture is presented. In this case, I used the acronym NE $\mu$ C to refer to the process and specified in the text that the capture involves a free particle, although it would have been less plausible to have target muons. As Latins would say: “*de gustibus non est disputandum*”.

## Statement on my contribution

In the following section, I included the integral publication “S. Gargiulo, I. Madan, & F. Carbone. Nuclear excitation by electron capture in excited ions. *Physical Review Letters*, 128(21), 212502, (2022).” mentioned in this thesis as Ref. [119]. My investigation began in April 2020, focusing on the possible role of electron screening in the emergence of nearly-resonant capture channels, which could have potentially enhanced the NEEC cross-section. I was the initiator and executor of this research project. I developed and implemented a theoretical framework for studying nuclear excitation in  $^{73}\text{Ge}$  ions with electronic shells containing up to 4 electrons, taking into account all possible excitation states. Further details regarding the recoupling schemes employed for this work are available in Section A.3. Throughout my research, Ivan Madan and Fabrizio Carbone offered invaluable supervision and played a crucial role in guiding me to effectively discuss, present the results, and convey the scientific message.

In Section 2.4, the complete publication “Y. Wu, S. Gargiulo, F. Carbone, C. H. Keitel, & A. Pálffy. Dynamical control of nuclear isomer depletion via electron vortex beams. *Physical Review Letters*, 128(16), 162501, (2022)” is included and cited in this thesis as Ref. [120]. In relation to this topic, I contributed to the idea that electron vortex beams could have potentially enhanced the NEEC cross-section, as initially published in our perspective paper referenced as Ref. [123]. Concerning Ref. [120], my involvement encompassed discussing the results and the potential realization of dynamical control using an external vortex electron beam. The theoretical framework was developed by Yuanbin Wu and Adriana Pálffy.



## Nuclear Excitation by Electron Capture in Excited Ions

Simone Gargiulo<sup>1</sup>,\* Ivan Madan<sup>1</sup>, and Fabrizio Carbone<sup>1</sup>†

*Institute of Physics (IPhys), Laboratory for Ultrafast Microscopy and Electron Scattering (LUMES),  
École Polytechnique Fédérale de Lausanne (EPFL), Lausanne 1015 CH, Switzerland*

(Received 21 October 2020; revised 10 November 2021; accepted 4 April 2022; published 27 May 2022)

A nuclear excitation following the capture of an electron in an empty orbital has been recently observed for the first time. So far, the evaluation of the cross section of the process has been carried out widely using the assumption that the ion is in its electronic ground state prior to the capture. We show that by lifting this restriction new capture channels emerge resulting in a boost of more than three orders of magnitude to the electron capture resonance strength.

DOI: 10.1103/PhysRevLett.128.212502

Innovative technologies for harvesting and long-duration storing of energy are currently highly desired [1,2]. In this context, isomers are particularly attractive as they provide the potential for on-demand clean energy release combined with reliability, compactness, high stored energy density, and the ability to operate in extreme environment. The achievement of a controlled and efficient extraction of the isomeric energy has been a milestone for decades and is recently attracting growing attention [3–10]. In particular, recently demonstrated Nuclear Excitation by Electron Capture (NEEC) [11] could possibly offer gains in terms of control, as the electron switch of the process can be manipulated by means of electron optics and wave function engineering [10,12].

NEEC is a process in which the capture of a free or target electron by an ion results in the resonant excitation of a nucleus. The kinetic energy of the free electron  $E_r$  needs to equal the difference between the nuclear transition energy,  $E_n$ , and the atomic binding energy released through electron capture,  $E_b$  (i.e.,  $E_r = E_n - E_b$ ). The first isomer depletion induced by electron capture was recorded in a beam-based setup in 2018 [11], albeit the strength of the detected signal is unexplained by state-of-the-art theory [13], presenting a discrepancy of about nine orders of magnitude. Till today, NEEC is an object of a live debate [14–16].

Until this Letter, the NEEC process has been considered only in ions which are in their electronic ground states (ground state assumption, GSA) [17–20], in ground state ions with a single inner-shell hole created by  $x$  rays [21] or considering a statistical approach for electronic populations in an average atom model [22–24]. In this Letter, we examine the role of excited electronic configurations without any restrictions on the initial levels population. While the GSA allows for a straightforward account of the capture channels, it is too restrictive to unequivocally represent the real conditions taking place in out of equilibrium scenarios. In fact, it has been shown that, for a given charge state  $q$ , the ground state configuration

usually is not the most probable [25]. It is therefore important to evaluate the cross sections of nuclear processes for a wider range of electronic configurations.

The GSA rules out the capture in the innermost shells for partially filled ions. For example, one can have  $K$  capture till two electrons fill the  $1s$  orbital. However, even for fully ionized nuclei, NEEC into  $K$  shell may be forbidden if the energy released through a  $K$  capture ( $E_b^K$ ) exceeds the nuclear transition energy (i.e.,  $E_r < 0$ ). Therefore, for such nuclei, under the GSA, NEEC with capture in the  $K$  shell is never possible. These channels can be re-enabled if sufficient screening is provided by an out of equilibrium electronic configuration, as we show for the example of  $^{73}\text{Ge}$ .

In Fig. 1 we compare both the conventional and our approach. In Fig. 1(a) NEEC takes place in an ion under the GSA. A variant of NEEC—i.e., NEEC followed by a fast x-ray emission (NEECX)—considers the capture of the electron in a higher energy electronic shell while the ion is still in its electronic ground state, a situation in which the

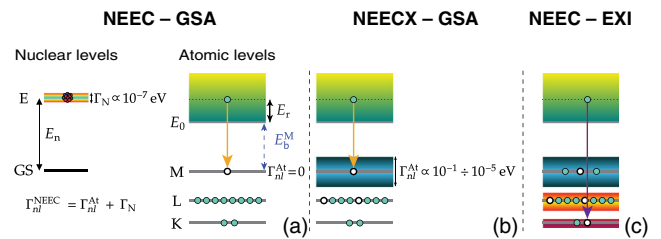


FIG. 1. Atomic configurations in case of electron capture: conventionally, the ion is considered to be in its nuclear and electronic ground states, while the capture either leaves the ion in the electronic ground state (a) referred to as NEEC, or brings it in an electronic excited state (b), referred to as NEECX. In (c), electrons can be distributed all over  $K$ ,  $L$ , and  $M$  shells.  $\Gamma$  represents the width of the atomic ( $\Gamma_{nl}^{\text{At}}$ ) and nuclear ( $\Gamma_N$ ) transitions. For atomic ground states  $\Gamma_{nl}^{\text{At}} = 0$ , while for excited configurations  $\Gamma_{nl}^{\text{At}} \gg \Gamma_N$ .

GSA still holds [17,26], see Fig. 1(b). Instead, Fig. 1(c) represents the case in which the GSA does not hold: here, NEEC can occur even in excited ions (NEEC-EXI) and the consequences of such a scenario are discussed below.

The integrated NEEC cross section, called resonance strength  $S_{\text{NEEC}}^{q,\alpha_r}$ , can be expressed as [19,27–31]:

$$S_{\text{NEEC}}^{q,\alpha_r} = \int dE \frac{\lambda_e^2}{2} \hbar Y_{\text{NEEC}}^{q,\alpha_r}(E) L_r(E - E_r), \quad (1)$$

where  $\lambda_e$  is the electron wavelength and  $L_r$  is a Lorentzian function centered at the resonance energy of the free electron  $E_r$ . The width of such Lorentzian is given by the combination of both atomic configuration and nuclear level,  $\Gamma_{nl}^{\text{NEEC}} = \Gamma_{nl}^{\text{At}} + \Gamma_N$ .  $Y_{\text{NEEC}}^{q,\alpha_r}$  is the microscopic NEEC rate that depends on the final electronic configuration ( $\alpha_r$ ) and on the ion charge state  $q$  prior to the electron capture. Under the GSA, the initial electronic configuration ( $\alpha_0$ ) is uniquely defined by the charge state  $q$  and the number of available channels for capture in a particular subshell  $nl_j$  is strongly limited. By contrast, in NEEC-EXI the rate  $Y_{\text{NEEC}}^{q,\alpha_r}$  also depends on  $\alpha_0$ , thus it has to be expressed as  $Y_{\text{NEEC}}^{q,\alpha_0,\alpha_r}$ .

In NEEC-EXI, for a given charge state  $q$ , electrons are assigned to a particular shell from the innermost to the outermost ( $K$ ,  $L$ , and  $M$ ) encompassing all possible combinations. All these states are used as initial configurations  $\alpha_0$ . In case the electron involved in the capture breaks the orbital angular momentum coupling in the initial atomic configuration  $\alpha_0$ , the expression of the NEEC resonance strength in Eq. (1) is further complicated by an additional coefficient  $\Lambda$ , expressing the recoupling probability between the initial ( $\alpha_0$ ) and final electronic configurations ( $\alpha_r$ ) [32–37]:

$$S_{\text{NEEC}}^{q,\alpha_0,\alpha_r} = \Lambda \int dE \frac{\lambda_e^2}{2} \hbar Y_{\text{NEEC}}^{q,\alpha_0,\alpha_r}(E) L_r(E - E_r). \quad (2)$$

In this Letter, the recoupling schemes for ions with up to four electrons filling the orbitals have been considered. Further details about the expression of  $\Lambda$  and electron recoupling are given in Supplemental Material [38]. The microscopic NEEC rate  $Y_{\text{NEEC}}$  is related to the process of internal conversion by time reversal. Using the principle of detailed balance [30],  $Y_{\text{NEEC}}$  can be expressed as a function of the internal conversion coefficients (ICCs)  $\alpha_{\text{IC}}$ .

The determination of the ICCs for ions requires the knowledge of the electronic configuration and of the bound and free electron wave functions. In first approximation, ICCs for ions can be estimated from those of neutral atoms applying a scaling procedure, which relates ICC with the binding energy and occupancy of a specific subshell [20,22,39–42]. In this case, ICCs for neutral atoms are theoretically computed using the frozen orbital approximation based on the Dirac-Fock calculations [43]. Albeit ICCs for neutral atoms have been shown to have less than

1% uncertainty compared to experimental data [43–45], no detailed uncertainty analysis has been performed on ions for this scaling procedure.

For this reason, we compute  $Y_{\text{NEEC}}$  of selected channels also with the more advanced theory presented in Ref. [46], based on Feshbach projection operator formalism and compare these results with the ones obtained from the ICCs scaling procedure. Binding energies for a specific subshell and wave functions for a specific atomic configuration are computed using FAC [47]. FAC is a fully relativistic atomic code taking configuration interaction into account. Accuracy for the computed energy levels is assessed to be in the order of few electron volts [48].

Applying the GSA to the  $^{73}\text{Ge}$  nuclear transition of  $E_n = 13.2845$  KeV between the  $9/2^+$  ground and the  $5/2^+$  first excited states provides 47  $L$  and  $M$  channels for  $q = [29+, 32+]$ , shown in Fig. 2(a) and tabulated in Supplemental Material [38]. Here, the  $K$  shell is energetically forbidden and  $L$  channels are the innermost available. The GSA allows for a drastic reduction of computational effort, as by lifting it, a total of 32 723 capture channels can be found in the same charge state range for  $L$  and  $M$  shells. Moreover, upon filling the orbitals, the electron screening lowers the binding energy of the  $K$  shell. Once  $E_b^K$  becomes smaller than  $E_n$ , NEEC into the  $K$  shell is possible. For  $^{73}\text{Ge}$  this condition is met for  $q = 29+$ , for which 100  $K$ -capture channels have been unveiled, as shown in Fig. 2(b). Most of these  $K$  channels (78) are characterized by an initial electronic configuration  $\alpha_0$  of the type  $1s^1 2nl_j^1 3nl_j^1$  and occur in the energy range  $E_r = [0, 38.8]$  eV, while for the remaining ones  $\alpha_0$  is  $1s^1 2nl_j^2$ , and  $E_r = [48.2, 144.6]$  eV. All these  $K$  channels have one electron in the  $K$  shell prior to the electron capture: in fact,  $K$  captures with  $\alpha_0 = \{2nl_j^3\}$  are still forbidden, since  $E_b^K$  is larger than  $E_n$  by about 200 eV at  $q = 29+$ . Resonance strengths for higher charge states are shown in Supplemental Material [38]. For  $L$  and  $M$  channels the widths of the atomic configurations  $\Gamma_{nl}^{\text{At}}$  is much smaller than the resonance energy  $E_r$  and  $Y_{\text{NEEC}}$  can be moved out of the integral in Eq. (2). In the case of  $K$  channels instead  $\Gamma_{nl}^{\text{At}} \approx E_r$ , and the integral of  $Y_{\text{NEEC}}$  has to be performed. The widths for the atomic configurations leading to a  $K$  capture have been calculated using the XATOM code [49–51]. Notably, the higher number of channels identified in NEEC-EXI is not only due to the several initial configurations considered, but also to the increase of the capture channels available for a single excited configuration  $\alpha_0$  compared to the ground state counterpart. The reason is that excited configurations can have a larger number of open shells, thus the number of final configurations that can be generated are generally more numerous due to the higher number of combinations possible for the electron couplings.

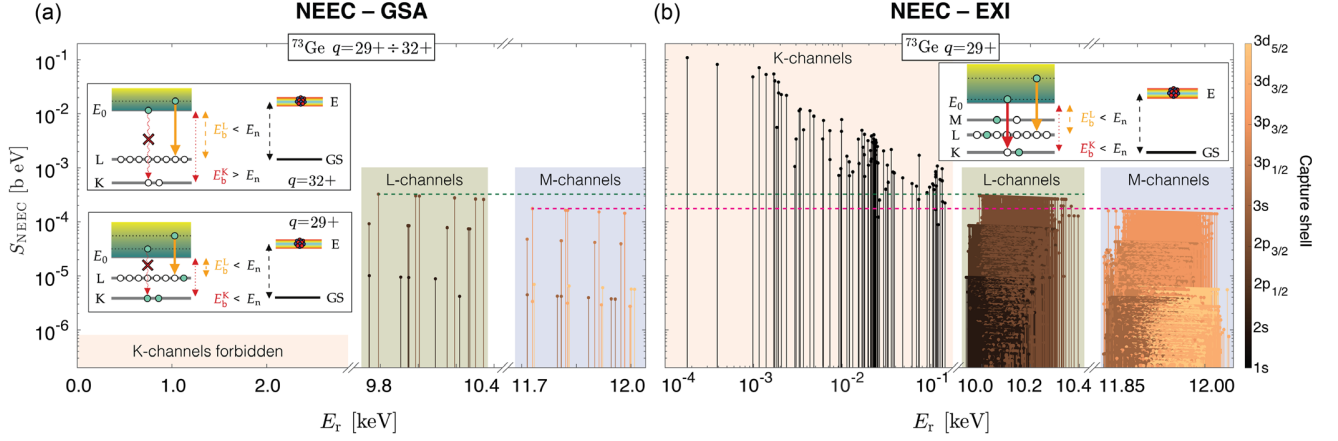


FIG. 2. (a) Resonance strengths for capture in the  $L$  shell (green box) and  $M$  shell (blue box) in case of  $^{73}\text{Ge}$  with  $q = [29+, 32+]$ . NEEC in the  $K$  shell is energetically forbidden (pink box), since for high charge states the binding energy released for a  $K$  capture is bigger than the nuclear transition ( $E_b^K > E_n$ ). For  $q = 29 + E_b^K < E_n$ , however the  $K$  shell is completely filled and capture cannot occur (insets). (b) Resonance strengths for  $^{73}\text{Ge}$  in case all the possible combinations of initial and final electronic configurations are taken into account, for  $q = 29+$ . Each resonant channel is represented by a solid line, with its colors indicating the capture orbital. The horizontal green and magenta lines indicate the highest  $S_{\text{NEEC}}$ , under GSA, for  $L$  and  $M$  shells—occurring at  $[q, \alpha_r] = [32+, 2p_{3/2}]$  and  $[q, \alpha_r] = [32+, 3p_{3/2}]$ —respectively.

Figure 2 compares the resonance strengths of the newly opened  $K$  channels with the  $L$  and  $M$  channels for NEEC-GSA and NEEC-EXI. Here, only shells up to the  $M$  have been considered, since  $\alpha_0$  with electrons in higher shells do not provide sufficient screening for a  $K$  capture at  $q = 29+$ . Selected channels are reported in Table I and, when possible, are compared with those evaluated with the GSA procedure for which Eq. (2) reduces to Eq. (1), since  $\Lambda = 1$ , and results coincide. Results for NEEC-EXI have been also evaluated using the wave function formalism (indicated as WF) and reported in Table I. The maximum value obtained in this case is of  $5.18 \times 10^{-1}$  beV. This allows us to comment on the accuracy of the ICC scaling procedure. Although the resonance strength obtained for a specific channel can be inaccurate by one order of magnitude, the ICC scaling reproduces the overall trend and the higher cross-section values in the case of NEEC-EXI. Furthermore, it allows us to have an easy estimate of the order of magnitude of the NEEC cross section in different experimental scenarios.

It is worth mentioning that the maximum value obtainable for the resonance strength with and without GSA differs by more than 3 orders of magnitude in the interval  $q = [29+, 32+]$ , due to the presence of the  $K$  channels. The highest values of the  $S_{\text{NEEC}}$  in the  $L$  and  $M$  shells instead are comparable between the two cases. There are two main factors defining the final  $S_{\text{NEEC}}$  value for a given character of the nuclear transition and  $E_n$ : (i) the resonance energy of the capture channel and (ii) the value of the microscopic NEEC rate  $Y_{\text{NEEC}}^{q, \alpha_0, \alpha_r}$ . (i) Because of the resonant nature of the NEEC process,  $S_{\text{NEEC}}$  increases dramatically when the energy released through electron capture nearly matches the nuclear transition. (ii)  $Y_{\text{NEEC}}^{q, \alpha_0, \alpha_r}$  depends on the overlap

between the bound and free electron wave functions. In the case of  $^{73}\text{Ge}$ , the enhancement found for the  $K$  shell, compared to the highest value obtained under the GSA occurring for an  $L3$  subshell, is due to an increase of the electron wavelength, since  $Y_{\text{NEEC}}^{q, K} \leq Y_{\text{NEEC}}^{q, L3}$ .

It is thus important to comment on the accuracy of the calculated energy levels. In Supplemental Material [38], we compare the 38 energy levels available for Ge, obtained from the NIST website [52], and the same reproduced by FAC. The results show a good agreement with discrepancies between these levels usually smaller than 1 eV and in all cases comparable with the accuracy reported for the  $E2$  nuclear transition of  $^{73}\text{Ge}$ . Although the  $S_{\text{NEEC}}$  values of the nearly resonant energy levels are affected by the accuracy of FAC, 27  $K$  channels are present in the range  $E_r = [0, 10]$  eV and 18 still forbidden in the range  $E_r = [-10, 0]$  eV. Thus, a shift of few eV does not affect our conclusions. Similar screening effect on  $K$  channels can be found in other isotopes as  $^{98}\text{Tc}$  and  $^{125}\text{Te}$ . In the latter case, contrary to what happens for  $^{73}\text{Ge}$ , a further increase of  $S_{\text{NEEC}}$  is expected due to a higher value of  $\alpha_{\text{IC}}^{q=0, K}$  compared to  $\alpha_{\text{IC}}^{q=0, Li}$ , with  $i \in \{1, 2, 3\}$ .

An increase of the resonance strength is particularly valuable when NEEC is compared to competitive processes, such as the direct photoexcitation (DP) in the laser-generated plasma scenario [19,22,24,53]. Here, the discrimination of the two processes relies on the total number of excited nuclei, proportional to the corresponding photon or electron flux in plasma and the corresponding resonance strengths. In a tabletop laser based setup, the photon flux can exceed the electron flux by several orders of magnitude [19,38,54,55]. This might hinder the observation of NEEC even for such

TABLE I. Resonance strengths for  $^{73}\text{Ge}$  in case of NEEC-EXI considering both the ICCs scaling procedure and the wave function (WF) formalism. For a given final electronic state ( $\alpha_r$ ) all the relative parent configurations  $\alpha_0$ , that through electron capture can lead to it, are taken into consideration. Resonance energies are intended as  $E_r = E_n - E_b$ . When possible, a comparison with the conventional derivation (GSA) is also presented. Bold the subshell  $nl_j$  in which the capture occurs.

$q$	$^{73}\text{Ge}$		$E_r$ (eV)	NEEC GSA	NEEC-EXI	
	Initial configuration ( $\alpha_0$ )	Final configuration ( $\alpha_r$ )		$S_{\text{NEEC}}$ (b eV)	$S_{\text{NEEC}}$ (b eV)	
				ICC's scaling	ICC's scaling	WF
32+	...	<b>2p</b> $_{3/2}^1$	$9.79 \times 10^3$	$3.26 \times 10^{-4}$	$3.26 \times 10^{-4}$	$1.25 \times 10^{-4}$
32+	...	<b>2p</b> $_{1/2}^1$	$9.74 \times 10^3$	$9.21 \times 10^{-5}$	$9.21 \times 10^{-5}$	$6.76 \times 10^{-5}$
31+	$1s^1$	$1s^1$ <b>2s</b> $^1$	$9.91 \times 10^3$	$9.49 \times 10^{-6}$	$9.49 \times 10^{-6}$	$8.37 \times 10^{-6}$
31+	$3d^1_{3/2}$	<b>2p</b> $_{1/2}^1$ $3d^1_{3/2}$	$9.82 \times 10^3$	Not allowed	$8.92 \times 10^{-5}$	$6.56 \times 10^{-5}$
30+	$1s^2$	$1s^2$ <b>2s</b> $^1$	$10.09 \times 10^3$	$8.82 \times 10^{-6}$	$8.82 \times 10^{-6}$	$7.47 \times 10^{-6}$
30+	$3d^1_{3/2} 3d^1_{5/2}$	<b>2p</b> $_{3/2}^1$ $3d^1_{3/2} 3d^1_{5/2}$	$9.96 \times 10^3$	Not allowed	$2.67 \times 10^{-4}$	$1.05 \times 10^{-4}$
29+	$1s^2 2s^1$	$1s^2 2s^1$ <b>2p</b> $_{1/2}^1$	$10.26 \times 10^3$	$7.46 \times 10^{-5}$	$7.46 \times 10^{-5}$	$5.19 \times 10^{-5}$
29+	$3p^1_{3/2} 3d^1_{3/2} 3d^1_{5/2}$	<b>2p</b> $_{3/2}^1$ $3p^1_{3/2} 3d^1_{3/2} 3d^1_{5/2}$	$10.06 \times 10^3$	Not allowed	$6.30 \times 10^{-5}$	$2.53 \times 10^{-5}$
29+	$3p^1_{3/2} 3d^1_{3/2} 3d^1_{5/2}$	<b>2p</b> $_{1/2}^1$ $3p^1_{3/2} 3d^1_{3/2} 3d^1_{5/2}$	$10.03 \times 10^3$	Not allowed	$7.18 \times 10^{-5}$	$5.58 \times 10^{-5}$
29+	$1s^1 2p^1_{1/2} 2p^1_{3/2}$	<b>1s</b> $^2$ $2p^1_{1/2} 2p^1_{3/2}$	144.62	Not allowed	$2.23 \times 10^{-4}$	$9.40 \times 10^{-4}$
29+	$1s^1 2s^2$	<b>1s</b> $^2$ $2s^2$	73.87	Not allowed	$1.71 \times 10^{-3}$	$7.28 \times 10^{-3}$
29+	$1s^1 2s^1 3d^1_{5/2}$	<b>1s</b> $^2$ $2s^1 3d^1_{5/2}$	4.32	Not allowed	$1.14 \times 10^{-2}$	$4.94 \times 10^{-2}$
29+	$1s^1 2s^1 3p^1_{1/2}$	<b>1s</b> $^2$ $2s^1 3p^1_{1/2}$	1.15	Not allowed	$7.14 \times 10^{-2}$	$3.10 \times 10^{-1}$
29+	$1s^1 2p^1_{3/2} 3d^1_{3/2}$	<b>1s</b> $^2$ $2p^1_{3/2} 3d^1_{3/2}$	0.98	Not allowed	$4.82 \times 10^{-2}$	$2.32 \times 10^{-1}$
29+	$1s^1 2p^1_{3/2} 3d^1_{3/2}$	<b>1s</b> $^2$ $2p^1_{3/2} 3d^1_{3/2}$	0.39	Not allowed	$8.25 \times 10^{-2}$	$3.61 \times 10^{-1}$
29+	$1s^1 2s^1 3p^1_{3/2}$	<b>1s</b> $^2$ $2s^1 3p^1_{3/2}$	0.18	Not allowed	$1.09 \times 10^{-1}$	$5.18 \times 10^{-1}$

promising nuclei as  $^{73}\text{Ge}$ , for which the DP resonance strength of the  $E2$  transition is  $S_\gamma = 1.93 \times 10^{-6}$  beV, significantly smaller than the highest  $S_{\text{NEEC}} = 1.25 \times 10^{-4}$  beV, obtained under the GSA. Conversely, lifting the GSA allows for the appearance of capture channels in the  $K$  shell characterized by higher  $S_{\text{NEEC}}$  values. This is particularly relevant if an additional external electron source is considered. For a few kilo electron volts temperature plasma, the flux of electrons at low energies corresponding to  $K$  channels is small and of the order of  $10^{21} \text{ cm}^{-2} \text{ s}^{-1} \text{ eV}^{-1}$ . Under this condition, the use of an external adjustable electron source [38,56] could allow us to overcome the deficit in the electron flux and decouple it from other plasma parameters. We point out here that the determination of the total number of excited nuclei would require the knowledge of the survival time of each atomic configuration in a specific experimental scenario. To the best of our knowledge, this level of detail is not available with current simulation tools.

In out-of-equilibrium scenarios, excited electronic configurations might be more likely to occur [25] and the same can hold true for the  $^{93}\text{Mo}$  isomer depletion of Ref. [11]. Indeed, during the entire impact with the carbon target,  $^{93}\text{Mo}$  ions are considered to be in their electronic ground state. This makes the contributions from the  $L$  shell negligible, although the resonance strengths for the  $L$  channels are the highest [13]. This happens because

the ion fraction in the charge state  $q \geq 33+$  required for  $L$ -shell vacancies is extremely small when the resonant conditions are met. Recently, a study considering the Compton profile of target electrons [16] shed new light on the importance of these  $L$  channels, shifting upward by several orders of magnitude their theoretical contribution to the partial NEEC probability. In particular, this study shows that the  $L$  channels are no longer insignificant and their contribution is comparable with that of higher shells. Nevertheless, the total NEEC probability, accounting for charge state distribution and available vacancies, only slightly increases leaving the current discrepancy mostly unaltered. Indeed, under the GSA, the  $L$  channels are not available at low projectile energies, where they give most of their contribution [16]. If instead electronic excitations would make  $L$  vacancies survive even for  $q < 33+$ , NEEC-EXI might reveal new capture  $L$  channels even at low ion beam energy. The presence of these new channels, combined with their persistence over an energy continuum [16], might possibly reduce the discrepancy between the experimental observation and theoretical predictions.

In NEEC scenarios only the energy matching between free electrons, bound states, and nuclear transitions has been historically addressed. Since selection rules for NEEC require  $j_c - L \leq j_f \leq j_c + L$ , where  $L$  is the multipolarity of the transition, in Ref. [12] we proposed that angular



momentum matching could have given the possibility to select and enhance the capture in the innermost shells, by tuning the individual orbital angular momentum (OAM)  $l\hbar$  of an external free electron beam [57–60], using phase plates or chiral plasmons [61–63]. When using such OAM-carrying electrons (called vortex beam) the expressions used for  $Y_{\text{NEEC}}$  do not hold in the same form, thus leading to different values for the  $S_{\text{NEEC}}$ . Recently, this has been shown in detail to be a way to increase the NEEC cross section by several orders of magnitude [64]. The combination of this additional degree of freedom with the presence of excited electronic configurations could open a possibility to further boost the NEEC rate in a plasma scenario by providing specific atomic vacancies and pulsed vortex electrons at the resonant energy to selectively choose the capture in the desired shell.

In conclusion, we have shown that the common assumption that NEEC takes place in an ion in its electronic ground state significantly restricts the available channels. By lifting this condition, we have shown that in  $^{73}\text{Ge}$  the NEEC resonance strengths gain more than three orders of magnitude. Thus, this work heralds the possibility of a reevaluation of the isotopes prematurely disregarded and those already in use in out-of equilibrium scenarios. These findings could open a new route for an externally controlled nuclear excitation by providing excited configurations and resonant engineered electrons from an external source, thus selecting the promising channels for on-demand isomer depletion. In particular, the inclusion of excited electronic configurations in the theoretical model describing the first NEEC observation in  $^{93}\text{Mo}$ , as here done for  $^{73}\text{Ge}$ , could reduce the discrepancy between the actual theoretical predictions and experimental observation.

The LUMES laboratory acknowledges support from the NCCR MUST and Google Inc. The authors would like to thank G. M. Vanacore, C. J. Chiara, and J. J. Carroll for insightful discussions. The authors are indebted to A. Pálffy and Y. Wu for their useful feedback and for providing details on the derivation of the theory presented in Ref. [46].

\*simone.gargiulo@epfl.ch

†fabrizio.carbone@epfl.ch

- [1] R. Koningstein and D. Fork, *IEEE Spectrum* **51**, 30 (2014).
- [2] N. A. Sepulveda, J. D. Jenkins, A. Edington, D. S. Mallapragada, and R. K. Lester, *Nat. Energy* **6**, 506 (2021).
- [3] P. Walker and G. Dracoulis, *Nature (London)* **399**, 35 (1999).
- [4] C. B. Collins, F. Davanloo, M. C. Iosif, R. Dussart, J. M. Hicks, S. A. Karamian, C. A. Ur, I. I. Popescu, V. I. Kirischuk, J. J. Carroll, H. E. Roberts, P. McDaniel, and C. E. Crist, *Phys. Rev. Lett.* **82**, 695 (1999).
- [5] M. Litz and G. Merkel, Controlled extraction of energy from nuclear isomers, Technical Report No. ADA433348, Army Research Laboratory, Adelphi, MD, 2004.
- [6] C. B. Collins, N. C. Zoita, F. Davanloo, S. Emura, Y. Yoda, T. Uruga, B. Patterson, B. Schmitt, J. M. Povesle, I. Popescu *et al.*, *Radiat. Phys. Chem.* **71**, 619 (2004).
- [7] A. Aprahamian and Y. Sun, *Nat. Phys.* **1**, 81 (2005).
- [8] A. Y. Dzyublik, *Nucl. Phys. At. Energy* **14**, 11 (2013).
- [9] J. Carroll, M. Litz, K. Netherton, S. Henriquez, N. Pereira, D. Burns, and S. Karamian, in *AIP Conference Proceedings* (American Institute of Physics, Melville, 2013), Vol. 1525, pp. 586–594.
- [10] G. M. Vanacore, I. Madan, G. Berruto, K. Wang, E. Pomarico, R. Lamb, D. McGrouther, I. Kaminer, B. Barwick, F. J. G. de Abajo, and F. Carbone, *Nat. Commun.* **9**, 2694 (2018).
- [11] C. J. Chiara, J. J. Carroll, M. P. Carpenter, J. P. Greene, D. J. Hartley, R. V. Janssens, G. J. Lane, J. C. Marsh, D. A. Matters, M. Polasik, J. Rzakiewicz, D. Seweryniak, S. Zhu, S. Bottoni, and A. B. Hayes, *Nature (London)* **554**, 216 (2018).
- [12] I. Madan, G. M. Vanacore, S. Gargiulo, T. Lagrange, and F. Carbone, *Appl. Phys. Lett.* **116**, 230502 (2020).
- [13] Y. Wu, C. H. Keitel, and A. Pálffy, *Phys. Rev. Lett.* **122**, 212501 (2019).
- [14] S. Guo, Y. Fang, X. Zhou, and C. Petrache, *Nature (London)* **594**, E1 (2021).
- [15] C. Chiara, J. Carroll, M. Carpenter, J. Greene, D. Hartley, R. Janssens, G. Lane, J. Marsh, D. Matters, M. Polasik *et al.*, *Nature (London)* **594**, E3 (2021).
- [16] J. Rzakiewicz, M. Polasik, K. Słabkowska, L. Syrocki, J. J. Carroll, and C. J. Chiara, *Phys. Rev. Lett.* **127**, 042501 (2021).
- [17] A. Pálffy, Z. Harman, C. Kozhuharov, C. Brandau, C. H. Keitel, W. Scheid, and T. Stöhlker, *Phys. Lett. B* **661**, 330 (2008).
- [18] Y. Wu, J. Gunst, C. H. Keitel, and A. Pálffy, *Phys. Rev. Lett.* **120**, 052504 (2018).
- [19] J. Gunst, Y. Wu, C. H. Keitel, and A. Pálffy, *Phys. Rev. E* **97**, 063205 (2018).
- [20] J. Rzakiewicz, M. Polasik, K. Słabkowska, L. Syrocki, E. Wéder, J. J. Carroll, and C. J. Chiara, *Phys. Rev. C* **99**, 044309 (2019).
- [21] Y. Wu, C. H. Keitel, and A. Pálffy, *Phys. Rev. A* **100**, 063420 (2019).
- [22] G. Gosselin and P. Morel, *Phys. Rev. C* **70**, 064603 (2004).
- [23] G. D. Doolen, *Phys. Rev. Lett.* **40**, 1695 (1978).
- [24] G. D. Doolen, *Phys. Rev. C* **18**, 2547 (1978).
- [25] S.-K. Son, R. Thiele, Z. Jurek, B. Ziaja, and R. Santra, *Phys. Rev. X* **4**, 031004 (2014).
- [26] M. Polasik, K. Słabkowska, J. J. Carroll, C. J. Chiara, Ł. Syrocki, E. Weder, and J. Rzakiewicz, *Phys. Rev. C* **95**, 034312 (2017).
- [27] S. S. Wong, *Introductory Nuclear Physics* (John Wiley & Sons, New York, 2008).
- [28] A. Zadernovsky and J. Carroll, *Hyperfine Interact.* **143**, 153 (2002).
- [29] M. R. Harston and J. F. Chemin, *Phys. Rev. C* **59**, 2462 (1999).
- [30] J. Oxenius, *Springer Series in Electrophysics* (Springer Science & Business Media, Berlin, 1986).
- [31] A. Pálffy, W. Scheid, and Z. Harman, *Phys. Rev. A* **73**, 012715 (2006).

- [32] P. V. Bilous, G. A. Kazakov, I. D. Moore, T. Schumm, and A. Pálffy, *Phys. Rev. A* **95**, 032503 (2017).
- [33] A. P. Yutsis, V. Vanagas, and I. B. Levinson, *Mathematical Apparatus of the Theory of Angular Momentum* (Israel Program for Scientific Translations, Jerusalem, 1962).
- [34] L. C. Biedenharn and J. D. Louck, *The Racah-Wigner Algebra in Quantum Theory* (Addison-Wesley, Reading, MA, 1981).
- [35] V. Aquilanti, A. C. P. Bitencourt, C. D. S. Ferreira, A. Marzuoli, and M. Ragni, *Phys. Scr.* **78**, 058103 (2008).
- [36] V. Fack, S. N. Pitre, and J. Van der Jeugt, *Comput. Phys. Commun.* **86**, 105 (1995).
- [37] V. Fack, S. Lievens, and J. Van Der Jeugt, *Comput. Phys. Commun.* **119**, 99 (1999).
- [38] See Supplemental Material at <http://link.aps.org/supplemental/10.1103/PhysRevLett.128.212502> for further details on the ICC scaling procedure and wave function formalism, the computed values in case of GSA for  $^{73}\text{Ge}$ , recoupling coefficients, accuracy of the FAC calculations, the 3D plot showing  $S_{\text{NEEC}}$  for NEEC-EXI in  $^{73}\text{Ge}$  with  $q = [29+, 32+]$ , and NEEC-GSA in the laser-plasma scenario (2021).
- [39] M. Rysavý and O. Dragoun, *J. Phys. G* **26**, 1859 (2000).
- [40] F. Larkins, *At. Data Nucl. Data Tables* **20**, 311 (1977).
- [41] K. D. Sevier, *At. Data Nucl. Data Tables* **24**, 323 (1979).
- [42] J. Kantele, *Nucl. Instrum. Methods Phys. Res., Sect. A* **275**, 149 (1989).
- [43] T. Kibedi, T. Burrows, M. B. Trzhaskovskaya, P. M. Davidson, and C. W. Nestor, Jr., *Nucl. Instrum. Methods Phys. Res., Sect. A* **589**, 202 (2008).
- [44] T. Kibédi, T. W. Burrows, M. B. Trzhaskovskaya, C. W. Nestor, Jr., and P. M. Davidson, *Int. Conf. Nucl. Data Sci. Technol.* **57** (2007).[10.1051/ndata:07771](https://doi.org/10.1051/ndata:07771)
- [45] S. Raman, C. W. Nestor, Jr., A. Ichihara, and M. B. Trzhaskovskaya, *Phys. Rev. C* **66**, 044312 (2002).
- [46] A. Pálffy, Theory of nuclear excitation by electron capture for heavy ions, Ph.D. thesis, Justus-Liebig-Universität, 2006.
- [47] M. F. Gu, *Can. J. Phys.* **86**, 675 (2008).
- [48] G. Massacrier and M.-C. Artru, *Astron. Astrophys.* **538**, A52 (2012).
- [49] Z. Jurek, S.-K. Son, B. Ziaja, and R. Santra, *J. Appl. Crystallogr.* **49**, 1048 (2016).
- [50] S.-K. Son, L. Young, and R. Santra, *Phys. Rev. A* **83**, 033402 (2011).
- [51] B. Murphy, T. Osipov, Z. Jurek, L. Fang, S.-K. Son, M. Mucke, J. Eland, V. Zhaunerchyk, R. Feifel, L. Avaldi *et al.*, *Nat. Commun.* **5**, 1 (2014).
- [52] A. Kramida, Yu. Ralchenko, J. Reader, and NIST ASD Team, NIST Atomic Spectra Database (ver. 5.6.1) (2015), Available: <https://physics.nist.gov/asd>, National Institute of Standards and Technology, Gaithersburg, MD, 2018.
- [53] J. F. Gunst, Mutual control of x-rays and nuclear transitions, Ph.D. thesis, Ruprecht-Karls-Universität Heidelberg, 2015.
- [54] P. Gibbon and E. Förster, *Plasma Phys. Controlled Fusion* **38**, 769 (1996).
- [55] H.-K. Chung, M. Chen, W. Morgan, Y. Ralchenko, and R. Lee, *High Energy Density Phys.* **1**, 3 (2005).
- [56] D. Filippetto, P. Musumeci, M. Zolotorev, and G. Stupakov, *Phys. Rev. ST Accel. Beams* **17**, 024201 (2014).
- [57] J. Verbeeck, H. Tian, and P. Schattschneider, *Nature (London)* **467**, 301 (2010).
- [58] S. Lloyd, M. Babiker, G. Thirunavukkarasu, and J. Yuan, *Rev. Mod. Phys.* **89**, 035004 (2017).
- [59] J. Verbeeck, A. Béché, K. Müller-Caspary, G. Guzzinati, M. A. Luong, and M. Den Hertog, *Ultramicroscopy* **190**, 58 (2018).
- [60] G. M. Vanacore, I. Madan, and F. Carbone, *Riv. Nuovo Cimento* **43**, 567 (2020).
- [61] K. Y. Bliokh, I. P. Ivanov, G. Guzzinati, L. Clark, R. Van Boxem, A. Béché, R. Juchtmans, M. A. Alonso, P. Schattschneider, F. Nori, and J. Verbeeck, *Phys. Rep.* **690**, 1 (2017).
- [62] G. M. Vanacore, G. Berruto, I. Madan, E. Pomarico, P. Biagioni, R. J. Lamb, D. McGrouther, O. Reinhardt, I. Kaminer, B. Barwick, H. Larocque, V. Grillo, E. Karimi, F. J. García de Abajo, and F. Carbone, *Nat. Mater.* **18**, 573 (2019).
- [63] V. Grillo, A. H. Tavabi, F. Venturi, H. Larocque, R. Balboni, G. C. Gazzadi, S. Frabboni, P.-H. Lu, E. Mafakheri, F. Bouchard *et al.*, *Nat. Commun.* **8**, 15536 (2017).
- [64] Y. Wu, S. Gargiulo, F. Carbone, C. H. Keitel, and A. Pálffy, *Phys. Rev. Lett.* **128**, 162501 (2022).

## Supplemental Material: Nuclear Excitation by Electron Capture in Excited Ions

Simone Gargiulo,\* Ivan Madan, and Fabrizio Carbone†

*Institute of Physics (IPhys), Laboratory for Ultrafast Microscopy and Electron Scattering (LUMES),  
École Polytechnique Fédérale de Lausanne (EPFL), Lausanne 1015 CH, Switzerland*

### NEEC RESONANCE STRENGTH DERIVATION

Formally, the NEEC cross-section can be written similarly to the cross-section for the formation of an excited compound nucleus, in which the entrance channel  $\alpha$  is represented by the incoming electron. Thus, it is possible to write the NEEC cross section as the *Breit-Wigner* one-level formula [1–3]:

$$\begin{aligned}\sigma_{\text{NEEC}} &= \frac{\pi}{k_e^2} \Gamma_\alpha \frac{\Gamma_r}{(E - E_r)^2 + \Gamma_r^2/4} \\ &= \frac{2\pi^2}{k_e^2} \Gamma_\alpha L_r(E - E_r),\end{aligned}\quad (\text{S1})$$

where  $k_e$  is the electron wave-number,  $\Gamma_r$  is the natural resonance width given by the sum of the atomic ( $\Gamma^{\text{At}}$ ) and nuclear ( $\Gamma_{\text{N}}$ ) widths,  $\Gamma_\alpha$  represents the transition width of the entrance channel  $\alpha$  and  $L_r$  is a Lorentzian function centered at the resonance energy of the free electron  $E_r$ .  $\Gamma_\alpha$  is defined by the microscopic NEEC reaction rate  $Y_{\text{NEEC}}$ , via  $\Gamma_\alpha = \hbar Y_{\text{NEEC}}$ :

$$\sigma_{\text{NEEC}} = \frac{\lambda_e^2}{2} \hbar Y_{\text{NEEC}}^{q,\alpha_r}(E) L_r(E - E_r), \quad (\text{S2})$$

The integrated NEEC cross section, called resonance strength  $S_{\text{NEEC}}$ , is then defined as:

$$S_{\text{NEEC}}^{q,\alpha_r} = \int dE \sigma_{\text{NEEC}}(E) = \int dE \frac{\lambda_e^2}{2} \hbar Y_{\text{NEEC}} L_r(E - E_r). \quad (\text{S3})$$

### Internal Conversion Coefficients (ICC) scaling procedure

The microscopic NEEC rate  $Y_{\text{NEEC}}$  [4] is related to the internal conversion rate ( $A_{\text{IC}}$ ) through the principle of detailed balance [5]. Thus, in case of unpolarized beams we have:

$$Y_{\text{NEEC}} = \frac{(2J_E + 1)(2j_c + 1)}{(2J_G + 1)(2j_f + 1)} A_{\text{IC}} \quad (\text{S4})$$

where  $J_E$ ,  $J_G$  and  $j_c$  and  $j_f$  represent the nuclear spins of the excited and ground states and the total angular momenta of the captured and free electrons, respectively [3]. The NEEC cross section is then given by:

$$\sigma_{\text{NEEC}} = \frac{(2J_E + 1)(2j_c + 1)}{(2J_G + 1)(2j_f + 1)} \frac{\lambda_e^2}{2} \Gamma_{\text{IC}} L_r(E - E_r), \quad (\text{S5})$$

where  $\lambda_e$  is the electron wavelength and  $\Gamma_{\text{IC}} = \hbar A_{\text{IC}}$ . More precisely, the microscopic NEEC and IC rate depend on the particular subshell  $nl_j$  in which the electron is captured and charge state  $q$  of the ion prior the electron capture. This information is condensed in the evaluation of the partial internal conversion coefficient  $\alpha_{\text{IC}}^{q,\alpha_r}$ , that depends on the final electronic configuration ( $\alpha_r$ ) and on the ion charge state  $q$  prior to the electron capture. Under the GSA, the initial electronic configuration ( $\alpha_0$ ) is uniquely defined by the charge state  $q$  — i.e. the electronic ground state — while the final electronic configuration ( $\alpha_r$ ) depends also on the particular capture channel. Thus, Eq. (S5) can be expressed as:

$$\sigma_{\text{NEEC}}^{q,\alpha_r} = S \frac{\lambda_e^2}{2} \alpha_{\text{IC}}^{q,\alpha_r} \Gamma_\gamma L_r(E - E_r), \quad (\text{S6})$$

where  $S = (2J_E+1)(2j_c+1)/(2J_G+1)(2j_t+1)$  and  $\Gamma_\gamma$  is the width of the electromagnetic nuclear transition. ICCs for neutral atoms are estimated by using the frozen orbital (FO) approximation based on the Dirac-Fock calculations [6], while for ionized atoms a linear scaling dependence is assumed [7, 8]:

$$\frac{\alpha_{\text{IC}}^{q,\alpha_r}}{E_b^{q,\alpha_r}} = \frac{\alpha_{\text{IC}}^{q=0,nl_j}}{E_b^{q=0,nl_j}} \left( \frac{n_h}{n_{\text{max}}} \right), \quad (\text{S7})$$

where  $E_b^{q,\alpha_0,\alpha_r}$  and  $E_b^{q=0,nl_j}$  are the binding energies for ions in the charge state  $q$  and neutral atoms, respectively. Their ratio accounts for the increase of the ICCs with the ionization level [8, 9]. The ratio between the present  $n_h$  and the maximum  $n_{\text{max}}$  number of holes in the capture subshell  $nl_j$  accounts for the decrease of the ICCs for partially filled subshells [8]. The binding energies for neutral atoms were taken from tables [10], while the ones for highly ionized atoms are calculated with FAC [11], obtained as energy difference between the initial ( $\alpha_0$ ) and final electronic configurations ( $\alpha_r$ ). The resonance energy  $E_r$  is then obtained as  $E_n - E_b$  for the specific channel considered. Accuracy of these levels is assessed to be in the order of few eV [12]. As described in the main text, when NEEC is occurring in excited ions, the coefficient  $\alpha_{\text{IC}}^{q,\alpha_r}$  also depends on the particular initial electronic configuration  $\alpha_0$  and it has to be expressed as  $\alpha_{\text{IC}}^{q,\alpha_0,\alpha_r}$ :

$$\frac{\alpha_{\text{IC}}^{q,\alpha_0,\alpha_r}}{E_b^{q,\alpha_0,\alpha_r}} = \frac{\alpha_{\text{IC}}^{q=0,nl_j}}{E_b^{q=0,nl_j}} \left( \frac{n_h}{n_{\text{max}}} \right), \quad (\text{S8})$$

As a consequence, also the NEEC cross-section and the resonance strength have to be represented as  $\sigma_{\text{NEEC}}^{q,\alpha_0,\alpha_r}$  and  $S_{\text{NEEC}}^{q,\alpha_0,\alpha_r}$ , respectively. When approaching the threshold  $E_r \leq 1$  keV, to account for the non-linear trend of the ICCs, Eq. S8 is replaced with a non-linear model. For K-channels a fourth-order polynomial has been used, as similarly done in Ref. 13, to extrapolate the value of  $\alpha_{\text{IC}}^{q=0,nl_j}$  as function of the energy. This non-linear fit replaces Eq. S8, as follow:

$$\alpha_{\text{IC}}^{q,\alpha_0,\alpha_r} = \alpha_{\text{IC}}^{q=0,nl_j} \left( E_n - (E_b^{q,\alpha_0,\alpha_r} - E_b^{q=0,K}) \right) \left( \frac{n_h}{n_{\text{max}}} \right), \quad (\text{S9})$$

where the energies inside the parenthesis are the argument of the ICC. To improve comparison with the wavefunction formalism presented in Ref. 14 we used  $S = (2J_E+1)(2j_c+1)/(2J_G+1)$  as statistical factor given that different values of  $j_t$  contribute to the final  $\alpha_{\text{IC}}^{q,\alpha_r}$ .

### Wavefunction Formalism

The relativistic bound and continuum wavefunctions, solution of the Dirac equations, are written as:

$$\Psi_{n_b \kappa_b m_b}(\mathbf{r}) = \frac{1}{\mathbf{r}} \begin{pmatrix} P_{n_b \kappa_b}(r) \chi_{\kappa_b}^m(\theta, \phi) \\ i Q_{n_b \kappa_b}(r) \chi_{-\kappa_b}^m(\theta, \phi) \end{pmatrix} \quad (\text{S10})$$

$$\Psi_{E \kappa m}(\mathbf{r}) = \frac{1}{\mathbf{r}} \begin{pmatrix} P_{E \kappa}(r) \chi_{\kappa}^m(\theta, \phi) \\ i Q_{E \kappa}(r) \chi_{-\kappa}^m(\theta, \phi) \end{pmatrix} \quad (\text{S11})$$

where,  $P(r) = rg(r)$  and  $Q(r) = rf(r)$  are the Dirac spin orbitals, while  $f(r)$  and  $g(r)$  are the large and small radial components. As shown in Ref. 14, in the case of an electric transition the NEEC rate can be written in atomic unit as:

$$Y_n^{(e)L} = \frac{1}{4\pi\alpha} \frac{4\pi^2 \rho_i}{(2L+1)^2} B \uparrow (2j_b+1) \sum_{\kappa} |\tilde{R}_{L,\kappa_b,\kappa}|^2 C(j_b \ L \ j; 1/2 \ 0 \ 1/2)^2 \quad (\text{S12})$$



In Eq. S12  $B\uparrow$  is the reduced transition probability of the  $L^{\text{th}}$  multipolar transition,  $C(j_1 j_2 j; m_1 m_2 m)$  is the Clebsch-Gordan coefficient.  $j_b$  and  $j$  are the total angular momentum, while  $k_b$  and  $k$  are the Dirac angular momentum of the bound and free electron, respectively.  $\kappa$  assumes only the values allowed by selection and parity rules. In this formalism  $j_b$  and  $j$  are equivalent to  $j_c$  and  $j_f$ , respectively.  $\tilde{R}_{L,\kappa_b,\kappa}$  is the radial integral and its expression is

$$\tilde{R}_{L,\kappa_b,\kappa} = \int_0^{+\infty} dr r^{-L-1} [P_{\kappa_b}(r)P_{E\kappa}(r) + Q_{\kappa_b}(r)Q_{E\kappa}(r)] \quad (\text{S13})$$

and depends on the bound ( $P_{\kappa_b}, Q_{\kappa_b}$ ) and free ( $P_{E\kappa}, Q_{E\kappa}$ ) electron wavefunctions, which are obtained as solutions of the Dirac equations for a particular atomic configuration using FAC [11]. Compared to Ref. 14 a different normalization of the free wavefunctions is performed by FAC, thus  $P_{E\kappa}$  and  $Q_{E\kappa}$  have to be furtherly normalized to  $\sqrt{\pi}$ .

### Atomic Widths for K-channels

In case of K-channels the width of the resonant process  $\Gamma_{\text{NEEC}} = \Gamma_{nl}^{\text{At}} + \Gamma_{\text{N}} \approx \Gamma_{nl}^{\text{At}}$  can be comparable with the resonance energy  $E_r$ . Thus,  $Y_{\text{NEEC}}$  can not be moved out of the integral in Eq. S3. Atomic widths for all the specific 100 excited electronic configurations leading to a K-capture have been evaluated using the XATOM code [15–17]. Integral have been performed over an interval of  $8 \times \Gamma_{nl}^{\text{At}}$  in all the cases, apart from the first two channels where the lower limit for the integration has been set to 0.01 eV. This choice does not affect the main result of NEEC-EXI since the third and fourth channels at 0.98 eV and 1.15 eV, not affected by the truncation of the lower limit of the integral, have resonance strengths comparable to the first two.

### RECOUPLING COEFFICIENTS

In NEEC-EXI, for a given charge state  $q$ , electrons are assigned to a particular shell from the innermost to the outermost (K, L, M) encompassing all possible combinations (e.g., for 3 electrons all the cases between  $1s^2 2s^1$  and  $3d_{5/2}^3$  are considered; for 4 electrons all the cases between  $1s^2 2s^2$  and  $3d_{5/2}^4$ ). All these electronic states are used as initial configurations  $\alpha_0$ .

When considering the electron capture in this context, it has to be taken into account the possible recoupling between the electron involved in the capture and those that are already in the atom. The case of initially fully ionized atom is trivial since no recoupling is occurring. In case the capture leads to the formation of an ion having two electrons, the selection rules are satisfied if the spectator electron (not involved in NEEC) preserves its orbital angular momentum during the process. The NEEC cross-section would be non-zero only if this condition is satisfied. For the case of three electrons, we can recognize two situations: (i) the capture does not break the coupling or (ii) the capture breaks the coupling. With  $j_1$ ,  $j_2$  and  $j_c$  we denote the total angular momenta of the two spectator electrons and the one involved in the capture, respectively. Case (i) occurs when [18]:

1.  $j_1$  and  $j_2$  firstly couple to  $J_{12}$ ,
2.  $J_{12}$  then couples with  $j_c$  forming  $J$ ,

where  $J_{12}$  is the initial angular momentum, not broken by the capture. The NEEC cross-section can be considered non-zero only when the orbital angular momenta of the two spectator electrons and their coupling (thus  $j_1, j_2, J_{12}$ ) remain unchanged among the initial and final states. The other possibility is (ii):

1.  $j_2$  and  $j_c$  firstly couple to  $J_{2c}$ ,
2.  $J_{2c}$  then couples with  $j_1$  forming  $J$ .

Here, the capture breaks the initial coupling and the expression of the resonance strength in Eq. S3 has an additional coefficient [18–20]:

$$\Lambda = |\langle [(j_1, j_2)J_{12}, j_c]; J | [j_1, (j_2, j_c)J_{2c}]; J \rangle|^2 = (2 \cdot J_{12} + 1)(2 \cdot J_{2c} + 1) \left\{ \begin{matrix} j_1 & j_2 & J_{12} \\ j_c & J & J_{2c} \end{matrix} \right\}^2, \quad (\text{S14})$$

where  $\Lambda$  expresses the probability that a system with a coupling scheme defined by the bra vector  $\langle [(j_1, j_2)J_{12}, j_c]; J |$  will be found in the scheme  $[[j_1, (j_2, j_c)J_{2c}]; J]$  [20]. Whether a peculiar coupling is possible or not depends on the Wigner 6j-symbol. Notice that here  $J_{12}$  also represents the total orbital angular momentum of the two-electron atomic system *before* the electron capture. With three electrons, three nontrivial coupling schemes exist and as soon as more electrons ( $n$ ) are added to the ion, the number of possible couplings increases as  $(2n - 3)!!$  [20].

Indeed, in case of four electrons it is possible to distinguish fifteen nontrivial coupling schemes. Considering an initial electronic configuration  $\alpha_0$  having a charge state  $q = (Z - 3)^+$ , with all the three electrons belonging to different orbitals, the electron capture (EC) of a fourth electron can lead to various final configurations. In this circumstances, it is possible to distinguish the following substantially different scenarios:

- $2p_{1/2}^1 3s^1 3d_{5/2}^1 \rightarrow 1s^1 2p_{1/2}^1 3s^1 3d_{5/2}^1$  ;
- $1s^1 3s^1 3d_{5/2}^1 \rightarrow 1s^1 2p_{1/2}^1 3s^1 3d_{5/2}^1$  ;
- $1s^1 2p_{1/2}^1 3d_{5/2}^1 \rightarrow 1s^1 2p_{1/2}^1 3s^1 3d_{5/2}^1$  ;
- $1s^1 2p_{1/2}^1 3s^1 \rightarrow 1s^1 2p_{1/2}^1 3s^1 3d_{5/2}^1$  .

The recoupling coefficients associated with the first three cases are:

$$\langle [(j_1, j_2)J_{12}, j_3]J_{123}, j_4; J | [(j_2, j_3)J_{23}, j_4]J_{234}, j_1; J \rangle = (-1)^{\theta_1} R_1 \begin{Bmatrix} j_1 & j_2 & J_{12} \\ j_3 & J_{123} & J_{23} \end{Bmatrix} \begin{Bmatrix} j_1 & J_{23} & J_{123} \\ j_4 & J & J_{234} \end{Bmatrix}, \quad (\text{S15})$$

$$R_1 = \sqrt{(2 \cdot J_{12} + 1)(2 \cdot J_{123} + 1)(2 \cdot J_{23} + 1)(2 \cdot J_{234} + 1)},$$

$$\langle [(j_1, j_2)J_{12}, j_3]J_{123}, j_4; J | [(j_1, j_3)J_{13}, j_4]J_{134}, j_2; J \rangle = (-1)^{\theta_2} R_2 \begin{Bmatrix} j_2 & j_1 & J_{12} \\ j_3 & J_{123} & J_{13} \end{Bmatrix} \begin{Bmatrix} j_2 & J_{13} & J_{123} \\ j_4 & J & J_{134} \end{Bmatrix}, \quad (\text{S16})$$

$$R_2 = \sqrt{(2 \cdot J_{12} + 1)(2 \cdot J_{123} + 1)(2 \cdot J_{13} + 1)(2 \cdot J_{134} + 1)},$$

$$\langle [(j_1, j_2)J_{12}, j_3]J_{123}, j_4; J | [(j_1, j_2)J_{12}, j_4]J_{124}, j_3; J \rangle = (-1)^{\theta_3} R_3 \begin{Bmatrix} j_3 & J_{12} & J_{123} \\ j_4 & J & J_{124} \end{Bmatrix}, \quad (\text{S17})$$

$$R_3 = \sqrt{(2 \cdot J_{123} + 1)(2 \cdot J_{124} + 1)},$$

respectively. In these equations, the phase factor — indicated by  $\theta_i$  — is not reported since it is irrelevant in the evaluation of the probability  $\Lambda = |\langle \mathbf{a} | \mathbf{b} \rangle|^2$ , with  $\mathbf{a}$  and  $\mathbf{b}$  being the two state vectors expressing the coupling. Differently, the selection rule for the capture in the outermost shell requires that the electrons not involved in NEEC conserve their individual  $j_i$  and their intermediate couplings  $J_{ik}, J_{ikl}$ .

These recoupling coefficients, reported in Eqs. S15-S17, can be understood by graphical means using Yutsis notation [19] and binary trees [20, 21], presented in Fig. S1. Each pair of binary trees, whose leaves are labelled with the four uncoupled angular momenta, can be connected by two types of elementary operations: *exchange* and *flop* [20, 22, 23]. An *exchange*, represented by a dashed arrow, does not lead to a rearrangement of the orbital angular momenta, but to a swap of the  $j_i$  around one node. Thus, the relative transformation coefficient corresponds to a phase factor. The *flop* operation instead, shown as a solid arrow, is effectively a recoupling relating two trees with two alternative nets connecting the leaves. This latter transformation is defined by a Racah coefficient, proportional to a *6j-symbol* (represented by the rhomboidal Yutsis graph in Fig. S1).

Electron capture can occur in many other circumstances. As for example, we can have an initial configuration  $\alpha_0$  with  $q = (Z - 3)^+$  but with two out of three electrons belonging to the same orbital:

- $2p_{1/2}^1 3d_{5/2}^2 \rightarrow 1s^1 2p_{1/2}^1 3d_{5/2}^2$  ;
- $2p_{1/2}^1 3d_{5/2}^2 \rightarrow 2p_{1/2}^1 2p_{3/2}^1 3d_{5/2}^2$  ;
- $2p_{1/2}^1 3d_{5/2}^2 \rightarrow 2p_{1/2}^1 3d_{5/2}^3$  .

In Eqs. S18-S20 we report the associated recoupling coefficients.

$$\langle [(j_1, j_2)J_{12}, (j_3, j_4)J_{34}]; J | [j_2, (j_3, j_4)J_{34}]J_{234}, j_1; J \rangle = (-1)^{\theta_4} R_4 \begin{Bmatrix} j_1 & j_2 & J_{12} \\ J_{34} & J & J_{234} \end{Bmatrix}, \quad (\text{S18})$$

$$R_4 = \sqrt{(2 \cdot J_{12} + 1)(2 \cdot J_{234} + 1)},$$

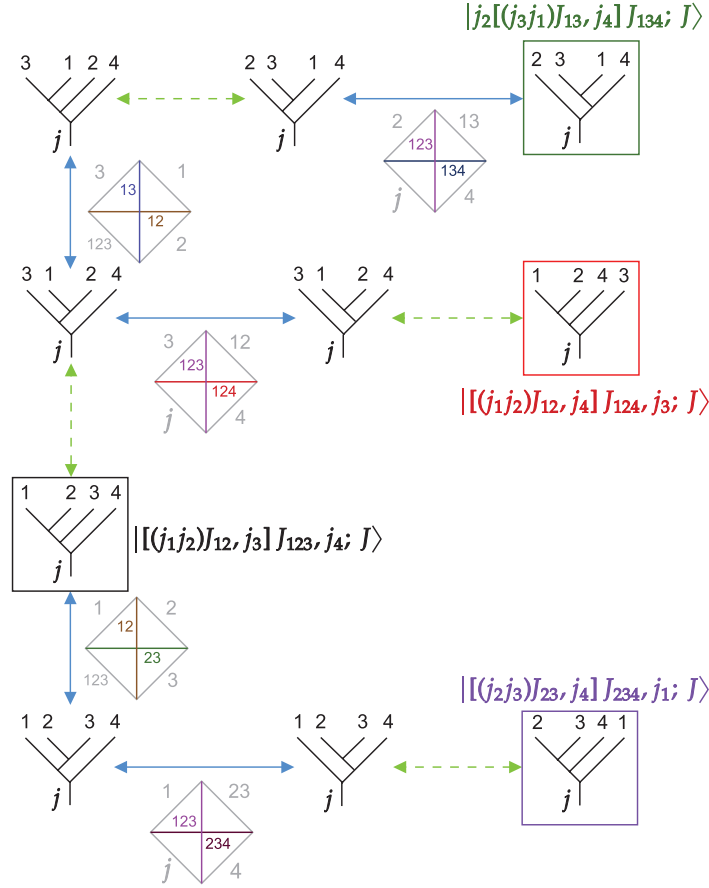


FIG. S1. Binary trees connecting the three coupling schemes given in Eqs. S15-S17. Starting from one state, applying a sequence of the elementary operations presented, it is possible to arrive at the desired final state. *Exchange* and *flop* operations are represented by green dashed and blue solid lines, respectively. The rhombuses graphically represent, in Yutsis notation [19], the Wigner 6-j symbols for the considered *flop* operation. Eq. S15, for example, can be obtained following the path going from the state  $|[(j_2, j_3)j_4]j_1\rangle$ , boxed in purple, to the state vector  $|[(j_1, j_2)j_3]j_4\rangle$ , indicated by a black square, as multiplication of two Wigner 6-j symbols (with the relative square root terms  $R_i$  due to the two *flop* operations) and an additional phase factor coming from the *exchange* operation. Eq. S16 is given by the path going from the green to the black boxes, while Eq. S17 is the path connecting the red and black boxes.

$$\langle [(j_1, j_2)J_{12}, (j_3, j_4)J_{34}]; J | [(j_1, (j_3, j_4)J_{34})J_{134}, j_2; J \rangle = (-1)^{\theta_5} R_5 \left\{ \begin{matrix} j_2 & j_1 & J_{12} \\ J_{34} & J & J_{134} \end{matrix} \right\}, \quad (\text{S19})$$

$$R_5 = \sqrt{(2 \cdot J_{12} + 1)(2 \cdot J_{134} + 1)},$$

$$\langle j_1, [(j_2, j_3)J_{23}, j_4]J_{234}; J | [j_1, (j_2, j_3)J_{23}]J_{123}, j_4; J \rangle = (-1)^{\theta_6} R_6 \left\{ \begin{matrix} j_4 & J_{23} & J_{234} \\ j_1 & J & J_{123} \end{matrix} \right\}, \quad (\text{S20})$$

$$R_6 = \sqrt{(2 \cdot J_{234} + 1)(2 \cdot J_{123} + 1)},$$

Another relevant case is given by the initial electronic configuration ( $\alpha_0$ ) of the type  $1s^1 2l^1 3l^1$  with  $q = (Z - 3)^+$ . In fact, a final configuration ( $\alpha_r$ ) resulting from a capture in the K-shell would lead to the following scenario:

- $1s^1 2p_{1/2}^1 3d_{3/2}^1 \rightarrow 1s^2 2p_{1/2}^1 3d_{3/2}^1$ .

This is an example of the 100 K-capture channels identified in the manuscript. The associated recoupling coefficient is:

$$\langle [(j_1, j_2)J_{12}, j_3]J_{123}, j_4; J | [(j_1, j_3)J_{13}, j_4]J_{134}, j_2; J \rangle = (-1)^{\theta_7} R_7 \left\{ \begin{matrix} j_2 & j_1 & \cancel{J_{12}^0} \\ j_3 & J_{123} & J_{13} \end{matrix} \right\} \left\{ \begin{matrix} j_2 & J_{13} & J_{123} \\ j_4 & J & J_{134} \end{matrix} \right\}, \quad (\text{S21})$$

$$R_7 = \sqrt{(2 \cdot J_{12} + 1)(2 \cdot J_{123} + 1)(2 \cdot J_{13} + 1)(2 \cdot J_{134} + 1)} = \sqrt{(2 \cdot J_{123} + 1)(2 \cdot J_{13} + 1)(2 \cdot J_{134} + 1)}.$$

## NEEC RESONANCE STRENGTH FOR $^{73}\text{Ge}$ UNDER GROUND STATE ASSUMPTION

Considering the framework here presented, Eq. S3 leads to the resonance strengths shown in Fig. S2 and in Table I for  $^{73}\text{Ge}$ . Here, only the capture up to the L-shells has been considered, while the charge state varied between the one of the bare nucleus ( $q = Z+$ ) all the way down to the closure of the K- and L-shells ( $q = (Z - 8)+$ ). The direct consequence of using GSA is the fact that for  $^{73}\text{Ge}$  only 27 L-channels exist in the interval  $q = [23+, 32+]$ , since NEEC in the K-shell is energetically forbidden.

TABLE I. NEEC resonance strength  $S_{\text{NEEC}}$ , partial internal conversion coefficient  $\alpha_{\text{IC}}^{q, \alpha_r}$  and the energy of the continuum electron  $E_r$  for various charge state  $q$  (before the capture) and capture shells  $\alpha_r$ , in case of  $^{73}\text{Ge}$ .  $^{73}\text{Ge}$  has its first excited state at 13.2845 keV. Here, the symbol for the final electronic configuration  $\alpha_r$  is used to indicate the capture channel, as they are uniquely connected once the charge state  $q$  is assigned.

$q$	$\alpha_r$	$E_r$ [keV]	$\alpha_{\text{IC}}^{q, \alpha_r}$	$S_{\text{NEEC}}$ [b-eV]
32+	2s <sub>1/2</sub>	9.74	72.02	$1.01 \times 10^{-5}$
32+	2p <sub>1/2</sub>	9.74	655.55	$9.21 \times 10^{-5}$
32+	2p <sub>3/2</sub>	9.79	1167.65	$3.26 \times 10^{-4}$
31+	2p <sub>1/2</sub>	9.95	617.59	$8.50 \times 10^{-5}$
31+	2p <sub>3/2</sub>	9.99	1101.94	$3.02 \times 10^{-4}$
30+	2s <sub>1/2</sub>	10.09	64.93	$8.82 \times 10^{-6}$
30+	2p <sub>1/2</sub>	10.15	579.29	$7.82 \times 10^{-5}$
29+	2p <sub>3/2</sub>	10.30	996.35	$2.65 \times 10^{-4}$
26+	2p <sub>3/2</sub>	10.71	859.36	$2.20 \times 10^{-4}$
25+	2p <sub>3/2</sub>	10.84	611.68	$1.55 \times 10^{-4}$
23+	2p <sub>3/2</sub>	11.11	181.81	$4.50 \times 10^{-5}$

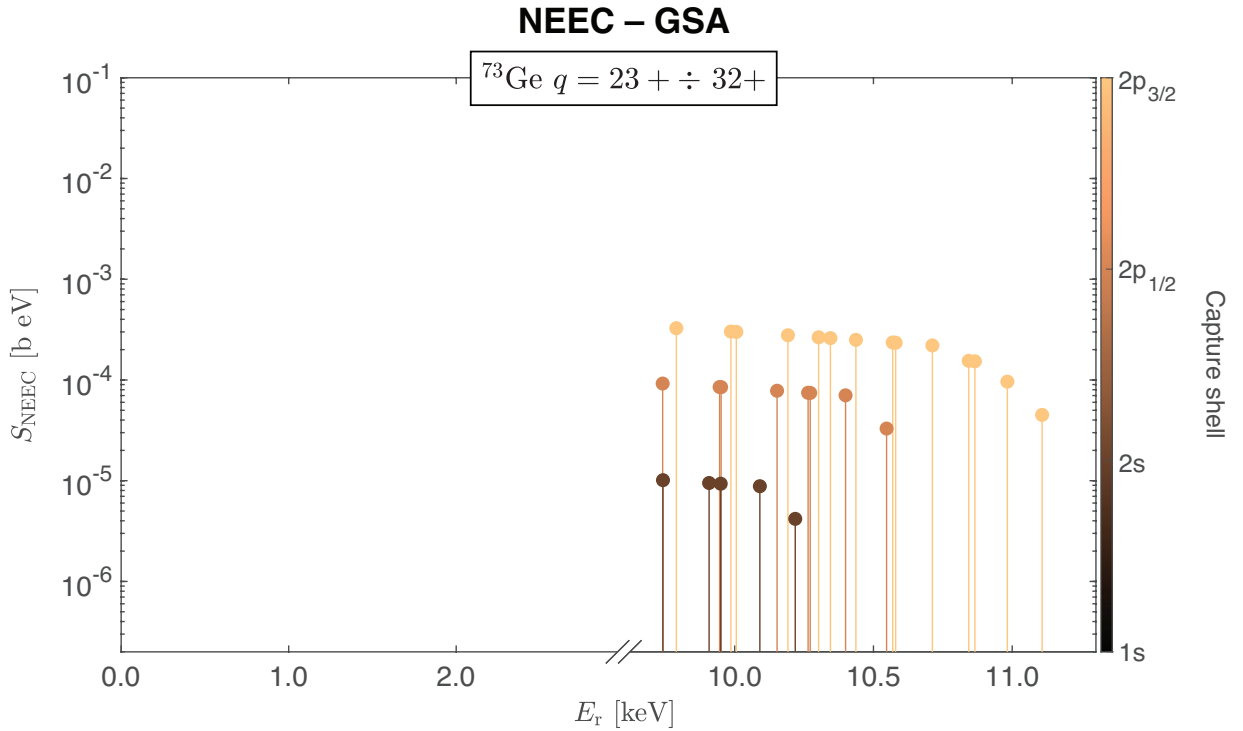


FIG. S2. Resonance strengths for the L-shell channels of  $^{73}\text{Ge}$ , under the GSA. Charge state  $q$  ranges between 32+ (bare nucleus) to  $q = 23+$  (after the electron capture the K and L shells are both closed).

## ACCURACY OF THE ENERGY LEVELS COMPUTED WITH THE FLEXIBLE ATOMIC CODE (FAC)

For the four ions of Ge, i.e.  $q = [29+, 32+]$ , and the generic electronic configurations considered in the main text, our computation with the Flexible Atomic Code (FAC) [11] leads to a total of 4565 energy levels. For the same ions and shells involved, the NIST database [24] contains only 38 energy levels corresponding to 34 electronic excited states and 4 ionization energies. Thus, less than 1% of the total energy levels reproduced by FAC can be compared with NIST data. This comparison is shown in Fig. S3 as energy differences between the levels computed with FAC and those obtained from the NIST database as a function of the NIST energy levels, as similarly done in Ref. 12. The correspondence between the FAC and the NIST levels is established in terms of electronic configuration and total angular momentum.

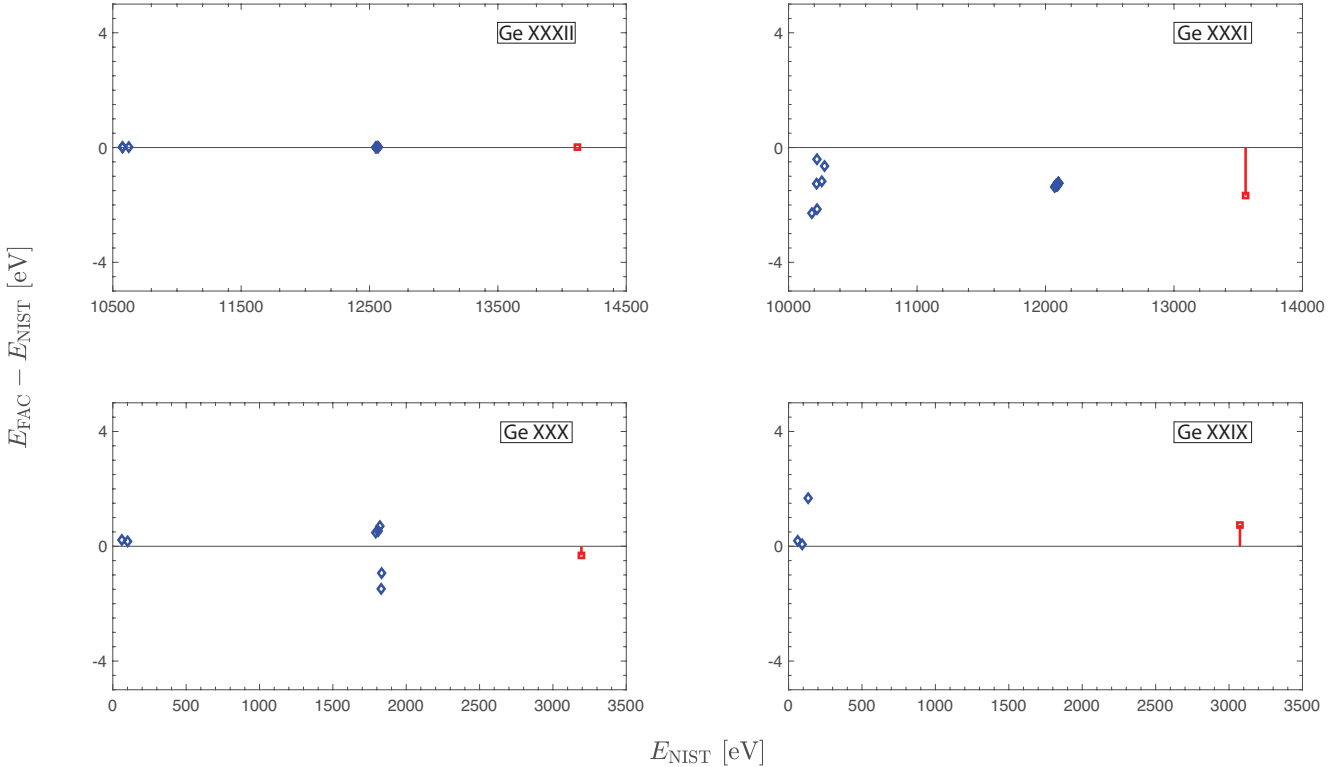


FIG. S3. Energy differences between the levels computed with FAC and the same energy levels available from the NIST database [24] for the charge state interval  $q = [29+, 32+]$  of Ge. Differences between excited electronic states are shown as blue solid lines, while in red the differences between ionization energies.

Agreement is excellent for the Hydrogen-like ion Ge XXXII, where the standard deviation of the energy differences is of 6.4 meV. The mean value of the energy differences is of 13.5 meV. For this ion, the 9 levels reported in the NIST database are also theoretically evaluated. For the ion Ge XXXI is observed the maximum discrepancy. Here, the average differences for the 17 levels compared is of 1.32 eV, while their standard deviation is of 0.44 eV. The largest discrepancy of  $-2.38$  eV is for the  $1s^1 2s^1$  ( $^3S_1$ ) level. 14 of these NIST levels are extrapolated or interpolated starting from the two known experimental values. A good agreement, with a standard deviation of 0.78 eV and an average value of the energy differences of  $-0.08$  eV, is found also for the Ge XXX ion. Apart from the  $1s^2 3d^1$  ( $^2D_{3/2}$ ) level, all the energy differences are  $< 1$  eV. The  $^2D_{3/2}$  level reports a discrepancy of  $-1.48$  eV. The 7 energy levels reported on the NIST database for this ion are experimentally observed, while the ionization energy is theoretically predicted. For Ge XXIX, only 4 suitable levels are present on the NIST database. The mean value of the energy difference is of 0.67 eV, while the standard deviation is of 0.73 eV, mainly given by the discrepancy observed for the  $1s^2 2s^1 2p^1$  ( $^1P_1$ ) level, that is of 1.68 eV. Here, the 3 electronic excited states are experimentally observed, while the ionization energy is obtained from extrapolation.

The quality of the FAC calculations can be appreciated when discrepancies here reported are compared with the energy spread over which the studied electronic configurations persist, i.e. of few keV.

### NEEC IN EXCITED $^{73}\text{Ge}$ IONS

As described in the main text, lifting the GSA provides a total of 32823 capture channels in the charge state interval  $q = [29+, 32+]$ , considering K-, L- and M-shells. From Fig. S4 it is possible to observe that, upon filling the orbitals, electron screening lowers the energy release through the electron capture in the K-shell ( $E_b^K$ ), till it becomes smaller than  $E_n$ , and NEEC into the K shell starts to be possible. In particular, for  $^{73}\text{Ge}$  this condition is met for  $q \leq 29+$ , for which 100 K-capture channels have been unveiled.

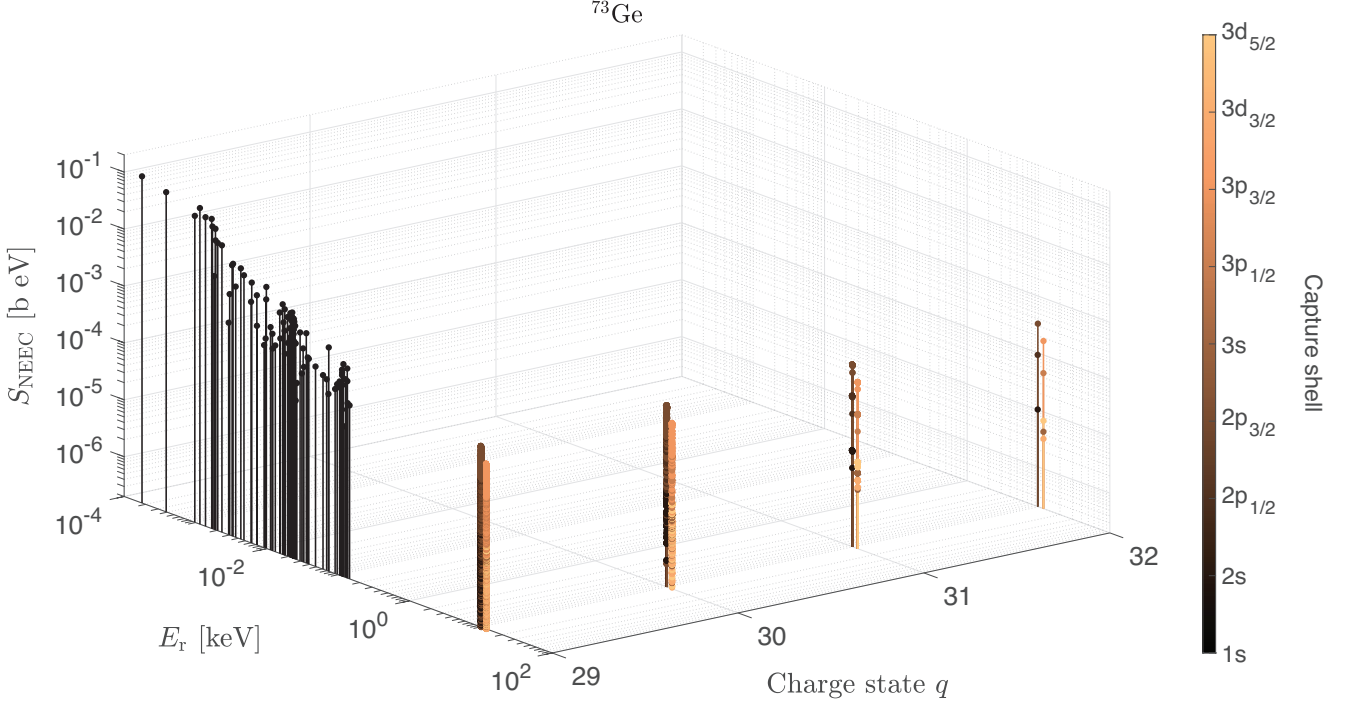


FIG. S4. Resonance strengths for  $^{73}\text{Ge}$  with  $q = [29+, 32+]$ , in case all the possible combinations of initial ( $\alpha_0$ ) and final ( $\alpha_r$ ) electronic configurations are taken into account, as a function of the charge state  $q$  and of the resonance energy  $E_r$ . Each resonant channel is represented by a solid line, with its colors indicating the capture orbital, ranging from the K to the M shell. It is clear that when  $q = 29+$ ,  $E_b^K$  becomes smaller than  $E_n$  and nuclear excitation induced by a K-capture is possible.  $q$  indicates the ion charge state before the electron capture.

## NEEC IN LASER-PLASMA SCENARIO WITH GSA

Following the theory presented in Ref. 4, it is possible to compare the reaction rates provided by NEEC and the process of direct photoexcitation. In particular, considering the parameters reported in Table II and using the first scaling law of Ref. 25, we obtain  $T_e = 2.5 \text{ keV}$  and  $n_e = 9 \times 10^{19} \text{ cm}^{-3}$  as plasma temperature and electron density, respectively.

TABLE II. Laser characteristics and absorption coefficient.

$E_{\text{pulse}}$	0.7 mJ
$R_{\text{focal}}$	$6.5 \mu\text{m}$
$\tau_{\text{pulse}}$	50 fs
$\lambda$	800 nm
$f$	0.1

By means of the radiative collisional code FLYCHK [26] it is possible to determine the ion charge state distribution, considering a non-local thermodynamical equilibrium steady state for the plasma. Fig. S5 shows the results obtained for the electron flux  $I_e$  and the charge state distribution  $P_q$  considering this scenario.

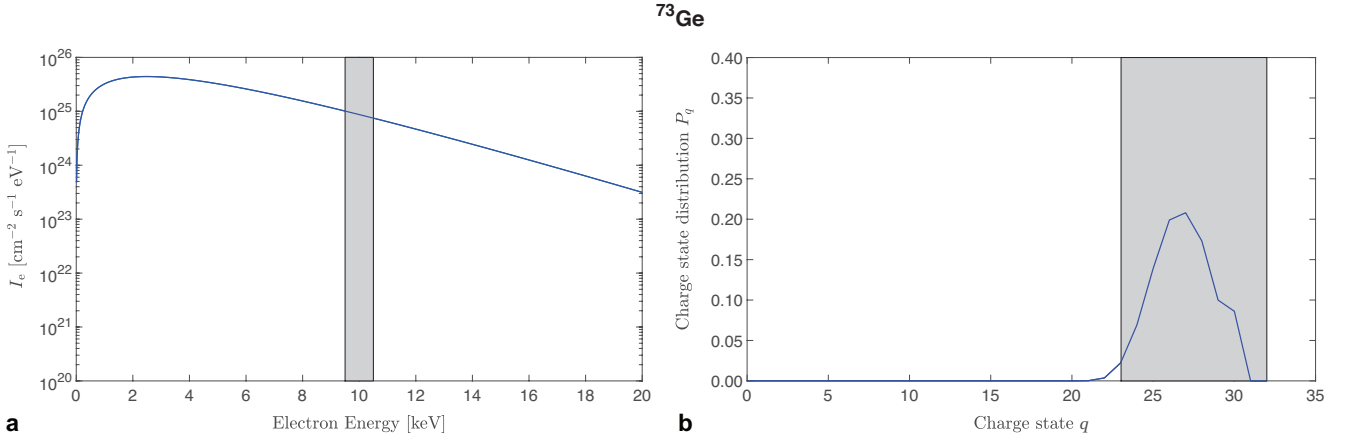


FIG. S5. (a) Relativistic electron flux distribution produced by a 2.5 keV plasma temperature. Gray box highlights the L-channels energy range. (b) Ion charge state distribution obtained with FLYCHK. The gray box indicates the charge state interval  $q = [23+, 32+]$ , for which the resonance strengths of Table I have been evaluated.

Continuing the derivation of Eq. S3, the partial NEEC rate for the capture level  $\alpha_r$  in an ion characterized by a charge state  $q$  can be written as [4]:

$$\lambda_{\text{NEEC}}^{q, \alpha_r} = S_{\text{NEEC}}^{q, \alpha_r} I_e(E_{\alpha_r}), \quad (\text{S22})$$

where  $E_{\alpha_r}$  represents the resonance energy of the capture channel  $\alpha_r$  and  $I_e$  the electron flux. Considering NEEC into ions which are in their ground state (GSA), the total NEEC rate can be written as summation over all the capture channels  $\alpha_r$  and all over the charge state  $q$  present in the plasma:

$$\lambda_{\text{NEEC}} = \sum_q \sum_{\alpha_r} P_q \lambda_{\text{NEEC}}^{q, \alpha_r}. \quad (\text{S23})$$

As evidenced in Fig. S5b, more than 99.6% of the ions fall in the range  $q = [23+, 32+]$ , thus a good estimate of the total NEEC rate, in case of GSA, can be obtained using the resonance strengths reported in Table I. In the presented experimental scenario, this results in a total NEEC rate  $\lambda_{\text{NEEC}} = 2.63 \times 10^{-3} \text{ s}^{-1}$ , while for direct photoexcitation the total rate is  $\lambda_\gamma = 6.65 \times 10^{-1} \text{ s}^{-1}$ . The strongest resonance channel of Table I is contributing to the partial NEEC rate as  $\lambda_{\text{NEEC}}^{32+, 2p_{3/2}} = 3.03 \times 10^{-3} \text{ s}^{-1}$  and  $P_q = 2.97 \times 10^{-8}$ . Even if  $P_q$  of this channel would have been 1, it would have been not enough to compensate the photoexcitation rate  $\lambda_\gamma$ .



In case of NEEC-EXI, it is necessary to sum also all over the initial electronic configurations  $\alpha_0$ , thus Eq. S23 modifies as following:

$$\lambda_{\text{NEEC}} = \sum_q \sum_{\alpha_0} \sum_{\alpha_r} P_q^{\alpha_0} \lambda_{\text{NEEC}}^{q, \alpha_0, \alpha_r}. \quad (\text{S24})$$

A direct comparison with NEEC-EXI rate is not straightforward and beyond the scope of this paper. Indeed, a dynamical study of the plasma formation and expansion is needed through particle-in-cell (PIC) codes. Nonetheless, it is worth to mention that for the resonance energy of the K-channels the electron flux provided by the plasma, evaluated in Fig. S5a, is few orders of magnitude less than that for the L-channels range. In this case, either a more proper choice of the electron temperature has to be done, or a free electron source in resonance with the desired channels has to be provided. For example, considering the  $1s^1 2s^1 3p_{3/2}^1$  electronic configuration at  $q = 29+$ , assuming  $P_q^{\alpha_0} \simeq 1$  and an electron flux of  $1 \times 10^{25} \text{ cm}^{-2} \text{ s}^{-1} \text{ eV}^{-1}$  at low energy (e.g., with an optimized external electron source), the total NEEC rate could reach the value of  $\lambda_{\text{NEEC}} = 8.64 \text{ s}^{-1}$  for the highest resonance strength of the K-shell, significantly higher than the one obtained with the direct photoexcitation. In these circumstances, the external source can act as an *electron switch* that boosts the isomer depletion.

---

\* simone.gargiulo@epfl.ch

† fabrizio.carbone@epfl.ch

- [1] S. S. Wong, *Introductory nuclear physics* (John Wiley & Sons, 2008).
- [2] A. Zadernovsky and J. Carroll, *Hyperfine interactions* **143**, 153 (2002).
- [3] M. Harston and J. Chemin, *Physical Review C* **59**, 2462 (1999).
- [4] J. Gunst, Y. Wu, C. H. Keitel, and A. Pálffy, *Physical Review E* **97**, 1 (2018), arXiv:arXiv:1804.03694v1.
- [5] J. Oxenius, *Springer Series in Electrophysics, Berlin: Springer, 1986* (Springer Science & Business Media, 1986).
- [6] T. Kibedi, T. Burrows, M. B. Trzhaskovskaya, P. M. Davidson, and C. W. Nestor Jr, *Nuclear Instruments and Methods in Physics Research Section A: Accelerators, Spectrometers, Detectors and Associated Equipment* **589**, 202 (2008).
- [7] J. Rzadkiewicz, M. Polasik, K. Słabkowska, L. Syrocki, E. Węder, J. J. Carroll, and C. J. Chiara, *Phys. Rev. C* **99**, 044309 (2019).
- [8] M. Rysavý and O. Dragoun, *Journal of Physics G: Nuclear and Particle Physics* **26**, 1859 (2000).
- [9] G. Gosselin and P. Morel, *Physical Review C* **70**, 064603 (2004).
- [10] F. Larkins, *Atomic Data and Nuclear Data Tables* **20**, 311 (1977).
- [11] M. F. Gu, *Canadian Journal of Physics* **86**, 675 (2008).
- [12] G. Massacrier and M.-C. Artru, *Astronomy & Astrophysics* **538**, A52 (2012).
- [13] J. Kantele, *Nuclear Instruments and Methods in Physics Research Section A: Accelerators, Spectrometers, Detectors and Associated Equipment* **275**, 149 (1989).
- [14] A. Pálffy, W. Scheid, and Z. Harman, *Physical Review A* **73**, 012715 (2006), arXiv:0701206 [physics].
- [15] Z. Jurek, S.-K. Son, B. Ziaja, and R. Santra, *Journal of Applied Crystallography* **49**, 1048 (2016).
- [16] S.-K. Son, L. Young, R. Santra, *et al.*, *Physical Review A* **83**, 033402 (2011).
- [17] B. Murphy, T. Osipov, Z. Jurek, L. Fang, S.-K. Son, M. Mucke, J. Eland, V. Zhaunerchyk, R. Feifel, L. Avaldi, *et al.*, *Nature communications* **5**, 1 (2014).
- [18] P. V. Bilous, G. A. Kazakov, I. D. Moore, T. Schumm, and A. Pálffy, *Physical Review A* **95**, 1 (2017).
- [19] A. P. Yutsis, V. Vanagas, and I. B. Levinson, *Mathematical apparatus of the theory of angular momentum* (Israel program for scientific translations, 1962).
- [20] L. C. Biedenharn and J. D. Louck, *The Racah-Wigner algebra in quantum theory* (Addison-Wesley, 1981).
- [21] V. Aquilanti, A. C. P. Bitencourt, C. D. S. Ferreira, A. Marzuoli, and M. Ragni, *Physica Scripta* **78**, 58103 (2008).
- [22] V. Fack, S. N. Pitre, and J. Van der Jeugt, *Computer Physics Communications* **86**, 105 (1995).
- [23] V. Fack, S. Lievens, and J. Van Der Jeugt, *Computer Physics Communications* **119**, 99 (1999).
- [24] A. Kramida, Yu. Ralchenko, J. Reader, and NIST ASD Team, NIST Atomic Spectra Database (ver. 5.6.1), [Online]. Available: <https://physics.nist.gov/asd> [2015, April 16]. National Institute of Standards and Technology, Gaithersburg, MD. (2018).
- [25] P. Gibbon and E. Förster, *Plasma physics and controlled fusion* **38**, 769 (1996).
- [26] H.-K. Chung, M. Chen, W. Morgan, Y. Ralchenko, and R. Lee, *High energy density physics* **1**, 3 (2005).

**Dynamical Control of Nuclear Isomer Depletion via Electron Vortex Beams**Yuanbin Wu<sup>1,\*</sup>, Simone Gargiulo<sup>2</sup>, Fabrizio Carbone<sup>2</sup>, Christoph H. Keitel<sup>1</sup>, and Adriana Pálffy<sup>1,3,†</sup><sup>1</sup>Max-Planck-Institut für Kernphysik, Saupfercheckweg 1, D-69117 Heidelberg, Germany<sup>2</sup>Institute of Physics, Laboratory for Ultrafast Microscopy and Electron Scattering,

École Polytechnique Fédérale de Lausanne, Station 6, Lausanne 1015, Switzerland

<sup>3</sup>Department of Physics, Friedrich-Alexander-Universität Erlangen-Nürnberg, D-91058 Erlangen, Germany

(Received 22 October 2021; revised 19 February 2022; accepted 21 March 2022; published 22 April 2022)

Some nuclear isomers are known to store a large amount of energy over long periods of time, with a very high energy-to-mass ratio. Here, we describe a protocol to achieve the external control of the isomeric nuclear decay by using electron vortex beams whose wave function has been especially designed and reshaped on demand. Recombination of these electrons into the isomer's atomic shell can lead to the controlled release of the stored nuclear energy. On the example of  $^{93m}\text{Mo}$ , we show theoretically that the use of tailored electron vortex beams increases the depletion by 4 orders of magnitude compared to the spontaneous nuclear decay of the isomer. Furthermore, specific orbitals can sustain an enhancement of the recombination cross section for vortex electron beams by as much as 6 orders of magnitude, providing a handle for manipulating the capture mechanism. These findings open new prospects for controlling the interplay between atomic and nuclear degrees of freedom, with potential energy-related and high-energy radiation source applications.

DOI: [10.1103/PhysRevLett.128.162501](https://doi.org/10.1103/PhysRevLett.128.162501)

Nuclear isomers are metastable, long-lived excited states of atomic nuclei. Their direct decay to lower-lying levels is strongly suppressed, typically due to large differences in either spin, nuclear shape, or spin projection on the nuclear symmetry axis [1,2]. In some nuclei with an advantageous level configuration, an excitation to a level above the isomeric state (termed gateway state) can lead to decay directly to a level below the isomer itself, thus reaching the ground state in a fast cascade in a process called isomer depletion. A typical example is the case of the 2425 keV  $^{93m}\text{Mo}$  isomer with a half life of 6.8 h, for which we present the relevant partial level scheme in Fig. 1. A 4.85 keV excitation from the isomer to the gateway state at 2430 keV [3] should release the entire stored energy within only 4 ns. Isomer depletion has often been mentioned in the context of potential nuclear energy storage solutions without involving fission or fusion [1,4–6].

One of the most intriguing means to externally drive the transition to the gateway state is via coupling to the atomic shell. In the process of nuclear excitation by electron capture (NEEC), an electron recombining into an atomic vacancy of an ion transfers resonantly its energy

to the nucleus. The sum of the free electron energy and capture orbital binding energy must thereby match, within the uncertainty relations, the nuclear transition energy. This process, originally predicted in 1976 [7], attracted a number of theoretical studies [8–12] prior to the first claim of experimental observation in  $^{93}\text{Mo}$  [6]. As theoretical works contradict the experimental results [13,14], the subject is at present a matter of vivid debate [15,16]. Controversy aside, the overall consensus is that, due to the small nuclear transition energy to the gateway state of  $^{93m}\text{Mo}$ , NEEC should be stronger than photoexcitation.

So far, the NEEC process has been considered for the case of plane wave electrons captured by ions that are initially in their electronic ground state. However, few recent works suggested that the NEEC cross section can be influenced by the ion's out of equilibrium conditions [17,18] or a different shape of the electronic wave function [19]. In this Letter, we take an important step to investigate the process of NEEC considering specially designed electron vortex beams, which are tailored to enhance the nuclear excitation. Electron vortex beams carry both orbital angular momentum about their beam axis and the electron's intrinsic spin momentum. The angular momentum aspect is particularly important for nuclear transitions that display in the low-energy region mostly a dipole-forbidden character. Our results show that capturing an electron with a properly reshaped wave function can lead to an increase of the NEEC cross section by a few orders of magnitude, depending on the specific situation considered. Furthermore, by manipulating the wave function of the incident electronic

Published by the American Physical Society under the terms of the [Creative Commons Attribution 4.0 International license](https://creativecommons.org/licenses/by/4.0/). Further distribution of this work must maintain attribution to the author(s) and the published article's title, journal citation, and DOI. Open access publication funded by the Max Planck Society.

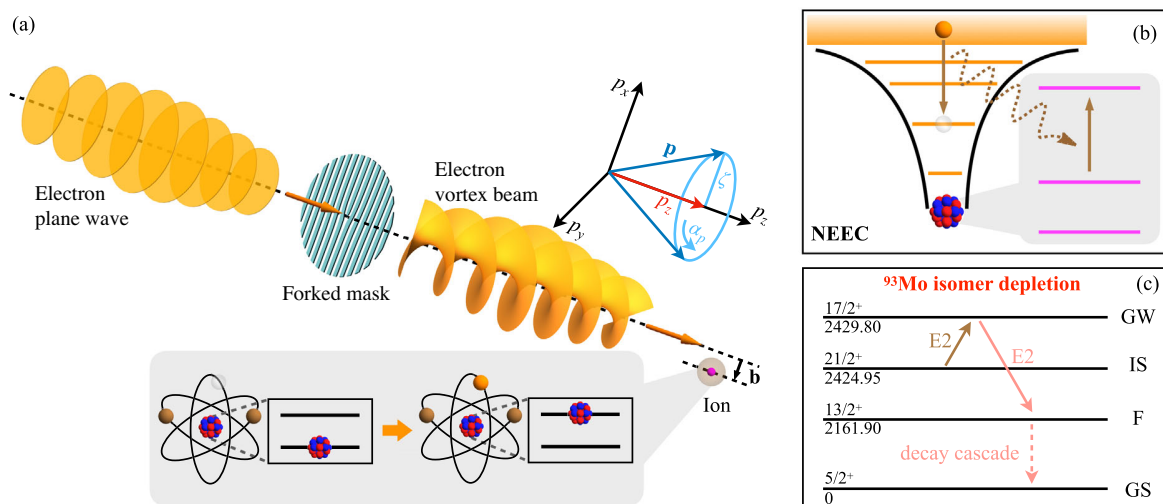


FIG. 1. (a) A plane wave electron beam incident on a forked mask generates the electron vortex beam. Upon hitting on an ion beam with impact parameter  $\mathbf{b}$ , the electrons recombine into atomic vacancies. (b) At the resonant continuum electron energy, electron recombination (orange atomic shell levels on the left) will be accompanied by nuclear excitation (magenta nuclear states on the right) in the process of NEEC. (c) Partial level scheme of  $^{93}\text{Mo}$ . The nuclear isomeric (IS), gateway (GW), intermediate ( $F$ ) and ground state (GS) levels are labeled by their spin, parity, and energy in keV [3]. The transitions  $IS \rightarrow GW$  and  $GW \rightarrow F$  are both of  $E2$  type. Energy intervals are not to scale.

beam, the maximum effect can be shifted between capture orbitals, thus opening a route for dynamical control of isomer depletion.

In recent years, the achieved capability to fabricate phase masks with nanometer precision rendered possible to control the coherent superposition of matter waves producing typical interference patterns by spatial wave function reshaping [20–24]. Particularly interesting are vortex beams with a chiral wave function spatial profile that carry an orbital angular momentum. Optical vortices have been studied in the context of quantum communications, nanoplasmonics, and optical trapping [25,26], while imparting chirality to massive composite particles has been proposed as a method to study [27–30] and even manipulate [19,23,31,32] the inner structure of neutrons, protons, ions, and molecules. Electron vortex beams are produced by a number of techniques such as phase plates, holographic gratings, magnetic monopole fields, or chiral plasmonic near fields [20–22,27–29], with angular momenta of up to  $1000\hbar$  already demonstrated. For NEEC, the nuclear transition multipolarity together with the recombination orbital impose strict selection rules on which angular momentum components of the incoming electron beam will undergo the process. While plane wave electron beams have a fixed partial wave expansion in all multipoles, vortex beams can be shaped on purpose to enhance and control the NEEC outcome.

A possible experimental implementation of this idea is depicted in Fig. 1(a). A plane wave electron beam is incident on a phase mask (for example, a forked mask), which reshapes the wave function generating an electron

vortex beam. The vortex beam is incident on ions with atomic vacancies that facilitate the NEEC process. The electron energy is chosen such as to match resonantly the nuclear transition energy upon recombination into a chosen orbital as shown in Fig. 1(b). As examples, we consider the canonical case of  $^{93}\text{Mo}$ , whose partial level scheme is depicted in Fig. 1(c). The NEEC transition between the isomer and gateway states has 4.85 keV and electric quadrupole ( $E2$ ) multipolarity. A second example envisaging a 19.70 keV magnetic dipole ( $M1$ ) transition from the  $^{152m}\text{Eu}$  isomer at 45.60 keV [3] to a gateway state will also be considered. These examples are generic and were chosen to demonstrate the effect on the two most frequently occurring nuclear transition multiplicities ( $E2$  and  $M1$ ) in the energy range relevant for NEEC. For a plane wave electron beam, the maximal NEEC cross section for depletion of  $^{93m}\text{Mo}$  occurs for recombination into the  $2p_{3/2}$  orbital of a  $\text{Mo}^{36+}$  ion [33,34]. This charge state is sufficient for providing the maximum number of vacancies in the  $2p_{3/2}$  orbital. On the other hand, it ensures that the NEEC channel is allowed, with the resonance continuum electron energy of only approximately 52 eV. The resonant energy is given by the difference between nuclear transition energy and the orbital binding energy that we calculate for each specific electronic configuration using GRASP92 [35]. A higher charge state would close the NEEC channel due to the slight increase of electronic binding energies.

We consider a vortex beam with the longitudinal linear momentum  $p_z$ , the modulus of the transverse momentum  $|\mathbf{p}_\perp| = \zeta$ , and the topological vortex charge, a quantity

related to the electron orbital angular momentum, denoted by  $m$  [28,36]. The corresponding electron wave function can be written as

$$\psi_s(\mathbf{r}) = \int \frac{d^2\mathbf{p}_\perp}{(2\pi)^2} a_{\zeta m}(\mathbf{p}_\perp) u_{\mathbf{p}_s} e^{i\mathbf{p}\cdot\mathbf{r}}, \quad (1)$$

where  $a_{\zeta m}(\mathbf{p}_\perp) = (-i)^m e^{im\alpha_p} \delta(|\mathbf{p}_\perp| - \zeta)/\zeta$  and  $u_{\mathbf{p}_s}$  is the electron bispinor that corresponds to the plane wave solution with momentum  $\mathbf{p}$  and spin state  $s$ . The linear momenta of the plane wave components are given by  $\mathbf{p} = (\mathbf{p}_\perp, p_z) = (\zeta \cos \alpha_p, \zeta \sin \alpha_p, p_z)$ , as sketched in Fig. 1. We choose the  $Oz$  axis parallel to the incident electron beam. To specify the lateral position of the ion with regard to the central axis of the incident electron beam, we consider an impact parameter  $\mathbf{b}$  and average over the incident electron current [28,37]. The advantage of the vortex beam comes into play when restricting the impact parameter to  $|\mathbf{b}| \leq b$ , with  $b$  chosen accordingly as a function of the incoming electron momentum [28,37]. Otherwise, an average over arbitrary impact parameters up to infinity will limit the enhancement factor for the NEEC rate to a factor  $p/p_z$ . Similar behavior is known also from the interaction of optical vortices with atomic or nuclear systems, e.g., Refs. [38–44].

The NEEC rate  $Y_{\text{NEEC}}^{i \rightarrow g}$  is proportional to the modulus squared of the electron-nucleus interaction Hamiltonian matrix element  $|\langle \Psi_g^N | \langle \Psi_g^e | H_N | \Psi_i^e, \psi_s \rangle | \Psi_i^N \rangle|^2$ , where  $|\Psi_g^e \rangle | \Psi_g^N \rangle$  is the state vector describing the total wave function of the nuclear gateway ( $\Psi_g^N$ ) and electronic ( $\Psi_g^e$ ) states reached by NEEC, and  $|\Psi_i^e, \psi_s \rangle | \Psi_i^N \rangle$  describes the total wave function of the initial states. The total NEEC cross section can be written as a function of the continuum electron energy  $E$ ,

$$\sigma_{\text{NEEC}}^{i \rightarrow g}(E) = \frac{4\pi^2}{pJ_z} Y_{\text{NEEC}}^{i \rightarrow g} \mathcal{L}(E - E_0), \quad (2)$$

where  $p$  is the modulus of the continuum electron momentum,  $J_z$  is the total incident current [36], and  $\mathcal{L}(E - E_0)$  is a Lorentz profile centered on the resonance energy  $E_0$  and with a full width at half maximum given by the width of the nuclear excited state. Typically, the nuclear widths are very narrow (for example,  $\Gamma_g = 10^{-7}$  eV for the case of  $^{93m}\text{Mo}$ ), such that  $\mathcal{L}(E - E_0)$  is approximated with a Dirac-delta-like profile. Integrating over the continuum electron energy, we obtain the so-called resonance strength  $S_v$ . We compare this value with the resonance strength  $S_p$  obtained for the case of a plane wave electron beam.

In order to calculate the NEEC rate  $Y_{\text{NEEC}}^{i \rightarrow g}$ , the vortex beam is mapped upon the partial wave expansion of the continuum electron wave function (see details in the Supplemental Material [45], which includes Ref. [46]),

$$Y_{\text{NEEC}}^{i \rightarrow g} = \frac{b^2}{4\pi} \int_0^{2\pi} \int_0^{2\pi} \frac{d\alpha_p}{2\pi} \frac{d\alpha_k}{2\pi} e^{im(\alpha_p - \alpha_k)} \mathcal{Y}_{\text{NEEC}}^{i \rightarrow g}(\mathbf{p}, \mathbf{k}) \times {}_0F_1(2; u), \quad (3)$$

with the condition  $|\mathbf{p}_\perp| = |\mathbf{k}_\perp| = \zeta$  and the two polar angles  $\alpha_p$  and  $\alpha_k$  spanning the interval  $[0, 2\pi)$ . The notation  ${}_0F_1$  stands for the confluent hypergeometric limit function and  $u = -b^2 \zeta^2 [1 - \cos(\alpha_k - \alpha_p)]/2$ . For a nuclear transition of multipolarity  $\lambda L$  with  $\lambda = E/M$  we have

$$\mathcal{Y}_{\text{NEEC}}^{i \rightarrow g}(\mathbf{p}, \mathbf{k}) = \frac{16\pi^3 (2J_g + 1)}{(2J_i + 1)(2L + 1)^2} \times \mathcal{B} \uparrow (\lambda L) \rho_i \sum_{\kappa, m_l} \frac{\mathcal{Y}_b}{2l + 1} Y_{lm_l}^*(\theta_k, \varphi_k) \times Y_{lm_l}(\theta_p, \varphi_p), \quad (4)$$

with  $J_i$  and  $J_g$  the total angular momenta of the initial and final electronic configuration of the ion, respectively. Furthermore,  $\mathcal{B} \uparrow (E/ML)$  is the reduced transition probability for the nuclear transition,  $\rho_i$  is the initial density of continuum electron states, and  $Y_{lm_l}$  stand for the spherical harmonics with quantum numbers  $l$  and  $m_l$ , with  $\theta_p$  ( $\theta_k$ ) and  $\varphi_p$  ( $\varphi_k$ ) as the polar and azimuthal angles of the electron momentum  $\mathbf{p}$  ( $\mathbf{k}$ ) in the spherical coordinate of the ion, respectively. For  $\lambda = E$ ,  $\mathcal{Y}_b = [C(j_g L j; \frac{1}{2} 0 \frac{1}{2})]^2 |R_{L, \kappa_g, \kappa}^{(E)}|^2 / R_0^{2(L+2)}$ , whereas for  $\lambda = M$ ,  $\mathcal{Y}_b = (2j + 1)(\kappa_g + \kappa)^2 \times \left( \begin{matrix} j_g & j & L \\ \frac{1}{2} & -\frac{1}{2} & 0 \end{matrix} \right)^2 |R_{L, \kappa_g, \kappa}^{(M)}|^2 / L^2$ . Here,  $j$  is the total angular momentum of the continuum electron that connects with the Dirac angular momentum quantum number  $\kappa$  via  $j = |\kappa| - 1/2$ ,  $j_g$  is the total angular momentum of the bound electron in the capture orbital, and  $\kappa_g$  is the Dirac angular momentum quantum number of the bound electron in the capture orbital.  $R_0$  denotes the nuclear radius. The radial integrals  $R_{L, \kappa_g, \kappa}^{(E)}$  and  $R_{L, \kappa_g, \kappa}^{(M)}$  for electric and magnetic multiplicities, respectively, are given in Refs. [12,47] and in the Supplemental Material [45].

We focus first on the case of  $^{93m}\text{Mo}$  considering initially the ground state configuration of  $\text{Mo}^{36+}$  and NEEC into orbitals ranging from  $2p_{3/2}$  to  $4f_{7/2}$ . The continuum electron resonance energy for recombination into  $2p_{3/2}$  is 52 eV, while for the higher shell orbitals the values lie between 2.7 and 2.9 keV for the  $M$  shell and between 3.6 and 3.8 keV for the  $N$  shell. The vortex beam parameters are chosen such that  $\zeta = p_z$  for the impact parameter range  $b = 1/\zeta$ . The resonance strength ratio  $S_v/S_p$  as a function of the capture orbital for three values of topological charge  $m = 3, 4, 5$  is presented in Fig. 2(a). Depending on the recombination orbital, the tailored vortex electron beam leads to an enhancement between two ( $p$  orbitals) and 6 orders of magnitude ( $f$  orbitals) in the NEEC resonance

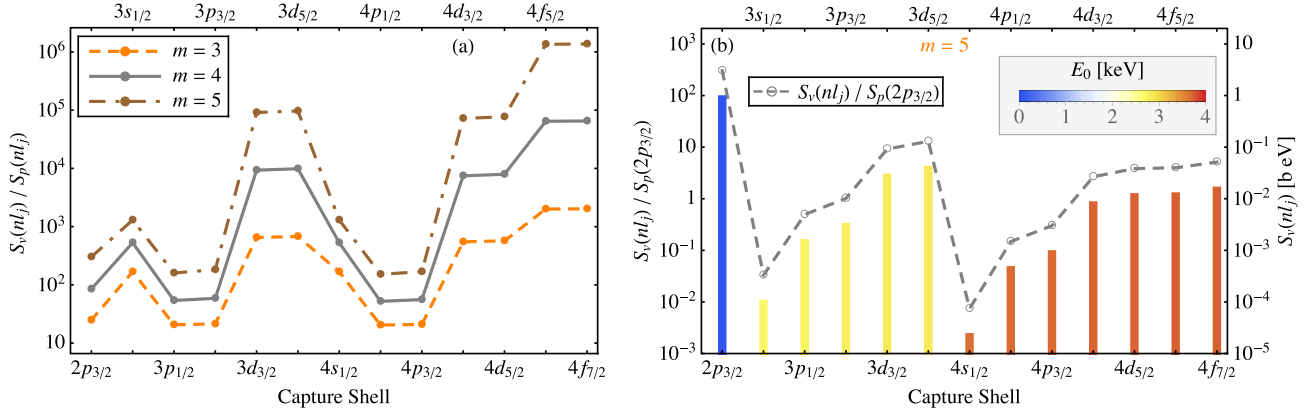


FIG. 2. NEEC integrated cross section enhancement for the 4.85 keV nuclear transition depleting  $^{93m}\text{Mo}$ . (a) The enhancement ratio  $S_v(nl_j)/S_p(nl_j)$  comparing vortex and plane wave electron beams for recombination orbitals in the range  $2p_{3/2}$ – $4f_{7/2}$ . (b) The ratio  $S_v(nl_j)/S_p(2p_{3/2})$  of vortex beam versus maximal plane wave NEEC resonance strengths corresponding to recombination into the  $2p_{3/2}$  orbital (left-hand axis, gray dashed curve with circle) and the absolute values of  $S_v(nl_j)$  (right-hand axis, vertical colored bars). We consider (a)  $m = 3, 4, 5$  or (b)  $m = 5$ , with  $\zeta = p_z$  and impact parameter range  $\zeta b = 1$ . The resonant electron energy  $E_0$  is presented in color coding.

strength. The physical mechanism of this enhancement is related to our choice of  $b$ . By restricting the impact parameter, we are considering the most favorable spatial region of the vortex beam, where the spherical partial wave maximizes its contribution to NEEC. This feature is missing in the case of the plane wave.

Although the enhancement for the capture into  $M$ - and  $N$ -shell orbitals is impressive, these are not the capture orbitals with the largest cross section. Provided atomic vacancies are available, NEEC into the  $2p_{3/2}$  is the most efficient isomer depletion channel. We consider this value as reference for our results in Fig. 2(b) showing the vortex beam resonance strength scaled by the maximum value reached for a plane wave setup. For an incident vortex beam, the resonance strength for NEEC into this orbital is increased by 2 orders of magnitude as compared to the plane wave electron beams so far considered in the literature. In addition, also NEEC into the  $3d$ ,  $4d$ , or  $4f$  orbitals exceeds the plane wave value for recombination into  $2p_{3/2}$  by factors ranging between 12.96 ( $3d_{5/2}$ ) and 2.66 ( $4d_{3/2}$ ). This might become advantageous to ease the charge state requirements or when the continuum electron energy cannot be decreased to very small energies.

NEEC angular momentum selection rules reflect upon and determine the most efficient vortex charge  $m$  for a particular NEEC process. For instance, a vortex beam with  $m > 5$  would further increase NEEC into  $d$  and  $f$  orbitals. However, increasing  $m$  at values above  $m = 5$  has less further enhancement effect on the NEEC resonance strength for the  $2p_{3/2}$  orbitals. Depending on the envisaged electron beam energy (and, therefore, capture orbital), the proper choice of vortex beam topological charge  $m$  can maximize the NEEC resonance strength. The new aspect related to vortex beams is that  $m$  acts as a new degree of

freedom and can be dynamically controlled on an ultrafast timescale, as detailed below.

We now turn to a different example that investigates NEEC into a bare ion for a  $M1$  nuclear transition in  $^{152}\text{Eu}$ . This isotope has an isomer with 9.3 h half life lying 45.60 keV above the ground state. The envisaged  $\mu\text{s}$ -lived gateway state lies at 65.30 keV and has a branching ratio to the ground state [5]. Table I displays the plane wave and vortex electron beam NEEC resonance strengths for the cases of  $m = 3$  and  $m = 5$ , assuming  $\zeta = p_z$  and  $\zeta b = 1$ . The enhancements compared to the equivalent plane wave case are less dramatic, with factors between 1.4 and approximately 600. The lowest factor of 1.4 occurs in the case of NEEC into the  $2s_{1/2}$  orbital and stems mainly from the factor  $p/p_z$ . However, the startling feature in the case of  $^{152}\text{Eu}$  is the ability to change the most efficient capture orbital. For a  $M1$  transition, the strongest NEEC resonance strength for a plane wave electron beam occurs for the recombination into the lowest available  $s$  orbital. For the specific case of  $^{152}\text{Eu}$ , with its nuclear transition and electronic binding energies, this would be the  $2s$  orbital. Surprisingly, the tailored vortex beam changes this rule of

TABLE I. NEEC resonance strength for isomer depletion of  $^{152m}\text{Eu}$  for both plane wave  $S_p$  and vortex  $S_v$  electron beams. We assume  $\zeta = p_z$  and  $\zeta b = 1$  and consider two values of the topological charge  $m = 3, 5$ .

$nl_j$	$E_0$ (keV)	$S_p$ (b eV)	$S_v$ (b eV)	
			$m = 3$	$m = 5$
$2s_{1/2}$	5.20	$8.05 \times 10^{-4}$	$1.14 \times 10^{-3}$	$1.14 \times 10^{-3}$
$2p_{1/2}$	5.19	$7.85 \times 10^{-5}$	$1.35 \times 10^{-3}$	$3.34 \times 10^{-3}$
$2p_{3/2}$	6.02	$1.25 \times 10^{-5}$	$4.21 \times 10^{-4}$	$7.61 \times 10^{-3}$



thumb, as the strongest NEEC occurs for the  $2p_{1/2}$  orbital (for  $m = 3$ ) or for the  $2p_{3/2}$  orbital ( $m = 5$ ). Thus, by manipulating the wave function of the incident electronic beam, it is possible not only to enhance rates but also to shift the maximum effect between orbitals.

In view of the many methods developed to produce specific atomic vacancies [48,49], this result can have important consequences for our ability to manipulate nuclear excitation. Vortex beam angular momentum, electron energy, and atomic vacancies can be dynamically and simultaneously controlled to optimize isomer depletion. The value of  $m$  can be switched dynamically on an ultrafast timescale by modulating the properties of plasmonic [29,50,51] and light phase masks [52,53]. Also when using physical phase plates such as the forked mask in Fig. 1, deflector coils or apertures can select the desired vortex topological charge [54]. With such dynamical control to optimize isomer depletion, clear experimental signals can be targeted, aiming at efficient nuclear energy release from isomers.

Let us now finally turn to the magnitude of isomer depletion for the  $^{93m}\text{Mo}$  isomer. Considering the most efficient capture orbital  $2p_{3/2}$  and topological charge  $m = 5$ , the NEEC resonance strength reaches the value  $\sim 1$  beV. In order to obtain a reaction rate per ion, we multiply this value by the vortex beam flux. We assume here the generic flux of  $10^{24} \text{ cm}^{-2} \text{ s}^{-1} \text{ eV}^{-1}$  [55,56]. The NEEC reaction rate per ion reaches the value of approximately  $1 \text{ s}^{-1}$ . Compared to the natural decay of the isomer (half life 6.8 h), this represents an enhancement of approximately 4 orders of magnitude for the isomer depletion rate. The isomers can be obtained in nuclear reactions such as  $^{93}\text{Nb}(p, n)^{93m}\text{Mo}$  [4] or  $^7\text{Li}(^{90}\text{Zr}, p3n)^{93m}\text{Mo}$  [6]. Since the resonance condition for electron recombination needs to be fulfilled in the rest frame of the nucleus, the ion preparation is equally important to the vortex electron beam generation. The required ion charge state breeding, storage, and cooling requires, for instance, a storage ring or an electron beam ion trap in conjunction with a radioactive beam facility. Isomeric beams have been successfully produced and stored at facilities such as the GSI Darmstadt [57–59]. At a storage ring, the condition  $\zeta = p_z$  could be easily fulfilled by exploiting the Lorentz boost of the ions. The required impact parameter  $b = 1/\zeta$  for this case is approximately  $0.4 \text{ \AA}$ . While this should be accessible with current vortex beam focus [28,55], the spatial charge of the ion beam severely limits the number of isomers that can be addressed. A dedicated ion and electron vortex beam setup needs to be designed in order to fulfill all experimental requirements for isomer production, resonance condition match, impact parameter, and dynamical control of vortex beam properties.

Isomer depletion is a very desirable goal in view of the current search for energy storage solutions [60,61]. However, the potential of dynamically controlled vortex

beams extends further than that. We anticipate new opportunities in nuclear physics, where projectile beams starting, for instance, from protons, neutrons, or muons with reshaped wave fronts [24,30] would enhance and dynamically control nuclear reactions. The beam angular momentum is ideal to specifically select reaction channels according to the final-state spin. This would enable, for instance, the targeted production of isotopes or isomers for medical applications [62,63] or the search for dark matter [64].

The authors thank I. Madan and G. M. Vanacore for fruitful discussions. S. G., F. C. and A. P. acknowledge support from Google, Inc. A. P. gratefully acknowledges the Heisenberg Program of the Deutsche Forschungsgemeinschaft (DFG).

\*yuanbin.wu@mpi-hd.mpg.de

†adriana.palfy-buss@physik.uni-wuerzburg.de

- [1] P. Walker and G. Dracoulis, *Nature (London)* **399**, 35 (1999).
- [2] P. Walker and Z. Podolyák, *Phys. Scr.* **95**, 044004 (2020).
- [3] Evaluated Nuclear Structure Data Files, <https://www.nndc.bnl.gov/ensdf/> (2022).
- [4] J. Gunst, Y. A. Litvinov, C. H. Keitel, and A. Pálffy, *Phys. Rev. Lett.* **112**, 082501 (2014).
- [5] A. Pálffy, J. Evers, and C. H. Keitel, *Phys. Rev. Lett.* **99**, 172502 (2007).
- [6] C. J. Chiara, J. J. Carroll, M. P. Carpenter, J. P. Greene, D. J. Hartley, R. V. F. Janssens, G. J. Lane, J. C. Marsh, D. A. Matters, M. Polasik *et al.*, *Nature (London)* **554**, 216 (2018).
- [7] V. I. Goldanskii and V. A. Namiot, *Phys. Lett.* **62B**, 393 (1976).
- [8] N. Cue, J.-C. Poizat, and J. Remillieux, *Eurphys. Lett.* **8**, 19 (1989).
- [9] Z.-S. Yuan and J. C. Kimball, *Phys. Rev. C* **47**, 323 (1993).
- [10] M. R. Harston and J. F. Chemin, *Phys. Rev. C* **59**, 2462 (1999).
- [11] G. Gosselin and P. Morel, *Phys. Rev. C* **70**, 064603 (2004).
- [12] A. Pálffy, W. Scheid, and Z. Harman, *Phys. Rev. A* **73**, 012715 (2006).
- [13] Y. Wu, C. H. Keitel, and A. Pálffy, *Phys. Rev. Lett.* **122**, 212501 (2019).
- [14] J. Rzadkiewicz, M. Polasik, K. Stabkowska, L. Syrocki, J. J. Carroll, and C. J. Chiara, *Phys. Rev. Lett.* **127**, 042501 (2021).
- [15] S. Guo, Y. Fang, X. Zhou, and C. M. Petrache, *Nature (London)* **594**, E1 (2021).
- [16] C. J. Chiara, J. J. Carroll, M. P. Carpenter, J. P. Greene, D. J. Hartley, R. V. F. Janssens, G. J. Lane, J. C. Marsh, D. A. Matters, M. Polasik *et al.*, *Nature (London)* **594**, E3 (2021).
- [17] Y. Wu, C. H. Keitel, and A. Pálffy, *Phys. Rev. A* **100**, 063420 (2019).
- [18] S. Gargiulo, I. Madan, and F. Carbone, *arXiv:2102.05718*.
- [19] I. Madan, G. M. Vanacore, S. Gargiulo, T. LaGrange, and F. Carbone, *Appl. Phys. Lett.* **116**, 230502 (2020).
- [20] M. Uchida and A. Tonomura, *Nature (London)* **464**, 737 (2010).
- [21] J. Verbeeck, H. Tian, and P. Schattschneider, *Nature (London)* **467**, 301 (2010).

- [22] B. J. McMorran, A. Agrawal, I. A. Anderson, A. A. Herzing, H. J. Lezec, J. J. McClelland, and J. Unguris, *Science* **331**, 192 (2011).
- [23] C. Clark, R. Barankov, M. Huber, M. Arif, D. G. Cory, and D. A. Pushin, *Nature (London)* **525**, 504 (2015).
- [24] A. Luski, Y. Segev, R. David, O. Bitton, H. Nadler, A. R. Barnea, A. Gorlach, O. Cheshnovsky, I. Kaminer, and E. Narevicius, *Science* **373**, 1105 (2021).
- [25] Y. Shen, X. Wang, Z. Xie, C. Min, X. Fu, Q. Liu, M. Gong, and X. Yuan, *Light Sci. Appl.* **8**, 90 (2019).
- [26] K. Y. Bliokh and F. Nori, *Phys. Rep.* **592**, 1 (2015).
- [27] S. M. Lloyd, M. Babiker, G. Thirunavukkarasu, and J. Yuan, *Rev. Mod. Phys.* **89**, 035004 (2017).
- [28] K. Y. Bliokh, I. Ivanov, G. Guzzinati, L. Clark, R. Van Boxem, A. B  ch  , R. Juchtmans, M. A. Alonso, P. Schattschneider, F. Nori *et al.*, *Phys. Rep.* **690**, 1 (2017).
- [29] G. M. Vanacore, G. Berruto, I. Madan, E. Pomarico, P. Biagioni, R. J. Lamb, D. McGrouther, O. Reinhardt, I. Kaminer, B. Barwick *et al.*, *Nat. Mater.* **18**, 573 (2019).
- [30] P. Zhao, I. P. Ivanov, and P. Zhang, *Phys. Rev. D* **104**, 036003 (2021).
- [31] H. Larocque, I. Kaminer, V. Grillo, R. W. Boyd, and E. Karimi, *Nat. Phys.* **14**, 1 (2018).
- [32] I. Kaminer, J. Nemirovsky, M. Rechtsman, R. Bekenstein, and M. Segev, *Nat. Phys.* **11**, 261 (2015).
- [33] Y. Wu, J. Gunst, C. H. Keitel, and A. P  lffy, *Phys. Rev. Lett.* **120**, 052504 (2018).
- [34] J. Gunst, Y. Wu, C. H. Keitel, and A. P  lffy, *Phys. Rev. E* **97**, 063205 (2018).
- [35] F. A. Parpia, C. F. Fischer, and I. P. Grant, *Comput. Phys. Commun.* **94**, 249 (1996).
- [36] K. Y. Bliokh, M. R. Dennis, and F. Nori, *Phys. Rev. Lett.* **107**, 174802 (2011).
- [37] V. Serbo, I. P. Ivanov, S. Fritzsche, D. Seipt, and A. Surzhykov, *Phys. Rev. A* **92**, 012705 (2015).
- [38] C. T. Schmiegelow, J. Schulz, H. Kaufmann, T. Ruster, U. G. Poschinger, and F. Schmidt-Kaler, *Nat. Commun.* **7**, 12998 (2016).
- [39] S. Franke-Arnold, *Phil. Trans. R. Soc. A* **375**, 20150435 (2017).
- [40] A. Afanasev, C. E. Carlson, and M. Solyanik, *Phys. Rev. A* **97**, 023422 (2018).
- [41] A. Afanasev, C. E. Carlson, C. T. Schmiegelow, J. Schulz, F. Schmidt-Kaler, and M. Solyanik, *New J. Phys.* **20**, 023032 (2018).
- [42] S. A.-L. Schulz, S. Fritzsche, R. A. M  ller, and A. Surzhykov, *Phys. Rev. A* **100**, 043416 (2019).
- [43] A. Afanasev and C. E. Carlson, *Ann. Phys. (Berlin)* **2021**, 2100228 (2021).
- [44] A. Afanasev, C. E. Carlson, and A. Mukherjee, *Phys. Rev. Research* **3**, 023097 (2021).
- [45] See Supplemental Material at <http://link.aps.org/supplemental/10.1103/PhysRevLett.128.162501> for the detailed NEEC rate expressions for vortex electron beams.
- [46] J. Gunst, Y. Wu, N. Kumar, C. H. Keitel, and A. P  lffy, *Phys. Plasmas* **22**, 112706 (2015).
- [47] A. P  lffy, Z. Harman, and W. Scheid, *Phys. Rev. A* **75**, 012709 (2007).
- [48] B. Rudek, S.-K. Son, L. Foucar, S. W. Epp, B. Erk, R. Hartmann, M. Adolph, R. Andritschke, A. Aquila, N. Berrah *et al.*, *Nat. Photonics* **6**, 858 (2012).
- [49] M. Steck and Y. A. Litvinov, *Prog. Part. Nucl. Phys.* **115**, 103811 (2020).
- [50] H. Kim, J. Park, S.-W. Cho, S.-Y. Lee, M. Kang, and B. Lee, *Nano Lett.* **10**, 529 (2010).
- [51] S. Wang, C. Zhao, and X. Li, *Appl. Sci.* **9**, 3297 (2019).
- [52] V. E. Lembessis, D. Ellinas, M. Babiker, and O. Al-Dossary, *Phys. Rev. A* **89**, 053616 (2014).
- [53] V. E. Lembessis, *Phys. Rev. A* **96**, 013622 (2017).
- [54] D. Pohl, S. Schneider, P. Zeiger, J. Ruzs, P. Tiemeijer, S. Lazar, K. Nielsch, and B. Rellinghaus, *Sci. Rep.* **7**, 934 (2017).
- [55] A. B  ch  , R. Juchtmans, and J. Verbeeck, *Ultramicroscopy* **178**, 12 (2017).
- [56] L. Reimer and H. Kohl, *Transmission Electron Microscopy* (SpringerScience+Business Media, New York, 2008).
- [57] Y. A. Litvinov, S. Bishop, K. Blaum, F. Bosch, C. Brandau, L. X. Chen, I. Dillmann, P. Egelhof, H. Geissel, R. E. Grisenti *et al.*, *Nucl. Instrum. Methods Phys. Res., Sect. B* **317**, 603 (2013).
- [58] M. Grieser, Y. A. Litvinov, R. Raabe, K. Blaum, Y. Blumenfeld, P. A. Butler, F. Wenander, P. J. Woods, M. Aliotta, A. Andreyev *et al.*, *Eur. Phys. J. Special Topics* **207**, 1 (2012).
- [59] T. Dickel, W. R. Pla  , S. Ayet San Andres, J. Ebert, H. Geissel, E. Haettner, C. Hornung, I. Miskun, S. Pietri, S. Purushothaman *et al.*, *Phys. Lett. B* **744**, 137 (2015).
- [60] R. Koningstein and D. Fork, *IEEE Spectrum* **51**, 30 (2014).
- [61] M. Prelas, M. Matthew Boraas, F. De La Torre Aguilar, and J.-D. Seelig, *Nuclear Batteries and Radioisotopes* (Springer, Cham, 2016).
- [62] D. Habs and U. K  ster, *Appl. Phys. B* **103**, 501 (2011).
- [63] W.-T. Pan, T. Song, H.-Y. Lan, Z.-G. Ma, J. Zhang, Z. Zhu, and W. Luo, *Appl. Radiat. Isot.* **168**, 109534 (2021).
- [64] M. Pospelov, S. Rajendran, and H. Ramani, *Phys. Rev. D* **101**, 055001 (2020).

# Supplement to “Dynamical Control of Nuclear Isomer Depletion via Electron Vortex Beams”

Yuanbin Wu,<sup>1,\*</sup> Simone Gargiulo,<sup>2</sup> Fabrizio Carbone,<sup>2</sup> Christoph H. Keitel,<sup>1</sup> and Adriana Pálffy<sup>1,3,†</sup>

<sup>1</sup>Max-Planck-Institut für Kernphysik, Saupfercheckweg 1, D-69117 Heidelberg, Germany

<sup>2</sup>Institute of Physics, Laboratory for Ultrafast Microscopy and Electron Scattering,  
École Polytechnique Fédérale de Lausanne, Station 6, Lausanne 1015, Switzerland

<sup>3</sup>Department of Physics, Friedrich-Alexander-Universität Erlangen-Nürnberg, D-91058 Erlangen, Germany

## THEORETICAL APPROACH FOR NEEC WITH ELECTRON VORTEX BEAMS

In order to derive the NEEC rate for vortex electron beams, we relate to the plane wave results in Refs. [S1–S3] and expand the continuum electronic wave function into partial waves of definite angular momentum. To specify the lateral position of the ion with regard to the central axis of the incident electron beam, the impact parameter  $\mathbf{b}$  is introduced [S4, S5]. The NEEC rate can be written as

$$Y_{\text{NEEC}}^{i \rightarrow g} = \int \mathcal{Y}_{\text{NEEC}}^{i \rightarrow g}(\mathbf{p}, \mathbf{k}) a_{\zeta m}(\mathbf{p}_{\perp}) a_{\zeta m}^*(\mathbf{k}_{\perp}) e^{i(\mathbf{k}_{\perp} - \mathbf{p}_{\perp}) \cdot \mathbf{b}} \frac{d^2 \mathbf{p}_{\perp}}{(2\pi)^2} \frac{d^2 \mathbf{k}_{\perp}}{(2\pi)^2} d^2 \mathbf{b}, \quad (\text{S1})$$

where  $\mathcal{Y}_{\text{NEEC}}^{i \rightarrow g}(\mathbf{p}, \mathbf{k})$  is the squared transition amplitude for incoming momenta  $\mathbf{p}$  and  $\mathbf{k}$ . We restrict the impact parameter region to  $|\mathbf{b}| \leq b$ . The NEEC rate takes then the form

$$Y_{\text{NEEC}}^{i \rightarrow g} = \frac{b^2}{4\pi} \int_0^{2\pi} \int_0^{2\pi} \frac{d\alpha_p}{2\pi} \frac{d\alpha_k}{2\pi} e^{im(\alpha_p - \alpha_k)} \mathcal{Y}_{\text{NEEC}}^{i \rightarrow g}(\mathbf{p}, \mathbf{k}) {}_0F_1(2; u), \quad (\text{S2})$$

with the condition  $|\mathbf{p}_{\perp}| = |\mathbf{k}_{\perp}| = \zeta$ , and the two polar angles  $\alpha_p$  and  $\alpha_k$  spanning the interval  $[0, 2\pi)$ . The notation  ${}_0F_1$  stands for the confluent hypergeometric limit function, and  $u = -b^2 \zeta^2 [1 - \cos(\alpha_k - \alpha_p)] / 2$ .

The remaining factor  $\mathcal{Y}_{\text{NEEC}}^{i \rightarrow g}(\mathbf{p}, \mathbf{k})$  can be related to the plane-wave NEEC amplitude calculated in Refs. [S1, S2]

$$\begin{aligned} \mathcal{Y}_{\text{NEEC}}^{i \rightarrow g}(\mathbf{p}, \mathbf{k}) &= \frac{2\pi(4\pi)(2J_g + 1)\rho_i}{2(2I_i + 1)(2J_i + 1)(2j_g + 1)} \\ &\times \sum_{M_i s} \sum_{M_g m_g} \langle I_g M_g, n_g \kappa_g m_g | H_N | I_i M_i, \mathbf{p} s \rangle \langle I_g M_g, n_g \kappa_g m_g | H_N | I_i M_i, \mathbf{k} s \rangle^\dagger, \end{aligned} \quad (\text{S3})$$

where  $H_N$  is the electron-nucleus interaction Hamiltonian,  $J_i$  is the total angular momentum of the initial electronic configuration of the ion,  $J_g$  the total angular momentum of the final electronic configuration of the ion after NEEC, and  $\rho_i$  the initial density of continuum electron states, respectively. The nuclear initial state (final state after NEEC) is determined by the total angular momentum  $I_i$  ( $I_g$ ) and its projection  $M_i$  ( $M_g$ ). The bound electron in the capture orbital is determined by the principal quantum number  $n_g$ , the Dirac angular momentum quantum number  $\kappa_g$ , and projection  $m_g$  of the angular momentum. Furthermore,  $j_g$  is the total angular momentum of the bound electron in the capture orbital. The calculation of the electron matrix elements requires the continuum electron states with definite asymptotic momentum  $\mathbf{p}$  (or  $\mathbf{k}$ ) and spin projection  $s$  to be expanded in terms of partial waves  $|\varepsilon \kappa m_j\rangle$  [S1, S2], where  $\varepsilon$  is the kinetic energy,  $\kappa$  is the Dirac angular momentum quantum number, and  $m_j$  is the projection of the total angular momentum  $j$ . The contribution of each partial wave is given by [S1, S2]

$$\begin{aligned} &\langle I_g M_g, n_g \kappa_g m_g | H_N | I_i M_i, \varepsilon \kappa m_j \rangle \\ &= \frac{1}{R_0^{L+2}} \sum_M (-1)^{I_g + M_i + L + M + m_j + 3j_g} \left[ \frac{4\pi(2j_g + 1)}{(2L + 1)^3} \right]^{1/2} \langle I_g || \mathcal{Q}_L || I_i \rangle \\ &\times C(I_i I_g L; -M_i M_g M) C(j J_g L; -m_j m_g - M) C(j_g L j; \frac{1}{2} 0 \frac{1}{2}) R_{L, \kappa_g, \kappa}^{(E)}, \end{aligned} \quad (\text{S4})$$

for transitions of electric multipolarity  $L$ , and

$$\begin{aligned} &\langle I_g M_g, n_g \kappa_g m_g | H_N | I_i M_i, \varepsilon \kappa m_j \rangle \\ &= \sum_M (-1)^{I_i - M_i + M + j - L - 1/2} \left[ \frac{4\pi(2j + 1)}{L^2(2L + 1)^2} \right]^{1/2} \langle I_g || \mathcal{M}_L || I_i \rangle (\kappa + \kappa_g) \\ &\times C(j L j_g; m - M m_g) C(I_g I_i L; M_d - M_i M) \begin{pmatrix} j_g & j & L \\ \frac{1}{2} & -\frac{1}{2} & 0 \end{pmatrix} R_{L, \kappa_g, \kappa}^{(M)}, \end{aligned} \quad (\text{S5})$$



for transitions of magnetic multipolarity  $L$ . Here  $\langle I_g || \mathcal{Q}_L || I_i \rangle$  and  $\langle I_g || \mathcal{M}_L || I_i \rangle$  are the reduced matrix elements of the electric and magnetic multipole moments, respectively. They are connected to the reduced nuclear transition probabilities by the expression  $\mathcal{B} \uparrow (E/ML) = \langle I_g || \mathcal{Q}_L / \mathcal{M}_L || I_i \rangle / (2I_i + 1)$ . Furthermore,  $R_0$  in Eq. (S4) denotes the nuclear radius. The radial integrals  $R_{L,\kappa_g,\kappa}^{(E)}$  and  $R_{L,\kappa_g,\kappa}^{(M)}$  for electric and magnetic multipolarities, respectively, are given in Refs. [S1, S2],

$$R_{L,\kappa_g,\kappa}^{(E)} = \frac{1}{R_0^{L-1}} \int_0^{R_0} dr_e r_e^{L+2} [f_{n_g\kappa_g}(r_e) f_{\varepsilon\kappa}(r_e) + g_{n_g\kappa_g}(r_e) g_{\varepsilon\kappa}(r_e)] \\ + R_0^{L+2} \int_{R_0}^{\infty} dr_e r_e^{-L+1} [f_{n_g\kappa_g}(r_e) f_{\varepsilon\kappa}(r_e) + g_{n_g\kappa_g}(r_e) g_{\varepsilon\kappa}(r_e)], \quad (\text{S6})$$

and

$$R_{L,\kappa_g,\kappa}^{(M)} = \int_0^{\infty} dr_e r_e^{-L+1} [g_{n_g\kappa_g}(r_e) f_{\varepsilon\kappa}(r_e) + f_{n_g\kappa_g}(r_e) g_{\varepsilon\kappa}(r_e)]. \quad (\text{S7})$$

Here  $f_{\varepsilon\kappa}(r_e)$  and  $g_{\varepsilon\kappa}(r_e)$  are the the large and small radial components of the the relativistic continuum electron wave function

$$\Psi_{\varepsilon\kappa m_j}(\mathbf{r}_e) = \begin{pmatrix} g_{\varepsilon\kappa}(r_e) \Omega_{\kappa}^{m_j}(\theta_e, \varphi_e) \\ i f_{\varepsilon\kappa}(r_e) \Omega_{-\kappa}^{m_j}(\theta_e, \varphi_e) \end{pmatrix}, \quad (\text{S8})$$

and  $f_{n_g\kappa_g}(r_e)$  and  $g_{n_g\kappa_g}(r_e)$  are the components of the bound Dirac wave functions

$$\Psi_{n_g\kappa_g m_g}(\mathbf{r}_e) = \begin{pmatrix} g_{n_g\kappa_g}(r_e) \Omega_{\kappa_g}^{m_g}(\theta_e, \varphi_e) \\ i f_{n_g\kappa_g}(r_e) \Omega_{-\kappa_g}^{m_g}(\theta_e, \varphi_e) \end{pmatrix}, \quad (\text{S9})$$

with the spherical spinor functions  $\Omega_{\kappa}^{m_j}$ ,  $\Omega_{-\kappa}^{m_j}$ ,  $\Omega_{\kappa_g}^{m_g}$ , and  $\Omega_{-\kappa_g}^{m_g}$ .

With the expansion of the continuum electronic wave function into partial waves of definite angular momentum, and the above matrix elements for each partial wave, we obtain the factor

$$\mathcal{Y}_{\text{NEEC}}^{i \rightarrow g}(\mathbf{p}, \mathbf{k}) = 4\pi Y_a \sum_{\kappa, m_l} \frac{Y_b}{2l+1} Y_{l m_l}^*(\theta_k, \varphi_k) Y_{l m_l}(\theta_p, \varphi_p), \quad (\text{S10})$$

where  $Y_{l m_l}$  stand for the spherical harmonics with quantum numbers  $l$  and  $m_l$ . Furthermore,  $\theta_p$  ( $\theta_k$ ) and  $\varphi_p$  ( $\varphi_k$ ) are the polar and azimuthal angles of the electron momentum  $\mathbf{p}$  ( $\mathbf{k}$ ) in the spherical coordinate of the ion. For NEEC transitions of electric multipolarity  $L$ ,

$$Y_a = \frac{4\pi^2(2J_g + 1)}{(2J_i + 1)(2L + 1)^2} \frac{1}{R_0^{2(L+2)}} \mathcal{B} \uparrow (EL) \rho_i, \quad (\text{S11})$$

and

$$Y_b = \left[ C(j_g L j; \frac{1}{2} 0 \frac{1}{2}) \right]^2 \left| R_{L,\kappa_g,\kappa}^{(E)} \right|^2. \quad (\text{S12})$$

For NEEC transitions of magnetic multipolarity  $L$ ,

$$Y_a = \frac{4\pi^2(2J_g + 1)}{(2J_i + 1)L^2(2L + 1)^2} \mathcal{B} \uparrow (ML) \rho_i, \quad (\text{S13})$$

and

$$Y_b = (2j + 1)(\kappa_g + \kappa)^2 \left( \begin{matrix} j_g & j & L \\ \frac{1}{2} & -\frac{1}{2} & 0 \end{matrix} \right)^2 \left| R_{L,\kappa_g,\kappa}^{(M)} \right|^2. \quad (\text{S14})$$

In the equations above,  $j$  is the total angular momentum of the continuum electron which connects with  $\kappa$  via  $j = |\kappa| - 1/2$ . The radial integrals  $R_{L,j_g,j}^{(E/M)}$  that enter Eqs. (S12) and (S14) are calculated numerically. We use relativistic Coulomb-Dirac wave functions for the continuum electron and wave functions calculated with the GRASP92 package [S6] considering a homogeneously charged nucleus for the bound electron. The finite size of the nucleus is not affecting significantly the radial wave functions. We find the values of  $R_{L,j_g,j}^{(E/M)}$  are nearly constant whether or not we take into account the finite size of the nucleus or we use Coulomb-Dirac radial wave functions. However, the finite size of the nucleus has a sensitive effect on the

energy levels of the bound electron. The bound electron energy levels are calculated with GRASP92 and include quantum electrodynamics corrections.

---

\* yuanbin.wu@mpi-hd.mpg.de

† adriana.palffy-buss@physik.uni-wuerzburg.de

[S1] A. Pálffy, W. Scheid, and Z. Harman, *Phys. Rev. A* **73**, 012715 (2006).

[S2] A. Pálffy, Z. Harman, and W. Scheid, *Phys. Rev. A* **75**, 012709 (2007).

[S3] J. Gunst, Y. Wu, N. Kumar, C. H. Keitel, and A. Pálffy, *Physics of Plasmas* **22**, 112706 (2015).

[S4] K. Y. Bliokh, I. Ivanov, G. Guzzinati, L. Clark, R. Van Boxem, A. Béch e, R. Juchtmans, M. A. Alonso, P. Schattschneider, F. Nori, et al., *Physics Reports* **690**, 1 (2017).

[S5] V. Serbo, I. P. Ivanov, S. Fritzsche, D. Seipt, and A. Surzhykov, *Phys. Rev. A* **92**, 012705 (2015).

[S6] F. A. Parpia, C. F. Fischer, and I. P. Grant, *Computer Physics Communications* **94**, 249 (1996).



Our systems of post-experimental thought and our systems of motivation and action therefore co-exist in paradoxical union. One is “up-to-date”; the other, archaic. One is scientific; the other, traditional, even superstitious. We have become atheistic in our description, but remain evidently religious—that is, moral—in our disposition. What we accept as true and how we act are no longer commensurate. We carry on as if our experience has meaning—as if our activities have transcendent value—but we are unable to justify this belief intellectually. We have become trapped by our own capacity for abstraction: it provides us with accurate descriptive information but also undermines our belief in the utility and meaning of existence.

— Jordan Peterson, *Maps of Meaning*



# 3 Nuclear Excitation by Free Muon Capture

## 3.1 Why muons?

We have seen that many ingredients have to come together for the NEEC process to occur and to be efficient: (i) the presence of vacancies in which the capture can occur; (ii) a good match between atomic binding energies and nuclear transition energies (i.e.,  $E_b \sim E_n$ ); and (iii) a significant overlap between bound and continuum wavefunctions. While the first (i) and third (iii) requirements can be considered somewhat accessible, the range of nuclear levels efficiently reachable through NEEC is limited by the K-shell binding energy of a given nuclide. This is due to the inverse proportionality of the NEEC cross-section with the energy of the free particle that has to be captured, that is  $\sigma_{\text{NEEC}} \propto 1/(E_n - E_b)$ . Considering that  $E_b^K$  is approximately 110 keV for  $Z = 90$ , it becomes increasingly less probable to excite nuclear levels substantially higher in energy due to the growing energy mismatch. Moreover, 100 keV nuclear transitions could already be very challenging to achieve for much lighter atoms.

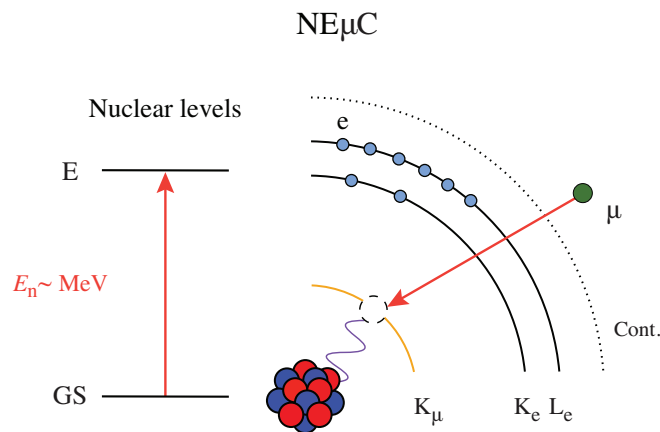


Figure 3.1: **The process of nuclear excitation by free muon capture (NE $\mu$ C).** The figure shows the muonic (yellow) and electronic (black) orbitals. Unlike electronic orbitals, muonic shells are always free for capture in atoms. As a result, ionization requirements are no longer necessary, breaking another paradigm of the NEEC process.

One of Italy's most renowned philosophers and poets, Giacomo Leopardi, regarded Nature as an evil and indifferent step-mother [168], creator of a need for pleasure that can never be satisfied, depriving human beings of the possibility of achieving happiness. Often, one can see the goal, but Nature does not provide an opportunity to reach it. Going beyond human perceptions of happiness in relation to their personal narratives [1, 169, 170], this philosophical thought is highly present in various aspects of physics: Nature presents us with trade-offs with which we must contend and often leaves us a little leeway, demanding greater effort to overcome them. The idea of a process equivalent to NEEC, occurring in exotic atoms, emerged from similar patterns of thought. If shells closer to the nucleus were available, they would have had higher binding energies: (i) making  $\sim \text{MeV}$  nuclear levels easier to excite and (ii) enhancing the interaction with the nucleus due to the increased proximity. However, within the realm of conventional atoms, possibilities are pretty much determined. As a result, our attention has turned to muonic atoms. Following this line of thinking, in 2022, we proposed the nuclear excitation by free muon capture ( $\text{NE}\mu\text{C}$ ) process [118], depicted in Fig. 3.1. Using muons has a first immediate advantage: the ionization requirement is no longer needed because muonic orbitals are always available for capture due to the instability of this subatomic particle.

A comparison between NEEC and its muonic counterpart ( $\text{NE}\mu\text{C}$ ) is presented in Fig. 3.2. In principle, both processes can excite the same nuclear transition with an energy of  $E_n \sim \text{MeV}$ . However, the roles of the resonance  $E_r$  and binding  $E_b$  energies are reversed between the two processes, while they add up to  $E_n$ . In conventional atoms, the binding energy  $E_b$  is generally smaller than 110 keV, which means that the remaining energy must be provided in the form of kinetic energy of the free particle to fulfill NEEC resonance conditions, as shown in Fig. 3.2a. This situation is reversed in the case of

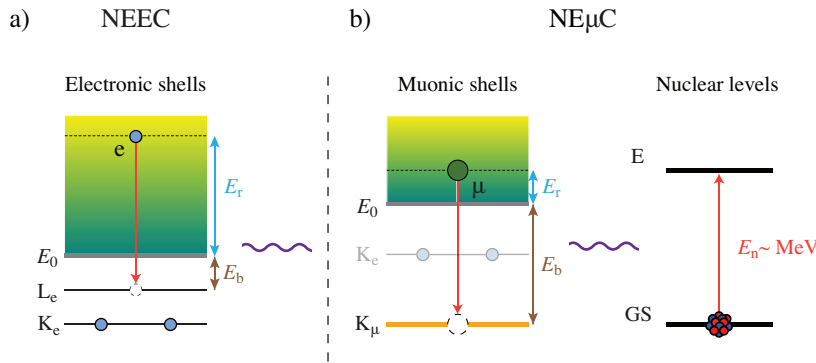


Figure 3.2: **Comparison between the NEEC and  $\text{NE}\mu\text{C}$  processes.** The energy diagrams for the NEEC (a) and  $\text{NE}\mu\text{C}$  (b) processes are displayed. The roles of the binding ( $E_b$ ) and resonance ( $E_r$ ) energies are reversed between the two mechanisms while adding up to reach a nuclear excitation in the MeV range ( $E_n = E_r + E_b$ ). Electronic shells are indicated with the label ‘e’ while muonic ones with a ‘ $\mu$ ’.  $E_0$  represents the vacuum level. In (b), the electronic shells are shaded to improve readability.

muonic atoms [171–173]. The binding energy for the K muonic shell is on the order of

$\sim 12$  MeV for  $Z = 90$  and up to  $\sim 17$  MeV for superheavy elements. As seen in Fig. 1.5, the highest isomeric energy state occurs in  $^{208\text{m}}\text{Pb}$  at 13.67 MeV. Therefore, in muonic atoms, it is much more likely to find situations where orbitals are almost resonant with such high-energy states, potentially covering the entire range of isomeric energies. In principle, NE $\mu$ C might be used to address both the depletion of an isomer inducing a transition towards an intermediate level – as seen in Fig. 1.14 for  $^{180\text{m}}\text{Ta}$ , where a  $\sim 1$  MeV excitation is needed to release the 77 keV stored in the long-lived isomer – as well as the activation of high-energy states, initiating the transition from the ground state.

In Ref. [118], we proposed NE $\mu$ C by examining all nuclear excited levels – regardless of their lifetime – connected to the ground state by low-order electric multipolar transitions, since these are generally dominant as discussed in Chapter 1. To perform the necessary calculations, the Dirac equations had to be solved for the Coulomb potential in the presence of muons [174, 175]. At that time, the most commonly used freely-available computational packages for atomic calculations, such as GRASP2K [176] and FAC [177], did not have the capability to handle muonic atoms, despite the similarity with the electronic case and the framework used therein. As part of the collaboration that arose for the realization of the work presented in the next section [118], the Flexible Atomic Code (FAC) was updated with state-of-the-art theoretical models to include muons as well. These modifications made the FAC the only freely-available online tool that can solve the Dirac equations for muonic atoms within 1 keV accuracy when compared to other state-of-the-art theoretical calculations [178]. As anticipated from our initial considerations, the integrated cross-section for NE $\mu$ C was found to be up to ten orders of magnitude larger than that of NEEC and two to five orders of magnitude higher than that of direct photoexcitation for  $\sim$  MeV quadrupolar transitions. This implies that in certain cases, NE $\mu$ C is the most efficient mechanism for exciting such nuclear levels, especially considering the absence of a tunable source of high-intensity MeV photons. It is worth noting, however, that the transitions identified in Ref. [118] do not lead – directly – to the population of isomers due to their selection criteria. The majority of these excited levels have half-lives  $T_{1/2} \ll 1$  ns, as shown in Fig. 3.3. Nevertheless, direct isomer feeding from the ground state is possible if different criteria are considered.

The unique properties of NE $\mu$ C call for its application to the isomer depletion scheme depicted in Fig. 1.15, where a long-lived isomer is connected to a fast-decaying depletion level through a low-order multipolar transition, followed by the release of energy via  $\gamma$ -ray emission or a converted electron. Identifying levels located above the isomer that can act as a depletion state is crucial, as these may have no direct transition to the isomer or their reduced transition probability  $B(\lambda L)$  may be unknown. A possible step forward in the foreseeable future might be the identification of such levels in the excitation spectra of  $^{178\text{m}}\text{Hf}$  (shown in Fig. 1.10) and  $^{180\text{m}}\text{Ta}$  (shown in Fig. 1.14) that could enable an efficient isomer depletion through NE $\mu$ C. In  $^{180\text{m}}\text{Ta}$ , NE $\mu$ C could provide an alternative method for depleting the 77.2 keV isomer by employing muons with much lower energies than those required by the photons for direct photoexcitation, which are typically on the



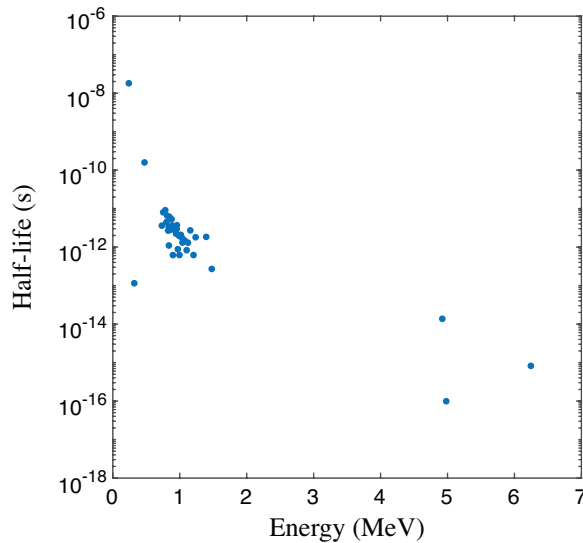


Figure 3.3: **Half-life and energy map of the nuclear levels excited through NE $\mu$ C, following the selection criteria of Ref. [118] for E1 and E2 transitions.**

order of  $\sim$  MeV [72, 81, 82].

Considering the high energy at play, it was reasonable to expect that NE $\mu$ C could have had a significant impact on inducing prompt fission of the nucleus by providing sufficient energy to overcome the barrier, which is  $E_f \sim 6$  MeV for actinides. It is well known that when muons slow down in a target medium, they are typically captured in high principal quantum number orbitals (with  $n \sim 14$ ). This initiates a cascade of multiple transitions that ends with the muon reaching the K-shell within 100 fs [171, 179]. During the cascade, muons can induce prompt nuclear fission by exciting the giant dipole (GDR) or quadrupole (GQR) resonances, transferring energy to the nucleus through radiationless transitions between two bound muonic states [179–181]. This excitation mechanism, shown in Fig. 3.4a, can be seen as the muonic analogous of the NEET process for electrons and could be called NE $\mu$ T, but it is more commonly referred to as nuclear excitation by muonic cascade. However, more likely, the muon will cascade down to the K-shell by emission of Auger electrons ( $n > 5$ ) or through radiative X-rays ( $n \leq 5$ ). At this point, the muon can be captured by a proton in the nucleus while it sits in the K-shell, resulting in the formation of a neutron and a muon neutrino [179], as shown in Fig. 3.4b. The average excitation energy provided to the nucleus is generally on the order of 15 MeV, which is sufficient to overcome the fission barrier for actinides  $E_f \sim 6$  MeV. The fission resulting from nuclear muon capture is delayed compared to the moment the muon entered the atom and the fragments produced by NE $\mu$ T, by the characteristic time of the weak decay process, which is  $\tau_{\text{capt}} \sim 75$  ns for actinides [182, 183].

Our work highlights a third channel, the fission induced by the radiationless capture of a free muon in a bound orbital (NE $\mu$ C), which seems not to have been taken into

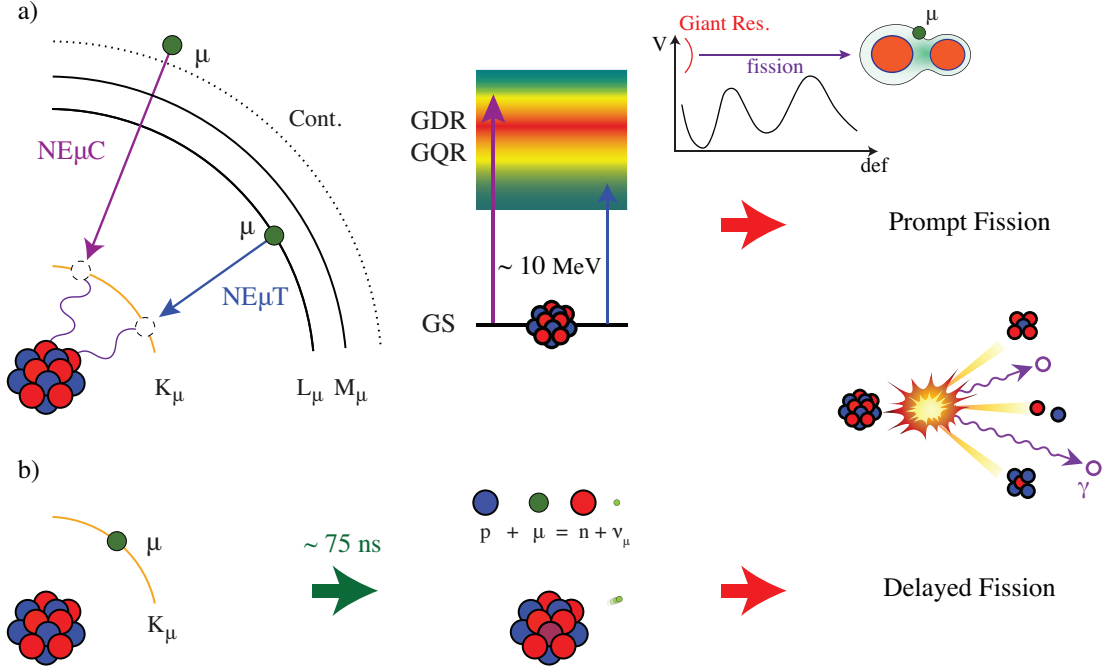


Figure 3.4: **Overview of the muon-induced fission processes.** In panel (a), radiationless transitions from free to bound states ( $\text{NE}_{\mu}\text{C}$ ) or between two bound states ( $\text{NE}_{\mu}\text{T}$ ) can provide enough energy to the nucleus to excite the giant dipole (GDR) or quadrupole (GQR) resonances. These states can act as a doorway to prompt fission having enough energy to overcome the double-humped barrier. In panel (b), the muon can be captured by a proton while it sits in the K-shell, leading to the reaction  $(Z, A) + \mu = (Z - 1, A)^* + \nu_{\mu}$  in a timescale of  $\tau_{\text{cap}} \sim 75$  ns for actinides [182, 183]. The resulting fission is therefore delayed compared to the fragments produced by the processes described in (a) by the lifetime of the weak decay process ( $\tau_{\text{cap}}$ ).

account in previous studies to explain the experimental observations [184–187]. This process is depicted in Fig. 3.4a, together with its competition with  $\text{NE}_{\mu}\text{T}$ . Therefore, we calculated the probability of inducing fission by  $\text{NE}_{\mu}\text{C}$  through the excitation of the GDR in  $^{238}\text{U}$  by capturing a free muon into the K-shell [118]. This probability was found to be equal to  $P_f \sim 4 \times 10^{-5}$  per incident muon. However, it should be noted that this value only accounts for the K-shell and does not include contributions from the excitation of the GQR. Having these aspects in mind, the probability of fission induced by  $\text{NE}_{\mu}\text{C}$  appears to be significantly weaker than the prompt fission induced by  $\text{NE}_{\mu}\text{T}$  (with  $P_f \sim 10^{-3} - 10^{-2}$ ) and the delayed fission resulting from nuclear muon capture ( $P_f \sim 10^{-2} - 10^{-1}$ ) [185]. Despite the results of our calculations, fission induced by  $\text{NE}_{\mu}\text{C}$  – occurring in shells higher than K – does not preclude the possibility of detecting a subsequent muonic X-ray<sup>1</sup> in coincidence with the fission event. Therefore, it is possible that the contribution of  $\text{NE}_{\mu}\text{C}$  to prompt fission has been incorrectly attributed and

<sup>1</sup>The term “muonic X-ray” refers to a photon emitted as a result of the transition of the muon between two states.

merged with the one caused by  $\text{NE}\mu\text{T}$  in experimental observations that rely on double ( $\gamma f$ ) or triple coincidences ( $\mu^- \gamma f$ ) events as a signature. Further investigations are desirable, particularly in light of the controversial experimental results discussed in Refs. [179, 188]. It is worth noting that when moving towards lighter isotopes, the innermost transitions (E1:  $2p - 1s$ ; E2:  $3d - 1s$ ) could eventually lose their overlap with the giant resonances, resulting in a weaker  $\text{NE}\mu\text{T}$ -induced fission. In this case, the additional degree of freedom provided by  $\text{NE}\mu\text{C}$ , in the form of the kinetic energy of the free lepton, may allow it to become the dominant process for prompt fission. However, a specific study is required to determine whether this is possible or not.

As mentioned in Chapter 1, the  $\text{NE}\mu\text{C}$  process could also be useful in the study of E0 monopole transitions, which are reported in Table A.2. These transitions cannot be excited by single-photon absorption, and  $\text{NE}\mu\text{C}$  may prove to be an efficient way to reach these low-lying  $0^+$  isomers directly from the ground state. Once excited, these  $0^+$  states cannot decay via a single gamma-ray emission, making higher-order processes such as internal conversion and pair production crucial for their deexcitation. If, as mentioned by Phil Walker in Ref. [20], one considers the scenario where all electrons have been removed, and the transition energy  $E_n$  is less than 1022 keV, then both channels of internal conversion and pair production are suppressed. In such cases, it should be possible to observe rarer decay modes. As an additional element to this recipe, it may be of interest to consider the excitation of the E0 transition through  $\text{NE}\mu\text{C}$  and the subsequent presence of a bound muon in the K-shell. Under specific conditions, such as when the muon capture rate is much smaller than the muon decay rate ( $\lambda_{\text{capt}} \ll \lambda_{\mu}$ ) and the isomer has a half-life in the presence of the bound muon (i.e., including the internal conversion of the bound muon)  $T_{1/2} \gg 1/\lambda_{\mu}$ , I can think of a special case, portrayed in Fig. 3.5, though perhaps quite impractical to study in reality. As the decay of a bound muon in a bound electron is a rare event [189, 190], the muon is likely to decay by emitting a free electron, leaving the isomer completely bare and with suppressed internal conversion (IC) channels, for both muons and electrons. If this sequence occurs, it could be possible to excite the  $0^+$  levels through  $\text{NE}\mu\text{C}$  from the ground state and have the opportunity to study rare decay modes afterward. However, several conditions must be met for this pattern to occur, and identifying a favorable excitation state is crucial.

Recently, I became aware of an earlier attempt by Kaufmann and Pilkuhn in 1977 to calculate the probability of inducing neutron emission in  $^{208}\text{Pb}$  through free-bound muon transitions, which corresponds to what we have referred to as  $\text{NE}\mu\text{C}$ , using a non-relativistic surface transition model [191]. It is surprising to learn that the theoretical backbone of the nuclear excitation through the radiationless capture of a free lepton was presented<sup>II</sup> just one year after the initial proposition of the NEEC process by Goldanskii and Namiot [99, 100]. Nonetheless, as discussed in Chapter 2, it took nearly 30 years for NEEC to have a more rigorous derivation [139, 140]. Curiously, subsequent works and reviews on the topic [171, 173, 181, 192, 193] seem to have lost trace of this process, and no direct connection with NEEC was ever drawn. In fact, the paper by Kaufmann and

<sup>II</sup>It appears that Kaufmann and Pilkuhn were not aware of the NEEC process.

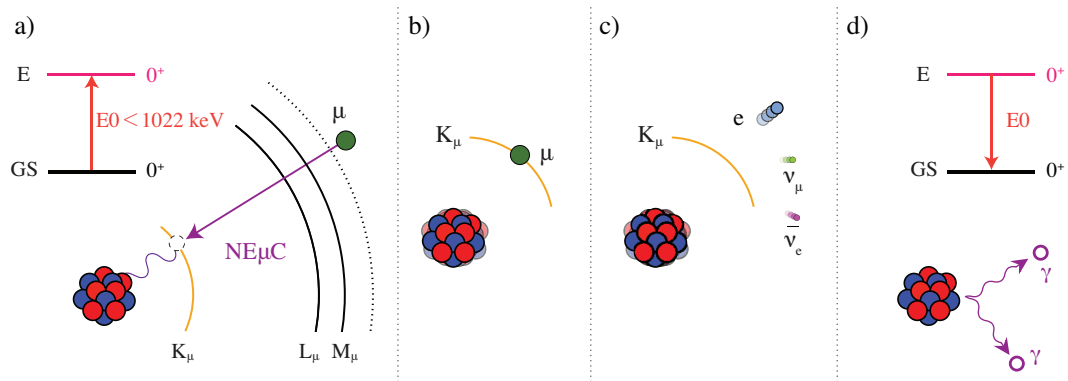


Figure 3.5: **Possible reaction pattern to study rare decay modes through monopole transitions:** in panel (a), the  $E0$  transition is induced by the capture of a free muon ( $NE\mu C$ ), connecting the ground state to a low-lying  $0^+$  isomer. (b) Thereafter, the nucleus will be in an excited state and the muon will be bound to the K-shell. In (c), the muon decays resulting in the emission of a free electron. In panel (d), the bare atom cannot decay by single-photon emission, internal conversion, or internal pair formation, leaving room for rare decay processes such as the two-photon decay mode. Between panels (b) and (c), it is possible for the nucleus to deexcite through internal conversion of the bound muon or to undergo nuclear muon capture.

Pilkuhn has received only two citations in 46 years and, in both cases, it is mentioned among “mechanisms that proceed via electron capture or scattering” [194, 195].

It is not uncommon for scientific discoveries to be made through a convoluted pattern of research efforts. On this aspect, it was extremely instructive for me to learn – from a talk by Prof. Barry Marshall – about the tortuous path that led to the discovery and oblivion, repetitively over a century, of the *Helicobacter pylori* [196–198].

This feels to me as an eternal return [199].

## Statement on my contribution

In the next section, I include the integral publication “S. Gargiulo, M. F. Gu, F. Carbone, & I. Madan. Nuclear Excitation by Free Muon Capture. *Physical Review Letters*, 129(14), 142501, (2022).”, mentioned in this thesis as Ref. [118]. The idea of having an equivalent excitation process in muonic atoms emerged during a casual conversation about NEEC with Ivan Madan as his response to my quotation of Giacomo Leopardi. We were immediately intrigued by the idea and that same day, we proposed almost all the relevant aspects that ultimately found confirmation in the calculations. The updates required for the FAC code to handle muonic atoms were carried out by Ming Feng Gu. I was responsible for all aspects of the paper, including conducting all theoretical calculations and simulations, performing an accuracy assessment of the FAC code, and identifying suitable isotopes. The discussion of the results and potential applications was supported by all the authors.

## Nuclear Excitation by Free Muon Capture

Simone Gargiulo<sup>1,\*</sup>, Ming Feng Gu<sup>2</sup>, Fabrizio Carbone<sup>1</sup>, and Ivan Madan<sup>1,†</sup>

<sup>1</sup>*Institute of Physics (IPhys), Laboratory for Ultrafast Microscopy and Electron Scattering (LUMES), École Polytechnique Fédérale de Lausanne (EPFL), Lausanne 1015 CH, Switzerland*

<sup>2</sup>*Space Science Laboratory, University of California, Berkeley, Berkeley, California 94720, USA*

(Received 11 March 2022; revised 24 June 2022; accepted 16 August 2022; published 27 September 2022)

Efficient excitation of nuclei via exchange of a real or virtual photon has a fundamental importance for nuclear science and technology development. Here, we present a mechanism of nuclear excitation based on the capture of a free muon into the atomic orbits (NE $\mu$ C). The cross section of such a proposed process is evaluated using the Feshbach projection operator formalism and compared to other known excitation phenomena, i.e., photoexcitation and nuclear excitation by electron capture (NEEC), showing up to 10 orders of magnitude increase in cross section. NE $\mu$ C is particularly interesting for MeV excitations that become accessible thanks to the stronger binding of muons to the nucleus. The binding energies of muonic atoms have been calculated introducing a state of the art modification to the Flexible Atomic Code. An analysis of experimental scenarios in the context of modern muon production facilities shows that the effect can be detectable for selected isotopes. The total probability of NE $\mu$ C is predicted to be  $P \approx 1 \times 10^{-6}$  per incident muon in a beam-based scenario. Given the high transition energy provided by muons, NE $\mu$ C can have important consequences for isomer feeding and particle-induced fission.

DOI: [10.1103/PhysRevLett.129.142501](https://doi.org/10.1103/PhysRevLett.129.142501)

Manipulating nuclear transitions is a highly desirable goal due to its implications in the energy sector [1–8]. Long-lived nuclear excitations, formally isomers, have lifetimes that are sometimes comparable to the age of the universe and have a potential to release hundreds of megajoules of energy stored in few cubic centimeters. The former aspect is crucial in designing new energy storage solutions: long duration has been suggested to be the key driver towards a decarbonized future [9]. Unfortunately, an efficient process to excite and control the lifetime of isomers is currently lacking.

Nuclear levels, in general, are not easily accessible: they often have high spin with respect to the ground state, the resonances are very narrow and predominantly in the MeV range, in which no high-intensity monochromatic light sources exist yet. Alternatively, to direct excitation via photon absorption, few other secondary electromagnetic processes exist—such as Coulomb excitation [10], nuclear excitation upon electron capture (NEEC) [11,12] or transition (NEET) [13–15] and excitation upon muon cascade [16]. Here we present an alternative electronucleus excitation mechanism that presents one of the highest excitation cross sections: the nuclear excitation by free muon capture (NE $\mu$ C). The high energy transferred to the nucleus expands the range of isotopes suitable for the process and makes NE $\mu$ C relevant for muon-induced fission [17–21] and for the feeding of long-lived isomers [1], as shown in Fig. 1.

It is instructive to compare electronic and muonic electronucleus processes. Excitation upon muon cascade

[22,23] and NEET occur as a result of the transition between bound muonic and electronic orbitals, respectively. The two processes have been experimentally observed [24–28] and are considered to be well established. Here, we shall also mention an excitation delayed with respect to the free muon capture and muonic cascade leading to nuclear transmutation by nuclear orbital muon capture [21], which is of electroweak and not of

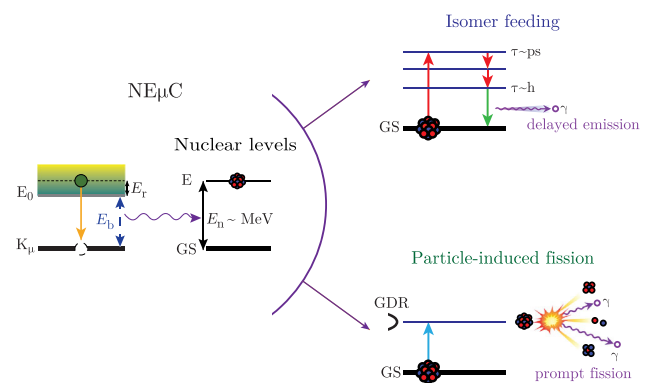


FIG. 1. Nuclear excitation by muon capture (NE $\mu$ C): the capture of a free muon leads to a resonant excitation of the nucleus. The excited nucleus can subsequently decay towards lower levels reaching a long-lived state, i.e., isomer feeding. Another possibility is present if the excitation of the nucleus is in resonance with the giant dipole (GDR) or quadrupole resonances (GQR), and the latter is above the fission barrier: the nucleus can undergo a prompt fission induced by NE $\mu$ C.

electromagnetic origin and it is thus omitted from most of the quantitative comparison in this Letter.

The NEEC process was claimed to have been observed in a single experiment [12,29–31] and its cross section differs from a theoretical estimate by 9 orders of magnitude [32]. To our knowledge, a muonic analogue of NEEC has never been proposed and in this Letter we investigate this possibility theoretically, underlining key differences with other excitation processes.

Similarly to NEEC and contrary to NEET and muon cascade excitation,  $NE\mu C$  describes the capture of a *free* lepton in a corresponding atomic orbital, and is thus not constrained by the restriction of matching the transition energies between *bound* atomic and nuclear levels. Since both NEEC and  $NE\mu C$  depend on the interaction between the nuclear and atomic environment, tight muon orbits are expected to provide a higher nuclear excitation cross section than their electronic counterparts. In particular, here we report findings of a  $NE\mu C$  integrated cross section up to  $1.82 \times 10^5$  b eV, that is 5 orders of magnitude higher than any corresponding NEEC cross section reported so far [33–37]. To evaluate the  $NE\mu C$  cross section we used the advanced theory based on the Feshbach projection operator formalism developed by A. Pálffy for the NEEC process and presented in Refs. [33] and [38]. In this context, the  $NE\mu C$  rate for an electric transition can be written in muonic atomic units as

$$Y_n^{(e)L} = \frac{1}{4\pi\alpha} \frac{4\pi^2\rho_i}{(2L+1)^2} R_0^{-2(L+2)} B\uparrow(EL)(2j_b+1) \times \sum_k |\tilde{R}_{L,k_b,k}|^2 C(j_b L j; 1/201/2)^2, \quad (1)$$

where  $B\uparrow(EL)$  is the reduced transition probability of the  $L$ th multipolar transition,  $C(j_1 j_2 j; m_1 m_2 m)$  is the Clebsch-Gordan coefficient,  $j_b$  and  $j$ , are the total angular momentum, while  $k_b$  and  $k$  are the Dirac angular momentum of the bound and free muon, respectively.  $\tilde{R}_{L,k_b,k}$  is the radial integral that depends on the muon bound and free wave functions, which are obtained as solutions of the Dirac equations for a specific atomic configuration using the modified version of the Flexible Atomic Code (FAC) [39].

The  $NE\mu C$  cross section can be expressed as

$$\sigma_{NE\mu C} = 2\pi^2 \lambda_\mu^2 Y_n \frac{\frac{\Gamma_r}{2\pi}}{(E - E_r)^2 + \frac{\Gamma_r^2}{4}}, \quad (2)$$

where  $\lambda_\mu$  is the free muon wavelength and  $E_r$  the resonance energy. The integration of the cross section over the continuum energies, considering that  $\Gamma_r \ll E_r$ , gives the so-called resonance strength:

$$S_{NE\mu C} = \int \sigma_{NE\mu C}(E) dE = 2\pi^2 \lambda_\mu^2 Y_n. \quad (3)$$

For  $NE\mu C$  to be possible the nuclear transition energy ( $E_n$ ) has to be larger than the muon binding energy ( $E_b$ ),

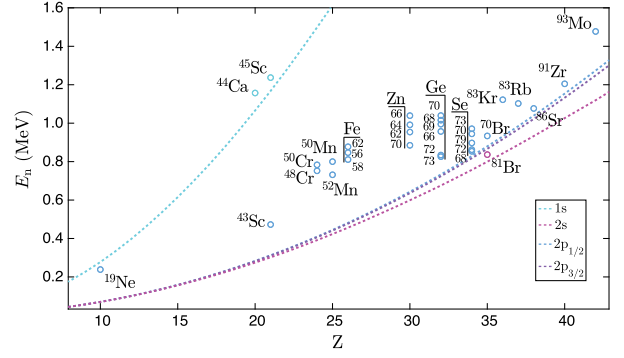


FIG. 2. Isotopes matching the search criteria in case of  $E2$  transition. Only the nuclear transitions with a  $B\downarrow(E2) > 10$  W.u. have been included in the plot. The color of the markers indicates the closest shell allowing  $NE\mu C$ . Vertical black lines group several isotopes of the same element.

and the free muon energy ( $E_r$ ) has to match their difference (i.e.,  $E_r = E_n - E_b$ ). This condition defines the search for the nuclear transitions that can be excited by the  $NE\mu C$  mechanism. In Fig. 2, we plot the muonic binding energies for  $K$  and  $L$  shells, calculated with the FAC [39] modified for muonic atoms, and nuclear excited levels that satisfy the above criteria with respect to the nuclear ground state for  $E_r$  up to 0.4 MeV above the corresponding muonic levels. For the sake of the presentation we only show the  $E2$  transitions, which are generally the strongest. The Table I reports the  $NE\mu C$  rates and resonance strengths for selected isotopes together with the nuclear transition energy and the required energy of the free muon, including several  $E1$  transitions.

Binding energies for muonic atoms are obtained by numerically solving the Dirac equation including the effect of the finite size of the nucleus using the Fermi distribution function with parameters adjusted to reproduce the rms charge radii of Ref. [40]. Vacuum polarization is taken into account using the standard Uehling potential, while self-energy correction is included using the method of Ref. [41]. The nucleus recoil effect is approximated with an effective Hamiltonian term proposed in Ref. [42].

In Table II we compare the  $NE\mu C$  and NEEC resonance strengths of a few of the strongest transitions. For all considered cases the  $NE\mu C$  is substantially stronger than NEEC. The enhancement found ranges between 5 to 10 orders of magnitude. Table II also offers a comparison with the direct process of photoexcitation. Results show that in the case of an  $E1$  transition, as for  $^{138}\text{Ba}$  and  $^{207}\text{Pb}$ ,  $S_\gamma$  and  $S_{NE\mu C}$  are comparable, while for quadrupolar excitations  $S_{NE\mu C}$  is substantially larger than  $S_\gamma$ . The choice of comparing  $NE\mu C$  with NEEC and direct photoexcitation is due to the fact that all these processes can excite the same generic nuclear level, having as the degree of freedom the energy of the free muon or electron and the energy of the photon. NEET, and excitation upon muon cascade, instead



TABLE I. Resonance strengths for the isotopes highlighted by the search criteria for  $E1$  and  $E2$  transitions and capture in the  $K$  and  $L$  shells. Isotopes are ordered with respect to the mass number.  $T_{1/2}$  indicates the half-life of the nuclear ground state.

Isotope	$T_{1/2}$	$L^{\text{th}}$	$E_n$ (keV)	$nl_j$	$E_r$ (keV)	$Y_{\text{NE}\mu\text{C}}$ (1/s)	$S_{\text{NE}\mu\text{C}}$ (b eV)
$^{11}\text{Be}$	13.76 s	$E1$	320.04	$1s_{1/2}$	275.54	$1.39 \times 10^{14}$	12.09
$^{19}\text{Ne}$	17.22 s	$E2$	238.27	$2p_{3/2}$	168.21	$1.16 \times 10^{14}$	16.58
$^{43}\text{Ca}$	Stable	$E1$	1394.47	$1s_{1/2}$	329.02	$4.95 \times 10^{10}$	$3.62 \times 10^{-3}$
$^{44}\text{Ca}$	Stable	$E2$	1157.02	$1s_{1/2}$	92.20	$4.14 \times 10^{12}$	1.08
$^{45}\text{Sc}$	Stable	$E2$	1236.70	$1s_{1/2}$	69.08	$2.84 \times 10^{12}$	0.99
$^{48}\text{Cr}$	21.56 h	$E2$	752.19	$2s_{1/2}$	360.43	$4.69 \times 10^{13}$	3.13
$^{48}\text{Cr}$	21.56 h	$E2$	752.19	$2p_{1/2}$	342.84	$2.63 \times 10^{16}$	$1.84 \times 10^3$
$^{48}\text{Cr}$	21.56 h	$E2$	752.19	$2p_{3/2}$	345.88	$5.15 \times 10^{16}$	$3.58 \times 10^3$
$^{52}\text{Mn}$	5.591 d	$E2$	731.66	$2p_{1/2}$	287.05	$9.28 \times 10^{15}$	771.14
$^{68}\text{Se}$	35.5 s	$E2$	853.75	$2s_{1/2}$	92.94	$3.52 \times 10^{14}$	90.87
$^{68}\text{Se}$	35.5 s	$E2$	853.75	$2p_{1/2}$	24.54	$1.42 \times 10^{17}$	$1.38 \times 10^5$
$^{68}\text{Se}$	35.5 s	$E2$	853.75	$2p_{3/2}$	36.18	$2.75 \times 10^{17}$	$1.82 \times 10^5$
$^{73}\text{Ge}$	Stable	$E2$	825.8	$2p_{1/2}$	92.66	$3.81 \times 10^{16}$	$9.85 \times 10^3$
$^{73}\text{Ge}$	Stable	$E2$	825.8	$2p_{3/2}$	101.84	$7.41 \times 10^{16}$	$1.75 \times 10^4$
$^{81}\text{Br}$	Stable	$E2$	836.8	$2s_{1/2}$	37.22	$1.43 \times 10^{14}$	91.82
$^{86}\text{Sr}$	Stable	$E2$	1076.7	$2p_{3/2}$	54.77	$9.52 \times 10^{15}$	$4.17 \times 10^3$
$^{91}\text{Zr}$	Stable	$E2$	1204.8	$2p_{1/2}$	51.18	$1.32 \times 10^{16}$	$6.19 \times 10^3$
$^{91}\text{Zr}$	Stable	$E2$	1204.8	$2p_{3/2}$	72.26	$2.56 \times 10^{16}$	$8.49 \times 10^3$
$^{93}\text{Mo}$	$4.0 \times 10^3$ y	$E2$	1477.2	$2p_{1/2}$	203.4	$6.25 \times 10^{16}$	$7.38 \times 10^3$
$^{93}\text{Mo}$	$4.0 \times 10^3$ y	$E2$	1477.2	$2p_{3/2}$	228.53	$1.21 \times 10^{17}$	$1.27 \times 10^4$
$^{138}\text{Ba}$	Stable	$E1$	6244.8	$1s_{1/2}$	44.19	$2.69 \times 10^{14}$	146
$^{202}\text{Hg}$	Stable	$E1$	4922	$2p_{1/2}$	329.41	$6.12 \times 10^{14}$	44.66
$^{207}\text{Pb}$	Stable	$E1$	4980.5	$2p_{1/2}$	165.51	$3.09 \times 10^{15}$	447.50
$^{207}\text{Pb}$	Stable	$E1$	4980.5	$2p_{3/2}$	350.64	$5.67 \times 10^{15}$	388.75

needs more strict conditions to take place, making a comparison for the same levels unsuitable.

Similarly to the NEEC case, the  $\text{NE}\mu\text{C}$  cross section is greatly enhanced if the resonance is met at low kinetic energy, given the  $\lambda^2$  prefactor in Eq. (2). In this respect it is important to inspect the precision of atomic orbital calculations. Considering that the FAC has never been used before to compute muonic binding energies, we compare in Fig. 3 the values obtained using the FAC with the state-of-the-art theoretical calculations for muonic atoms presented in Ref. [43], in the case of  $^{40}\text{Zr}$ ,  $^{147}\text{Sm}$ , and  $^{209}\text{Bi}$ . The

overall standard deviations between the differences in the binding energies range from 0.36 keV for  $^{40}\text{Zr}$  to 0.87 keV for  $^{209}\text{Bi}$ . Much of these discrepancies can be attributed to the self-energy correction included in the present Letter and omitted in Ref. [43]. The agreement between FAC and Ref. [43] improves significantly for the  $M$  shell, as the self-energy term becomes negligible. This assesses FAC as a valuable tool for the calculations of binding energies in muonic atoms (more detailed comparison is available in the Supplemental Material [44], which contains Ref. [45]).

 TABLE II. Comparison between  $\text{NE}\mu\text{C}$ , NEEC, and direct photoexcitation for the same nuclear transition for several isotopes. The apex  $i$  indicates a bare nucleus configuration while  $n$  the one for a neutral atom. Integrated cross sections are expressed in b eV, while  $E_n$  in keV.

Isotope	$E_n$	$nl_j$	$S_{\text{NE}\mu\text{C}}^i$	$S_{\text{NEEC}}^i$	$S_\gamma$	$S_{\text{NE}\mu\text{C}}^n$
$^{52}\text{Mn}$	731.66	$2p_{1/2}$	771.14	$6.83 \times 10^{-7}$	0.58	764.73
$^{68}\text{Se}$	853.75	$2p_{3/2}$	$1.82 \times 10^5$	$1.44 \times 10^{-5}$	4.29	$1.62 \times 10^5$
$^{73}\text{Ge}$	825.8	$2p_{1/2}$	$9.85 \times 10^3$	$4.35 \times 10^{-6}$	1.34	$9.45 \times 10^3$
$^{93}\text{Mo}$	1477.2	$2p_{3/2}$	$1.27 \times 10^4$	$8.91 \times 10^{-6}$	5.00	$1.24 \times 10^4$
$^{138}\text{Ba}$	6244.8	$1s_{1/2}$	146	$1.57 \times 10^{-2}$	164.74	120.66
$^{207}\text{Pb}$	4980.5	$2p_{1/2}$	447.5	$6.52 \times 10^{-2}$	713.96	432.6

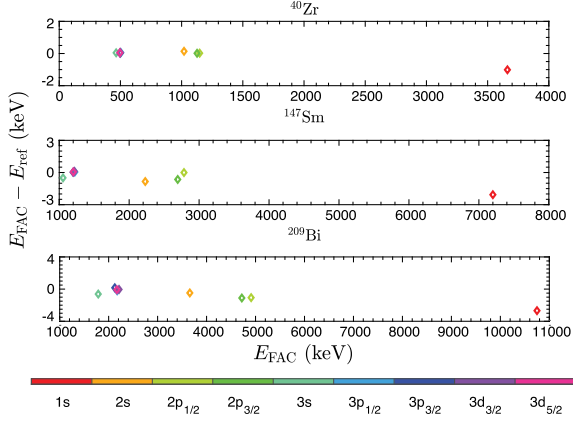


FIG. 3. Accuracy assessment of the FAC. Muonic binding energies computed with the FAC ( $E_{\text{FAC}}$ ) are compared with those of Ref. [43] ( $E_{\text{ref}}$ ). The color of the marker indicates the muonic state.

Another important difference with respect to NEEC is the absence of the high ionization state requirement. In the case of muons, the muonic inner shells are always available for capture and cannot be filled with electrons even for neutral atoms. The presence of electrons in the atomic environment will screen the muonic levels, making the muons less bound by up to few tens of keV, depending on the number of electrons in the shells [43,46,47]. This means that the resonance strengths evaluated for bare nuclei in Table I will be only slightly affected by the electronic charge state of the capturing ion. Thus,  $\text{NE}\mu\text{C}$  allows for a capture in the  $1s$  shell of an entirely filled atom. For this reason, we evaluated the  $\text{NE}\mu\text{C}$  resonance strengths for the isotopes with the highest  $S_{\text{NE}\mu\text{C}}$  of Table I, also in case of a neutral electronic configuration (see Supplemental Materials [44] for further details). Results are shown in Table II. Here we notice, as expected, that the  $S_{\text{NE}\mu\text{C}}^i$  and  $S_{\text{NE}\mu\text{C}}^n$  are very close to each other, with a slight difference due to the different resonance energy of the neutral case induced by the electron screening. Screening by an arbitrary electronic configuration has been included in the FAC by solving the Dirac equations of both the muon and electrons self-consistently via iteration.

From the experimental point of view, the possibility of capture in neutral atoms can be tremendously useful and could offer an interesting perspective lifting the stringent experimental requirements for NEEC. Indeed, as NEEC simultaneously requires a high ionization state and high density of resonant electrons, the parallel realization of both poses experimental challenges. Lifting the ionization requirement for  $\text{NE}\mu\text{C}$  simplifies the experimental scenario. For example, in a beam-based setup  $\text{NE}\mu\text{C}$  can be observed by sending a muon beam into a solid target. Analogously to NEEC, the  $\text{NE}\mu\text{C}$  probability can be written as [32,48]

$$P = \sum_{\alpha_r} n_i S_{\text{NE}\mu\text{C}}^{\alpha_r} \frac{1}{-(dE_\mu/dx)|_{E_r}}, \quad (4)$$

where  $\alpha_r$  represents the available capture channels,  $n_i$  is the density of atoms, and  $-(dE_\mu/dx)|_{E_r}$  is the muon stopping power at the resonance energy. The number of excited nuclei per second, assuming a continuous muon beam with a flux  $\phi_\mu$  (1/s), is given by

$$N_{\text{NE}\mu\text{C}}^{\text{exc}} = P\phi_\mu. \quad (5)$$

If we limit ourselves to solid targets with stable or long-lived ground states, essential for practical experiments,  $^{73}\text{Ge}$  and  $^{93}\text{Mo}$  are the most promising isotopes. The stopping power calculated with GEANT4 [49] is of  $dE_\mu/dx \simeq -501$  MeV/cm and  $-607$  MeV/cm at the resonant energies of 101.84 keV and 228.53 keV, respectively. Considering the capture only in the  $2p_{3/2}$  channel the resulting probabilities are  $P = 1.54 \times 10^{-6}$  and  $P = 1.39 \times 10^{-6}$ , respectively. Remarkably, these theoretical probabilities are 5 orders of magnitude larger than those theoretically estimated for the  $^{93}\text{Mo}$  isomer depletion through NEEC [32,50], although considering different excitation levels. If we expand the calculations to short-lived isotopes, e.g.,  $^{68}\text{Se}$ , the single channel excitation probability reaches  $P = 1.02 \times 10^{-5}$ . In practical terms, for efficient excitation, the initial energy of the incident muons is irrelevant provided that it is above the resonance energy  $E_r$ . Indeed, while traveling in the stopping medium, muons will experience a loss of energy due to subsequent collisions, guaranteeing that the resonant energy  $E_r$  will be achieved during the slow down process in the target. The precise depth at which it occurs depends on the incident muon energy. In a realistic setup, high-flux muon beams will have a substantial spread of incident muon energies, which will result in a distribution of resonance depth. This effect might reduce the efficiency of  $\text{NE}\mu\text{C}$  detection if the spread in depths exceeds the transmission depth of the nuclear emitted gamma photons. Considering 1 MeV energy spread of the muon beam at energies above  $E_r$ , the thickness of the target assuring resonance for all the particles is of several tens of microns (i.e.,  $50 \mu\text{m}$  for  $^{68}\text{Se}$ ). Depending on the target and the energy of the gamma photons involved in the transition, the gamma attenuation will be only up to 50% [51].

Currently, the brightest  $\mu^-$  beam facilities at PSI (Villigen, Switzerland) and MuSIC (Osaka, Japan) are able to deliver a continuous flux of  $10^7$  muons per second [52]. Planned upgrades would make it feasible in the next years to have fluxes up to  $10^8$  and  $10^9$  muons per second, resulting approximately in ten to one thousand nuclear excitations per second. Furthermore, an increase in the excitation cross section is expected if the wave function of the muon is engineered [53], i.e., considering muon vortex



beams [54], as recently suggested for NEEC [8,37,55]. This modification of the wave function could make unfavourable transitions with higher multipolarity more likely to happen.

Given the high energy of nuclear transitions involved in NE $\mu$ C and its increased efficiency compared to direct photoexcitation at higher multiplicities, NE $\mu$ C can be the most suitable process for isomer feeding. In this case the feeding, as shown in Fig. 1, will not happen directly to the isomer state, but arriving to it through subsequent decays upon the initial excitation from the ground state. This is, for example, the case of the energy level schemes of  $^{113}\text{In}$  and  $^{87}\text{Sr}$ .

Typically, at energies of tens of MeV above the ground state, the density of the excitation states is so high that they overlap in a broad energy range, giving rise to the so-called giant resonances. Excitation of these resonances, independently from the particular excitation mechanism, can lead to fission if the resonance is above the fission barrier. Prompt fission of the nucleus has been achieved under muon excitation and attributed to the muon cascade in  $^{238}\text{U}$  [21]. Yet, the possibility of the NE $\mu$ C has not been considered despite it could provide substantially better energy overlap given that one has an additional degree of freedom, that is the energy of the free lepton. Indeed, fission induced by muonic transitions is governed by the energy difference between two muonic bound states, while in the case of NE $\mu$ C the resonance condition is satisfied throughout the whole width of the giant resonance, that can be several MeV wide. To estimate the contribution of the NE $\mu$ C process to the muon induced fission, we calculated the fission cross section induced by NE $\mu$ C for  $^{238}\text{U}$  from the photofission process [56,57] and reported it in the Supplemental Material [44]. Integrating the cross section with the energy dependent stopping power retrieved from Ref. [58] (further details are available in the Supplemental Material [44]), provides us with a final fission probability of  $\sim 4.30 \times 10^{-5}$  per incident muon. This probability is still small if compared with prompt fission induced by muon cascade ( $\sim 10^{-3}$ ) and delayed fission induced by muon capture ( $\sim 10^{-2} - 10^{-1}$ ) [59]. Nevertheless, for lighter isotopes the muon cascade eventually becomes nonresonant with the giant resonances, while NE $\mu$ C is theoretically always possible.

Most remarkably, the NE $\mu$ C has the highest chance to be observed than the NEEC process in which disagreement between experiment and theory is of 9 orders of magnitude. Measuring the NE $\mu$ C rates and comparing to the estimates provided in the presented Letter will hopefully help to resolve the contradiction and establish the origins of the extremely high experimentally measured NEEC probability.

S. G. and F. C. acknowledge support from Google Inc. I. M. acknowledges support from the SMART-electron

project that has received funding from the European Union's Horizon 2020 Research and Innovation Program under Grant Agreement No. 964591. The authors would like to thank Giovanni dal Maso for the useful insights about muonic beam facilities.

\*simone.gargiulo@epfl.ch

†ivanmadan@gmail.com

- [1] A. Aprahamian and Y. Sun, Long live isomer research, *Nat. Phys.* **1**, 81 (2005).
- [2] P. Walker and G. Dracoulis, Energy traps in atomic nuclei, *Nature (London)* **399**, 35 (1999).
- [3] C. B. Collins, F. Davanloo, M. C. Iosif, R. Dussart, J. M. Hicks, S. A. Karamian, C. A. Ur, I. I. Popescu, V. I. Kirischuk, J. J. Carroll, H. E. Roberts, P. McDaniel, and C. E. Crist, Accelerated Emission of Gamma Rays from the 31-yr Isomer of 178 hf Induced by X-Ray Irradiation, *Phys. Rev. Lett.* **82**, 695 (1999).
- [4] M. Litz and G. Merkel, Controlled extraction of energy from nuclear isomers, technical report, Army Research Lab Adelphi MD, 2004, <https://apps.dtic.mil/sti/citations/ADA433348>.
- [5] C. Collins, N. Zoita, F. Davanloo, S. Emura, Y. Yoda, T. Uruga, B. Patterson, B. Schmitt, J. Pouvesle, I. Popescu *et al.*, Accelerated  $\gamma$ -emission from isomeric nuclei, *Radiat. Phys. Chem.* **71**, 619 (2004).
- [6] J. Carroll, M. Litz, K. Netherton, S. Henriquez, N. Pereira, D. Burns, and S. Karamian, Nuclear structure and depletion of nuclear isomers using electron linacs, *AIP Conf. Proc.* **1525**, 586 (2013).
- [7] G. M. Vanacore, I. Madan, G. Berruto, K. Wang, E. Pomarico, R. Lamb, D. McGrouther, I. Kaminer, B. Barwick, F. J. G. de Abajo, and F. Carbone, Attosecond coherent control of free-electron wave functions using semi-infinite light fields, *Nat. Commun.* **9**, 2694 (2018).
- [8] I. Madan, G. M. Vanacore, S. Gargiulo, T. Lagrange, and F. Carbone, The quantum future of microscopy: Wave function engineering of electrons, ions, and nuclei, *Appl. Phys. Lett.* **116**, 230502 (2020).
- [9] N. A. Sepulveda, J. D. Jenkins, A. Edington, D. S. Mallapragada, and R. K. Lester, The design space for long-duration energy storage in decarbonized power systems, *Nat. Energy* **6**, 506 (2021).
- [10] G. Pieper and N. Heydenburg, Coulomb excitation of iron-57, *Phys. Rev.* **107**, 1300 (1957).
- [11] V. Goldanskii and V. Namiot, On the excitation of isomeric nuclear levels by laser radiation through inverse internal electron conversion, *Phys. Lett.* **62B**, 393 (1976).
- [12] C. J. Chiara, J. J. Carroll, M. P. Carpenter, J. P. Greene, D. J. Hartley, R. V. Janssens, G. J. Lane, J. C. Marsh, D. A. Matters, M. Polasik, J. Rzadkiewicz, D. Seweryniak, S. Zhu, S. Bottoni, and A. B. Hayes, Isomer depletion as experimental evidence of nuclear excitation by electron capture, *Nature (London)* **554**, 216 (2018).
- [13] P. Morel, J. Daugas, G. Gosselin, V. Méot, and D. Gogny, Nuclear excitation by electronic processes: NEEC and NEET effects, *Nucl. Phys.* **A746**, 608 (2004).

- [14] P. Morel, V. Méot, G. Gosselin, G. Faussurier, and C. Blancard, Calculations of nuclear excitation by electron capture (NEET) in nonlocal thermodynamic equilibrium plasmas, *Phys. Rev. C* **81**, 034609 (2010).
- [15] A. Y. Dzyublik, General theory of nuclear excitation by electron transitions, *Phys. Rev. C* **88**, 054616 (2013).
- [16] D. F. Measday, The nuclear physics of muon capture, *Phys. Rep.* **354**, 243 (2001).
- [17] J. A. Wheeler, Some consequences of the electromagnetic interaction between  $\mu$ -mesons and nuclei, *Rev. Mod. Phys.* **21**, 133 (1949).
- [18] D. Zaretsky, On nuclear fission by mu mesons, in *Proceedings of the Second International Conference on the Peaceful Uses of Atomic Energy: Physics in Nuclear Energy* (United Nations Publication, 1958), Vol. 15, p. 175.
- [19] D. Zaretski and V. Novikov, Theory of nuclear excitations by muons in heavy mesic atoms, *Nucl. Phys.* **28**, 177 (1961).
- [20] S. Ahmad, G. Beer, M. Dixit, J. Macdonald, G. Mason, A. Olin, R. Pearce, O. Häusser, and S. Kaplan, Fission yields and lifetimes for muon induced fission in  $^{235}\text{U}$  and  $^{238}\text{U}$ , *Phys. Lett.* **92B**, 83 (1980).
- [21] V. E. Oberacker, A. S. Umar, J. C. Wells, C. Bottcher, M. R. Strayer, and J. Maruhn, Muon-induced fission: A probe for nuclear dissipation and fission dynamics, *Phys. Rev. C* **48**, 1297 (1993).
- [22] B. A. Jacobsohn, Nuclear fine structure in the  $\mu$ -mesonic atom, *Phys. Rev.* **96**, 1637 (1954).
- [23] L. Wilet, Excitation of nuclear rotational states in  $\mu$ -mesonic atoms, *Dan. Mat. Fys. Medd.* **29**, 1 (1954), <http://gymarkiv.sdu.dk/MFM/kdvs/mfm%2020-29/mfm-29-3.pdf>.
- [24] H. Backe, Intensity measurements of x-ray and nuclear gamma-ray transitions in some heavy muonic atoms., *Z. Phys.* **241**, 435 (1971).
- [25] M. V. Hoehn and E. B. Shera, Muonic resonance excitation of  $^{188}\text{Os}$  and  $^{172}\text{Yb}$ , *Phys. Rev. C* **20**, 1934 (1979).
- [26] C. Rösel, P. David, H. Folger, H. Hänscheid, J. Konijn, C. de Laat, C. Petitjean, H. Reist, F. Rissel, L. Schaller *et al.*, Radiationless transition probabilities in muonic  $^{208}\text{Pb}$ ,  $^{232}\text{Th}$ , and  $^{238}\text{U}$ , *Z. Phys. A Hadrons Nucl.* **340**, 199 (1991).
- [27] S. a. Kishimoto, Y. Yoda, M. Seto, Y. Kobayashi, S. Kitao, R. Haruki, T. Kawauchi, K. Fukutani, and T. Okano, Observation of Nuclear Excitation by Electron Transition in  $^{197}\text{Au}$  with Synchrotron X Rays and an Avalanche Photodiode, *Phys. Rev. Lett.* **85**, 1831 (2000).
- [28] S. Kishimoto, Y. Yoda, Y. Kobayashi, S. Kitao, R. Haruki, R. Masuda, and M. Seto, Nuclear excitation by electron transition on  $^{197}\text{Au}$  by photoionization around the k-absorption edge, *Phys. Rev. C* **74**, 031301(R) (2006).
- [29] S. Guo, Y. Fang, X. Zhou, and C. Petrache, Possible overestimation of isomer depletion due to contamination, *Nature (London)* **594**, E1 (2021).
- [30] C. Chiara, J. Carroll, M. Carpenter, J. Greene, D. Hartley, R. Janssens, G. Lane, J. Marsh, D. Matters, M. Polasik *et al.*, Reply to: Possible overestimation of isomer depletion due to contamination, *Nature (London)* **594**, E3 (2021).
- [31] S. Guo *et al.*, Probing  $^{93m}\text{Mo}$  Isomer Depletion with an Isomer Beam, *Phys. Rev. Lett.* **128**, 242502 (1999).
- [32] Y. Wu, C. H. Keitel, and A. Pálffy,  $^{93m}\text{Mo}$  Isomer Depletion via Beam-Based Nuclear Excitation by Electron Capture, *Phys. Rev. Lett.* **122**, 212501 (2019).
- [33] A. Pálffy, W. Scheid, and Z. Harman, Theory of nuclear excitation by electron capture for heavy ions, *Phys. Rev. A* **73**, 012715 (2006).
- [34] A. Pálffy, Z. Harman, and W. Scheid, Quantum interference between nuclear excitation by electron capture and radiative recombination, *Phys. Rev. A* **75**, 012709 (2007).
- [35] J. Rzadkiewicz, M. Polasik, K. Słabkowska, L. Syrocki, E. Węder, J. J. Carroll, and C. J. Chiara, Beam-based scenario for  $^{242m}\text{Am}$  isomer depletion via nuclear excitation by electron capture, *Phys. Rev. C* **99**, 044309 (2019).
- [36] Y. Wu, C. H. Keitel, and A. Pálffy, X-ray-assisted nuclear excitation by electron capture in optical laser-generated plasmas, *Phys. Rev. A* **100**, 063420 (2019).
- [37] S. Gargiulo, I. Madan, and F. Carbone, Nuclear Excitation by Electron Capture in Excited Ions, *Phys. Rev. Lett.* **128**, 212502 (2022).
- [38] A. Pálffy, Theory of nuclear excitation by electron capture for heavy ions, Ph.D. thesis, Justus-Liebig-Universität, 2006.
- [39] M. F. Gu, The flexible atomic code, *Can. J. Phys.* **86**, 675 (2008).
- [40] I. Angeli and K. P. Marinova, Table of experimental nuclear ground state charge radii: An update, *At. Data Nucl. Data Tables* **99**, 69 (2013).
- [41] R. C. Barrett, Radiative corrections in muonic atoms, *Phys. Lett.* **28B**, 93 (1968).
- [42] K. T. Cheng, W. R. Johnson, and J. Sapirstein, Screened Lamb Shift Calculations for Lithiumlike Uranium, Sodiumlike Platinum, and Copperlike Gold, *Phys. Rev. Lett.* **66**, 2960 (1991).
- [43] N. Michel, N. S. Oreshkina, and C. H. Keitel, Theoretical prediction of the fine and hyperfine structure of heavy muonic atoms, *Phys. Rev. A* **96**, 032510 (2017).
- [44] See Supplemental Material at <http://link.aps.org/supplemental/10.1103/PhysRevLett.129.142501> for further details on the theoretical calculations and the modifications of the flexible atomic code (FAC).
- [45] V. Yerokhin and V. Shabaev, Lamb shift of  $n = 1$  and  $n = 2$  states of hydrogen-like atoms,  $1 \leq Z \leq 110$ , *J. Phys. Chem. Ref. Data* **44**, 033103 (2015).
- [46] P. Vogel, Electron screening in muonic atoms, *Phys. Rev. A* **7**, 63 (1973).
- [47] B. Fricke, On the screening of muons by electrons in muonic atoms, *Lett. Nuovo Cimento (1969–1970)* **2**, 859 (1969).
- [48] M. Aikawa, S. Ebata, and S. Imai, Thick-target yields of radioactive targets deduced from inverse kinematics, *Nucl. Instrum. Methods Phys. Res., Sect. B* **353**, 1 (2015).
- [49] S. Agostinelli, J. Allison, K. a. Amako, J. Apostolakis, H. Araujo, P. Arce, M. Asai, D. Axen, S. Banerjee, G. Barrand *et al.*, GEANT4-a simulation toolkit, *Nucl. Instrum. Methods Phys. Res., Sect. A* **506**, 250 (2003).
- [50] J. Rzadkiewicz, M. Polasik, K. Słabkowska, L. Syrocki, J. J. Carroll, and C. J. Chiara, Novel Approach to  $^{93m}\text{Mo}$  Isomer Depletion: Nuclear excitation by Electron Capture in Resonant Transfer Process, *Phys. Rev. Lett.* **127**, 042501 (2021).

- [51] J. Hubbell and S. Seltzer, Nist standard reference database 126, Gaithersburg, (National Institute of Standards and Technology, MD, 1996).
- [52] S. Cook, R. D'arcy, A. Edmonds, M. Fukuda, K. Hatanaka, Y. Hino, Y. Kuno, M. Lancaster, Y. Mori, T. Ogitsu, H. Sakamoto, A. Sato, N. H. Tran, N. M. Truong, M. Wing, A. Yamamoto, and M. Yoshida, Delivering the world's most intense muon beam, *Phys. Rev. Accel. Beams* **20**, 030101 (2017).
- [53] G. M. Vanacore, I. Madan, and F. Carbone, Spatio-temporal shaping of a free-electron wave function via coherent light–electron interaction, *Riv. Nuovo Cimento* **43**, 567 (2020).
- [54] P. Zhao, I. P. Ivanov, and P. Zhang, Decay of vortex muon, *Phys. Rev. D* **104**, 036003 (2021).
- [55] Y. Wu, S. Gargiulo, F. Carbone, C. H. Keitel, and A. Pálffy, Dynamical Control of Nuclear Isomer Depletion via Electron Vortex Beams, *Phys. Rev. Lett.* **128**, 162501 (2022).
- [56] J. Gindler, J. Huizenga, and R. Schmitt, Photofission and photoneutron emission in thorium and uranium, *Phys. Rev.* **104**, 425 (1956).
- [57] J. M. Blatt and V. F. Weisskopf, *Theoretical Nuclear Physics* (Springer, New York, 1991).
- [58] D. E. Groom, N. V. Mokhov, and S. I. Striganov, Muon stopping power and range tables 10 MeV–100 TeV, *At. Data Nucl. Data Tables* **78**, 183 (2001).
- [59] T. Johansson, S. Polikanov, G. Tibell, T. Krogulski, J. Konijn, and H. Reist, Muon induced quadrupole photofission, *Phys. Lett.* **97B**, 29 (1980).

## Supplemental Material: Nuclear Excitation by Free Muon Capture

Simone Gargiulo,<sup>1,\*</sup> Ming Feng Gu,<sup>2</sup> Fabrizio Carbone,<sup>1</sup> and Ivan Madan<sup>1,†</sup>

<sup>1</sup>*Institute of Physics (IPhys), Laboratory for Ultrafast Microscopy and Electron Scattering (LUMES), École Polytechnique Fédérale de Lausanne (EPFL), Lausanne 1015 CH, Switzerland.*

<sup>2</sup>*Space Science Laboratory, University of California, Berkeley, CA 94720, USA*

### ACCURACY ASSESSMENT FOR MUONIC ATOM CALCULATIONS USING THE FLEXIBLE ATOMIC CODE

From Fig. S1 in the main text, we can see that the maximum discrepancy is obtained for the 1s shell with differences ranging between 1.08 keV for <sup>40</sup>Zr and 2.81 keV for <sup>209</sup>Bi. In the case of the 2s subshell, discrepancies drops down to a minimum of 0.07 keV for <sup>40</sup>Zr to a maximum of 0.94 keV for <sup>147</sup>Sm. For the 2p<sub>1/2</sub> the maximum disagreement, of about 1.19 keV, results from <sup>209</sup>Bi. Binding energies for the 2p<sub>3/2</sub> subshell similarly differ at most by 1.24 keV in the case of <sup>209</sup>Bi, while the discrepancies are smaller for <sup>40</sup>Zr and <sup>147</sup>Sm. In this context we used the rms nuclear charge radii reported in Ref. 1 and  $t = 2.30$  fm as the parameter of the Fermi-type charge distribution.

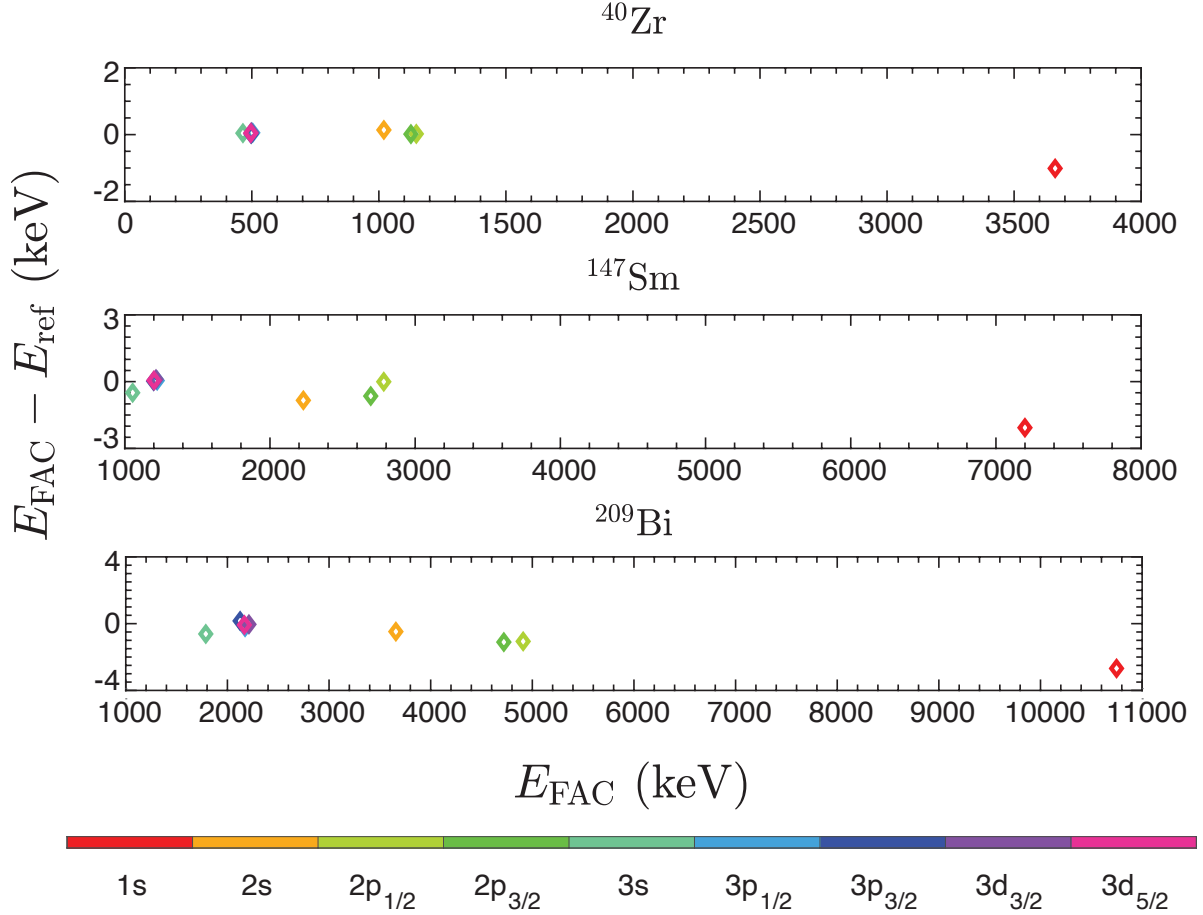


FIG. S1. Accuracy assessment of the Flexible Atomic Code for muonic atoms. Muonic binding energies computed with FAC ( $E_{\text{FAC}}$ ) are compared with those of Ref. 2 ( $E_{\text{ref}}$ ). The color of the marker indicates the muonic state.

## RADIAL INTEGRAL CALCULATION

The radial integral  $\tilde{R}_{L,k_b,k}$  has been calculated using its full expression, reported in Ref. 3, that is:

$$\tilde{R}_{L,k_b,k} = \frac{1}{R_0^{L-1}} \int_0^{R_0} dr r^{L+2} [f_{k_b}(r)f_{Ek}(r) + g_{k_b}(r)g_{Ek}(r)] + R_0^{L+2} \int_{R_0}^{+\infty} dr r^{-L+1} [f_{k_b}(r)f_{Ek}(r) + g_{k_b}(r)g_{Ek}(r)] , \quad (\text{S1})$$

where  $f(r)$  and  $g(r)$  are the large and small radial components of the bound and free muon wavefunctions.  $R_0$  is the nuclear radius for which we used the values reported in Ref. 1 for the available isotopes. For those not available we used the value reported by FAC, that is 3.562 08 fm for  $^{48}\text{Cr}$ , 3.964 75 fm for  $^{68}\text{Se}$  and 4.368 07 fm for  $^{93}\text{Mo}$ . These default values are taken from Ref. 4.

## NE $\mu$ C-INDUCED FISSION CROSS SECTION

$^{238}\text{U}$  presents the giant dipole resonance peak at  $E_{\text{GDR}} = 12.8$  MeV, that is slightly above the muonic binding energy of the K-shell,  $E_b^K = 12.12$  MeV. As similarly shown in Ref. 5, the NE $\mu$ C-induced fission has been related to the value of the photofission cross section through the matrix element of the dipole transition, thus to the photoexcitation cross section. Here, we use Eq. (XII, 7.27) of Ref. 6 as an expression for the direct photo-excitation cross section in case of high-energy nuclear transitions. Since, under Bohr assumption, the decay mode of the excited nucleus is independent from its formation, we express the relation between between NE $\mu$ C-induced fission cross section and the photo-fission cross section as:

$$\sigma_{\text{NE}\mu\text{C}}(\mu, F) = \left[ \frac{1}{4\pi\alpha} \frac{4\pi^2\rho_i}{(2L+1)^2} (2j_b+1) \times \sum_k |\tilde{R}_{L,k_b,k}|^2 C(j_b L j; 1/2 0 1/2)^2 \right] \times 2\pi^2 \lambda_\mu^2 \frac{3}{8\pi^3} \frac{1}{E} \sigma_\gamma(\gamma, F) , \quad (\text{S2})$$

where  $E$  is the energy of the transition. Photo-fission cross section has been retrieved from Fig. 4 of Ref. 7 and is also shown for comparison in the Extended Data Figure S2. The radial integral  $\tilde{R}_{L,k_b,k}$  has been calculated over the range 100 eV to 8 MeV for the free muon energy, considering a neutral electronic configuration for  $^{238}\text{U}$ . The probability of fission induced by the nuclear excitation by muon capture is then evaluated as:

$$P = n_i \int dE \frac{\sigma_{\text{NE}\mu\text{C}}(\mu, F)}{-(dE_\mu/dx)} \quad (\text{S3})$$

considering the only capture in the 1s shell. The stopping power is taken by Ref. 8, neglecting the small difference between positive and negative muons. The integral in Eq. S3 has been performed choosing  $E = 100$  eV as lower limit for the integration, that is the minimum energy for which the stopping power is available.

---

\* simone.gargiulo@epfl.ch

† ivanmadan@gmail.com

- [1] I. Angeli and K. P. Marinova, *Atomic Data and Nuclear Data Tables* **99**, 69 (2013).
- [2] N. Michel, N. S. Oreshkina, and C. H. Keitel, *Physical Review A* **96**, 032510 (2017).
- [3] A. Pálffy, *Theory of nuclear excitation by electron capture for heavy ions*, phdthesis, Justus-Liebig-Universität (2006), arXiv:0701206 [physics].
- [4] V. Yerokhin and V. Shabaev, *Journal of Physical and Chemical Reference Data* **44**, 033103 (2015).
- [5] D. Zaretski and V. Novikov, *Nuclear Physics* **28**, 177 (1961).
- [6] J. M. Blatt and V. F. Weisskopf, *Theoretical nuclear physics* (Springer, New York, 1991) p. 653.
- [7] J. Gindler, J. Huizenga, and R. Schmitt, *Physical Review* **104**, 425 (1956).
- [8] D. E. Groom, N. V. Mokhov, and S. I. Striganov, *Atomic Data and Nuclear Data Tables* **78**, 183 (2001).

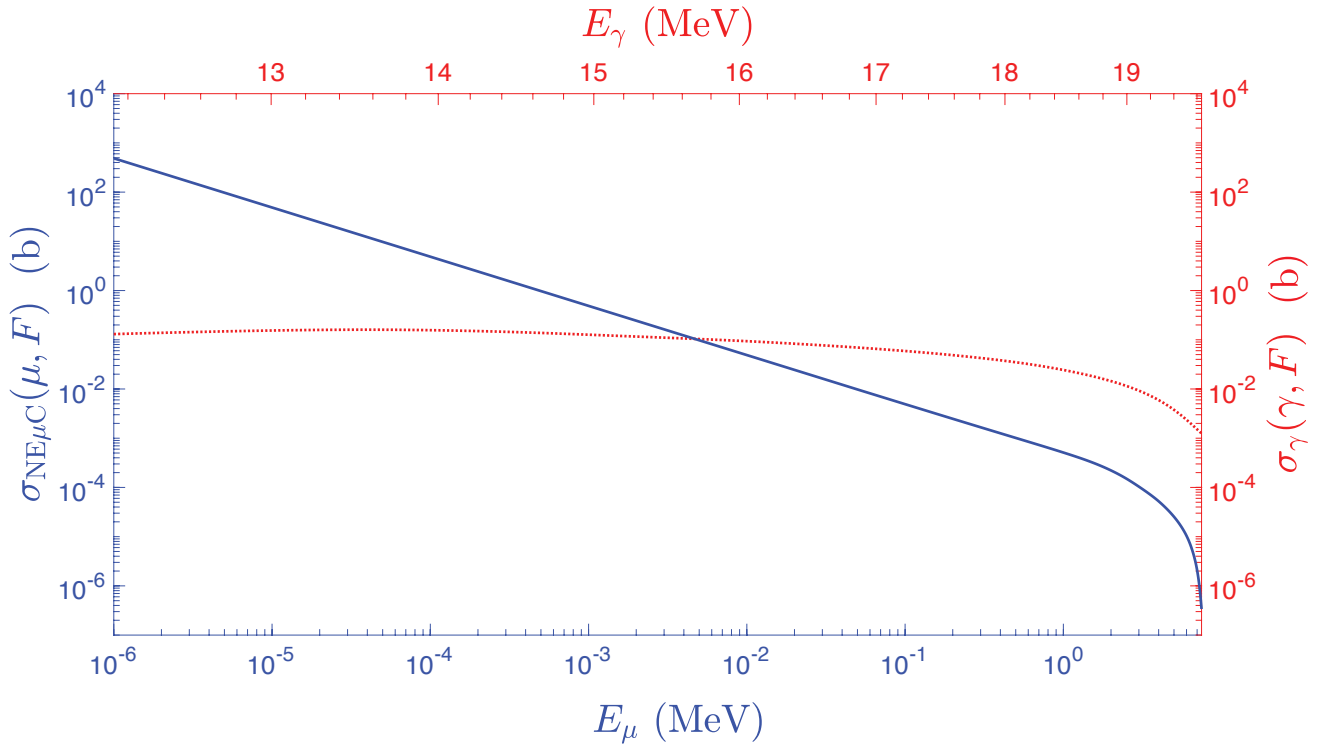


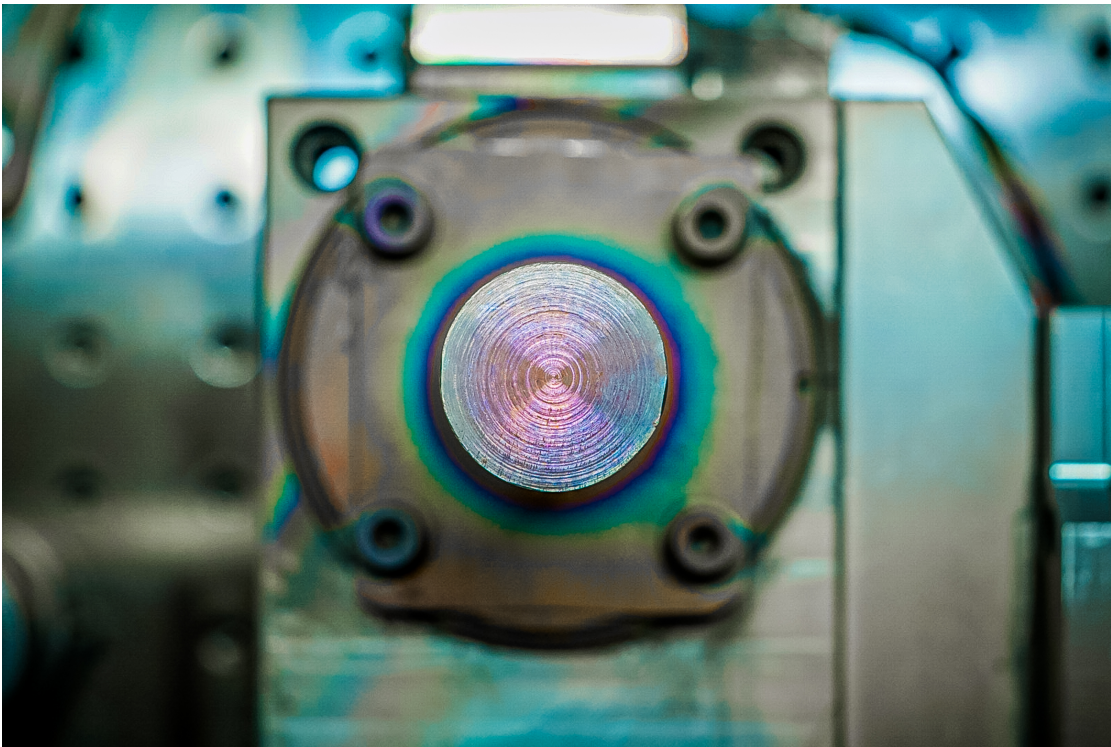
FIG. S2. NE $\mu$ C-induced fission cross section as function of the free muon kinetic energy  $E_\mu$  (blue axes and curve) and photo-fission cross section (red axes and curve) retrieved from Ref. 7 for  $^{238}\text{U}$ . X-axes are aligned considering the relation between the energy of the free muon and the nuclear transition, i.e.  $E_\mu = E_n - E_b^K$ . In this case,  $E_\gamma = E_n$  and  $E_b^K = 12.12$  MeV.



“Listen, Alěša”, Ivan began in a resolute voice, “if I am really able to care for the sticky little leaves I shall only love them, remembering you. It’s enough for me that you are somewhere here, and I shan’t lose my desire for life yet. Is that enough for you? Take it as a declaration of love if you like.”

— Fědor Dostoevskij, *The Brothers Karamazov*





Non Event Horizon.  
Simone Gargiulo

## 4 Nuclear excitations in optical-laser generated plasma

The advent of the high-intensity laser made it possible to study a variety of phenomena bridging nuclear and atomic physics [200, 201], as those seen in Chapter 1. Not only can the laser serve as a tool to alter the occurrence of these mechanisms, but it can also create the stage where these processes can enact. One possibility is the formation of a large concentration of free ions and electrons, formally a neutral plasma or cluster [202, 203], through ablation [204, 205] by shining high-intensity laser on nanoparticles or macroscopic solid targets. Plasma fulfills many of the conditions necessary for these processes to occur, at once. The simultaneous presence of free electrons, nuclei, vacancies, and broad spectra of X-ray photons, makes the study of low-energy nuclear excitations very appealing in this environment. This unique mixture allows for the coexistence of two or more processes competing for the excitation of nuclear levels, with the dominant one determined by plasma conditions and the specific isotope being studied. As a result, plasma could become the theater of simultaneous nuclear excitations due to direct photon absorption, NEEC [127, 144, 149, 150], NEET [127, 206], inverse electron bridge [207] and inelastic scattering of electrons with nuclei [201, 208, 209].

The study of nuclear excitation processes in a plasma scenario is of paramount significance in the determination of the population of long-lived excited nuclei in astrophysical plasma, as they can have a substantial impact on the nucleosynthesis pathways in stellar locations [210–212]. A long-standing dream was also the possibility of achieving population inversion between paired nuclear levels in stationary plasma, which was particularly captivating for the pursuit of  $\gamma$ -ray lasers [81, 82, 213]. However, despite numerous theoretical proposals, the experimental observation of many processes of nuclear excitation in the plasma environment is currently either lacking or controversial. One example, as discussed in detail in Chapter 2, is the experiment performed by Izawa and Yamanaka on laser-generated  $^{235}\text{U}$  plasma. Initially, the observed excitation was attributed to NEET [130] and later suggested to be due to NEEC [131]. However, a later repetition of the experiment produced no supporting evidence of the isomer excitation [137].

Even more conventional processes, such as direct photoexcitation, may still lack clear evidence in this chaotic scenario. In 1999, Andreev *et al.* [214] reported the observation of nuclear excitation of the low-lying  $^{181}\text{Ta}$  isomer (6.237 keV) in an expanding plasma generated by a femtosecond laser ( $\lambda = 600$  nm and  $\tau_{\text{pulse}} = 200$  fs). Their results have been redrawn and reported in Fig. 4.1, where the number of events as a function of time is shown. According to their calculations, direct photoexcitation was the dominant process leading to this nuclear transition [215]. In Ref. [214], the  $^{181}\text{Ta}$  signal was measured and compared to the signal originating from a tungsten target (W), which leads to comparable plasma properties, although the two nuclei have significantly different nuclear levels and half-lives (approximately 6  $\mu\text{s}$  for  $^{181}\text{Ta}$  and approximately 1 ns for W). The excess of 49 events in Ta compared to W was considered a sign of the achieved nuclear excitation. Nevertheless, the time dependence of both Ta and W signals are very similar and essentially overlap in case an aluminum foil is added as a filter. This could suggest that the time response is primarily dominated by the residual afterglow of the scintillator or by the recombination of the ions on the chamber walls (acting in the interval 1 – 100  $\mu\text{s}$  as stated in Ref. [214]). Since even subtle changes in surface properties or the presence of impurities can significantly affect the ablation process, it is desirable to obtain a clearer experimental observation that does not rely on excess counts. Specifically, it is hoped that a significant difference in the decay rates of the signals obtained with Ta and W targets could be observed.

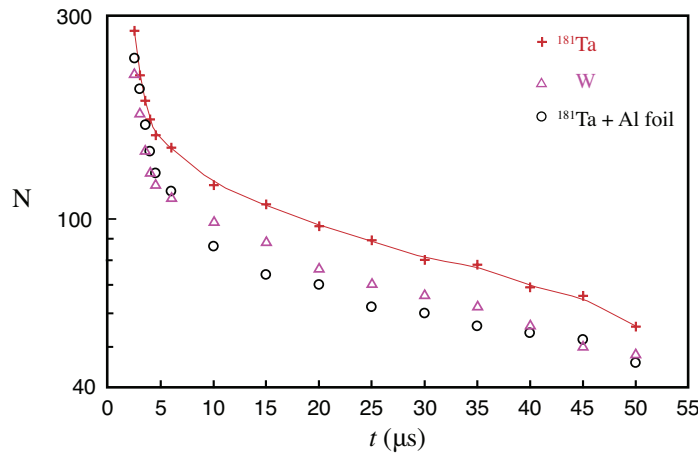


Figure 4.1: **Tantalum and tungsten deexcitation in laser-generated plasma experiments.** Total number (N) of detected events as a function of time  $t$  for  $^{181}\text{Ta}$  (+), W ( $\Delta$ ) and  $^{181}\text{Ta} + \text{Al foil}$  ( $\circ$ ) targets. The figure has been redrawn and adapted from Ref. [214].

Experimental challenges in the identification of the mechanisms leading to the nuclear transition are usually related to the fine-tuning of the plasma parameters and the possibility of having a sort of *switch* that could clearly enable one process over another. In many cases, a single mechanism dominates and leads to the excitation of the nuclei, making the identification clear. However, in other cases, this isolation is not possible,

and different processes may overlap and compete in intensity. This makes the theoretical description of the plasma crucial for the correct interpretation. An example of such a case is the competition between direct excitation through plasma thermal radiation and NEEC, as depicted in Fig. 4.2. This has been studied in detail for the isomer depletion of  $^{93m}\text{Mo}$  in Refs. [149, 150].

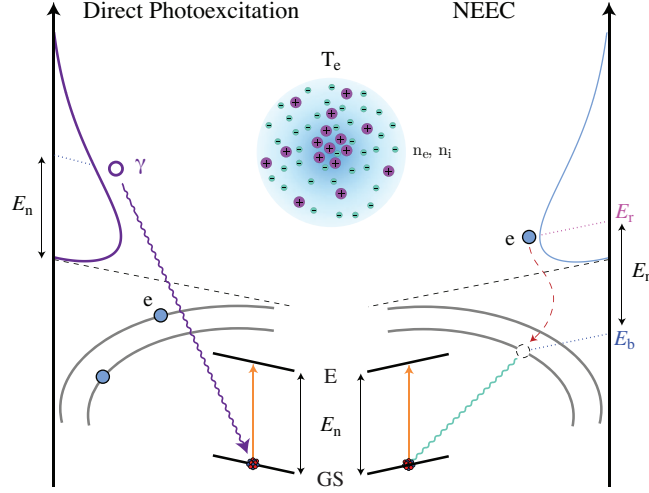


Figure 4.2: **Competition between direct photoexcitation through plasma resonant X-ray photons and NEEC in optical-laser generated plasma.** Excitation through NEEC is possible only if vacancies are present. Here, the kinetic energy of the free electron, able to induce the nuclear transition  $E_n$  through radiationless electron capture in a shell with binding energy  $E_b$ , has to satisfy the resonance condition  $E_r = E_n - E_b$ .  $T_e$ ,  $n_e$ , and  $n_i$  synthetically symbolize the plasma properties, which are the electron temperature, and electron and ion densities, respectively. The vacuum level is represented by the dashed black line. This image has been inspired by Fig. 1 of Ref. [152].

While the process of direct photoexcitation (DP) can take place independently from the charge state of the ions, NEEC requires the presence of vacant shells where the free electrons can be captured. A detailed description of the charge states of ions and populations of electronic levels becomes fundamental since, as seen in Chapter 2, NEEC is strongly influenced by the atomic surrounding. If we consider an expanding plasma in contrast to a confined one, the description of these properties becomes time-dependent. Currently, available particle-in-cell (PIC) simulations, such as EPOCH [216] and VLPL [217], or radiative-collisional codes as FLYCHK [218], only provide the average charge state of the ions during the expansion. Also for this reason, NEEC in expanding plasma has been extensively studied, assuming the electronic configuration to be in its ground state prior to the electron capture. A more detailed description of the properties of the plasma and their influence on the nuclear excitation rate would provide a more comprehensive understanding and potentially reveal interesting effects that have yet to be explored, as seen in the case of NEEC-EXI [119].

In this chapter, I will present the design and implementation of a table-top setup for studying nuclear excitations in expanding plasma generated by a femtosecond optical laser. Finally, I will discuss the outcomes of the experimental measurements.

Regardless of the excitation process, the sequence of events depicted in Fig. 4.3 can be imagined to occur. In principle, various pathways are available for the excitation of nuclei

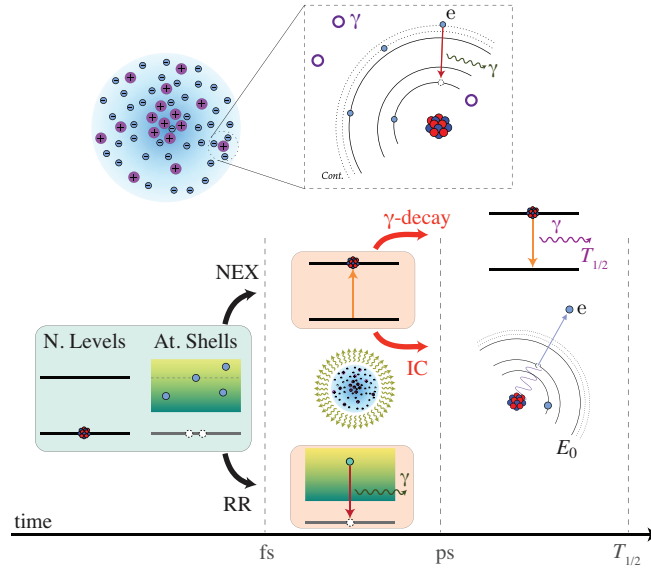


Figure 4.3: **Temporal discrimination between plasma radiation and delayed nuclear decay.** After laser ablation, atoms are in highly ionized states, while their nuclei are in the ground state. In this environment, the coexistence of photon and electron distributions can lead to nuclear excitation (NEX) through various mechanisms, such as direct photoexcitation, NEEC, inelastic scattering, NEET, and others. Regardless of the excitation process, the subsequent decay by  $\gamma$ -ray emission or IC will be delayed by the half-life  $T_{1/2}$  of the excited level. Thus, X-rays coming from the plasma radiation and  $\gamma$ -rays due to nuclear decay can be discriminated in the time domain.

in the presence of a population of photons and free electrons. These pathways can mainly be categorized as direct absorption of photons, atomically-assisted processes, or inelastic scattering with free electrons. Once the nucleus has been excited, it will generally decay by internal conversion (IC) or  $\gamma$ -emission with a characteristic time given by the half-life  $T_{1/2}$ . If an isomer is excited from the fundamental state, its subsequent nuclear decay would be delayed by at least several ns with respect to the background signal caused by plasma radiation and radiative recombinations (RR), which generally persist throughout the plasma lifetime (i.e., up to hundreds of ps). Although the different processes overlap in energy, their distinct timescales allow for the identification of nuclear decay through time-resolved spectroscopic techniques.

## 4.1 Search of suitable isotopes

As a first step, I performed an isotope scan using data from the IAEA's NDS LiveChart of Nuclides database [26]. The scan was based on criteria that favored isotopes with stable or long-lived ground states, a first excited state of a few tens of keV, and a half-life of the excited state higher than several tens of ps. These criteria were chosen for experimental feasibility and safety reasons, as well as to ensure detectability with commercially available X-ray detectors. More precisely, the following criteria were used:

- Transitions involving a nuclear excitation from the ground state;
- Stable or long-lived ground state ( $T_{1/2}^{\text{GS}} \geq 1 \times 10^3 \text{ y}$ );
- $E_n \leq 100 \text{ keV}$ ;
- Half-life of the excited state  $T_{1/2}^{\text{E}} \geq 100 \text{ ps}$ .

The outcomes of this investigation highlighted 80 isotopes and 507 nuclear transitions, shown in Fig. 4.4 with respect to the nuclear transition energy and in Fig. 4.5 with respect to the nuclear level half-life.

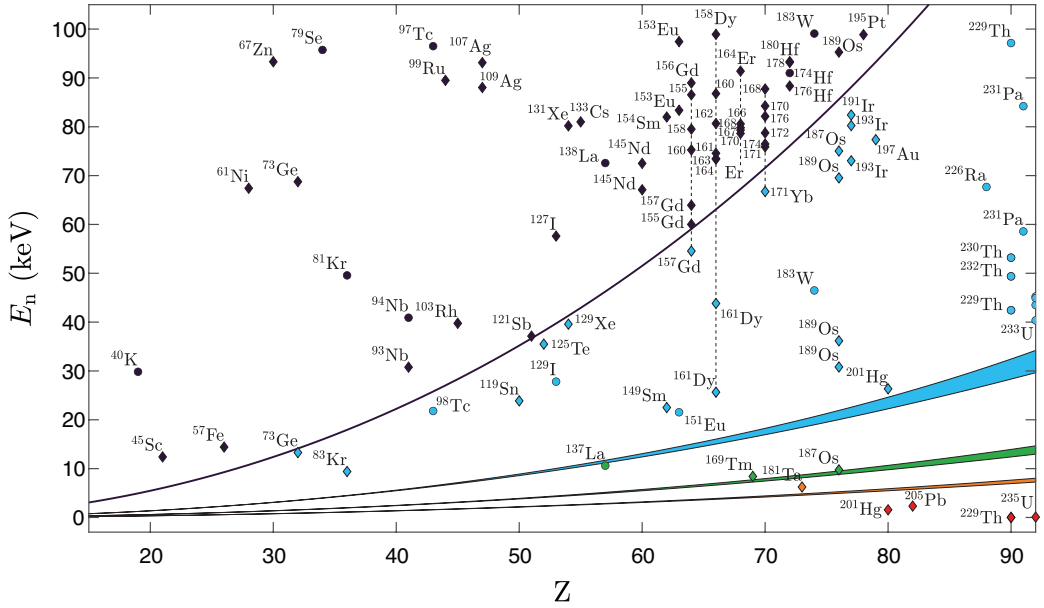


Figure 4.4: **Nuclear transition energies of the isotopes that meet the search criteria.** Excitation energies as a function of the atomic number  $Z$  for isotopes falling in the search criteria. The K (dark purple), L (blue), M (green), and N (orange) shell binding energies for bare nuclei have been included as colored lines. The vertical dashed lines group elements with the same atomic number. Diamond markers indicate stable ground states, and their color refers to the first inner shell for which NEEC is possible. The four isotopes noted with red markers are below the N shell binding energy.

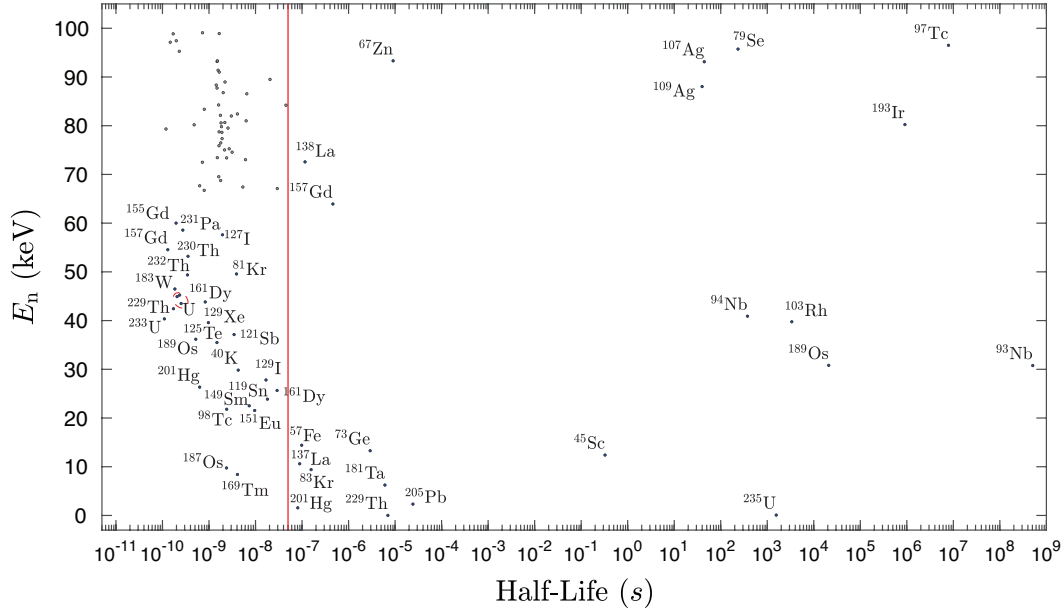


Figure 4.5: **Energy and half-life map of the isotopes meeting the search criteria.** The labels of the isotopes in the upper-left corner have been omitted to improve readability. The red line is at 50 ns.

Fig. 4.4 also includes the binding energies of K, L, M, and N shells in a bare nucleus – calculated using the Flexible Atomic Code (FAC) [177] – to aid in the selection of isotopes suitable for the NEEC process. As discussed in Chapter 2, exploring other experimental scenarios in which NEEC can take place could be invaluable in improving our understanding of this phenomenon, especially given the current controversy surrounding it. NEEC occurs only in shells with energy levels  $E_b$  below the nuclear transition energy  $E_n$ . The difference between these energies is known as the resonance energy  $E_r$  of the continuum free electron that must be captured. Since NEEC is a resonant process, its cross-section is proportional to  $\sigma_{\text{NEEC}} \propto 1/(E_n - E_b)$ , making it most efficient when there is a lower mismatch between these energies. The half-life ( $T_{1/2} = \hbar \ln 2 / \Gamma_n$ ) reported in Fig. 4.5 includes all decay channels, i.e.  $\Gamma_n = (1 + \alpha_{\text{IC}})\Gamma_\gamma$ , where  $\Gamma_n$  is the level width,  $\Gamma_\gamma$  is the width due to the  $\gamma$ -decay channel and  $\alpha_{\text{IC}}$  is the internal conversion coefficient for a neutral atom [219].

Whether an isomeric decay is within experimental reach depends on the choice of the detector and the nature of the measured signal, i.e., converted electrons or  $\gamma$ -rays. In designing our experiment, we have chosen the Timepix3 [220], provided with a time resolution of 1.25 ns and a pixel energy threshold of  $D_{\text{th}} = 3$  keV. Therefore, with this device, it is possible to detect electrons, ions, and photons, provided that the energy deposited in each individual pixel exceeds 3 keV. However, if we consider the delayed nuclear decay shown in Fig. 4.3, a difference arises in relation to the pixel threshold. While photons emitted in the decay have an energy of  $\hbar\omega = E_n$ , the energy of converted



electrons is reduced by the binding energy of the shell from which it originates, resulting in  $E_{ce} = E_n - E_b$ . This latter signal could potentially be lost for nuclear transitions close to the detector threshold ( $E_n \sim D_{th}$ ). On the other hand, in terms of time resolution, one can expect the signal generated by plasma radiation to be broadened by the charge transport along the thickness of the silicon chip. This broadening could be of several hundreds of ns, strongly inhibiting the detection of short-lived excitations. Therefore, we can safely disregard from further consideration all the states having  $T_{1/2} \leq 50$  ns, resulting in a reduced set of 22 isotopes. Considering the excitations that can be realistically achieved with the characteristics of our laser, we need to further constrain the selection to transitions with  $E_n \leq 20$  keV.

Several of these highlighted isotopes, including  $^{235}\text{U}$ ,  $^{57}\text{Fe}$ ,  $^{181}\text{Ta}$ ,  $^{201}\text{Hg}$ , have historical significance. The ease with which  $^{181}\text{Ta}$  can be found commercially makes it a suitable test sample to prototype our experiment and obtain a comparison with the experiment in Ref. [214].

$^{181}\text{Ta}$  has a  $9/2^-$  excited level connected to the ground state by a 6.237 keV dipolar (E1) transition and a half-life  $T_{1/2} = 6.05 \mu\text{s}$ : these properties are within reach for the Timepix3 detector. We have thus considered a solid cylinder with a 99.98% abundance of  $^{181}\text{Ta}$  as a target for the optical laser-plasma experiment. The choice of  $^{181}\text{Ta}$  also facilitates the selection of a control sample (i.e., one that will not produce a delayed nuclear decay) and makes it fall on tungsten (W). These two elements are consecutive on the periodic table and will have similar characteristics in terms of plasma formation and evolution. The composition of the W sample includes different isotopes according to their abundance.  $^{183}\text{W}$  has an abundance of about 14% and has the lowest excitation level at 46.48 keV with a half-life  $T_{1/2} = 0.185$  ns. The remaining three most abundant isotopes of W account for 85.57% and have their first excited state at about 100 keV with a half-life  $T_{1/2} \sim 1$  ns. This is the reason why the signals generated by the two targets are expected to differ significantly in the time domain, even in the remote eventuality to induce a nuclear excitation in W.

## 4.2 Design of the experimental setup

The experimental apparatus, depicted in Figure 4.6a, is situated within a square-shaped vacuum chamber with dimensions of  $41.0 \times 41.0 \times 42.6$  cm. The chamber is designed with a removable lid to facilitate access to its components. The sample is mounted on a four-axis motorized stage, which offers a rotational degree of freedom as its end effector. A laser source is directed into the chamber and subsequently redirected towards the sample through the use of a  $90^\circ$  off-axis parabolic mirror with a focal length of 10 cm. Upon illumination of the sample by a high-intensity fs-laser, a keV-hot plasma is generated. The plasma plume is known to expand predominantly along the surface normal of the laser incident point [221]. Therefore, the detector has been positioned in the direction of the plasma expansion. To mitigate the deposition of ablated nanoparticles on the optical components, a sapphire-windows motorized wheel, and a protection screen have been



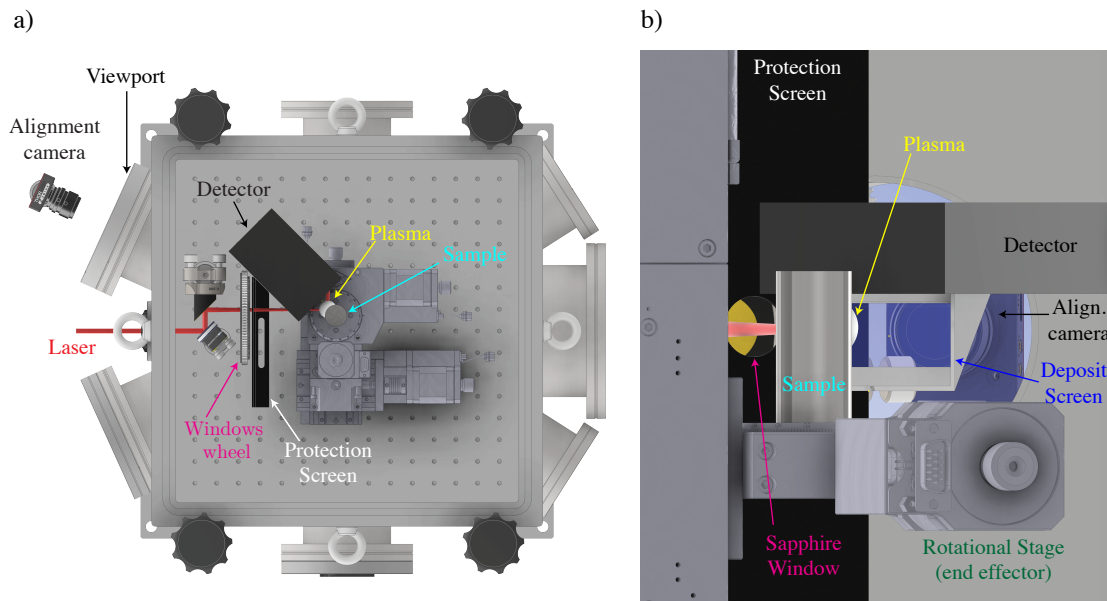


Figure 4.6: **3D CAD of the experimental setup designed at EPFL.** In (a) the top view of the 3D CAD of the vacuum chamber. The experimental setup includes a four-axis mechanical stage, a Timepix3 detector, a plane and a parabolic mirror, a protection screen, and a motorized sapphire-windows wheel, all housed inside the vacuum chamber. The sample is placed on the rotational stage, and the detector is positioned to face the plasma plume generated by the laser, which mostly develops along the surface normal of the laser incident point. An alignment camera – placed outside the chamber – looks at the sample through the viewport flange to aid in alignment. In panel (b), a closer view inside the chamber reveals the details of the protection and deposit screens. The protection screen has a through-hole covered by a sapphire window, which protects the parabolic mirror from deposition. The deposit screen is equipped with borosilicate glass, enabling inspection and alignment from the camera located outside the chamber.

installed between the target and the parabolic mirror. Over time, the sapphire window can accumulate nanoparticles due to ablation, which may reduce the effective laser intensity reaching the sample. However, the motorized wheel enables the replacement of the sapphire window without requiring the chamber to be vented, thereby prolonging the overall lifespan of the experiment. The TimePix3 CCD is protected by a 25 or 50  $\mu\text{m}$  layer of Kapton and placed downwards to prevent the deposition of nanoparticles on its surface. This layer has only a slight effect on X-ray absorption, while it can completely block electrons.

To address the potential issue of atomic recombinations happening at the chamber walls and to increase the detection angle of view for slower decaying nuclei (i.e., those that did not decay transiting from the target to the detector), a deposit screen has been incorporated into the design. This screen is placed in close proximity to the sample and directly on the detector itself, as illustrated in Fig. 4.6b. The central portion of this screen is composed of borosilicate glass, which facilitates visual inspection using the

external alignment camera, as explained in the following section. The cylindrical sample is mounted on a four-axis motorized stage, which continuously moves to keep a fresh portion of the sample at the focal point. The rotational and Z-axis stages are responsible for refreshing the surface, while the X and Y axes maintain the cylinder surface under laser focus during the ablation process. Fig. 4.7 shows pictures of the setup implemented at EPFL.

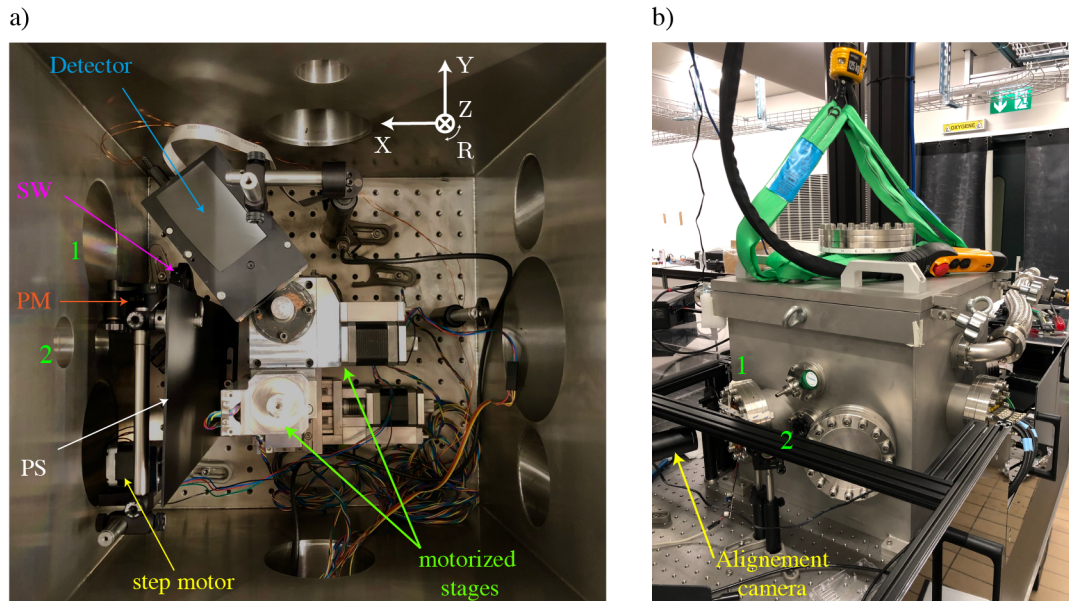


Figure 4.7: **Pictures of the experimental setup implemented at EPFL.** In panel (a), the inner part of the vacuum chamber is visible, with the sample placed on the four-axis motorized stage. The axes are labeled in white on the upper-right side. SW indicates the sapphire-windows wheel, PM the parabolic mirror, and PS the protection screen. In panel (b), the vacuum chamber is seen placed on the optical table. The lid is attached to a crane for lifting. The numbers (1) and (2) refer to the viewport flanges used for the alignment (1) and for the laser insertion (2).

### 4.3 Alignment procedure

Before the experiment can be performed, three crucial alignment steps must be completed. As it will become clearer in Section 4.4, these steps guarantee optimal plasma conditions – in terms of the highest temperature achievable – and stable counts throughout the measurements. These steps are:

1. Aligning the parabolic mirror to minimize monochromatic aberrations and produce the smallest possible focus spot;
2. Aligning the sample with the axis of rotation of the rotational stage;
3. Placing the sample surface at the laser focus and orienting it normally with respect

to the direction of the detector.

For step 1, a beam profiler is positioned on the rotational stage (in place of the sample) to visualize the beam size, as depicted in Figure 4.8a. Once the smallest focus has been obtained and the parabolic mirror aligned, the Y axis of the mechanical stage can be moved such that the laser spot hits the lateral edge of the beam profiler CCD (it is the beam profiler that moves and not the laser), as shown in Figure 4.8b. At this point, the external alignment camera can be used to store the position of the focus through a digital marker. To effectively observe the edge of the CCD through the alignment camera, it is necessary to remove the protective neutral density (ND) filter from the beam profiler. When the target sample is positioned in place of the beam profiler, the laser impinging on its surface will produce a reflection that can be seen by the alignment camera, as shown in Fig. 4.8c,d.

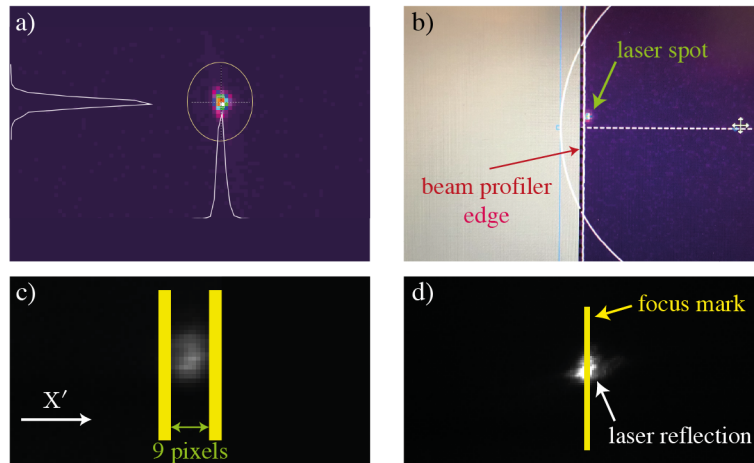


Figure 4.8: **Alignment procedures to be performed before the laser-plasma experiment.** In (a), the beam profiler is used to align the parabolic mirror to achieve the minimum possible spot size. (b) The Y-axis is driven to move the beam profiler so that the laser hits one of the lateral edges. (c) Laser reflection observed through the alignment camera during the self-alignment procedure. The spot has a width of 9 pixels ( $\sim 31 \mu\text{m}$ ), showing no further lateral movements. (d) The laser reflection is placed on the digital marker, which represents the position of the focus. This is achieved by driving the X and Y axes of the mechanical stage.

At this point, the cylindrical sample can be accurately aligned along the axis of rotation of the mechanical stage through the utilization of a pointed metal rod while continuously rotating the cylinder (step 2). This rod is placed on a micro-stage and is gradually brought closer to the sample as the procedure goes on. Initially, the cylinder is misaligned, and the rotation of the stage will result in a contemporaneous shift in X and Y of the sample with respect to the axis of rotation. These deviations in the XY plane, combined with the curved surface of the cylinder, will change the position

at which the laser impacts the target. As a consequence, the laser reflection observed through the alignment camera will begin to oscillate on the  $X'$  axis (defined in Fig. 4.8c), with decreasing swing amplitudes as the cylinder self-aligns. The process is terminated when the spot remains still or the motion is only a small fraction of its dimension. For example, as shown in Figure 4.8c, the reflection on the alignment camera has a size of 9 pixels, which corresponds to  $\simeq 31\ \mu\text{m}$ , and does not display any noticeable motion (boundaries are marked by the yellow vertical lines).

Finally, in step 3, the X and Y axes are adjusted to place the cylinder in the focus of the parabolic mirror. The position of the focus has been saved in step 1 through the digital marker, and now the laser reflection must be placed on it by moving the sample with the mechanical stages. In the scenario where the sample surface is flat and positioned perpendicular to the laser beam, a displacement of the sample along the Y-axis would not produce any change in the reflection observed by the alignment camera, as shown in Fig. 4.9. Therefore, the position along the X-axis of the mechanical stage at which the surface is in focus corresponds to a unique point on the  $X'$  axis of the alignment camera. This is why the digital marker is saved as a vertical line in Fig. 4.8d. In contrast, when using a cylindrical sample, both the X- and Y-axes need to be adjusted to position the cylinder at the laser focus. The impact point on the sample must be chosen in such a way that the detector is placed orthogonal to the surface. Furthermore, choosing an incident angle within the range of  $25^\circ$  to  $45^\circ$  decrease significantly – compared to normal incidence – the accumulation of nanoparticles on the sapphire window that protects the parabolic mirror.

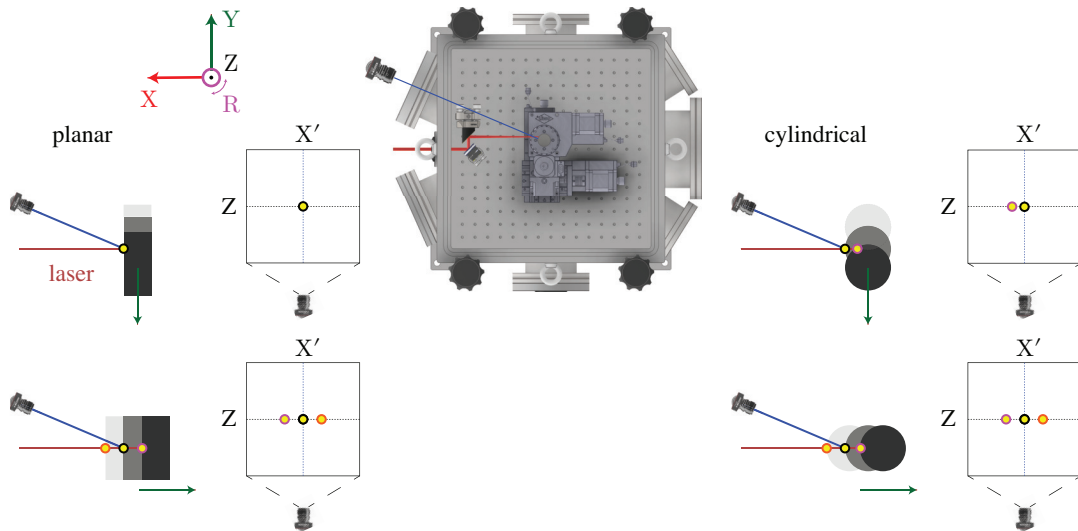


Figure 4.9: **Observing the movements of planar and cylindrical samples via the alignment camera.** The blue line represents the optical axis of the camera, while the red line the laser beam. X, Y, Z, and R refer to the axes of the mechanical stage, while  $X'$  is the horizontal axis of the alignment camera. The sample moves towards darker regions, as indicated by the green arrows.

#### 4.4 Plasma hydrodynamic model: properties and evolution of the optical-laser generated plasma

By examining the properties of the ultrafast laser used in these experiments [222], summarized in Table 4.1, it is possible to produce an initial estimate of the electron and photon distributions, along with the plasma temperature and other important plasma expansion properties. Even though the question may seem simple, the actual effects of

Table 4.1: **Characteristics of the laser pulse.**  $f_{\text{rep}}$  is the repetition rate, while  $D_{\text{focal}}$  is the FWHM of the laser spot at the focus of the parabolic mirror measured with a beam profiler.

$E_{\text{pulse}}$	1.25 mJ
$f_{\text{rep}}$	4 kHz
$P$	5 W
$D_{\text{focal}}$	10 $\mu\text{m}$
$\tau_{\text{pulse}}$	31 fs
$\lambda$	0.78 $\mu\text{m}$
$I\lambda^2$	$\sim 3 \times 10^{16} \text{ W cm}^{-2} \mu\text{m}^2$

short-pulse laser irradiation on a solid target are complex and cover a broad range of physical phenomena [202, 223–225]. When matter experiences interactions with high-intensity short-pulse lasers, regardless of the target type, a variety of physical processes take place, such as ionization, propagation, refraction, and plasma wave generation, as well as the consequent thermal and hydrodynamic expansion in the target material [202]. When the laser intensity exceeds  $I \geq 10^{16} \text{ W cm}^{-2}$ , many of these effects depend on the laser irradiance<sup>1</sup>  $I\lambda^2$ . Experimental findings showed that collisional absorption alone could not have accounted for the significant rise in plasma temperature at irradiance conditions  $I\lambda^2 \geq 10^{15} \text{ W cm}^{-2} \mu\text{m}^2$ . In fact, at these irradiance levels, the rate of electron-ion collisions ( $v_{\text{ei}} \sim I^{-3/4}$ ) diminishes significantly. This reduction is further amplified as the quiver velocity, which is the velocity with which the laser field drags the electrons, becomes comparable to the thermal velocity [202].

Therefore, other “collisionless” mechanisms needed to be identified in order to explain the high absorption observed in this regime. One such process is the resonance absorption in the case of obliquely incident laser fields [223, 226, 227]. Here, the component of the field that is perpendicular to the density profile has the potential to resonantly excite a plasma wave – oscillations of the free electrons – along its direction. This resonance appears as a singularity in the analytical expression of the electric field, which

<sup>1</sup>Generally, the irradiance represents a radiant flux per unit surface; hence it is expressed in units of  $\text{W m}^{-2}$ . Here, we call irradiance the quantity  $I\lambda^2$  in accordance with Ref. [202].

is located at the critical surface. The critical surface is defined as the surface where the electron density ( $n_e$ ) equals the critical density ( $n_c = \epsilon_0 m_e \omega^2 / e^2$ ) such that the field cannot penetrate it. However, this resonance breaks for sharp-edge density profiles, as the amplitude of these oscillations ( $v_{\text{os}}/\omega$ ) exceeds the electron density gradient length ( $L$ ). Another collisionless process was proposed by Brunel in 1987 [228]. In his model, the laser field directly pulls electrons away from the surface into the vacuum during the first half-cycle. During the second half-cycle, the electrons are driven back into the plasma with a velocity of approximately  $v \sim v_{\text{osc}} = eE/m_e\omega$ , where  $v_{\text{osc}}$  refers to the quiver velocity. This process was found to be more efficient than resonant absorption when ( $v_{\text{os}}/\omega L > 1$ ), as it might be in the case of a femtosecond laser hitting a solid target. Specifically, for  $\tau_{\text{pulse}} \sim 100$  fs, the target is heated at a rate faster than the hydrodynamic expansion timescale. Consequently, the plasma medium retains its initial sharp solid-state density profile throughout the duration of the laser pulse [223].

In this collisionless heating regime, the scaling of the electron temperature with respect to the laser irradiance can be inferred through models or electrostatic PIC simulations [229, 230]. In this context, we will examine the two scaling laws (SL) outlined in Ref. [202], which are the following:

$$T_e \text{ (keV)} = \begin{cases} 3.6 I_{16} \lambda_\mu^2 & \text{SL1} \\ 8 \sqrt[3]{I_{16} \lambda_\mu^2} & \text{SL2} \end{cases} \quad (4.1)$$

These scaling laws, along with the hydrodynamic model presented in this section, have been applied in Refs. [149, 150] to determine the rates of nuclear excitation through photon absorption and NEEC in plasma generated by optical lasers. The intensity  $I_{16}$  in Eq. 4.1 is expressed in units of  $10^{16} \text{ W cm}^{-2}$ , while the wavelength  $\lambda_\mu$  is expressed in  $\mu\text{m}$ . The plasma volume,  $V_p$ , generated by laser ablation can be described as a function of the focal radius,  $R_{\text{focal}}$ , and the pulse duration,  $\tau_{\text{pulse}}$ , as follows:

$$V_p = \pi R_{\text{focal}}^2 d_p = \pi R_{\text{focal}}^2 c \tau_{\text{pulse}}. \quad (4.2)$$

Here,  $d_p$  represents the plasma thickness, which can be estimated as  $c \cdot \tau_{\text{pulse}}$ , with  $c$  being the speed of light in vacuum. The total number of electrons present in the neutral plasma,  $N_e$ , and the electron density,  $n_e$ , can be estimated as follows:

$$N_e = f \frac{E_{\text{pulse}}}{T_e} \quad \text{and} \quad n_e = \frac{N_e}{V_p}. \quad (4.3)$$

The number of free electrons in the plasma is determined by the absorption coefficient  $f$ , which – for the previously mentioned irradiance and steep density profiles – is approximately 0.11 [231]. When using the first scaling law (SL1), the number of free electrons is independent of the pulse energy  $E_{\text{pulse}}$ , as long as  $f$  remains relatively constant. By using the free-electron model, the chemical potential  $\mu$  – appearing in the Fermi-Dirac distribution  $f_{\text{FD}}$  – can be obtained by imposing that the total number of

electrons in the plasma is equal to  $n_e$ :

$$\int_0^\infty g_e(E_e) f_{\text{FD}}(E_e) dE_e = n_e, \quad (4.4)$$

and considering  $E_e \gg \mu$ , it results:

$$\mu = T_e \ln \left( \frac{2n_e}{\gamma \sqrt{\pi} (T_e)^{3/2}} \right). \quad (4.5)$$

The electron flux  $\phi_e$  within the plasma is defined as follows:

$$\phi_e(E_e) = g_e(E_e) f_{\text{FD}}(E_e) v(E_e). \quad (4.6)$$

In this expression,  $g_e$  represents the electron density of states,  $f_{\text{FD}}$  represents the Fermi-Dirac distribution, and  $v$  represents the electron speed; all these variables are functions of the electron energy  $E_e$ . Under the assumption of thermodynamic equilibrium (TDE) between the photon and electron gases, the photon flux can be defined using a blackbody distribution as follows [149, 150]:

$$\phi_\gamma^{\text{TDE}}(E_\gamma, T_e) = \epsilon c g_\gamma(E_\gamma) f_{\text{BE}}(E_\gamma, T_e). \quad (4.7)$$

Here,  $g_\gamma$  represents the photonic density of states and  $f_{\text{BE}}$  represents the Bose-Einstein distribution [232]. Compared to the model presented in Refs. [149, 150], the emissivity  $\epsilon$  has been introduced to impose the energy balance between the electron and photon gases. The energy contained in the photon gas is otherwise unrelated to the energy of the pulse and might exceed it. Both electron ( $\phi_e$ ) and photon ( $\phi_\gamma$ ) fluxes are expressed in units of  $\text{cm}^{-2} \text{eV}^{-1} \text{s}^{-1}$ . Another possibility is to consider the bremsstrahlung process as responsible for the origin of photons in the plasma. In this case, the emitted flux can be defined as [127]:

$$\phi_\gamma^{\text{B}}(E_\gamma, E_e, T_e, n_e) = t_i \left( \frac{d\sigma_{\text{B}}(E_\gamma, E_e)}{dE_\gamma} \right) \phi_e(E_e, T_e, n_e) \quad (4.8)$$

where  $d\sigma_{\text{B}}(E_\gamma, E_e)/dE_\gamma$  is the differential cross-section of the bremsstrahlung emission of photons having energy  $E_\gamma$  by electrons of energy  $E_e$  and  $t_i$  is the target thickness expressed in  $\text{atoms} \cdot \text{m}^{-2}$ . The values for the differential cross-section of Ta can be found in Ref. [233]. The target thickness  $t_i = n_i R$  is given in terms of ion density  $n_i$  and plasma radius  $R$ . The two photon fluxes  $\phi_\gamma^{\text{TDE}}$  and  $\phi_\gamma^{\text{B}}$  are shown in Fig. A.5 calculated in the case outlined by SL1.

To determine the plasma lifetime, an estimate of the charge state distribution is necessary. This feature is also crucial for identifying the shells that can be targeted for electron capture. The radiative-collisional code FLYCHK [218] can be employed for this purpose once  $T_e$  and  $n_e$  are provided as input, assuming the plasma to be in its

non-local thermodynamical equilibrium (non-LTE<sup>II</sup>) steady-state. Although steady-state conditions may not be reached for such short laser pulses (tens of fs), this approach can still serve to obtain an initial estimate of several properties of the plasma. The results obtained from FLYCHK can be used to calculate the ion average charge state  $\bar{Z}$ , as follows:

$$\bar{Z} = \sum_q (q P_q). \quad (4.9)$$

In this context, the variable  $q$  is used to denote the ion charge state, while  $P_q$  represents the probability of its presence in the plasma. The ion density ( $n_i$ ) and the number of ions in the plasma ( $N_i$ ) can be evaluated as follows:

$$N_i = n_i V_p \quad \text{and} \quad n_i = \frac{n_e}{\bar{Z}}. \quad (4.10)$$

To compute the hydrodynamic expansion of plasma, it is necessary to consider the energy conservation during collisions of cold ions and hot electrons in the expanding gases. The expansion rate is governed by the following non-linear differential equation, which is detailed in Ref. [203]:

$$\left(\frac{dR}{dt}\right)^2 = \frac{3 T_{e0} R_0^2 Z}{M_i} \left(1 - \frac{R_0^2}{R^2}\right), \quad (4.11)$$

under the assumption that the initial velocity of the plasma is equal to zero and that no electrons definitely escape from it. It is worth noting that the charge state  $Z$  in Eq. 4.11 hides an implicit dependence on the plasma radius  $R$ . By taking the smaller of the values between  $R_{\text{focal}}$  and  $d_p$  as the initial plasma radius  $R_0$ , a lower limit estimate can be obtained for the plasma lifetime ( $\tau_{\text{plasma}}$ ). The plasma lifetime is defined as the duration required by the plasma to double its initial radius and in our scenario, where  $R_{\text{focal}} \leq d_p$ , it can be expressed as:

$$\tau_{\text{plasma}} = R_{\text{focal}} \sqrt{\frac{m_i}{T_e \bar{Z}}}, \quad (4.12)$$

that is an approximate solution of Eq. 4.11. The electron temperature evolution during this adiabatic<sup>III</sup> expansion can be expressed as follows:

$$T_e = T_{e0} \left(\frac{R_0}{R}\right)^2. \quad (4.13)$$

In the following, I will discuss the implementation of this hydrodynamic model to the  $^{181}\text{Ta}$  target and experimental setup that has been presented in this Chapter. However, it is worth mentioning that a more detailed description could be made by employing PIC simulations. The duration of the laser pulse, as reported in Table 4.1, is measured

<sup>II</sup>The non-LTE solutions are the most general descriptions of the thermodynamic conditions and population distribution of the plasma since the atomic processes are considered in detail through the solution of rate matrices [218].

<sup>III</sup>Thus, this model does not account for the additional power radiated during the plasma expansion.



at the immediate output of the laser. Before interacting with the sample, the laser beam is directed through four low-GDD ultrafast mirrors, a parabolic mirror, and two sapphire windows (yielding a total thickness of 5.5 mm). The pulse broadening is primarily attributed to the sapphire windows, as the GVD for sapphire is  $49.9 \text{ fs}^2$ , resulting in a broadened pulse duration of  $\tau_{\text{pulse}} \simeq 40 \text{ fs}$  and a laser irradiance of  $I\lambda^2 = 2.42 \times 10^{16} \text{ W cm}^{-2} \mu\text{m}^2$ . The outcomes of this analysis, for both scaling laws, are presented in Table 4.2 and are found to be in agreement with each other. Regardless of

	SL1	SL2
$T_e$	8.71 keV	10.74 keV
$n_e$	$1.05 \times 10^{20} \text{ cm}^{-3}$	$8.48 \times 10^{19} \text{ cm}^{-3}$
$n_i$	$1.86 \times 10^{18} \text{ cm}^{-3}$	$1.44 \times 10^{18} \text{ cm}^{-3}$
$\bar{Z}$	56.18	58.89
$\tau_{\text{plasma}}$	9.79 ps	8.61 ps
$\phi_e^{\text{max}}$	$2.72 \times 10^{25} \text{ cm}^{-2} \text{ s}^{-1} \text{ eV}^{-1}$	$1.98 \times 10^{25} \text{ cm}^{-2} \text{ s}^{-1} \text{ eV}^{-1}$
$\phi_\gamma^{\text{TDE,max}}$	$5.40 \times 10^{25} \text{ cm}^{-2} \text{ s}^{-1} \text{ eV}^{-1}$	$3.60 \times 10^{25} \text{ cm}^{-2} \text{ s}^{-1} \text{ eV}^{-1}$
$\phi_\gamma^{\text{B,max}}$	$6.75 \times 10^{18} \text{ cm}^{-2} \text{ s}^{-1} \text{ eV}^{-1}$	$4.31 \times 10^{18} \text{ cm}^{-2} \text{ s}^{-1} \text{ eV}^{-1}$

Table 4.2: **Application of the plasma hydrodynamic model to our experimental conditions in case of a  $^{181}\text{Ta}$  sample.** Plasma properties obtained using the scaling laws (SL) outlined in Eq. 4.1 and the laser parameters reported in Table 4.1.  $\phi_\gamma^{\text{TDE,max}}$  refers to the maximum (peak) photon flux obtained using the blackbody distribution of Eq. 4.7, while  $\phi_\gamma^{\text{B,max}}$  represents the maximum photon flux originated by the bremsstrahlung process described in Eq. 4.8.

the model chosen, it is crucial to make at least a consideration. In some circumstances, electron and photon fluxes might differ significantly by several orders of magnitude – generally to the advantage of photons [150]. Nuclear excitation processes, such as NEEC and direct photoexcitation, can occur as long as free electrons, vacancies, and photons are available. Since both electrons and photon fluxes persist for a duration assumed to be of the order of  $\tau_{\text{plasma}}$ , the NEEC cross-section must be large enough to overcome this difference in the fluxes to become the dominant process. Otherwise, the NEEC excitation rate can be enhanced by supplying an external electron beam. In the case under study, the electron and photon fluxes are comparable in the case of TDE, while they differ significantly if the bremsstrahlung model is used. Which model will correctly represent the experimental conditions will depend on the dynamics and conditions of plasma formation and on the electron density (i.e., overdense or underdense plasma) [234, 235]. TDE conditions can be considered as the best-case scenario (upper limit), and consequently, so will the resulting photoexcitation rate. The results of the

hydrodynamic model, when applied in accordance with scaling law SL1, are presented in Fig. 4.10. Specifically, Fig. 4.10a displays the ion charge state distribution probability ( $P_q$ ) calculated using FLYCHK. The temporal evolution of the plasma temperature and

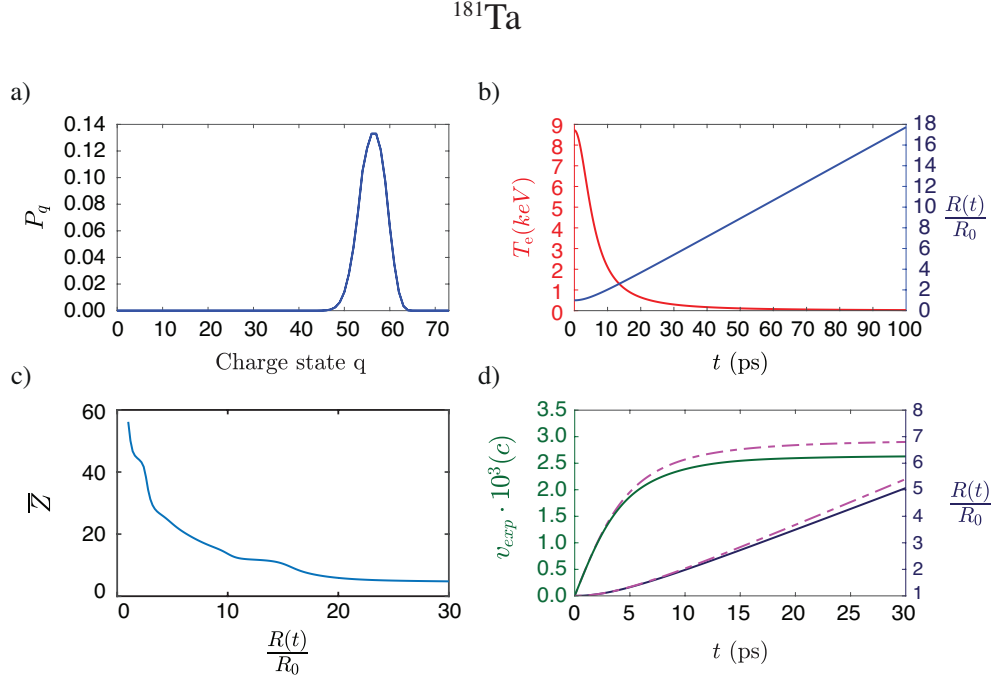


Figure 4.10: **Plasma hydrodynamic model applied to the case of  $^{181}\text{Ta}$  interacting with a femtosecond laser.** Panel (a) displays the ion charge state distribution calculated using the FLYCHK code. The temporal evolution of both the plasma temperature (in red) and radius (in blue) is displayed in panel (b). The average charge state as a function of the plasma radius  $R(t)$ , and thus implicitly as a function of time, is presented in panel (c). Finally, panel (d) displays the expansion velocity  $v_{\text{exp}}$  (in green), normalized to the speed of light, and the radius (in blue) obtained as solutions of Eq. 4.11, employing the average charge state  $Z = \bar{Z}(R)$  presented in panel (c). To facilitate comparison, the solutions obtained using a constant average charge state of  $Z=56.18$  are displayed in dashed magenta lines.

its radius is depicted in Fig. 4.10b, assuming a constant value of  $Z = \bar{Z} = 56.18$  over the expansion. This approximation enables the calculation of the plasma lifetime as defined in Eq. 4.12. However, this picture is not entirely representative of reality, as illustrated in Fig. 4.10c, which shows the evolution of the average charge state throughout the plasma expansion. This evolution has been computed using FLYCHK, with  $n_i$  and  $T_e$  provided as input for each value of the radius  $R(t)$ . In performing these calculations, it was assumed that the steady state for atomic processes is reached at each time instant over the expansion, which generally is slower and can last from tens to hundreds of ps [149, 150]. As anticipated, highly ionized atoms are predominantly present for  $R(t)/R_0 \leq 2$ , with a significant drop in  $\bar{Z}$  in the first hundreds of picoseconds. Fig. 4.10d presents the

solutions of Eq. 4.11 in terms of the radius and velocity of expansion calculated with two approaches: one using the time-dependent average charge state  $Z = \bar{Z}(R)$  of Fig. 4.10c (solid lines), and the other obtained assuming  $Z = \bar{Z} = 56.18$ . Although differences are evident, the approximate solutions ( $Z = \bar{Z} = 56.18$ ) presented in Fig. 4.10b are reasonably accurate.

The calculated average charge state of the  $^{181}\text{Ta}$  ions is estimated to be around  $\bar{Z} \sim 5$  using the SL1 model and  $\bar{Z} \sim 11$  using SL2 at  $R(t)/R_0 = 30$ , where the expansion velocity remains relatively constant, as shown in Fig. 4.10d. This indicates that in both models, the M shell is expected to be completely filled in hundreds of picoseconds or faster, whereas the N shell is only expected to be partially filled within the same time. Therefore, the models suggest that no increase (or only marginal) in the nuclear lifetime should be observed, as these two shells play a crucial role in determining the overall internal conversion coefficient  $\alpha_{\text{IC}} = 70.5$  [236, 237]. This conclusion is in contrast with the findings presented in the study by Andreev et al. [214], where the measured time decay – depicted in Fig. 4.1 – necessitates a ten-fold enhancement in the nuclear half-life to be attributed to the first excited level of  $^{181}\text{Ta}$ . With this being said, a comprehensive PIC simulation will be useful to better describe the evolution and the relative charge state of the ions throughout the plasma expansion.

By following the hydrodynamic model, it is possible to calculate the nuclear excitation rate resulting from the resonant absorption of a photon within the plasma with energy  $E_\gamma = \hbar ck = E_n$  for the TDE and bremsstrahlung models, as follows:

$$\lambda_\gamma^{\text{TDE}} = \int \sigma_\gamma(E_\gamma) \phi_\gamma^{\text{TDE}}(E_\gamma, T_e, n_e) dE_\gamma, \quad (4.14)$$

$$\lambda_\gamma^{\text{B}} = \int \int \sigma_\gamma(E_\gamma) \phi_\gamma^{\text{B}}(E_\gamma, E_e, T_e, n_e) dE_\gamma dE_e. \quad (4.15)$$

Here,  $\sigma_\gamma$  is the photoexcitation cross-section and it is expressed as [238]:

$$\sigma_\gamma(E_\gamma) = \frac{\pi^2 \hbar}{k^2} W_\gamma^{\text{E} \rightarrow \text{G}} \frac{2J_{\text{E}} + 1}{2J_{\text{G}} + 1} L_{\text{r}}(E_\gamma - E_n). \quad (4.16)$$

This equation links the photoexcitation cross-section  $\sigma_\gamma$  (which has a Lorentzian shape  $L_{\text{r}}$  centered at  $E_n$ ) to the corresponding decay rate  $W_\gamma^{\text{E} \rightarrow \text{G}}$  from the excited (E) to the ground (G) nuclear state, having angular momenta  $J_{\text{E}}$  and  $J_{\text{G}}$ , respectively. The decay rate  $W_\gamma^{\text{E} \rightarrow \text{G}}$  is defined according to Eq. 1.16 for the electric and magnetic multipolar radiations. In first approximation, assuming a constant and homogeneous electron temperature  $T_e$  and density  $n_e$  over the plasma lifetime  $\tau_{\text{plasma}}$ , the number of excited nuclei per laser pulse can be calculated as:

$$N_{\text{exc}} = N_i \lambda_\gamma \tau_{\text{plasma}}. \quad (4.17)$$

Subsequently, as illustrated in Fig. 4.3, the excited nucleus can decay via either  $\gamma$ -ray emission or internal conversion (IC). It is worth noting that the energy range of the

converted electrons ejected from the M and N-shells – which contribute significantly to  $\alpha_{IC}$  – resulting from the nuclear decay of the first isomeric state of  $^{181}\text{Ta}$  are between 3.5 keV and 6.2 keV [219]. This range is above the detector threshold of  $D_{th} = 3$  keV. However, since we have protected the TimePix3 CCD with a Kapton foil to prevent deposition, we can only be sensitive to  $\gamma$ -decays. Therefore, the number of radiative deexcitations can be estimated as:

$$N_{deexc}^{\gamma} = \frac{1}{1 + \alpha_{IC}} N_{exc}. \quad (4.18)$$

Fig. 4.11 shows the photoexcitation rate  $\lambda_{\gamma}^{\text{TDE}}$  calculated for the E1 nuclear transition from the ground to the first isomeric state of  $^{181}\text{Ta}$  – located at 6.237 keV – as a function of the plasma temperature  $T_e$ , assuming the TDE photon distribution  $\phi_{\gamma}^{\text{TDE}}$  of Eq. 4.7. For comparison, the photoexcitation rate obtained using the bremsstrahlung photon flux distribution of Eq. 4.8 – shown in Fig. A.5 – is equal to  $\lambda_{\gamma}^{\text{B}} = 5.84 \times 10^{-11} \text{ s}^{-1}$  at  $E_{\gamma} = E_n$ .

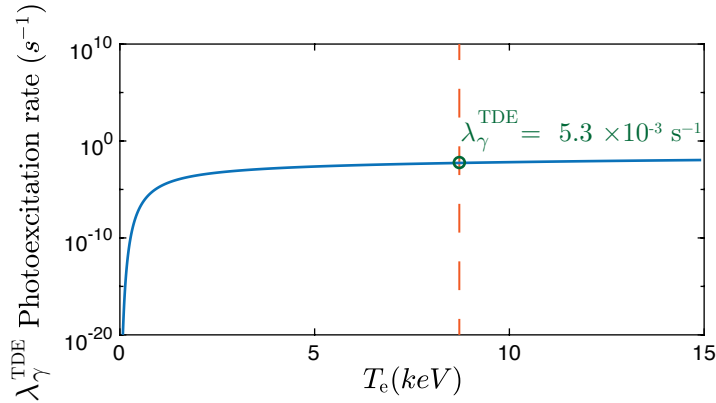


Figure 4.11: **Isomer photoexcitation rate as a function of the plasma temperature assuming TDE.** Photoexcitation rate  $\lambda_{\gamma}^{\text{TDE}}$  of the 6.237 keV isomer in  $^{181}\text{Ta}$  for plasma temperatures  $T_e \leq 15$  keV. The vertical dashed line corresponds to  $T_e = 8.71$  keV, which is the plasma temperature obtained with SL1. The photon flux of Eq. 4.7 has been used for this calculation.

The outcomes of the SL1 – when used in combination with the TDE assumption – indicate that each laser pulse results in approximately  $N_{exc} \sim 9 \times 10^{-5}$  excited nuclei and in  $N_{deexc}^{\gamma} \sim 1.27 \times 10^{-6}$  nuclei decaying by radiative emission. At a laser repetition rate of  $f_{rep} = 4$  kHz, the rate of formation of excited nuclei and the corresponding rate of deexcitation are  $N_{exc}^{rep} \sim 0.36 \text{ s}^{-1}$  and  $N_{deexc}^{\gamma, rep} \sim 5.09 \times 10^{-3} \text{ s}^{-1}$ , respectively. To provide a term of comparison, it is valuable to estimate the total number of photons emitted by the plasma surface throughout its lifetime as:

$$N_{plasma}^{\gamma} = S_p \tau_{plasma} \int \phi_{\gamma}(E_{\gamma}, T_e, n_e) dE_{\gamma}, \quad (4.19)$$

where  $S_p$  is the plasma radiating surface, which is assumed to be cylindrical with a radius  $R_{\text{focal}}$  and thickness of  $d_p$ . By restricting the integration between  $D_{\text{th}} = 3 \text{ keV} \leq E \leq 50 \text{ keV}$ , one obtains  $N_{\text{plasma}}^\gamma \sim 4 \times 10^{13}$ . Therefore, the efficiency ratios are  $N_{\text{exc}}/N_{\text{plasma}}^\gamma \sim 10^{-18}$  and  $N_{\text{deexc}}^\gamma/N_{\text{plasma}}^\gamma \sim 10^{-20}$ . A similar order of magnitude for  $N_{\text{plasma}}^\gamma$  could have been obtained by starting with the Stefan–Boltzmann blackbody emissive power  $P = \epsilon\sigma T_e^4$  [239] radiated by the plasma surface  $S_p$  over a time  $\tau_{\text{plasma}}$  and then normalizing for the weighted average energy of the emitted photons. For simplicity, the values discussed here have been reported in Table 4.3 for the TDE case and in Table 4.4 for the bremsstrahlung model.

	Per laser pulse	$\cdot \times f_{\text{rep}} \text{ (s}^{-1}\text{)}$
$N_{\text{exc}}^{\text{TDE}}$	$9.10 \times 10^{-5}$	0.36
$N_{\text{deexc}}^{\gamma, \text{TDE}}$	$1.27 \times 10^{-6}$	$5.09 \times 10^{-3}$
$N_{\text{plasma}}^{\gamma, \text{TDE}}$	$4.34 \times 10^{13}$	$1.73 \times 10^{17}$

Table 4.3: **Number of excited nuclei, deexcitations, and photons in plasma, considering the TDE case.** This table reports the number of excited nuclei ( $N_{\text{exc}}$ ), the number of nuclei that deexcite through  $\gamma$ -decay ( $N_{\text{deexc}}^\gamma$ ), and the total number of photons radiated by the plasma ( $N_{\text{plasma}}^\gamma$ ) in the energy range  $3 \text{ keV} \leq E \leq 50 \text{ keV}$ . These values have been calculated per laser pulse and then scaled by the repetition rate  $f_{\text{rep}}$ .

	Per laser pulse	$\cdot \times f_{\text{rep}} \text{ (s}^{-1}\text{)}$
$N_{\text{exc}}^{\text{B}}$	$1 \times 10^{-12}$	$4 \times 10^{-9}$
$N_{\text{deexc}}^{\gamma, \text{B}}$	$1.4 \times 10^{-14}$	$5.6 \times 10^{-11}$
$N_{\text{plasma}}^{\gamma, \text{B}}$	$3.98 \times 10^5$	$1.59 \times 10^9$

Table 4.4: **Number of excited nuclei, deexcitations, and photons in plasma, considering bremsstrahlung as the origin of the photons gas.** This table reports the number of excited nuclei ( $N_{\text{exc}}$ ), the number of nuclei that deexcite through  $\gamma$ -decay ( $N_{\text{deexc}}^\gamma$ ), and the total number of photons radiated by the plasma ( $N_{\text{plasma}}^\gamma$ ) in the energy range  $3 \text{ keV} \leq E \leq 50 \text{ keV}$ . These values have been calculated per laser pulse and then scaled by the repetition rate  $f_{\text{rep}}$ .

## 4.5 Experimental prototyping

In the early phases of the experimental setup characterization, measurements were conducted using the AdvaPix TPX3 [240] in the configuration depicted in Fig. 4.7. The spectra acquired through the “spectral imaging” function over a duration of 500s with a laser power of 5 W and repetition rate of 4 kHz is shown Fig. 4.12a.

The acquired spectra exhibit an excellent match with the black-body distribution  $B_\lambda$  for

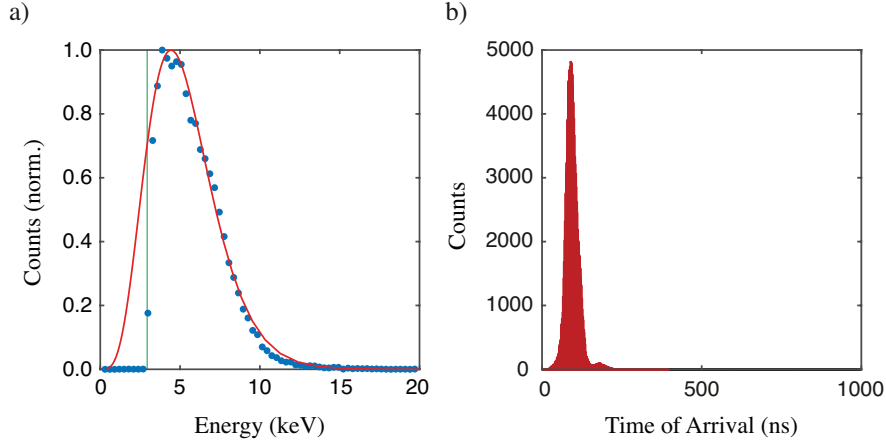


Figure 4.12: **Experimentally measured plasma radiation as a function of energy and time.** Panel (a) shows the spectra acquired with a laser power of 5 W (blue dots) and the relative Planck's  $B_\lambda$  distribution fit with  $T_\gamma = 0.89$  keV (red curve). The frequency parametrization  $B_\nu$  yields a higher temperature  $T_\gamma = 1.6$  keV, but is less accurate in fitting the measured spectrum. A green vertical line has been included to indicate the pixel threshold  $D_{th}$  of 3 keV. In panel (b), the histogram for each recorded event is shown with respect to the time of arrival. This histogram has been extracted from a very narrow integration window.

energies greater than 3 keV. This energy corresponds to the pixel threshold  $D_{th}$  (denoted by a green vertical line), below which the detector disregards the event. The fit reveals a temperature of the distribution of  $T_\gamma = 0.89$  keV. The measured temperature  $T_\gamma$  is much lower than the electron temperature  $T_e$  estimated based on the scaling laws presented in Table 4.2. This can be attributed mainly to three factors. (i) Firstly, the measured radiation results from averaging over the plasma lifetime. (ii) Additionally, the photon gas might not be in thermal equilibrium with the electron gas, in opposition to the hypothesis of the TDE case. (iii) Finally, the interplay between the pixel threshold and charge sharing, as discussed in the literature by Jakubek *et al.* [241], can result in the loss of events, leading to distortions in the measured spectrum and in a lower measured  $T_\gamma$ . Fig. 4.12b displays a histogram of the recorded events as a function of their time of arrival (ToA) relative to the laser trigger. Despite the plasma having an emission lifetime on the order of hundreds of picoseconds, the trace left on the detector is approximately 40 ns in FWHM and has a total temporal spread of 236 ns. The response observed in these measurements, which in the first approximation is attributed solely to plasma radiation, shows that after a few hundreds of ns the initial plasma afterglow does not produce any appreciable effect. This is particularly important since the ToA is a critical observable that enables differentiation between plasma radiation and nuclear decay. These measurements also confirm – as initially expected – that despite the time resolution of the detector being of about 1.25 ns, only nuclear decays that have  $T_{1/2} \geq 100$  ns could be easily detected.

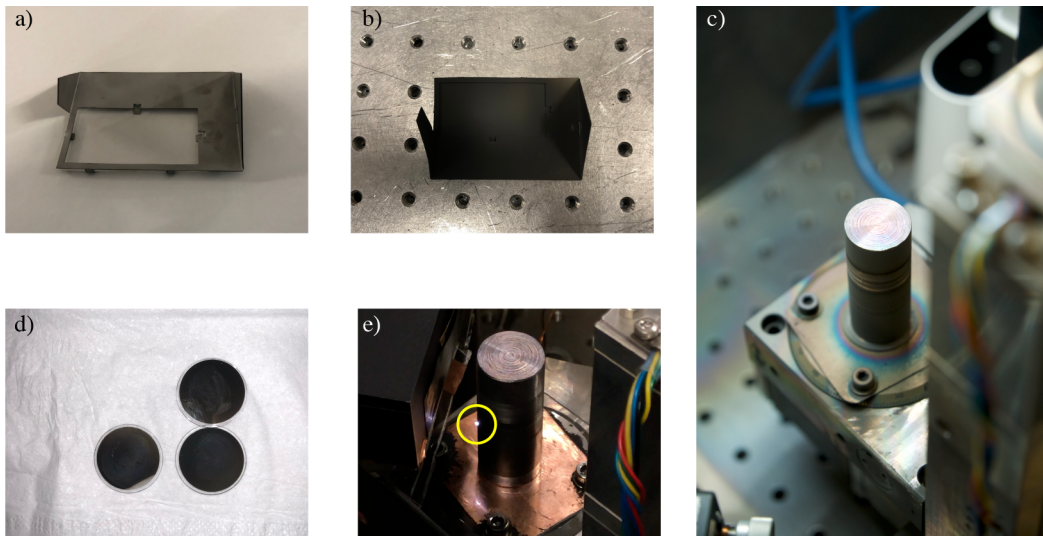


Figure 4.13: **Pictures showing film deposition on some of the components of the experimental setup.** Panels (a) and (b) show the deposit screen placed on the detector before and after running the experiment. From panel (b), it is evident that a tantalum film was deposited. Panel (c) shows the tantalum cylindrical sample on the rotational stage. Grooves left from laser ablation are clearly visible in the upper part. Panel (d) shows the sapphire windows with tantalum film deposition. In panel (e), the region where the laser impacts the sample, resulting in photoemission, is indicated by a yellow circle.

With each laser pulse, a portion of the sample material is ablated and mainly ends its journey forming a thin film on the deposit screen, shown in Fig. 4.13a,b as it looks before and after the experiment. The ablation process will leave grooves on the sample surface, visible in Fig. 4.13c. The film deposition, which is effectively a pulsed laser deposition (PLD) [242], will also affect the sapphire windows placed on the motorized wheel behind the protection screen, shown in Fig. 4.13d. The motorized wheel can be operated whenever the detected counts decrease significantly: this is an indication that a new sapphire window should be placed as protection for the optics. Fig. 4.13e shows instead the region of photoemission on the sample (i.e., where the laser impact on it), obtained at low laser intensity (hundreds of mW). The rotational and Z-axis stages are in charge of doing a surface refresh continuously. These expedients make it possible to keep the detected events almost constant for several hours. Additionally, if required, the movement of the XY stages can be employed to maintain the outermost portion of the surface within the laser focus once the entire length of the sample has been scanned.

To ensure accurate positioning and spacing of the laser pulses along the Z-axis and XY plane, as well as to validate some of the assumptions made in the hydrodynamic model, it was necessary to characterize the ablated surface. To accomplish this, profile measurements were performed using a 3D optical profilometer on the tungsten (W)

sample<sup>IV</sup>. The profiles obtained are shown in Fig. 4.14, which displays the outcome for three fluences: 1 W (red), 3 W (blue) and 7 W (purple) at a repetition frequency of 4 kHz. The depth and width of the grooves formed by the laser beam were determined by applying a median filter to the profiles following the alignment of their minima at each y-position. The median and 95% percentile of these profiles, across all 1200 y-positions, are presented in Figure 4.14d. The FWHM of the grooves was found to be  $9.81\ \mu\text{m}$  for a fluence of 1 W,  $9.68\ \mu\text{m}$  at 3 W and  $15.13\ \mu\text{m}$  for a fluence of 7 W. The traces left for 1 W and 3 W have lateral dimensions that are comparable with FWHM of the laser spot at the focus of the parabolic mirror ( $2R_{\text{focal}} \sim 10\ \mu\text{m}$ ), as shown in Fig. 4.15a. However, for the highest possible fluence at 4 kHz, which is 7 W, the width of the groove is noticeably larger. This can be attributed to the monochromatic aberrations of the parabolic mirror, particularly to coma [243].

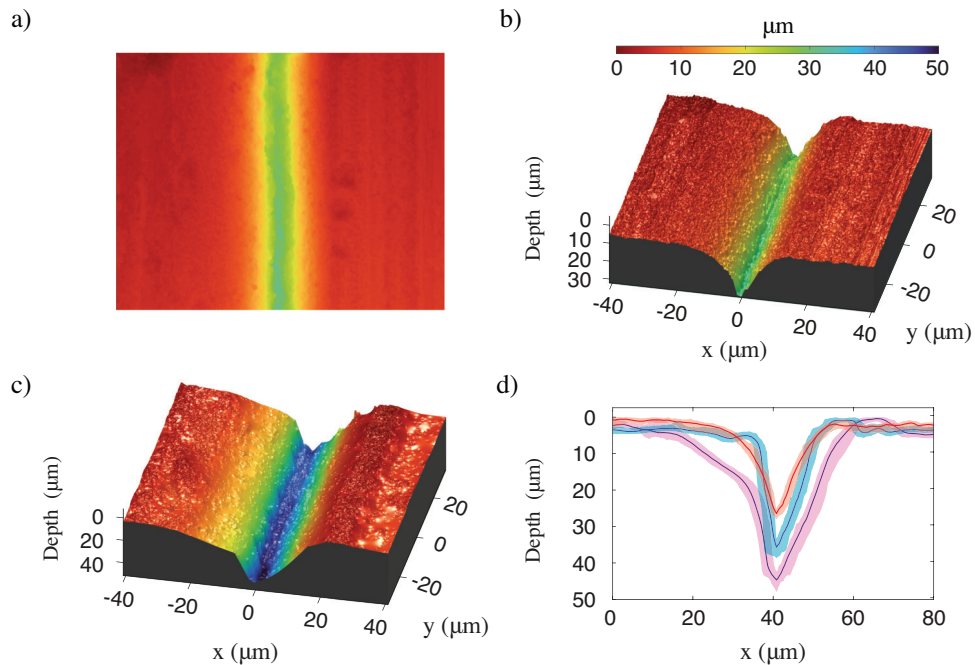


Figure 4.14: **Surfaces of the W cylindrical sample acquired through 3D optical profilometer.** A 2D (a) and 3D (b) maps of an  $80 \times 60\ \mu\text{m}$  section of the W (tungsten) sample. This section of the sample was irradiated with a laser power of 1 W. Panel (c) displays the 3D profile of the groove left by the laser at a power of 7 W. The colormap is shared among panels (a), (b) and (c). 3D profiles of the tungsten surface, such as those shown in (b) and (c), are used to extract the median (solid curve) and 95% percentile (shaded area) plotted in panel (d) for laser powers of 1 W (red), 3 W (blue), and 7 W (purple).

According to the hydrodynamic model presented in Section 4.4, the width of the grooves provides insight into the maximum temperature reached by the plasma during

<sup>IV</sup>The Ta sample had already grooves along its entire length, and it was not possible to relate the size of the grooves with the laser power.



its formation, while the depth acts on the determination of the plasma volume ( $V_p$ ) and in turn on the electron density (in SL1 the  $n_e$  is independent of  $R_{\text{focal}}$ ) as seen in Eq. 4.3. Depths extracted from the 3D profiles are shown in Fig. 4.15b. They result to

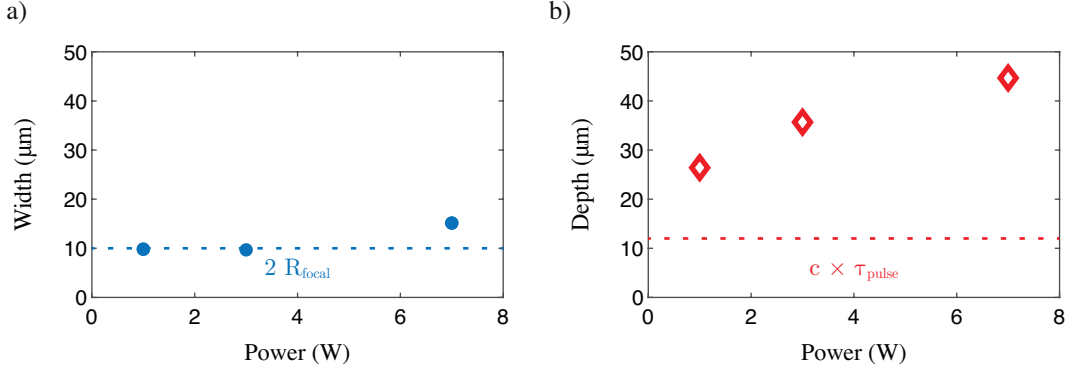


Figure 4.15: **Widths and depths of the grooves left by laser ablation on the W sample.** Panel (a) displays the FWHM of the three profiles reported in Fig. 4.14d, plotted as a function of the laser power. For comparison, the FWHM of the laser spot measured at the focal point ( $D_{\text{focal}}$ ) is added as a horizontal dashed line. The groove depths are shown in (b), along with the value of  $d_p$  represented as a horizontal dashed line.

be  $26.41 \mu\text{m}$  for 1 W,  $35.67 \mu\text{m}$  for 3 W and  $44.67 \mu\text{m}$  for 7 W. The surface motion of the sample is estimated to be no greater than  $0.6 \mu\text{m}$  per laser pulse at 4 kHz. Due to this limitation, only a small fraction of the sample is refreshed between two consecutive pulses. As a result, the groove depth cannot be attributed to a single laser pulse. Similar considerations may also apply to the full width at half maximum (FWHM). Considering the depth of focus of the beam ( $\sim 80 \mu\text{m}$ ) and the fact that it takes approximately 20 pulses to move the surface by one spot dimension ( $D_{\text{focal}}$ ), it can be concluded that the grooves are likely the result of multiple laser pulse hits. For comparison, the value of the plasma thickness  $d_p (= c \times \tau_{\text{pulse}})$ , used in the Eq. 4.2 of the hydrodynamic model, has been added in Fig. 4.15b. The definition of  $d_p$  is independent of the laser power and ranges between one-fourth to one-half of the measured depth of the groove across the different fluences. The considerations outlined in this Section, along with the other assumptions discussed in Section 4.4, suggest that while  $R_{\text{focal}}$  and  $d_p$  are consistent with the observed grooves on the sample, the hydrodynamic model may overestimate the actual experimental conditions that are present in the laboratory.

Preliminary time series (15 seconds each) acquired for the tantalum and tungsten samples are shown in Figs. 4.16 and 4.17, respectively. One can immediately distinguish a sharp peak with multiple bumps due to the plasma radiation (in blue), which could be overimposed to the time response of the silicon detector. A delayed response (shown in red) is also visible, likely originating from the plasma plume reaching the deposit screen positioned beneath the detector or hitting the chamber walls. A third feature, shown in green, accompanying the initial plasma radiation may also be present. It is possible to

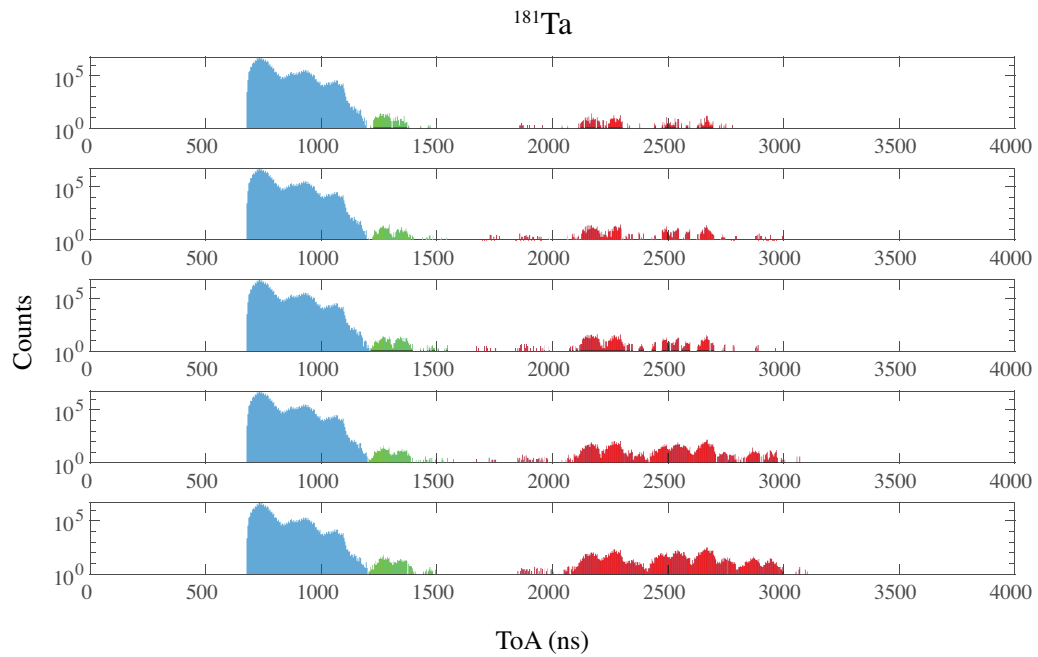


Figure 4.16: Optical-laser generated plasma: time series acquisitions with the Tantalum sample.

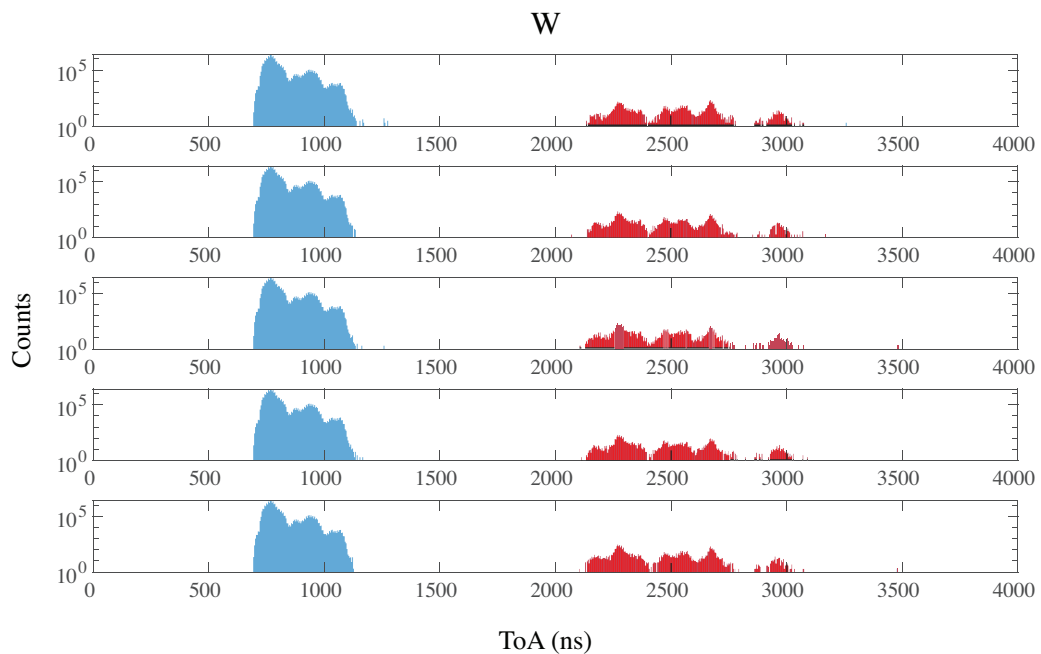


Figure 4.17: Optical-laser generated plasma: time series acquisitions with the Tungsten sample.

see that despite elements of high repeatability among different time series acquired at nominally equal laser conditions, there is a visible variation in the number of total counts measured in the region  $2 \mu\text{s} \leq \text{ToA} \leq 3 \mu\text{s}$  of Fig. 4.16. Suppose we integrate the total counts present in the intervals  $0.5 \mu\text{s} \leq \text{ToA} \leq 1.7 \mu\text{s}$  (prompt, integrated counts  $\simeq 10^7$ ) and  $1.7 \mu\text{s} < \text{ToA} \leq 3.5 \mu\text{s}$  (delayed, integrated counts  $\simeq 10^3 - 10^4$ ) among different time series, and then we normalize to their average, we obtain the 68% confidence interval shown in Fig. 4.18. This demonstrates that even though the X-ray yield of the prompt plasma radiation is comparable among the five series shown in Figs. 4.16 and 4.17, the detected counts in the delayed region can exhibit a broader variation in relative terms. These findings suggest that if the signal emitted by the ions interacting with the metallic

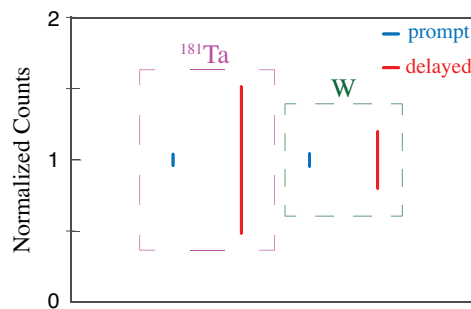


Figure 4.18: **Count dispersion among different time series.** The 68% confidence interval is obtained by integrating the counts of Figs. 4.16 and 4.17 over two different time intervals:  $0.5 \mu\text{s} \leq \text{ToA} \leq 1.7 \mu\text{s}$  for prompt radiation (blue) and  $1.7 \mu\text{s} < \text{ToA} \leq 3.5 \mu\text{s}$  for the delayed events (red). The prompt and delayed integrated counts for each time series are then normalized to their respective average counts calculated across all the series. The bars represent the dispersion range of the normalized counts with a 68% confidence level for the Tantalum (Ta, in a magenta box) and Tungsten (W, green box) samples.

walls of the chamber extends over the time interval when nuclear decay is expected, as it happens in Ref. [214], the excess of counts cannot be reliably used to discriminate the nuclear deexcitation. Instead, the time response and the energy spectrum must be considered as the distinctive signature of the process. In Fig. 4.19 the two last time series of Figs. 4.16 and 4.17 are superimposed and aligned in time to the peak of the prompt region to facilitate comparison. This confirms that, while being measured in different moments, the plasma produced with Ta and W are quite similar in terms of counts and overall dynamics of the plasma (for example, the ToA of the delayed X-rays).

If the delayed portion of the signal – depicted in red – is interpreted as due to ions hitting and interacting with the deposit screen<sup>V</sup>, it would suggest that the plasma expansion occurs at much lower velocities than those predicted by the hydrodynamic model presented in Section 4.4. Solution of Eq. 4.11, shown in Fig. 4.10, predicts an ion

<sup>V</sup>Further discussion on this topic can be found in the following section.

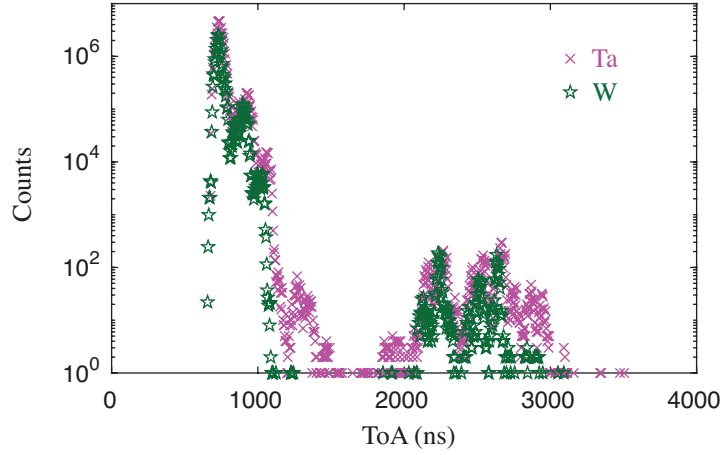


Figure 4.19: **Comparing the time-dependent signals measured with the Tantalum and Tungsten samples.** The last time series in Figs. 4.16 and 4.17 have been superimposed and aligned to the peak of the prompt radiation to facilitate comparison. The two signals have not been normalized to each other, highlighting the high repeatability of the experimental conditions.

expansion velocity of  $v_{\text{exp}} = 2.63 \times 10^{-3}c$  at  $R(t)/R_0 = 30$ . This corresponds to a travel time of approximately 70 ns for the plasma to cover the distance between the sample and the detector, which is between 4 cm and 6 cm, and approximately 250 ns to reach the chamber walls. On the other hand, the model suggests that an eventual signal resulting from the ions traveling at  $v_{\text{exp}}$  and reaching the detector would fall well within the time window of the prompt radiation. To better comprehend the structure of the delayed events, the time interval between the peak of the prompt radiation and the subsequent peaks in the delayed events was calculated. The time distance between the prompt and the first (1) and second (2) delayed peaks are shown in Fig. 4.20.

The time intervals measured are on the order of  $\sim 1.5 \mu\text{s}$  both for Ta and W, which is roughly twenty times larger than the time predicted by the hydrodynamic model to reach the deposit screen and roughly six times larger the time predicted to reach the chamber walls. If these counts were associated with the ions of the primary hot plume, it would indicate a  $T_e \ll 500 \text{ eV}$ , which seems not compatible with the measured spectra. Therefore, these delayed events are presumably associated with the ions interacting with the chamber walls. Another possible explanation could be the presence of hot and cold ion distributions within the plasma. This raises the question of whether the green peak observed in Fig. 4.16 and other bumps in the blue prompt radiation could be attributed to the portion of plasma traveling at  $v_{\text{exp}} \sim 3 \times 10^{-3}c$  – and thus reaching the screen within hundreds of ns, while the red delayed events occurring after  $\sim 1.5 \mu\text{s}$  associated with the cold bulk part of the plume. A 2D energy-time histogram (discussed in the next section) and PIC simulations could help to shed light on this question. However, further analysis in different geometries is needed to identify these contributions uniquely.

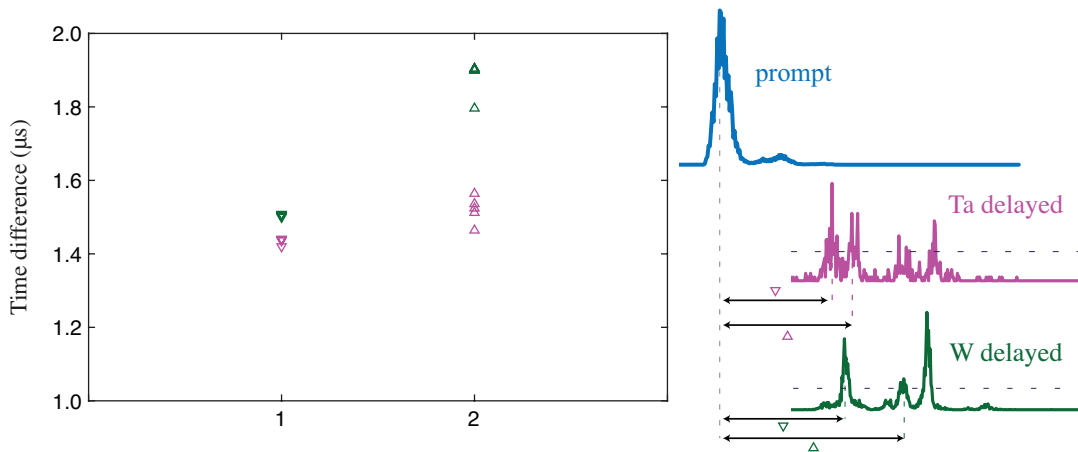


Figure 4.20: **Time difference between the prompt peak and the following peaks in the delayed events.** The time intervals between the prompt radiation and the first peak of the delayed events are indicated with  $\nabla$  and plotted along the label ‘1’. Those relative to the second peak are indicated with  $\Delta$  and plotted along the label ‘2’. The horizontal gray dashed lines in the figure indicate that the first and second peaks for the delayed events were defined using a threshold of 35% of the maximum value measured in the corresponding time interval for each time series. The time intervals for Ta have been plotted in magenta, while those for W are in green. As one would expect, the interval with respect to the first peak is a much more reliable measure, showing high repeatability between Ta and W. Prompt and delayed signals, shown on the right side, are not to scale.

## 4.6 Experimental results

After following all the procedures discussed in this chapter, the experiment – aimed at the observation of the isomer decay – can proceed by acquiring data for several hours. At the time I started these measurements, the laser had a maximum output power of 5 W at a repetition rate of 4 kHz. As indicated in Table 4.1, the pulse duration was measured to be 31 fs at the laser output, and the FWHM of the focal spot on the sample was 10  $\mu\text{m}$ , which is very close to the diffraction limit. A digital pixel mask was prepared to immediately remove false events due to defective pixels. In the case of uniform illumination, as should be the case in our experiment, a flat histogram of occurrences relative to the pixel number is expected. Thus, any events originating from pixels with substantially higher statistics than their surroundings were disregarded. Histograms illustrating the distribution of the detected events as a function of the pixel number before and after pixels removal are shown in Fig. A.2. AdvaPix TPX3 does not provide the capability to start a new measurement every 250  $\mu\text{s}$ , which is the period between two consecutive laser pulses. Instead, it offers the option to refresh the 14-bit ToA counter through an external trigger. In our case, this signal has been driven by the laser trigger. Over the course of  $\sim 10$  h, a total of approximately 17 billion counts were

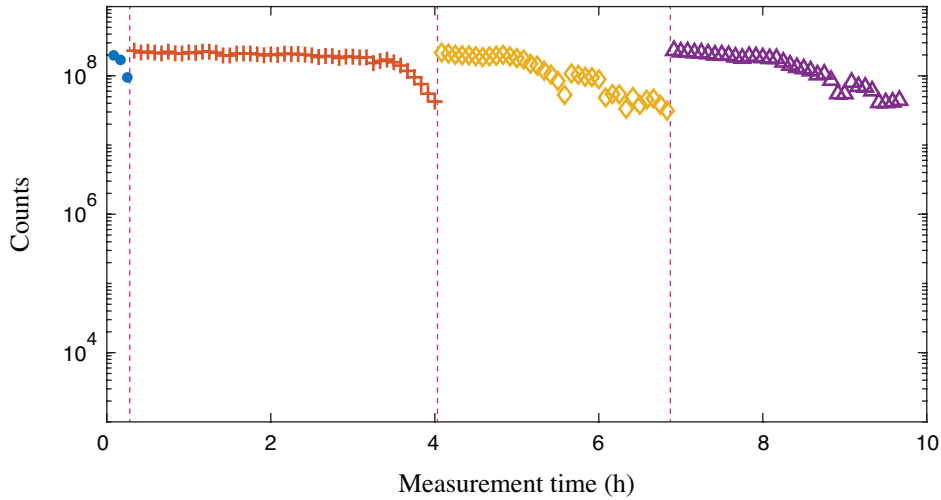


Figure 4.21: **Optical-laser generated plasma experiment: total number of events over time.** Each marker represents the total number of events detected within a time window of 300 s. Different markers represent runs obtained after replacing the sapphire window with a clean one, and a dashed vertical line indicates the replacement. The total number of detected events from the raw data amounts to  $\sim 1.7 \times 10^{10}$ , collected over a total of 116 time series. Compared to the others, the first sapphire window had to be replaced quite early. This was probably due to an intensified accumulation of Ta nanoparticles on the sapphire window, potentially influenced by the surface properties of the sample or laser pointing.

collected, as depicted in Fig. 4.21. During this time, the sapphire window protecting the optics was replaced three times with the motorized wheel as soon as the rate was observed to decrease. A substantial fraction of these 17 billion counts<sup>VI</sup> originated from pixels considered malfunctioning after plasma radiation, and therefore possessing higher statistics than their surrounding. Some of these events, despite originating from pixels with regular activation statistics (see Fig. A.2), were characterized by values of ToA preceding the arrival of the laser pulse on the sample. These events consistently showed a ToA value  $\sim 0$  (in the detector units), even when the laser trigger was shifted. This could indicate a malfunction in the detector electronics, probably caused by the high photon flux. Additionally, the built-in software of the AdvaPix TPX3 does not handle energy and time information directly, therefore to obtain an energy-time map it is necessary to apply an energy calibration function to each event. This energy calibration function depends on the particular pixel from which the event originated.

Fig. 4.22 shows the reconstructed 2D energy-time histogram obtained by considering a time window of  $10 \mu\text{s}$  – starting few hundreds of ns before plasma onset – and an energy window of 50 keV. A dashed red line indicates the energy at which the nuclear decay is expected. The total number of  $6.2 \times 10^9$  events<sup>VII</sup> contained in this window seems

<sup>VI</sup>This is the total number of events detected before the pixels removal shown in Fig. A.2 was applied.

<sup>VII</sup>This is the total number of unclustered events; therefore, an N-pixel trace generated by a single photon

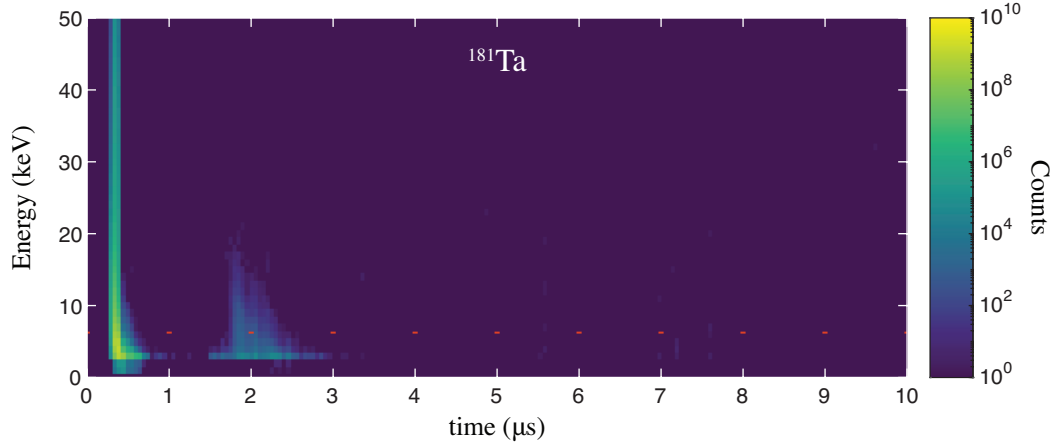


Figure 4.22: **Optical-laser generated plasma experiment: 2D energy-time map.** The time bin has been chosen to be 50 ns, while the energy bin is of 1 keV. The total number of events in this image is approximately equal to  $6.2 \times 10^9$ . The red dashed line indicates the energy position at which it would have been expected to see the nuclear decay of the first isomeric state of  $^{181}\text{Ta}$ . Since the color axis starts from  $10^0$ , energy-time bins with a single count are indistinguishable from those with zero counts. This choice has been made to facilitate readability. However, in Fig. A.3, the same histogram is replicated using a different colormap and a lower limit for the color axis.

compatible with the bremsstrahlung photon flux described in Eq. 4.8. Considering the rate of radiated photons  $N_{\text{plasma}}^{\gamma, \text{B}} = 1.59 \times 10^9 \text{ s}^{-1}$  within the energy range  $3 \text{ keV} \leq E_{\gamma} \leq 50 \text{ keV}$  (as determined in Table 4.4), along with a solid angle of  $\Omega \sim 0.04 \text{ sr}$  compared to  $4\pi$ , we can estimate a total photon count of  $\sim 2 \times 10^{11}$  for an integration time of 10 h. It is important to note that the photon rate calculated in Table 4.4 assumes constant plasma radiation over its lifetime  $\tau_{\text{plasma}}$ . In reality,  $T_e$  and, consequently,  $\phi_{\gamma}$  will significantly decrease over this timescale. This, along with the other hypothesis discussed in Section 4.4, may lead to overestimation. Detector efficiency and absorption of the 25  $\mu\text{m}$  Kapton foil (used to protect the CCD) have only a minor impact on correcting the total counts, which becomes  $7.4 \times 10^9$  after efficiency adjustments and  $9.3 \times 10^9$  accounting also for the transmittance of Kapton. Although the bremsstrahlung model roughly reproduces the number of events detected, it does not reproduce the measured photon distribution, as can be seen in Fig. A.6. The energy spectrum is more accurately described by a Planck distribution  $B_{\lambda}$  with a specific emissivity  $\epsilon$ , as can be deduced from Fig. 4.12, and later from Fig. 4.24.

A broad-energy signal associated with the prompt plasma radiation is observed in Fig. 4.22 at the beginning of the window. After approximately 1.5  $\mu\text{s}$ , delayed events are detected, less intense and less extended in energy than the initial radiation. It appears that no signal related to a decay consistent with  $T_{1/2} \sim 6 \mu\text{s}$  and  $E \sim 6 \text{ keV}$ , which might

---

will result in N events. According to the AdvaPIX TPX3 built-in clustering software, our preliminary data (the code can handle only a small subset compared to Fig. 4.22) were strongly dominated by 1-pixel traces, thus we assume in the first approximation that  $N_{\text{events}} \sim N_{1\text{pix}}$ .

be associated with the  $^{181}\text{Ta}$  isomer, is observed.

There may be several reasons that could explain the absence of a signal originating from nuclear deexcitation. The first potential explanation arises from the theoretical predictions discussed in Section 4.4. If the hydrodynamic model presented accurately describes the conditions of our experiment, the calculated efficiency ratio according to Table 4.3 is expected to be  $N_{\text{deexc}}^{\gamma}/N_{\text{plasma}}^{\gamma} \sim 10^{-20}$ . Both the TDE and bremsstrahlung models return a similar order of magnitude for this efficiency ratio. This value might be additionally corrected by accounting for the difference in the solid angles with which we detect plasma radiation and nuclear deexcitation, which are in a ratio of  $\Omega_{\gamma}^{\text{deexc}}/\Omega_{\gamma}^{\text{plasma}} \sim 10$ . This implies that in order to observe a single  $\gamma$ -decay, we would need to integrate for  $10^9 \text{ h} - 10^{10} \text{ h} = 1 \text{ My}$  to observe a single nuclear deexcitation<sup>VIII</sup>. Therefore, a nonobservation of the nuclear deexcitation is consistent with the theoretical predictions presented in Section 4.4.

These findings also raise the question of whether a signal related to the decay of the  $^{181}\text{Ta}$  isomer was ever detected in Refs. [214, 244], which ran in approximately similar conditions. Both works attributed the excess events measured in Ta compared to W to nuclear deexcitations. In Ref. [214], the experiment was performed in 100 time series, but the integration time for each series was not specified. However, since their target was fixed, it could be reasonable to assume that their total integration time was shorter than ours. It is also difficult to compare the total X-ray yield. In Ref. [214], the prompt plasma radiation is said to determine a single pulse, whereas the reported total counts ( $\sim 10^5$ ) are probably collected at delay times  $t \geq 3 \mu\text{s}$  following plasma ignition. In our study,  $10^8$  events were measured in a 300 s timeframe, recording all the events detected from plasma ignition with  $E_{\gamma} \geq 3 \text{ keV}$ . Presumably, we could have obtained higher statistics, although it is difficult to make a direct comparison based on the published information. This noted, the authors assert that they have observed 49 excess events in  $^{181}\text{Ta}$  that can be attributed to its isomer decay. This leads to an average of one isomer decay detected event for every two time series.

Similarly, in Ref. [244], excess counts measured in the signal generated by delayed electrons were attributed to the depletion of the  $^{181}\text{Ta}$  isomer. In this work, with only 8000 laser shots<sup>IX</sup> at a repetition rate of 1 kHz, delayed electrons were measured in excess for a Ta sample that – based on their estimates – yielded to  $N_{\text{exc}} \sim 30$  to 50 excited nuclei per laser shot. Accounting for the difference in the IC and  $\gamma$ -decay channels, this should have produced in our geometry and measurement window  $\sim 10^5 - 10^6$  detectable events. As discussed in detail in Section 4.5 and particularly in Fig. 4.18, it seems that the excess counts of Ta with respect to W are not a reliable signature of the isomer decay in this scenario.

Another potential explanation for the apparent absence of signal from  $^{181\text{m}}\text{Ta}$  could

<sup>VIII</sup>Altering the orientation of the detector to face the sample directly rather than downwards could potentially increase the counts. However, this change may also shorten the longevity of the experiment due to increased depositions.

<sup>IX</sup>For comparison, the data presented in Fig. 4.22 were collected over a period that encloses  $1.44 \times 10^8$  laser shots.



be the low detection efficiency in measuring photons at  $\sim 6$  keV due to its proximity to the detector threshold  $D_{\text{th}} = 3$  keV. If, for example, a photon releases its energy in multiple pixels, the energy deposited in each pixel may be lower than the threshold, resulting in lost events. Therefore, a calibration of the AdvaPix TPX3 using a  $^{55}\text{Fe}$  source (emitting Mn X-rays,  $K_{\alpha}$  at 5.9 keV and  $K_{\beta}$  at 6.5 keV) – as it was done in Ref. [214] – is necessary to estimate the detection efficiency of an eventual  $\gamma$ -ray emitted by the nuclear deexcitation.

Of course, there is always the possibility that the scaling laws in Eq. 4.1 are overestimating the real electron temperature  $T_e$  that we can achieve in the experiment, which could make nuclear excitation even more challenging than what predicted by Tables 4.3 and 4.4. To address this concern, we can take a closer look at the signals observed in the energy-time map and highlight two different time windows, as shown in Fig. 4.23. It can be observed that the events in the time window  $t_1 = 250 \text{ ns} \leq t \leq 1000 \text{ ns}$  can be divided into two further portions: labeled as ‘P1’ in the interval  $t_1 \leq t \leq t_2 = 450 \text{ ns}$ , and ‘P2’ in the interval  $t_2 < t \leq 1000 \text{ ns}$ . The first portion P1 displays a broad energy spectrum with significant counts up to 50 keV, while P2 shows a different behavior, with the energy decreasing with time. Interestingly, this behavior is similar to that observed in the delayed portion of the signal, labeled with ‘D,’ in the time interval  $1200 \text{ ns} \leq t \leq 3200 \text{ ns}$ .

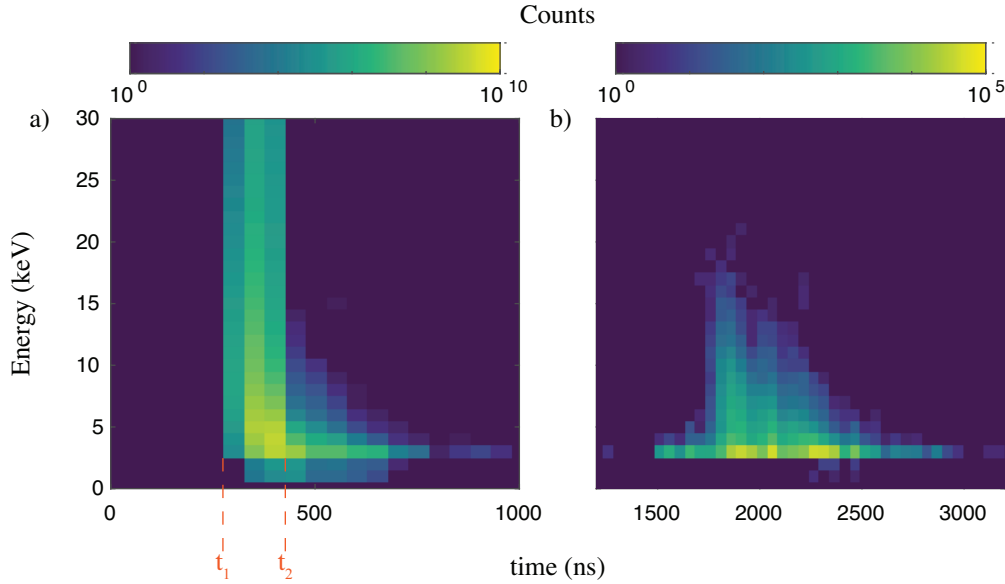


Figure 4.23: **Optical-laser generated plasma experiment: taking a closer look at the prompt and delayed signals.** The 2D histogram of Fig. 4.22 has been divided in two smaller portions: in (a) the time interval  $0 \leq t \leq 1000 \text{ ns}$  is highlighted, while in (b)  $1200 \text{ ns} \leq t \leq 3200 \text{ ns}$ . The time instants  $t_1 = 250 \text{ ns}$  and  $t_2 = 450 \text{ ns}$  are indicated with vertical dashed red lines.

In Fig. 4.24, the spectra for the three different subsets of detected events are shown. In panel (a) of Fig. 4.24, P1 is fitted with a Planck’s distribution  $B_{\lambda}$  having a temperature

$T_\gamma \sim 794 \text{ eV}$  and a peak at  $E_\gamma \sim 4 \text{ keV}$ . Since the time response of the detector is much slower than the plasma lifetime, this spectrum has to be interpreted as an average of the plasma emission over its entire expansion. Therefore, we could reasonably expect that the temperature of the photon gas  $T_\gamma$  is greater than  $1 \text{ keV}$ , as discussed in Section 4.5.

P2 could offer additional elements in support of an experimental  $T_e$  compatible with the value of  $8 \text{ keV}$  derived with SL1. In order to comment on these aspects, a comparison between the spectra of these three portions is shown in panel (b) of Fig. 4.24. Resemblances in the time dependence and energies spectra of P2 and D signals may

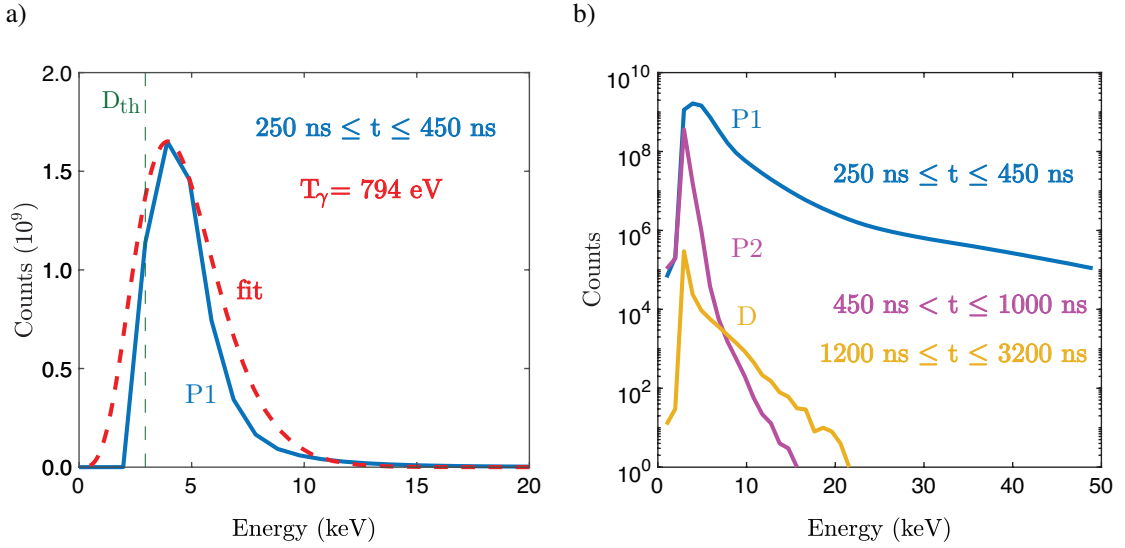


Figure 4.24: **Optical-laser generated plasma experiment: spectra of the prompt and delayed signals.** Panel (a) shows the spectrum obtained by summing the events in the time intervals  $250 \text{ ns} \leq t \leq 450 \text{ ns}$  from Fig. 4.23a. The dashed red line represents the fit obtained using Planck's  $B_\lambda$  distribution. The frequency parametrization  $B_\nu$  results in a higher temperature  $T_\gamma = 1.3 \text{ keV}$ , but is less accurate in fitting the data. Panel (b) displays the spectra of P1 (blue), P2 (magenta), and D (yellow) in a logarithmic scale.

suggest that these events share a similar origin, potentially associated with the interaction of plume ions with the deposit screen or chamber walls. As seen in Fig. 4.23, the signal P2 follows the peak of P1 by  $\sim 100 \text{ ns}$ . If P2 represents the hot portion of the plasma hitting the screen, this time delay is coherent with the travel time predicted by the hydrodynamic model ( $\sim 70 \text{ ns}$ ), thus indicating that the electron temperature could be  $T_e \sim 8 \text{ keV}$ . Additionally, signal D exhibits similar behavior to P2 but with much fewer counts. This signal could be related to the colder region of the plume reaching the deposit screen after  $\sim 1.5 \mu\text{s}$  or to the plume interacting with the chamber walls, as discussed in the previous section. Both P2 and D have energies below  $20 \text{ keV}$ , which is consistent with the ionization of the L-shell of Ta [245]. As previously noted, the eventual signal of an ion striking the deposit screen while traveling at  $v_{\text{exp}} = 2.63 \times 10^{-3}c$  will overlap with the prompt plasma radiation and the time response of the silicon detector, as could be the case for P2.

The discussions in this Chapter have shown that the current experimental setup can reliably reproduce plasma conditions where nuclear excitation might occur. However, the absence of detected isomer decay leaves many questions open. At this stage, it is essential to identify other isotopes from those shown in Fig. 4.4 that could provide a higher photoexcitation rate  $\lambda_\gamma$ . This would enable us to study the nuclear excitations and offer a comparison with the theoretical models of the laser-generated plasma scenario.

Each one of us has within him a whole world of things, each man of us his own special world. And how can we ever come to an understanding if I put in the words I utter the sense and value of things as I see them; while you who listen to me must inevitably translate them according to the conception of things each one of you has within himself. We think we understand each other, but we never really do.

— Luigi Pirandello, *Six Characters in Search of an Author*





## Beyond Dichotomies: Reflections and Takeaways

I find it fascinating how we construct our conversations and the manner in which we incorporate *logos* within them. And to be honest, I do it since I was a teenager. The moment I was able to learn and apply a more rigorous framework, rather than relying solely on intuition, was truly enlightening. Perelman and Olbrechts-Tyteca [246] write: «*dialogue, as we consider it, is not supposed to be a debate in which the partisans of opposed settled convictions defend their respective views, but rather a discussion in which the interlocutors search honestly and without bias for the best solution to a controversial problem. Certain contemporary writers who stress this heuristic viewpoint, as against the eristic one, hold that discussion is the instrument for reaching objectively valid conclusions*». *Dissensus* [247] and *pro-contra*<sup>X</sup> arguments [170] lie at the very heart of the scientific method. We are encouraged to subject every idea to rigorous scrutiny and doubt, forge them in the *crucible of doubt*. However, this ideal is not always achieved in practice – more often than we would like to admit. As Perelman and Olbrechts-Tyteca note: «*in a debate, on the other hand, each interlocutor advances only arguments favorable to his own thesis, and his sole concern for arguments unfavorable to him is for the purpose of refuting them or limiting their impact. The man with a settled position is thus one-sided, and because of his bias and the consequent restriction of his efforts to those pertinent arguments that are favorable to him, the others remain frozen, as it were, and only appear in the debate if his opponent puts them forward*». By acknowledging the importance of dialogue in our research and conversations, we can strive to create a more balanced and constructive discourse. This approach not only benefits the scientific community but also promotes the growth and development of knowledge for society as a whole [247].

In my experience participating in various panels, as well as engaging in both in-person and virtual discussions about addressing climate change, I have observed the influence of individual ideologies on the conversations (which may seem quite obvious). It is intriguing how these discussions often shift from the primary goal of addressing a global issue to defending one's rationale for choosing a particular solution or joining a specific

---

<sup>X</sup>Every *pro* arguments is countered by a *contra* argument. This is the typical dichotomy with which Dostoevskij built *The Karamazov Brothers*.

project. It might seem naive to express this opinion, and I could be accused of such. Rather than thoughtfully examining the challenges and selecting the most effective tools to combat them, we often start and lean toward the tools that are accessible and familiar. It is this inclination that subsequently influences the problems we decide to address. In other words, our assessments of feasibility within our existing cognitive framework shape the narrative and build the connections necessary to bridge the gap between our present achievements and the issues that truly require our attention (i.e. what we should be addressing). This idea can be better illustrated using Fig. BD.1, where I have adapted<sup>XI</sup> the representation of the structure of the *known* from Ref. [1]. This observation may help to partially understand why science has demonstrated reduced disruptiveness across all disciplines over time, even though the number of researchers involved and the volume of literature produced have reached unprecedented levels in recent decades [248].

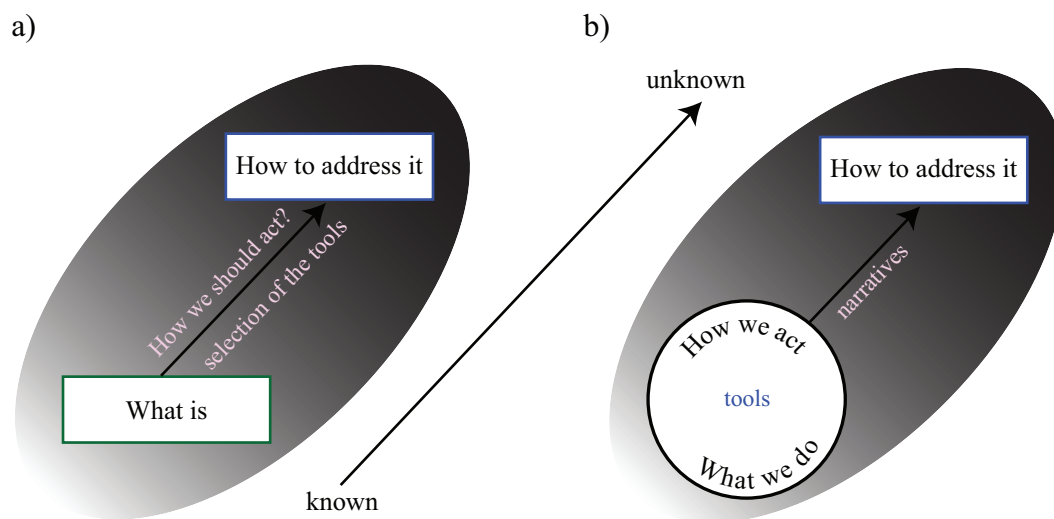


Figure BD.1: **Navigating the Unknown.** Panel (a) shows the cognitive framework where we are supposed to decide the tools and the actions to be taken in order to solve the challenge, moving from the known (in white) to the unknown (black). Panel (b) illustrates a pattern of thought that may be observed in many discussions. One often begins with the tools that are somewhat accessible and proceed to construct narratives that help bridge the gap between the current position and the challenges one aims to address. This figure is inspired by Ref. [1].

The question remains: how can we break this spell? Could it be beneficial to cease identifying ourselves in our current activities – that might be a construct of our training [249] – and instead concentrate on addressing the issues that truly warrant our attention and concern? We are caught in a circular definition. Do we not already believe that what we do aligns with our genuine interests and priorities?

<sup>XI</sup>Panel (a) is adapted from Fig. 1 of Ref. [1], where it is used to depict the structure of the *known* and how we plan our actions to move from the significance of the current state of experience to what we envision as a desirable future.

As I look forward to the future, my aspiration is to expand and evolve in both thought and action. Cultivating self-awareness of our current thought patterns and limitations is likely the starting point that can lay the foundation for the innovations we may need. By recognizing and acknowledging our cognitive biases and constraints, we can initiate the exploration of diverse perspectives and formulate novel strategies, ultimately encouraging a more innovative and disruptive mindset. As we endeavor to liberate ourselves from the constraints of our beliefs, I will undertake this deconstructive exercise on myself, challenging the ideas presented in this thesis.

---

When I first became aware of the proposal to use isomers for energy storage, I was captivated, both by the inherent nature of isomerism and the remarkably long duration over which certain excitations could be maintained. The desire to harness control over nuclear decay is undeniably intriguing, as it presents a challenge against Nature that humanity may eventually win. In Chapter 1, we delved into the nature of isomers and their role as exceptional tools for probing nuclear structure, as well as their potential impact across various fields. As indicated by its title, the primary focus of this thesis was to explore the possibility of exciting nuclear levels through diverse processes, ranging from conventional photoabsorption to second-order processes like NEEC and NE $\mu$ C, which involve the capture of a free electron or muon. The historical perspectives examined throughout the thesis have offered us a chance to appreciate the intricate journey of studying these subjects, while also recognizing that in certain cases there is still much to discover or – conversely – how limited our knowledge may be. This opens up numerous possibilities for substantial advancements and potential breakthroughs as we persist in investigating aspects related to nuclear reactions and their capacity to store or produce energy. Without any doubt, the interest generated by the work on NEEC [148] has sparked a resurgence of curiosity, as demonstrated by recent publications centered on nuclear excitations, which include contributions from groups that typically operate in other fields.

Nonetheless, with the current understanding, all the processes investigated continue to exhibit complexities that make them unsuitable for a practical future in storage devices. Even if the excitation probability of NEEC for  $^{93\text{m}}\text{Mo}$  is confirmed to be nine orders of magnitude higher than theoretical predictions, its inherent inefficiency would persist, particularly when considering the challenges and costs of producing the isomeric beam. Comparable considerations apply to other scenarios, such as ion-beam traps or laser-plasma scenarios (examined in Chapter 4), although with somewhat different issues.

The nuclear excitation processes examined, partially depicted in Fig. 1.17, involve interactions between particles or ion beams and targets under highly specific conditions. They generally display a very low occurrence rate and strict energy-matching requirements due to the narrow nuclear resonance width<sup>XII</sup>. This necessitates employing a broad

---

<sup>XII</sup>An exception is represented by the NEEC process that captures electrons initially bound in a solid target (NETEC), which requires an isomeric beam as discussed in Chapter 2.



---

energy distribution of photons or electrons to ensure that resonance can be achieved. As a result, only a small portion of these particles interact with the nucleus, ultimately leading to excitation. Thus, not only are these processes inherently inefficient, but the conditions necessary for their realization make them even less appealing. In fact, the expenditure required to store a single energy block in the form of isomers significantly outweighs any potential discussions on energy convenience.

It is challenging to conceive a scenario where isomeric energy release can be initiated and halted at will without the continuous provision of external particles such as photons, electrons, or muons. With muons, for instance, nuclei predominantly undergo fission, altering the nature of the interaction that one would like to exploit for isomer depletion. It is exactly the relative simplicity and self-sustainability of fission reactions in  $^{235}\text{U}$  with thermal neutrons that make it difficult to envision an equally efficient process for energy storage through the processes shown in Fig. 1.17. Direct energy production through fission would just be substantially more convenient; moreover, energy storage would not even be necessary. However, public opinion has largely turned against nuclear energy in recent years. At times the term “nuclear” itself – and I have experienced this personally – is not even well-received for public outreach efforts. This kind of hostility sometimes originates also between individuals of different fields, who tend to primarily advocate for the technology they personally invest their time in. This situation made me wonder whether, in the roles we assume, we are merely defending our preferences and beliefs – as if we were members of a cult – or we are using the *logos* to really seek an objective solution.

Instead of addressing the concerns related to nuclear fission, we have accepted its obsolescence, slowly dismissing the entire field. However, nuclear energy holds immense potential as a power source, and this potential could be further amplified if fusion technology delivers on its promises. As our understanding deepens, we may uncover groundbreaking mechanisms that capture interest and finally encourage global consensus for their advancement. Tackling climate change necessitates innovation across diverse fields since the true source of a transformative revolution might still be hidden. However, it is also crucial not to depend solely on the prospect of uncovering something new or extraordinary, especially given the urgency of the situation. Reevaluating and innovating<sup>XIII</sup> within existing nuclear technologies could help address concerns that currently hinder their wider adoption, providing a robust carbon-free energy foundation upon which we can pursue further discoveries in green solutions. A multidisciplinary scientific environment featuring a polyphony of opinions that may clash, intertwine, or remain distant, with the sole intent to support ideas with real potential for impact – irrespective of one’s original fields of expertise or personal narratives – could provide the framework that could help us in addressing this global challenge. Embracing such a mindset can be both enlightening and liberating.

---

<sup>XIII</sup>There are already companies that are, for example, trying to address safety and long-lived waste issues by reshaping and ‘reinventing’ the concept of nuclear energy.

# Addendum: Charge Dynamics Electron Microscopy

In this addendum, I would like to introduce an additional regime ( $I \sim 10^{13} \text{ W cm}^{-2}$ ) of ultrafast plasma dynamics that we have investigated using ultrafast transmission electron microscopy (UTEM) [250]. In Chapter 4, we have seen that accurately retrieving the evolution of an expanding neutral plasma using time-resolved X-ray spectroscopy can be quite challenging. While some concepts may appear similar to those discussed in that chapter, the advanced characterization technique provided by the UTEM in this particular regime presents a unique and unparalleled platform for validating theoretical predictions. The technique, named “Charge Dynamics Electron Microscopy (CDEM)”, aimed to investigate the generation and dynamics of emitted charges by metallic structures upon laser irradiation in the UTEM<sup>XIV</sup>, as illustrated in Fig. CD.1. In the experiment, a

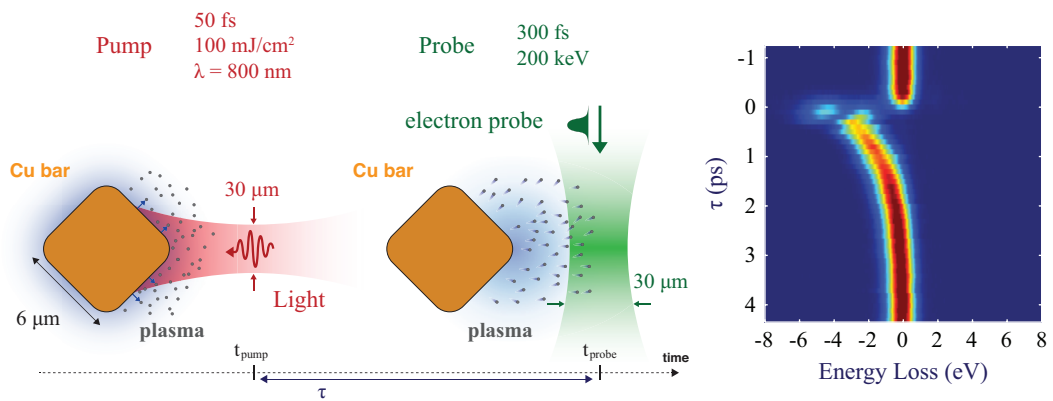


Figure CD.1: **Charge Dynamics Electron Microscopy.** (a) Charges are emitted upon laser irradiation and probed through a 200 keV electron beam with a delay  $\tau$  that can be varied. (b) The energy losses of the electron probe with respect to their average energy as a function of  $\tau$ . Negative energy losses mean that the electrons gained energy through the interaction.

femtosecond laser pulse acted as the pump, generating a charged plasma composed of

<sup>XIV</sup>A representation of the UTEM setup can be found in Fig. A.7

electrons emitted from the surface. After a specific time delay  $\tau$ , a 200 keV electron probe (e-beam generated in the UTEM through UV light) interacts with the plasma. By employing Electron Energy Loss Spectroscopy (EELS), we were able to image the interaction between the electron probe and the emitted charges, providing valuable insights into the dynamics of these charges. The CDEM technique enables the examination of the intricate behavior of emitted charges in metallic structures under laser irradiation, both spatially and temporally, by adjusting the delay  $\tau$  between the  $\lambda = 800$  nm laser pulse and the UV light that generates the electron probe. However, the significance of this ultrafast imaging method extends beyond the study of charges emitted into the vacuum, and it also finds applications in exploring previously inaccessible spatiotemporal regimes of charge dynamics in solids. In Ref. [251], CDEM provided valuable insights on the photo-Dember effect in InAs and enabled the spatial reconstruction of the spectrum of the THz field generated by moving charge carriers.

In the regime examined within this project, the behavior of emitted electrons exhibits notable distinctions from the neutral plasma dynamics explored in Chapter 4. The differences arise already from the processes underlying their generation. Under the irradiation conditions of CDEM ( $I \sim 10^{13}$  W cm<sup>-2</sup>), multiphoton ionization and thermal emission are the predominant emission processes [252–254]. As electrons are emitted from the metal, image charges form on the surface, creating an attractive force. This force initially slows down the expansion of the electron cloud and subsequently causes the electrons to be drawn back towards the metallic surface, leading to their recombination on the sample, as illustrated in Fig. CD.2.

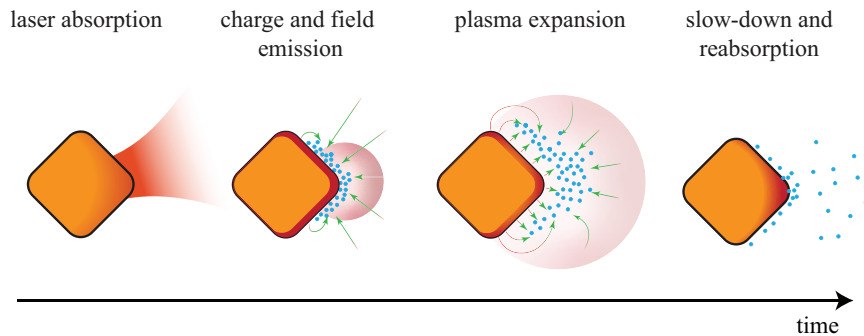


Figure CD.2: **Evolution of the emitted electron charges.**

In the absence of interaction, one would expect the EELS spectra to be peaked at zero, which is referred to as the zero-loss peak. In CDEM the signature of the interaction involved a shift in the energy spectra towards negative values (indicating that electrons were gaining energy) concurrently with the arrival of the laser on the sample ( $\tau \geq 0$ ). Depending on the experimental conditions, this manifested either as a complete shift of

the peak or as the emergence of a side peak in the EELS spectra.

Since this interaction was previously unobserved in UTEM experiments, it was crucial to understand its nature. To that end, I implemented a simplified simulation using EPOCH [216] to describe the interaction between the electron probe and a higher-density electron cloud, as depicted in Fig.CD.3. This initial model, despite lacking many

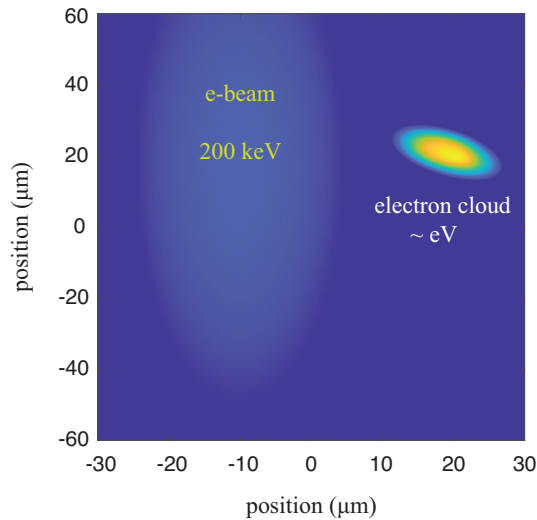


Figure CD.3: **Frame of the EPOCH simulation.** On the left side the e-beam probe, while on the right there is the high-density electron cloud moving and expanding with velocities of approximately  $\sim eV$ . The electron densities in the e-beam and electron cloud are significantly different and are not shown to scale in the image.

elements essential for a comprehensive description of the process, was able to capture the fundamental signatures of the experimental observation. In Fig. CD.4, panel (a) shows the experimental energy-position map, while panel (b) presents the same map obtained with EPOCH. The simulation successfully captured the acceleration of the probe electrons and the decaying trend as a function of distance. Moreover, these simulations demonstrated that the acceleration experienced by the probe electrons was significantly smaller when passing directly through the region where the electron cloud persisted, as illustrated in Fig. CD.5. This feature was also observed in the experimental data, and the insight gained from the simulations prompted us to investigate this phenomenon further and use it as a means to track the dynamics of the electron cloud.

These simulations – included in Ref. [255] – played a significant role in improving our understanding of the interaction and in guiding the development of a more comprehensive theory.

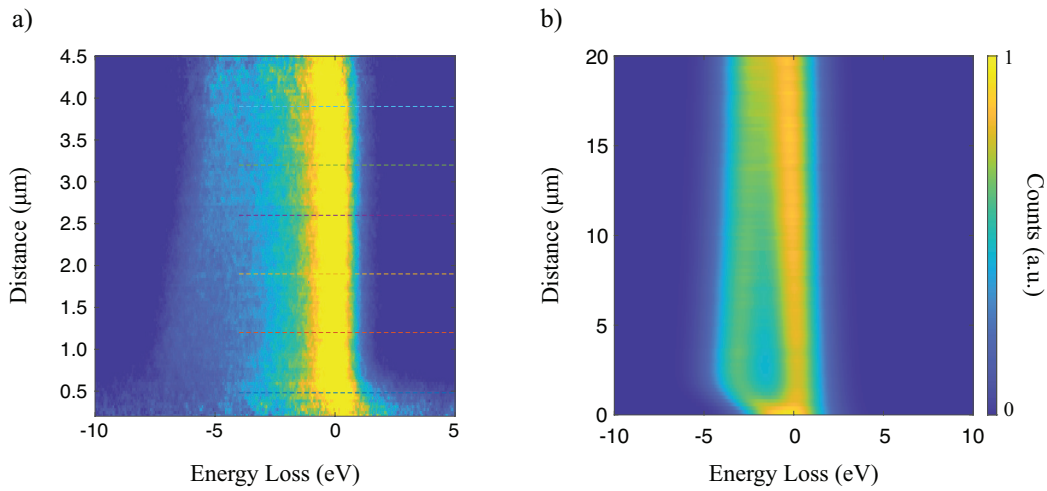


Figure CD.4: **Experimental and simulated energy-position map.** Measured (a) and simulated (b) energy-position map. In this case, the interaction manifests as the emergence of a side peak due to the accelerated electrons. In (a) the distance (0 – 4.5  $\mu\text{m}$ ) is intended with respect to the metal surface, while in (b) (0 – 20  $\mu\text{s}$ ) with the respect to the center of the electron cloud.

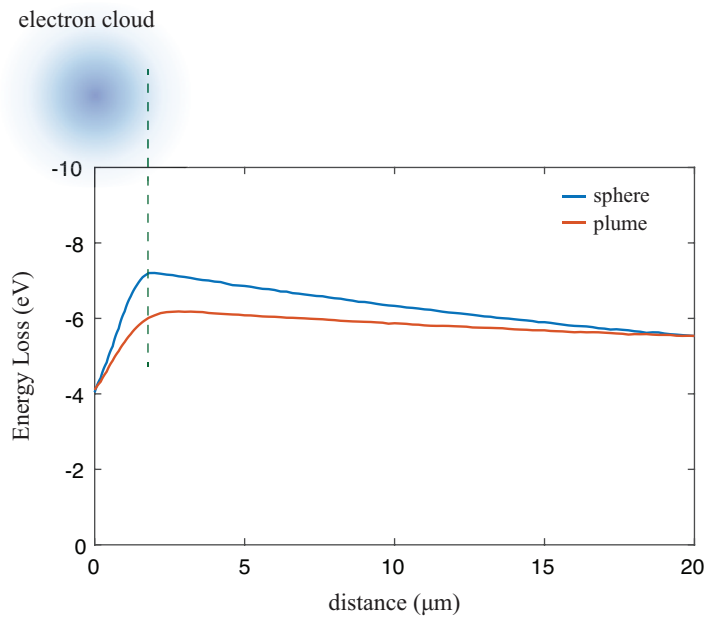


Figure CD.5: **Energy loss as a function of the distance from the center of the cloud.** A signature of the region where the cloud persists with higher density can be observed as the acceleration experienced by the e-beam diminishes when passing through it. Various geometries were tested, such as spherical and elliptical (plume), thus revealing that the behavior is also influenced by the shape of the cloud.

### Statement on my contribution

In the next section, I included the integral publication “I. Madan<sup>★</sup>, Eduardo JC Dias<sup>★</sup>, S. Gargiulo<sup>★</sup>, F. Barantani<sup>★</sup>, M. Yannai, G. Berruto, T. LaGrange, L. Piazza, T. T. Lummen, R. Dahan, I. Kaminer, G. M. Vanacore, F. J. García de Abajo, and Fabrizio Carbone. Charge dynamics electron microscopy: nanoscale imaging of femtosecond plasma dynamics, in ACS Nano, vol. 17, n. 4, p. 3657-3665, 2023.” [256]. A substantial amount of data was collected for this project across various geometries and conditions, spanning a period of approximately six years. My contribution include initial theoretical modeling and simulations (not included in the manuscript), experiments, and data analysis. Theory and simulations have been developed by Eduardo Dias and Javier García de Abajo, with inputs from me, Ivan, and Francesco.

# Charge Dynamics Electron Microscopy: Nanoscale Imaging of Femtosecond Plasma Dynamics

Ivan Madan,<sup>@</sup> Eduardo J. C. Dias,<sup>@</sup> Simone Gargiulo,<sup>@</sup> Francesco Barantani,<sup>@</sup> Michael Yannai, Gabriele Berruto, Thomas LaGrange, Luca Piazza, Tom T. A. Lummen, Raphael Dahan, Ido Kaminer, Giovanni Maria Vanacore, F. Javier García de Abajo, and Fabrizio Carbone\*



Cite This: *ACS Nano* 2023, 17, 3657–3665



Read Online

ACCESS |



Metrics & More



Article Recommendations

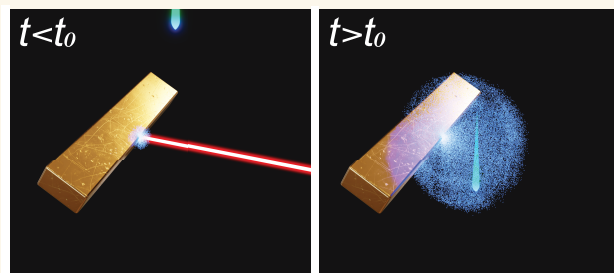


Supporting Information

**ABSTRACT:** Understanding and actively controlling the spatiotemporal dynamics of nonequilibrium electron clouds is fundamental for the design of light and electron sources, high-power electronic devices, and plasma-based applications. However, electron clouds evolve in a complex collective fashion on the nanometer and femtosecond scales, producing electromagnetic screening that renders them inaccessible to existing optical probes. Here, we solve the long-standing challenge of characterizing the evolution of electron clouds generated upon irradiation of metallic structures using an ultrafast transmission electron microscope to record the charged plasma dynamics.

Our approach to charge dynamics electron microscopy (CDEM) is based on the simultaneous detection of electron-beam acceleration and broadening with nanometer/femtosecond resolution. By combining experimental results with comprehensive microscopic theory, we provide a deep understanding of this highly out-of-equilibrium regime, including previously inaccessible intricate microscopic mechanisms of electron emission, screening by the metal, and collective cloud dynamics. Beyond the present specific demonstration, the here-introduced CDEM technique grants us access to a wide range of nonequilibrium electrodynamic phenomena involving the ultrafast evolution of bound and free charges on the nanoscale.

**KEYWORDS:** *Transmission electron microscopy, plasma dynamics, THz fields, nanoscale imaging, ultrafast dynamics*



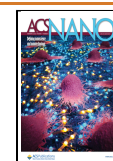
Modern ultrafast spectroscopy and microscopy strive to explore how electronic and crystal structures evolve on time scales of a few femtoseconds.<sup>1–3</sup> However, the complex spatiotemporal dynamics of charge carriers photoexcited/emitted from surfaces has so far remained largely inaccessible because of the intrinsic difficulty of simultaneously addressing the nanometer and femtosecond scales on which the associated charge and transient near-field dynamics takes place. Understanding such dynamics is essential for the exploration of previously inaccessible physics and the development of applications in high-brightness electron sources in wake-field accelerators<sup>4</sup> and RF/THz-driven emitters,<sup>5–7</sup> ultrafast power electronics,<sup>8</sup> plasma X-rays sources,<sup>9–13</sup> plasma tailoring for photon down-conversion,<sup>14</sup> and nuclear reactions in laser-generated plasma environments.<sup>15,16</sup> In these contexts, the evolution of plasma is commonly monitored through far-field radiation, and some of its properties are inferred by comparison to numerical simulations,<sup>5,17</sup> with no direct access into microscopic charge or field dynamics on their natural ultrafast

nanoscopic scale. An exemplary scenario involving complex charge dynamics is the ensuing electron cloud emission from a solid target upon irradiation by high-fluence femtosecond laser pulses (see Figure 1a). The emitted electrons evolve by following distinct stages after light absorption: electron emission, expansion, deceleration, and reabsorption (left to right in Figure 1b). These processes are strongly affected by repulsive Coulomb interactions among electrons and attractive interaction with the screening image charges created on the material surface.<sup>18,19</sup> As a result, the charge distribution close to the surface exhibits strong spatial inhomogeneities on the nanometer/femtosecond scales, which remain largely unex-

**Received:** October 20, 2022

**Accepted:** January 27, 2023

**Published:** February 13, 2023



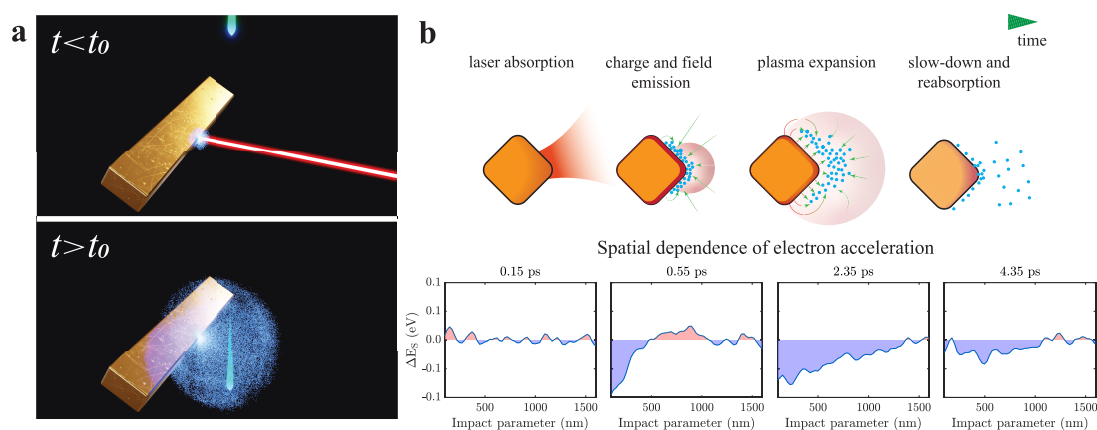


**Figure 1.** The CDEM technique and its application to image ultrafast nanoscale plasma dynamics. (a) Schematics of the studied phenomenon. A laser pulse (50 fs, 800 nm) generates a cloud of photoemitted electrons that is probed by an e-beam pulse (200 keV, 600 fs) with a tunable delay time relative to the laser pulse. (b) Differentiated stages (left to right) in the dynamics of the generated electron cloud (upper schemes) and its impact on the transmitted electrons (lower plots): initial laser irradiation; photoemission and THz field generation; explosive phase of rapid charge expansion; and charge density depletion via surface reabsorption. Lower plots show the average e-beam energy change  $\Delta E_S$  as a function of e-beam–surface distance at selected delay times (upper labels).

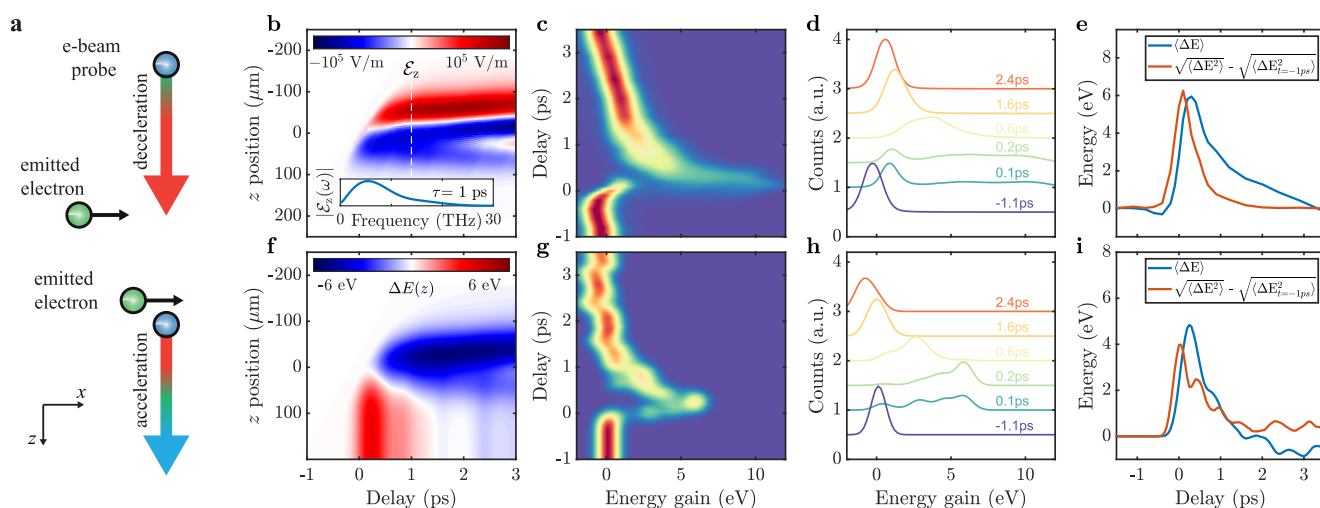


**Figure 2.** Ultrafast e-beam interactions in CDEM. (a) Sketches illustrating e-beam deceleration and acceleration stages, which result in an average net energy change, as well as spectral reshaping. (b) Simulated electric field  $E_z$  experienced by the e-beam as a function of delay and position along the trajectory ( $z = 0$  corresponding to the e-beam leveled with the tip of the metal corner in Figure 1) for an e-beam–surface separation of 100 nm. The inset shows the Fourier-transformed electric-field amplitude at a delay of 1 ps (white dashed line), peaking at 5.4 THz. (c) Transmitted electron spectra as a function of laser–e-beam delay for 100 nm e-beam–surface separation. (d) Profiles extracted from panel c at selected delays (see labels). (e) Variation of the average e-beam energy and spectrum variance as a function of delay. (f) Calculated modification of e-beam energy  $\Delta E(z)$  as a function of both electron position  $z$  and delay between optical and electron pulses as the electron experiences the effect of the electric field  $E_z$  in panel b. (g, h, i) Numerical simulations based on microscopic theory corresponding to the conditions in panels c, d, and e, respectively. The laser fluence is 189 mJ/cm<sup>2</sup>.

explored in experiments<sup>5,20</sup> despite their pivotal role in developing potential applications.

Here, we introduce an approach to access the spatiotemporal dynamics of high-density photoemitted electron clouds: charge dynamics electron microscopy (CDEM), performed in an ultrafast transmission electron microscope (UTEM) in which 50 fs, 800 nm laser pulses are used to irradiate a metallic target and 600 fs electron-beam (e-beam) pulses are probing the dynamics of the emitted electrons (Figure 1a). The spectra of the electron pulses are then recorded as a function of e-beam spatial position and delay time relative to the laser pulses. The emission and subsequent dynamics of the charge cloud generate broadband low-frequency (THz) nonconservative electromagnetic fields,

which produce a sizable overall acceleration of the transmitted e-beam. The dependence of the measured acceleration on e-beam position and delay time relative to the laser pulse reveals a wealth of information on the spatiotemporal dynamics of the electron cloud, as well as its interaction with the emitting material. The entire process involves strong dynamical screening of the exciting laser, ultrafast internal carrier dynamics and thermalization, thermionic and multiphoton photoemission, Coulomb interactions between free-space and image charges, electron–surface recollisions, the generation of low-frequency fields, and the interaction of the latter with the sampling e-beam. We supplement our experiments with a comprehensive microscopic theoretical analysis of these processes in excellent agreement



with the measured data, allowing us to conclusively establish four well-differentiated stages of charge evolution, as illustrated in Figure 1b.

## RESULTS AND DISCUSSION

The main observable in our measurements is the spatial pattern of acceleration experienced by the energetic e-beam probe after passing next to or through the emitted electron cloud. As the latter evolves, it produces time-varying electromagnetic fields that comprise low-frequency components interacting with the e-beam (1–10 THz, see inset to Figure 2b and Figure S3 in SI). The acceleration of free electrons by THz fields has been previously investigated using, for example, point-projection electron microscopy.<sup>21</sup> However, the CDEM technique performed in an UTEM represents a radical step forward in our ability to probe dense plasmas ( $10^{14}$  cm<sup>-3</sup>) of different geometries, sizes, and densities with a resolution in the nanometer/femtosecond range over a large field of view.

In our experiment, an electron cloud is photoemitted from a corner of a metal structure, expanding with drift kinetic energies of a fraction of an electronvolt. We find that the acceleration observed in the e-beam is predominantly caused by cloud charge motion along transverse directions, as schematically depicted in Figure 2a, while motion parallel to the e-beam contributes negligibly for the cloud velocities observed in our experiment. The dynamical character of the interaction is essential. In contrast, for quasi-static charge motion, as explored in deflectometry-based experiments,<sup>20,22–27</sup> the deceleration and acceleration of the probe electron before and after transit are perfectly balanced and produce no net effect. Instead, for rapidly and noninertially evolving charges, the two contributions are unbalanced and result in a net energy transfer to the e-beam (Figure 2a).

A typical temporal evolution of the measured e-beam acceleration is presented in Figure 2c,d, which shows the measured change in the electron spectrum as a function of the delay time relative to the laser pulse for a fluence of 189 mJ/cm<sup>2</sup>. The temporal dynamics consists of strong electron acceleration and spectral broadening at short delays, followed by a slow reduction of the acceleration and, eventually, even deceleration (Figure 2c,d). Qualitatively, as inferred from the schematics in Figure 2a, a net acceleration is observed if there is a current flowing perpendicularly to the motion of the e-beam, as it introduces an imbalance in the average e-beam–plasma distance as the interaction occurs. In an intuitive picture, the observed acceleration is the result of the work done on the electron by the electric field  $\mathcal{E}[\mathbf{r}_e(t), t]$  generated by the cloud electrons and image charges acting along the probe trajectory  $\mathbf{r}_e(t)$ . The electron energy change is given by the time integral

$$\Delta E = -e\mathbf{v}_e \cdot \int_{-\infty}^{\infty} dt \mathcal{E}[\mathbf{r}_e(t), t] \quad (1)$$

where  $\mathbf{v}_e$  is the e-beam velocity vector, taken to be approximately constant in the evaluation of eq 1. This expression, which represents the work done on a classical point-particle electron, can be rigorously derived from a quantum-mechanical treatment of the e-beam when the external THz field varies negligibly during the interaction time defined by  $\tau_{\text{interaction}} \sim L/v_e$ , which is  $\sim 1$  ps for an effective interaction length  $L \sim 200$   $\mu\text{m}$  (see Figure 2b) along the beam direction (see Methods).

To better understand the origin of the acceleration and estimate the effect of free and image charges, experimental

geometry, and material properties, we compare the measured data with simulations based on a comprehensive account of the different microscopic physical processes involved in the generation and evolution of the electron cloud, as well as its interaction with the probing electron (see details of the theory in Methods and Supporting Information (SI)). Figure 2b shows the calculated electric-field component parallel to the e-beam as a function of both (i) the delay between laser and e-beam pulses and (ii) the position along the electron trajectory, while the inset shows its spectral decomposition at 1 ps delay. The resulting delay- and position-dependent variation of the e-beam energy is shown in Figure 2f, as obtained from eq 1 by setting the upper integration limit to a finite time corresponding to each electron-probe position (see also Figure S3 in SI). We observe that the electric field rapidly decays away from the metal and becomes negligible at distances  $>100$   $\mu\text{m}$ , beyond which the e-beam energy remains unchanged (i.e., at the value recorded in experiment). Accounting for the finite e-beam pulse duration, we also calculate the e-beam spectrum as a function of probe delay (Figure 2g,h), finding qualitative and quantitative agreement with the experiment.

To quantitatively capture both the amplitude of the acceleration and the observed time scales, two different emission processes need to be considered: thermionic, due to the increase in electron temperature, which stays elevated during a picosecond time scale; and three-photon photoemission, which occurs within the 50 fs duration of the laser pulse (see Methods for details). At each time step in the simulation, the force exerted on every individual electron by the remaining electrons and their associated induced surface image charges is evaluated, and its position and velocity are evolved accordingly (see Figure S2 in SI for details on the plasma charge dynamics). Partial electron absorption upon recollision with the metal surface is also accounted for. The net energy variation of a probing electron after traversing the plasma is then calculated from eq 1, with the electric field obtained by summing the contributions from all emitted cloud electrons and their associated image charges, including the effect of surface geometry and retardation, and further averaging over the electron wavepacket density profile (see SI). Our simulations reveal that the contribution of the interactions with the electron cloud and the image charges produce two components of similar amplitude but with opposite signs (see Figure S1c in SI). However, image charges are constrained to the material surface, so their contribution is weaker than that of free-space charges. Effectively, the e-beam probe sees an effective dipolar field, with the dipole oriented nearly transversely with respect to the beam direction.

As shown in Figure 2e, our CDEM measurements unveil two main time scales: (i) fast plasma creation by thermionic and photoemission processes occurring faster than the electron pulse duration (fwhm  $\simeq 600$  fs); and (ii) plasma dynamics driven by space and image charges, which manifests as a gradual relaxation of the electron energy shift  $\Delta E$  over 1–2 ps. During the former, in addition to the net acceleration, we observe a substantial broadening of the electron spectrum, which we quantify by computing the second moment  $\sqrt{\langle \Delta E^2 \rangle}$ . This experimental broadening, which is also captured in our simulations, exhibits a maximum at the delay for which we encounter the largest variation of the average acceleration (Figure 2e,i), so that peak broadening and peak acceleration are mutually delayed by  $\sim 200$  fs.

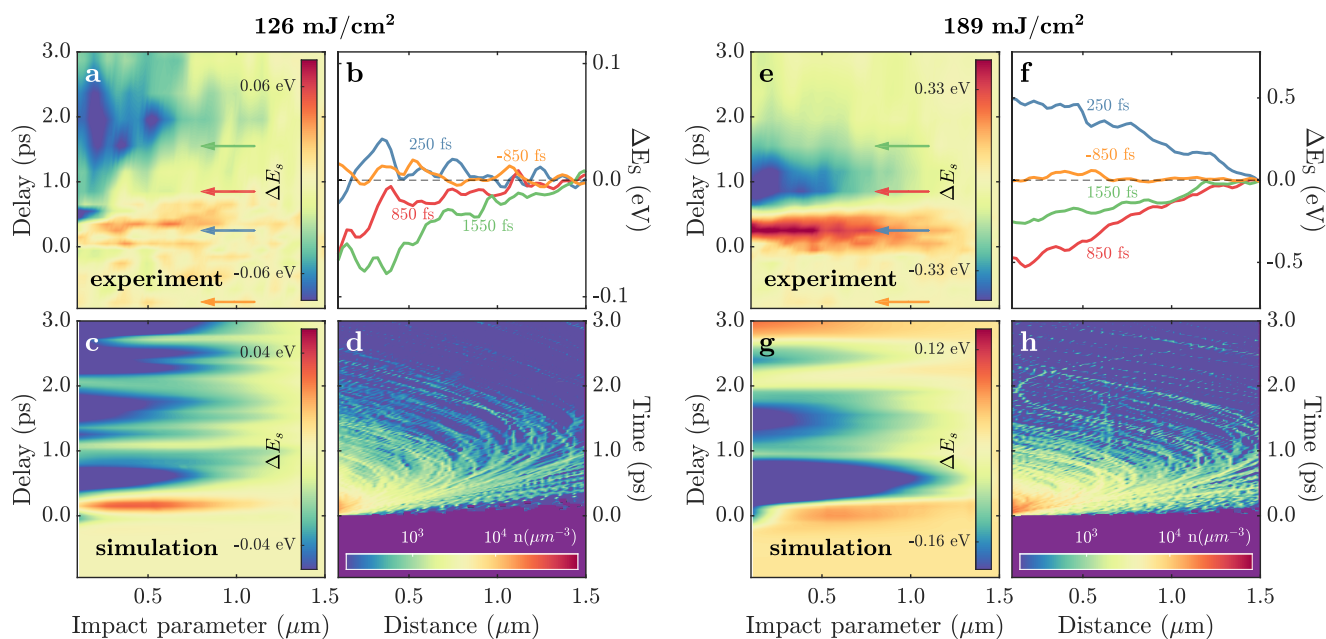


**Figure 3.** Temporal evolution of the spatial variation of the average electron acceleration. (a) Experimentally measured temporal evolution of the spatial variation of electron acceleration  $\Delta E_S$  under excitation with  $126 \text{ mJ/cm}^2$  laser pulse fluence. (b) Selected spatial profiles of  $\Delta E_S$  from panel a. (c) Theoretically calculated  $\Delta E_S$  with plasma evolution simulated under the same conditions as in panel a. (d) Simulated density of plasma electrons as a function of time and separation from the metallic surface. Panels e, f, g, and h are the same as panels a, b, c, and d, respectively, but for  $189 \text{ mJ/cm}^2$  laser pulse fluence.

The presence of free-space and image charges drastically affects the expansion and evolution of the electron cloud.<sup>18,28,29</sup> For example, charge expansion is close to ballistic at low fluences, when emitted charge densities are small. In contrast, when the cloud reaches large densities, newly emitted electrons are trapped closer to the surface due to the strong Coulomb repulsion by previously emitted electrons,<sup>18,19</sup> causing the number of electrons that permanently escape the photoexcitation region to be drastically reduced down to only a fraction  $\sim 10^{-6}$ – $10^{-8}$  of the total emission.<sup>18</sup> Those that acquire sufficient velocity to escape the photoexcitation region can be investigated by electron detectors and imaged with electron-deflection-based techniques,<sup>20,22–27</sup> while in this work we provide insight into the previously inaccessible high-density electron cloud that is eventually reabsorbed during the first few picoseconds after emission.

The spatial extension of the expanding charged plasma, its initial velocity, and the deceleration due to interaction with the image charges are all pivotal elements of information that can be extracted by studying the spatial variation of the e-beam probe acceleration in CDEM. In Figure 3, we present the spatial variation of the e-beam energy change as a function of delay time and beam position:  $\Delta E_S(t, d) = \langle E \rangle(t, d) - \langle E \rangle(t, d_{\text{max}})$ , referred to the e-beam–target separation for the maximum explored impact parameter  $d_{\text{max}} = 1.5 \mu\text{m}$ . This allows us to precisely follow the spatial dynamics developing over the average acceleration. Experimental results for  $126$  and  $189 \text{ mJ/cm}^2$  laser pulse fluence are shown in Figure 3a,e, respectively. Close to the metal surface,  $\Delta E_S$  is positive at early delay times, while it becomes negative at later delay times. This negative feature is characterized by faster rise and decay times when irradiating with a larger fluence (see selected profiles in Figure 3b,f).

Figure 3c,g shows the corresponding numerical simulations for  $\Delta E_S$ , qualitatively reproducing the experimental features,

including their time scales and variation with fluence. Some quantitative differences are observed, which we attribute to the limited precision of the theoretical results (note that  $\Delta E_S/\Delta E_{\text{max}} \sim 1\%$ ) associated with constraints on the minimum time step and spatial discretization grid in the simulations (see more details in SI). However, the order of magnitude of the observed effects is successfully reproduced.

A comparison with the evolution of the emitted electron density (Figure 3d,h) allows us to gain further insight into the relationship between the observed behavior of  $\Delta E_S$  and the charge dynamics, understand the origin of the spatial inhomogeneities in the acceleration, and hence derive important quantities such as the initial plasma expansion velocity. While Figure 3d,h shows the evolution of electron density as a function of distance from the surface, we probe experimentally the integral along the electron trajectory at a given impact parameter. At short delay times, the emitted charge cloud is localized close to the surface, and the spatial variation of the observed acceleration in Figure 3a,e is reminiscent of the power-law dependence of the near-field THz component, in accordance with eqs S12 and S13 in SI, taking into account the extended three-dimensional shape of the emitted charge. This regime is not directly observed in Figure 3d,h. As the charge cloud expands, at distances substantially outside the cloud, the acceleration displays a similar decaying component. However, as the probe electron passes through the cloud, the effect of partial screening causes a reduction in the electron beam acceleration, as manifested in the negative  $\Delta E_S$  region in Figure 3a,e, whose onset permits us to experimentally determine the initial charge expansion velocity as  $\sim 1.2 \text{ nm/fs}$ .

Due to the interaction with image charges, most of the emitted electrons slow down in the immediate vicinity of the surface and are eventually reabsorbed. This is confirmed upon inspection of individual particle trajectories in our theory (Figure 3d,h), which bend to the surface and eventually collide

Technique	PINEM	CDEM (this work)	Elastic scattering
Presence of charges	No charges	Dynamic charges	Quasistatic charges
Electron and EM timescales	$\tau_e \gg T_{EM}$	$T_{EM} \sim \tau_e \sim \tau_{Interaction}$	$T_{EM} \gg \tau_{Interaction} \sim \tau_e$
Schematics of EM fields and charges			
EM period in a typical UEM	High frequency EM fields (~1 fs)	Non-conservative EM fields (~0.1 - 1 ps)	Conservative EM fields (>1 ps)
Electron spectrum	 No net acceleration	 Acceleration	 No acceleration

**Figure 4.** Comparison between different ultrafast electron microscopy techniques and the corresponding interactions between the probe electrons and electromagnetic near fields. The table compares relevant parameters and the main differences between the techniques, relating to time scales and experimental observables. EM, electromagnetic; UEM, ultrafast electron microscope; CDEM, charge dynamics electron microscopy; PINEM, photon-induced near-field electron microscopy.

with it within a few hundred femtoseconds, while those that acquire higher speed in the initial stage are able to escape the surface-neighboring region. Electrons that are colliding with the surface do not observably influence the e-beam probe spectrum because of their reduced speed and the canceling fields originating in proximal positive (image) and negative (electron) charges.

Expansion and reabsorption of the electron cloud result in a reduction of the cloud density (see Figure S12a), which leads in turn to a gradual depletion of the negative  $\Delta E_s$  region close to the sample surface on a 1–2 ps time scale (see Figure 3a,c,e,g).

**Future Directions.** In perspective, CDEM covers a previously unexplored regime of ultrafast interaction between e-beams and near fields, as emphasized in Figure 4, which compares CDEM both to photon-induced near-field electron microscopy (PINEM)<sup>30–32</sup> and to electron microscopy methods based on elastic electron–field interactions.<sup>20,22–27</sup> The latter (Figure 4, right column) involves an optical cycle of the electromagnetic field  $T_{EM}$  that is large compared with both  $\tau_{interaction}$  and the electron pulse duration  $\tau_e$ . This regime includes Lorentz transmission electron microscopy, electron holography, deflectometry, and shadowgraphy, which are sensitive to slow quasistatic conservative electric fields.<sup>23,33</sup> On the opposite extreme, PINEM (Figure 4, left column) capitalizes on the effect of rapidly oscillating optical fields ( $T_{EM} \ll \tau_e$ ), which show up as inelastic peaks in the electron spectrum at multiples of the photon energy, usually configuring a symmetric spectrum (for nearly monochromatic illumination) with respect to the elastic peak due to the stimulated nature of the process and the large occupation number of the involved laser-driven optical modes. Under exposure to monochromatic fields, the net e-beam energy change in PINEM is zero, just like in elastic diffraction techniques. This is one key aspect by which CDEM deviates from other techniques: the electron spectrum is asymmetric, producing a sizable e-beam energy change. Indeed, the intermediate regime in which the interaction, electron-pulse,

and optical-cycle times are commensurate (Figure 4, central column) is where CDEM belongs: a natural domain to extract spatiotemporal information on the probed fields and associated sources. A unified, rigorous quantum-mechanical formalism can simultaneously capture all three regimes with a relatively simple theory (see Methods), under the approximation that the kinetic energy of the incident probe electron largely exceeds the energy change due to the interaction, as is the case here. In such a scenario, the incident wave function is multiplied by a factor involving the exponential of an action (the integrated field along the probe trajectory), which becomes an energy comb for monochromatic fields (i.e., the PINEM limit); in contrast, the same factor reduces to the energy shift given by eq 1 in the classical limit (see Methods).

In contrast to PINEM and elastic scattering, the CDEM approach allows us to follow the formation and evolution of dense plasma with nanometer/femtosecond space/time resolution. From a technological viewpoint, access to spatially resolved information offers the possibility to develop customized nanostructures that can be optimized to operate on ultrafast time scales.<sup>8</sup> Also, from a material science perspective, CDEM enables the investigation of image charge dynamics and screening time scales in out-of-equilibrium nanostructured materials, allowing us to map spatial inhomogeneities such as the formation of domains following a phase transition.

## CONCLUSIONS

Through the insight gathered from CDEM on free-space electron clouds, combined with a predictive degree of theoretical modeling, we introduce a powerful tool for the quantitative optimization of electron sources operating under extreme space-charge conditions. This has potential application in nano-patterned radiofrequency-gun electron emitters, where 100 nm sized features have been demonstrated to produce a 100-fold electron yield enhancement.<sup>34</sup> Similarly, periodic arrays of electron-plasma emitters can drastically improve the emission



efficiency on the femtosecond scale by operating in a high-plasma-density regime exceeding critical values by orders of magnitude.<sup>17</sup> CDEM is an ideal tool to diagnose such supercritical plasma, providing nanometer/femtosecond space/time-resolved imaging to optimize geometrical and compositional parameters. Similar benefits are expected in the development of plasma-based high-efficiency X-ray sources, nanoelectronic devices, and nuclear or astrophysics-in-a-lab experiments.<sup>35</sup>

The intense nanoscale THz fields produced by the diagnosed plasma hold strong potential for use in the spatial, angular, and spectral compression of e-beams, enabling finer spatiotemporal control with respect to traditional THz-based approaches.<sup>36,37</sup> CDEM could thus be applied to manipulate the wave function of free electrons in ways that existing techniques such as PINEM cannot. In addition, the photon statistics of the THz field associated with the out-of-equilibrium plasma remains as a fundamental question<sup>38</sup> that cannot be addressed with conventional quantum-optics techniques because of the limited speed and sensitivity of available THz photodetectors.<sup>39–41</sup> CDEM is thus offering a viable approach to characterize the statistics of near-field photons at low frequencies.

## METHODS

**Sample Preparation and UTEM Experiments.** For the experiments reported, we used a copper 100 Mesh PELCO grid. The grid was tilted by 45° with respect to the *z* direction (parallel to the TEM column axis) in order to expose the corner of a rectangular copper rod with a cross section of  $\sim 50 \times 25 \mu\text{m}^2$  (see Figure S1 in SI). The edge of the rod corner exhibited a radius of curvature of 4  $\mu\text{m}$ , as estimated from SEM micrographs. The sample was positioned such that only one of the edges of the rectangular rod was illuminated by the laser pulse.

To generate the charged plasma, we irradiated the copper rod with near-infrared laser pulses of 1.55 eV central photon energy (800 nm) and 50 fs temporal duration at a repetition rate of 100 kHz, which corresponds to  $\approx 2.5 \text{ TW}/\text{cm}^2$ . In the reported experiments, light polarization was vertical (i.e., along the propagation direction of the probe electron). Light entered the microscope through the zero-angle port and was focused under normal incidence on the copper rod via an external plano-convex lens. In such a geometry, the light beam was also perpendicular with respect to the electron propagation direction.

The dynamics of the photoemitted electrons was then probed by means of electron pulses with a temporal duration of about 600 fs and with a controlled delay between electron and laser pulses. All the experiments were performed in a modified JEOL 2100 TEM microscope at an acceleration voltage of 200 kV.<sup>42,43</sup> The probe electrons were generated by illuminating a LaB<sub>6</sub> cathode with third-harmonics UV light at 4.65 eV photon energy.

Our transmission electron microscope was equipped with EELS capabilities coupled to real-space imaging. Energy-resolved spectra were recorded using a Gatan-Imaging-Filter (GIF) camera operated with a 0.05 eV-per-channel dispersion setting and typical exposure times of the CCD sensor from 30 to 60 s. For the acquisition of space-energy maps (see Figure 3), special care was devoted to sample alignment. The copper rod was adjusted to be parallel to the energy dispersion direction and placed at the edge of the spectrometer entrance aperture.

The acquired position-dependent spectra were analyzed as a function of delay between the laser and electron pulses, with the time zero being determined as the peak of PINEM signal observed within 100 nm close to the sample surface at relatively low fluence ( $\approx 50 \text{ mJ}/\text{cm}^2$ ). Camera noise and signal from cosmic events were reduced by applying median filtering. Distortions of the spectrometer were corrected by aligning the spectrum according to the negative delay energy-space spectrographs ( $-2 \text{ ps}$ ). The first and second moments of the spectrum were calculated in a reduced energy window, which was taken 10 eV larger than the region in which the electron signal was above 10% of the peak value

(i.e., the maximum value among all delays and positions measured for a given fluence). This procedure helped to reduce contributions from the CCD background noise.

Regarding sample stability, special care was taken to ensure experimentally reproducible results and a controlled environment. Standard TEM grids from the same batch were used for all the experiments. The oxide layer was removed from the surface by washing the grids in acetic acid for approximately 5 min. Among other reasons, relatively fine-pitch grids were selected to avoid resonant vibrations due to a large periodic thermal load. In experiments, the smearing of the sample edge did not exceed the resolution of  $\approx 50 \text{ nm}$  defined by the magnification settings and aberrations in the photoelectron mode of TEM operation. At the highest measured fluence, we observed a degradation of the signal of the order of  $\approx 10\%$  of the peak acceleration over 2 h of experimental time. We made sure to expose a fresh part of the sample to laser illumination at least every 60 min. Sample edge images were realigned for each measurement during data analysis. At fluences above  $500 \text{ mJ}/\text{cm}^2$ , we observed ablation of the sample on a time scale of several minutes.

**Classical Limit for the Energy Loss Experienced by a Free Electron Traversing an Optical Field.** We derive a classical limit for the interaction between a collimated free electron and a classical electromagnetic field starting from a quantum-mechanical expression that bears general validity in the nonrecoil approximation.

Under the experimental conditions, the free electron probe has a small energy spread relative to its average kinetic energy both before and after the interaction. We can therefore adopt the nonrecoil approximation<sup>44</sup> and introduce the interaction with a classical field through the Hamiltonian  $(ev/c)A_z$ , where  $v$  is the electron velocity and  $A_z$  is the vector potential component along the beam direction  $z$  in the Coulomb gauge, for which the scalar potential vanishes within the vacuum space traversed by the electron. We further consider a finite interaction region, in which  $v$  is assumed to remain constant, such that the wave function depends on the longitudinal coordinate  $z$  and time  $t$  only through  $z - vt$ . Under these conditions, starting from an incident electron wave function  $\psi^0(z, t)$ , the postinteraction wave function reduces to<sup>32,44,45</sup>

$$\psi(z, t) = \psi^0(z, t) \exp \left\{ -\frac{iev}{\hbar c} \int_{-\infty}^{\infty} dt' A_z(z - vt + vt', t') \right\} \quad (2)$$

where an implicit dependence on transverse coordinates  $(x, y)$  is understood.

The evaluation of eq 2 for either monochromatic fields or optical pulses of short duration compared with the optical period reduces the exponential factor to a well-known sum over energy sidebands that accurately describes experimentally observed PINEM spectra.<sup>45</sup> In contrast, in the present work, the electron is exposed to external fields comprising components whose optical cycles are long compared to the interaction time  $L/v$  (see main text). It is then pertinent to Taylor-expand the slowly varying vector potential  $A_z(z - vt + z', t')$  around small values of  $z - vt$ , assuming the centroid of the electron wavepacket to follow the trajectory  $z = vt$ . The independent term in this expansion contributes with an overall phase  $\varphi = -(ev/\hbar c) \int_{-\infty}^{\infty} dt A_z(vt, t)$  that does not affect the transmitted electron spectrum. Retaining only the linear term in  $z - vt$ , eq 2 reduces to

$$\psi(z, t) = \psi^0(z, t) e^{i\varphi} \exp\{i(\Delta E/\hbar)(z/v - t)\} \quad (3)$$

where

$$\begin{aligned} \Delta E &= -\frac{ev}{c} \int_{-\infty}^{\infty} dz' \partial_z A_z(z', z'/v)|_{z'=z} \\ &= -\frac{e}{c} \int_{-\infty}^{\infty} dz' [v \partial_z A_z(z', z'/v) - \partial_t A_z(z', t)|_{t=z/v}] \\ &= -e \int_{-\infty}^{\infty} dz' \mathcal{E}_z(z', z'/v) \end{aligned} \quad (4)$$

represents the energy change experienced by a classical point electron moving along the noted trajectory. In the derivation of this expression, the first term in the second line cancels upon integration by parts for a

field of finite extension along the electron trajectory (i.e., localized at the interaction region), and we have identified

$$-(1/c)\partial_t A_z(z, t) = \mathcal{E}_z(z, t)$$

with the electric field component along the beam direction to obtain the third line. In summary, the wave function in eq 3 is the incident one multiplied by an irrelevant phase factor  $e^{i\phi}$  as well as by a plane wave  $e^{i(\Delta E/\hbar)(z/v-t)}$  representing a rigid shift in energy by  $\Delta E$  (and a corresponding change in momentum by  $\Delta E/v$  within the nonrecoil approximation). From eq 4, we then recover eq 1 by setting  $z' = vt$ . Corrections of higher-order terms in the aforementioned Taylor expansion may become relevant for electron wavepacket durations similar to or larger than either the optical cycle or the temporal extension of the external field.

**Numerical Simulations.** In this section, we describe the main aspects of the theoretical model employed to simulate the experimental results presented in this work. Additional details can be found in SI.

First, we model the temperature dynamics  $T(t, s)$  in the inner surface of the copper bar as a function of time  $t$  and surface position  $s$  using the two-temperature model (see Figure S1 in SI). The pump illumination is introduced through the near-field distribution calculated in the inner surface through the boundary-element method.<sup>46</sup>

We then model electron emission as a function of local temperature  $T$  from two different channels: thermionic emission, due to the heightened temperature of the surface electrons, which extends over a few picoseconds and we evaluate using a surface-barrier model; and three-photon photoemission, resulting from the absorption of three photons by one electron during the duration of the pumping <100 fs, calculated using the Fowler–Dubridge model (see SI for details). For the latter, we have used a likelihood of emission parameter  $a_3 \sim 0.5 \times 10^{-35} \text{ cm}^6/\text{A}^3$  that is an order of magnitude lower than previously reported estimates in copper,<sup>47,48</sup> which we attribute primarily to a saturation effect due to the high pump laser fluences used in this work<sup>49</sup> (see SI for further discussion).

Combining these results, we simulate the emission of photoelectrons at each instant of time and surface position, which gives rise to a density of photoemitted electrons  $\rho_e(\mathbf{R}, t)$  as a function of spatial position  $\mathbf{R}$  and time  $t$ . The evolution of the plasma density is then simulated by discretizing time and considering, at each time step, the force acting on each of the photoemitted electrons by all the remaining ones, as well as the interaction with the copper bar. The latter is introduced by rigorously accounting for the accumulation of positive image charges at the copper surface due to the presence of the negatively charged electrons in its vicinity. The position and velocity of each electron is then evolved according to the net force exerted on it. The eventual collision of the photoemitted electrons with the surface gives rise to partial reabsorption according to the barrier model, as well as specular reflection of the nonabsorbed electrons. This procedure allows us to determine  $\rho_e(\mathbf{R}, t)$  for the full duration of the simulation (see Figure S2 in SI).

Finally, we calculate the energy variation by a probe electron passing with velocity  $\mathbf{v}_e$  at a distance  $b$  from the copper bar along a trajectory  $\mathbf{r}_e(t) = \mathbf{r}_0 + \mathbf{v}_e(t - \tau)$ , where  $\mathbf{r}_0$  is the nearest point to the copper bar and  $\tau$  is the delay of the probe electron with respect to the laser pump. At each time  $t$ , we calculate the electric field  $\mathcal{E}$  at the probe electron position  $\mathbf{r}_e(t)$  generated by all of the plasma electrons and their corresponding surface charges, taking into account retardation effects and averaging over the time duration of the electron wavepacket (see SI for additional details). The net energy variation by the probe electron, which is a function of  $b$  and  $\tau$ , is finally obtained by using eq 1.

## ASSOCIATED CONTENT

### Supporting Information

The Supporting Information is available free of charge at <https://pubs.acs.org/doi/10.1021/acsnano.2c10482>.

Movie of time evolution of the electron energy variation (MP4)

Methods for numerical simulations of surface temperature dynamics, electronic emission, charge dynamics, and energy variation of the probe electron, numerical simulation details, plasma charge dynamics, energy variation of the probe electron, and ultrafast e-beam interactions in CDEM under 126 mJ/cm<sup>2</sup> laser pulse (PDF)

## AUTHOR INFORMATION

### Corresponding Author

Fabrizio Carbone – *Institute of Physics, École Polytechnique Fédérale de Lausanne, Lausanne 1015, Switzerland;*  
Email: [fabrizio.carbone@epfl.ch](mailto:fabrizio.carbone@epfl.ch)

### Authors

Ivan Madan – *Institute of Physics, École Polytechnique Fédérale de Lausanne, Lausanne 1015, Switzerland;* [orcid.org/0000-0002-0137-8537](https://orcid.org/0000-0002-0137-8537)

Eduardo J. C. Dias – *ICFO-Institut de Ciències Fotoniques, The Barcelona Institute of Science and Technology, Castelldefels, Barcelona 08860, Spain*

Simone Gargiulo – *Institute of Physics, École Polytechnique Fédérale de Lausanne, Lausanne 1015, Switzerland;*  
[orcid.org/0000-0002-7820-3372](https://orcid.org/0000-0002-7820-3372)

Francesco Barantani – *Institute of Physics, École Polytechnique Fédérale de Lausanne, Lausanne 1015, Switzerland;*  
*Department of Quantum Matter Physics, University of Geneva, Geneva 1211, Switzerland;* [orcid.org/0000-0002-2053-1365](https://orcid.org/0000-0002-2053-1365)

Michael Yannai – *Department of Electrical and Computer Engineering, Technion Israel Institute of Technology, Haifa 32000, Israel;* [orcid.org/0000-0002-8482-1871](https://orcid.org/0000-0002-8482-1871)

Gabriele Berruto – *Institute of Physics, École Polytechnique Fédérale de Lausanne, Lausanne 1015, Switzerland*

Thomas LaGrange – *Institute of Physics, École Polytechnique Fédérale de Lausanne, Lausanne 1015, Switzerland*

Luca Piazza – *Institute of Physics, École Polytechnique Fédérale de Lausanne, Lausanne 1015, Switzerland*

Tom T. A. Lummen – *BSSE Single Cell Facility, ETH Zurich, Basel 4058, Switzerland;* [orcid.org/0000-0003-0376-3794](https://orcid.org/0000-0003-0376-3794)

Raphael Dahan – *Department of Electrical and Computer Engineering, Technion Israel Institute of Technology, Haifa 32000, Israel*

Ido Kaminer – *Department of Electrical and Computer Engineering, Technion Israel Institute of Technology, Haifa 32000, Israel*

Giovanni Maria Vanacore – *Institute of Physics, École Polytechnique Fédérale de Lausanne, Lausanne 1015, Switzerland;*  
*Department of Materials Science, University of Milano-Bicocca, Milano 20126, Italy;* [orcid.org/0000-0002-7228-7982](https://orcid.org/0000-0002-7228-7982)

F. Javier García de Abajo – *ICFO-Institut de Ciències Fotoniques, The Barcelona Institute of Science and Technology, Castelldefels, Barcelona 08860, Spain;*  
*ICREA, Institució Catalana de Recerca i Estudis Avançats, Barcelona 08010, Spain;* [orcid.org/0000-0002-4970-4565](https://orcid.org/0000-0002-4970-4565)

Complete contact information is available at:  
<https://pubs.acs.org/doi/10.1021/acsnano.2c10482>

## Author Contributions

<sup>@</sup>I.M., E.J.C.D., S.G., and F.B. contributed equally to this work. F.C., G.M.V., and I.M. conceived the project. F.C. supervised the project. I.M., F.B., G.M.V., and S.G. performed the experiments. I.M., F.B., G.M.V., and S.G. analyzed the data. E.J.C.D. and F.J.G.A. developed the theory. E.J.C.D. performed the numerical simulations with input from S.G., I.M., F.B., and M.Y. All authors contributed to the writing of the paper. All authors discussed the results.

## Notes

We note that the parallel work (M. Yannai et al. "Ultrafast Electron Microscopy of Nanoscale Charge Dynamics in Semiconductors") has simultaneously demonstrated CDEM in a different field for the visualization of dynamic charges inside a semiconducting material. The preliminary results of both papers were first presented as two abstracts at CLEO 2021.<sup>50,51</sup> The preprint version of this paper is available on arXiv: Ivan Madan, Eduardo J. C. Dias, Simone Gargiulo, Francesco Barantani, Michael Yannai, Gabriele Berruto, Thomas LaGrange, Luca Piazza, Tom T. A. Lummen, Raphael Dahan, Ido Kaminer, Giovanni Maria Vanacore, F. Javier García de Abajo, Fabrizio Carbone, Charge dynamics electron microscopy: nanoscale imaging of femtosecond plasma dynamics, 2022, arXiv:2206.02546, <https://arxiv.org/abs/2206.02546>. The authors declare no competing financial interest.

## ACKNOWLEDGMENTS

We thank I. Furno and P. Ricci for insightful discussions, V. Leccese for sample dimensions characterization, and Y. Benhabib for help with graphics. This work is supported in part by European Union (Horizon 2020 Research and Innovation Program under Grant Agreement No. 964591 SMART-electron), the European Research Council (ERC Advanced Grant 789104-eNANO and ERC Staring Grant 851780-NanoEP), the Spanish MICINN (PID2020-112625GB-I00 and SEV2015-0522), the Catalan CERCA Program, the Generalitat de Catalunya, and Google Inc. M.Y. and R.D. are partially supported by the VATAT Quantum Science and Technology scholarship.

## REFERENCES

- (1) Vanacore, G. M.; Fitzpatrick, A. W.; Zewail, A. H. Four-Dimensional Electron Microscopy: Ultrafast Imaging, Diffraction and Spectroscopy in Materials Science and Biology. *Nano Today* **2016**, *11*, 228–249.
- (2) Sobota, J. A.; He, Y.; Shen, Z. X. Angle-Resolved Photoemission Studies of Quantum Materials. *Rev. Mod. Phys.* **2021**, *93*, 025006.
- (3) Maiuri, M.; Garavelli, M.; Cerullo, G. Ultrafast Spectroscopy: State of the Art and Open Challenges. *J. Am. Chem. Soc.* **2020**, *142*, 3–15.
- (4) He, Z.-H.; Thomas, A. G. R.; Beaulieu, B.; Nees, J. A.; Hou, B.; Malka, V.; Krushelnick, K.; Faure, J. Electron Diffraction Using Ultrafast Electron Bunches from a Laser-Wakefield Accelerator at kHz Repetition Rate. *Appl. Phys. Lett.* **2013**, *102*, 064104.
- (5) Musumeci, P.; Moody, J. T.; Scoby, C. M.; Gutierrez, M. S.; Westfall, M.; Li, R. K. Capturing Ultrafast Structural Evolutions with a Single Pulse of MeV Electrons: Radio Frequency Streak Camera Based Electron Diffraction. *J. Appl. Phys.* **2010**, *108*, 114513.
- (6) Lange, S. L.; Noori, N. K.; Kristensen, T. M. B.; Steenberg, K.; Jepsen, P. U. Ultrafast THz-Driven Electron Emission from Metal Metasurfaces. *J. Appl. Phys.* **2020**, *128*, 070901.
- (7) Huang, W. R.; Fallahi, A.; Wu, X.; Cankaya, H.; Calendron, A.-L.; Ravi, K.; Zhang, D.; Nanni, E. A.; Hong, K.-H.; Kärtner, F. X. Terahertz-Driven, All-Optical Electron Gun. *Optica* **2016**, *3*, 1209.
- (8) Samizadeh Nikoo, M.; Jafari, A.; Perera, N.; Zhu, M.; Santoruvo, G.; Matioli, E. Nanoplasma-Enabled Picosecond Switches for Ultrafast Electronics. *Nature* **2020**, *579*, 534–539.
- (9) Miaja-Avila, L.; O'Neil, G. C.; Joe, Y. I.; Alpert, B. K.; Damrauer, N. H.; Dorise, W. B.; Fatur, S. M.; Fowler, J. W.; Hilton, G. C.; Jimenez, R.; Reintsema, C. D.; Schmidt, D. R.; Silverman, K. L.; Swetz, D. S.; Tatsuno, H.; Ullom, J. N. Ultrafast Time-Resolved Hard X-Ray Emission Spectroscopy on a Tabletop. *Physical Review X* **2016**, *6*, 031047.
- (10) Fullagar, W.; Harbst, M.; Canton, S.; Uhlig, J.; Walczak, M.; Wahlström, C.-G.; Sundström, V. A Broadband Laser Plasma X-Ray Source for Application in Ultrafast Chemical Structure Dynamics. *Rev. Sci. Instrum.* **2007**, *78*, 115105.
- (11) Bargheer, M.; Zhavoronkov, N.; Gritsai, Y.; Woo, J. C.; Kim, D. S.; Woerner, M.; Elsaesser, T. Coherent Atomic Motions in a Nanostructure Studied by Femtosecond X-Ray Diffraction. *Science* **2004**, *306*, 1771–1773.
- (12) Sokolowski-Tinten, K.; Blome, C.; Dietrich, C.; Tarasevitch, A.; Horn von Hoegen, M.; von der Linde, D.; Cavalleri, A.; Squier, J.; Kammler, M. Femtosecond X-Ray Measurement of Ultrafast Melting and Large Acoustic Transients. *Phys. Rev. Lett.* **2001**, *87*, 225701–225701–4.
- (13) Higashiguchi, T.; Dojyo, N.; Hamada, M.; Sasaki, W.; Kubodera, S. Low-debris, Efficient Laser-Produced Plasma Extreme Ultraviolet Source by Use of a Regenerative Liquid Microjet Target Containing Tin Dioxide (SnO<sub>2</sub>) Nanoparticles. *Appl. Phys. Lett.* **2006**, *88*, 201503.
- (14) Nie, Z.; Pai, C. H.; Hua, J.; Zhang, C.; Wu, Y.; Wan, Y.; Li, F.; Zhang, J.; Cheng, Z.; Su, Q.; Liu, S.; Ma, Y.; Ning, X.; He, Y.; Lu, W.; Chu, H. H.; Wang, J.; Mori, W. B.; Joshi, C. Relativistic Single-Cycle Tunable Infrared Pulses Generated from a Tailored Plasma Density Structure. *Nat. Photonics* **2018**, *12*, 489–494.
- (15) Wu, Y.; Gunst, J.; Keitel, C. H.; Pálffy, A. Tailoring Laser-Generated Plasmas for Efficient Nuclear Excitation by Electron Capture. *Phys. Rev. Lett.* **2018**, *120*, 052504.
- (16) Gunst, J.; Wu, Y.; Keitel, C. H.; Pálffy, A. Nuclear Excitation by Electron Capture in Optical-Laser-Generated Plasmas. *Phys. Rev. E* **2018**, *97*, 063205.
- (17) Samsonova, Z.; Höfer, S.; Kaymak, V.; Ališauskas, S.; Shumakova, V.; Pugžlys, A.; Baltuška, A.; Siefke, T.; Kroker, S.; Pukhov, A.; Rosmej, O.; Uschmann, I.; Spielmann, C.; Kartashov, D. Relativistic Interaction of Long-Wavelength Ultrashort Laser Pulses with Nanowires. *Physical Review X* **2019**, *9*, 021029.
- (18) Wendelen, W.; Autrique, D.; Bogaerts, A. Space Charge Limited Electron Emission from a Cu Surface under Ultrashort Pulsed Laser Irradiation. *Appl. Phys. Lett.* **2010**, *96*, 051121.
- (19) Tao, S.; Wu, B. Early-Stage Effects of Residual Charges in a Metal Target on Emitted Electrons Induced by Femtosecond Laser–Metal Interactions. *Physics Letters A* **2017**, *381*, 404–407.
- (20) Schäfer, S.; Liang, W.; Zewail, A. H. Structural Dynamics and Transient Electric-Field Effects in Ultrafast Electron Diffraction from Surfaces. *Chem. Phys. Lett.* **2010**, *493*, 11–18.
- (21) Hergert, G.; Wöste, A.; Vogelsang, J.; Quenzel, T.; Wang, D.; Gross, P.; Lienau, C. Probing Transient Localized Electromagnetic Fields Using Low-Energy Point-Projection Electron Microscopy. *ACS Photonics* **2021**, *8*, 2573–2580.
- (22) Zandi, O.; Sykes, A. E.; Cornelius, R. D.; Alcorn, F. M.; Zerbe, B. S.; Duxbury, P. M.; Reed, B. W.; van der Veen, R. M. Transient Lensing from a Photoemitted Electron Gas Imaged by Ultrafast Electron Microscopy. *Nat. Commun.* **2020**, *11*, 3001.
- (23) Sun, S.; Sun, X.; Bartles, D.; Wozniak, E.; Williams, J.; Zhang, P.; Ruan, C. Y. Direct Imaging of Plasma Waves using Ultrafast Electron Microscopy. *Structural Dynamics* **2020**, *7*, 064301.
- (24) Scoby, C. M.; Li, R. K.; Musumeci, P. Effect of an Ultrafast Laser Induced Plasma on a Relativistic Electron Beam to Determine Temporal Overlap in Pump-Probe Experiments. *Ultramicroscopy* **2013**, *127*, 14–18.
- (25) Hebeisen, C. T.; Sciaini, G.; Harb, M.; Ernstorfer, R.; Kruglik, S. G.; Miller, R. J. D. Direct Visualization of Charge Distributions during



Femtosecond Laser Ablation of a Si (100) Surface. *Phys. Rev. B* **2008**, *78*, 081403.

(26) Li, J.; Wang, X.; Chen, Z.; Clinite, R.; Mao, S. S.; Zhu, P.; Sheng, Z.; Zhang, J.; Cao, J. Ultrafast Electron Beam Imaging of Femtosecond Laser-Induced Plasma Dynamics. *J. Appl. Phys.* **2010**, *107*, 083305.

(27) Raman, R. K.; Tao, Z.; Han, T. R.; Ruan, C. Y. Ultrafast Imaging of Photoelectron Packets Generated from Graphite Surface. *Appl. Phys. Lett.* **2009**, *95*, 181108.

(28) Riffe, D. M.; More, R. M.; Wang, X. Y.; Downer, M. C.; Fisher, D. L.; Tajima, T.; Erskine, J. L. Femtosecond Thermionic Emission from Metals in the Space-Charge-Limited Regime. *Journal of the Optical Society of America B* **1993**, *10*, 1424.

(29) Wendelen, W.; Mueller, B.; Autrique, D.; Rethfeld, B.; Bogaerts, A. Space Charge Corrected Electron Emission from an Aluminum Surface under Non-Equilibrium Conditions. *J. Appl. Phys.* **2012**, *111*, 113110.

(30) Barwick, B.; Flannigan, D. J.; Zewail, A. H. Photon-Induced Near-Field Electron Microscopy. *Nature* **2009**, *462*, 902–906.

(31) García de Abajo, F. J.; Asenjo-García, A.; Kociak, M. Multiphoton Absorption and Emission by Interaction of Swift Electrons with Evanescent Light Fields. *Nano Lett.* **2010**, *10*, 1859–1863.

(32) Park, S. T.; Lin, M.; Zewail, A. H. Photon-Induced Near-Field Electron Microscopy (PINEM): Theoretical and Experimental. *New J. Phys.* **2010**, *12*, 123028.

(33) Centurion, M.; Reckenthaler, P.; Trushin, S. A.; Krausz, F.; Fill, E. E. Picosecond Electron Deflectometry of Optical-Field Ionized Plasmas. *Nat. Photonics* **2008**, *2*, 315–318.

(34) Li, R. K.; To, H.; Andonian, G.; Feng, J.; Polyakov, A.; Scoby, C. M.; Thompson, K.; Wan, W.; Padmore, H. A.; Musumeci, P. Surface-Plasmon Resonance-Enhanced Multiphoton Emission of High-Brightness Electron Beams from a Nanostructured Copper Cathode. *Phys. Rev. Lett.* **2013**, *110*, 074801.

(35) Zhang, P.; Ang, Y. S.; Garner, A. L.; Valfells, Á.; Luginsland, J. W.; Ang, L. K. Space-Charge Limited Current in Nanodiodes: Ballistic, Collisional, and Dynamical Effects. *J. Appl. Phys.* **2021**, *129*, 100902.

(36) Ehberger, D.; Mohler, K. J.; Vasileiadis, T.; Ernstorfer, R.; Waldecker, L.; Baum, P. Terahertz Compression of Electron Pulses at a Planar Mirror Membrane. *Physical Review Applied* **2019**, *11*, 024034.

(37) Kealhofer, C.; Schneider, W.; Ehberger, D.; Ryabov, A.; Krausz, F.; Baum, P. All-Optical Control and Metrology of Electron Pulses. *Science* **2016**, *352*, 429–433.

(38) Dahan, R.; Gorlach, A.; Haeusler, U.; Karnieli, A.; Eyal, O.; Yousefi, P.; Segev, M.; Arie, A.; Eisenstein, G.; Hommelhoff, P.; Kaminer, I. Imprinting the Quantum Statistics of Photons on Free Electrons. *Science* **2021**, *373*, eabj7128.

(39) Kitaeva, G. K.; Yakunin, P. V.; Kornienko, V. V.; Penin, A. N. Absolute Brightness Measurements in the Terahertz Frequency Range using Vacuum and Thermal Fluctuations as References. *Appl. Phys. B: Laser Opt.* **2014**, *116*, 929–937.

(40) Kutas, M.; Haase, B.; Bickert, P.; Riexinger, F.; Molter, D.; von Freymann, G. Terahertz Quantum Sensing. *Science Advances* **2020**, *6*, eaaz8065.

(41) Prudkovskii, P.; Leontyev, A.; Kuznetsov, K.; Kitaeva, G. Towards Measuring Terahertz Photon Statistics by a Superconducting Bolometer. *Sensors* **2021**, *21*, 4964.

(42) Piazza, L.; Masiel, D.; LaGrange, T.; Reed, B.; Barwick, B.; Carbone, F. Design and Implementation of a fs-Resolved Transmission Electron Microscope Based on Thermionic Gun Technology. *Chem. Phys.* **2013**, *423*, 79–84.

(43) Piazza, L.; Cottet, M.; Carbone, F.; Masiel, D.; LaGrange, T. Principles and Implementation of an Ultrafast Transmission Electron Microscope. *Microscopy and Microanalysis* **2012**, *18*, 600–601.

(44) García de Abajo, F. J.; Di Giulio, V. Optical Excitations with Electron Beams: Challenges and Opportunities. *ACS Photonics* **2021**, *8*, 945–974.

(45) Vanacore, G. M.; Madan, I.; Berruto, G.; Wang, K.; Pomarico, E.; Lamb, R. J.; McGrouther, D.; Kaminer, I.; Barwick, B.; García de Abajo, F. J.; Carbone, F. Attosecond Coherent Control of Free-Electron Wave

Functions using Semi-Infinite Light Fields. *Nat. Commun.* **2018**, *9*, 2694.

(46) García de Abajo, F. J.; Howie, A. Retarded field calculation of electron energy loss in inhomogeneous dielectrics. *Phys. Rev. B* **2002**, *65*, 115418.

(47) Musumeci, P.; Cultrera, L.; Ferrario, M.; Filippetto, D.; Gatti, G.; Gutierrez, M.; Moody, J.; Moore, N.; Rosenzweig, J.; Scoby, C.; et al. Multiphoton Photoemission from a Copper Cathode Illuminated by Ultrashort Laser Pulses in an RF Photoinjector. *Physical review letters* **2010**, *104*, 084801.

(48) Tsang, T.; Srinivasan-Rao, T.; Fischer, J. Surface-Plasmon Field-Enhanced Multiphoton Photoelectric Emission from Metal Films. *Phys. Rev. B* **1991**, *43*, 8870.

(49) Fujimoto, J.; Liu, J.; Ippen, E.; Bloembergen, N. Femtosecond Laser Interaction with Metallic Tungsten and Nonequilibrium Electron and Lattice Temperatures. *Phys. Rev. Lett.* **1984**, *53*, 1837.

(50) Yannai, M.; Dahan, R.; Gorlach, A.; Rivera, N.; Wang, K.; Vanacore, G. M.; Carbone, F.; García de Abajo, F. J.; Kaminer, I. Demonstration of Near-field THz Spectroscopy Using Ultrafast Electron Microscopy. In *Conference on Lasers and Electro-Optics*; Kang, J., et al., Eds.; Optica Publishing Group, **2021**; paper SW2K.4.

(51) Gargiulo, S.; Madan, I.; Barantani, F.; Berruto, G.; Yannai, M.; Dias, E. J. C.; Dahan, R.; Kaminer, I.; Vanacore, G. M.; García de Abajo, F. J.; Carbone, F. Charge Dynamics Electron Microscopy. In *Conference on Lasers and Electro-Optics*; Kang, J., et al., Eds.; Optica Publishing Group, **2021**; paper FM1O.3.

## Recommended by ACS

### Plasmonic Nonlinear Energy Transfer Enhanced Second Harmonic Generation Nanoscopy

Yoonsoo Rho, Costas P. Grigoropoulos, et al.

FEBRUARY 27, 2023  
NANO LETTERS

READ 

### All-Water Etching-Free Electron Beam Lithography for On-Chip Nanomaterials

Xiaohan Wang, Guifu Zou, et al.

FEBRUARY 20, 2023  
ACS NANO

READ 

### “Trojan Horse” Type Internalization Increases the Bioavailability of Mercury Sulfide Nanoparticles and Methylation after Intracellular Dissolution

Yingying Guo, Guibin Jiang, et al.

JANUARY 23, 2023  
ACS NANO

READ 

### Multispectral Localized Surface Plasmon Resonance (msLSPR) Reveals and Overcomes Spectral and Sensing Heterogeneities of Single Gold Nanoparticles

Stephen Palani, Xiaolin Nan, et al.

JANUARY 19, 2023  
ACS NANO

READ 

Get More Suggestions >

# A Appendix

## A.1 $I=0^{+-}$ isomeric states

Table A.1: **Isomer states with  $0^{+-}$  total nuclear angular momentum.** Assignments between round brackets are uncertain. Data retrieved from the LiveChart of Nuclides database [26]. LiveChart values are extracted from the ENSDF snapshot of April 2022.

Isotope	$I^\pi$	Energy (keV)	Half-life
$^{12}\text{Be}$	0+	2251.0	230.0 ns
$^{16}\text{N}$	0-	120.4	5.3 us
$^{26}\text{Al}$	0+	228.3	6.3 s
$^{44}\text{S}$	0+	1365.0	2.6 us
$^{38}\text{K}$	0+	130.2	924.4 ms
$^{40}\text{K}$	0+	1643.6	0.3 us
$^{44}\text{Sc}$	0-	146.2	51.0 us
$^{68}\text{Ni}$	0+	<sup>I</sup> 1603.5	270.0 ns
$^{68}\text{Ni}$	<sup>II</sup> 0+	2511.9	$\leq 15.0$ ns
$^{70}\text{Ni}$	(0+)	1567.1	$\leq 70.0$ ns
$^{72}\text{Ga}$	(0+)	119.7	39.7 ms
$^{74}\text{Ga}$	(0+)	59.6	9.5 s
$^{72}\text{Ge}$	0+	691.4	444.2 ns
$^{72}\text{Se}$	0+	937.2	17.5 ns
$^{72}\text{Kr}$	0+	671.0	26.3 ns
$^{74}\text{Kr}$	0+	509.0	13.0 ns
$^{98}\text{Sr}$	0+	215.6	22.9 ns
$^{90}\text{Zr}$	0+	1760.7	61.3 ns
$^{96}\text{Zr}$	0+	1581.6	38.0 ns

Continued on next page

<sup>I</sup>See Ref. [257].

<sup>II</sup>See Ref. [258].



**Table A.1 – continued from previous page**

Isotope	$I^\pi$	Energy (keV)	Half-life
$^{98}\text{Zr}$	0+	854.1	64.0 ns
$^{98}\text{Mo}$	0+	734.8	21.8 ns
$^{102}\text{Pd}$	0+	1593.2	14.5 ns
$^{118}\text{Ag}$	0(-) TO 2(-)	45.8	$\approx 0.1$ us
$^{150}\text{Eu}$	0-	41.7	12.8 h
$^{152}\text{Eu}$	0-	45.6	9.3 h
$^{156}\text{Tb}$	(0+)	88.4	5.3 h
$^{158}\text{Tb}$	0-	110.3	10.7 s
$^{166}\text{Lu}$	0-	43.0	2.1 m
$^{176}\text{Ta}$	(0+)	100.2	30.5 ns
$^{180}\text{Ta}$	0-	107.8	19.2 ns
$^{204}\text{Tl}$	(0-)	145.9	18.7 ns
$^{234}\text{Pa}$	(0-)	<sup>III</sup> 73.92+X	1.2 m
$^{236}\text{U}$	(0+)	2750.0	67.0 ns
$^{236}\text{U}$	(0+)	3434.0	$\leq 20.0$ ns
$^{238}\text{U}$	0+	2557.9	280.0 ns

## A.2 $0 \rightarrow 0$ E0 isomeric transitions

Table A.2: **Isomeric E0 transitions towards a  $I = 0$  ground state.** Data retrieved from the LiveChart of Nuclides database [26]. Assignments between round brackets are uncertain. LiveChart values are extracted from the ENSDF snapshot of April 2022.

Isotope	$I^\pi$	Energy (keV)	Half-life
$^{12}\text{Be}$	0+	2251.0	230.0 ns
$^{44}\text{S}$	0+	1365.0	2.6 us
$^{68}\text{Ni}$	0+	<sup>IV</sup> 1603.5	270.0 ns
$^{68}\text{Ni}$	<sup>V</sup> 0+	2511.9	$\leq 15.0$ ns
$^{70}\text{Ni}$	(0+)	1567.1	$\leq 70.0$ ns
$^{72}\text{Ge}$	0+	691.4	444.2 ns
$^{72}\text{Se}$	0+	937.2	17.5 ns
$^{72}\text{Kr}$	0+	671.0	26.3 ns
$^{74}\text{Kr}$	0+	509.0	13.0 ns

Continued on next page

<sup>III</sup>In Ref. [259]  $X = 2.6 \text{ keV} \pm 0.5 \text{ keV}$ .

<sup>IV</sup>See Ref. [257].

<sup>V</sup>See Ref. [258].

**Table A.2 – continued from previous page**

Isotope	$I^\pi$	Energy (keV)	Half-life
$^{98}\text{Sr}$	0+	215.6	22.9 ns
$^{90}\text{Zr}$	0+	1760.7	61.3 ns
$^{96}\text{Zr}$	0+	1581.6	38.0 ns
$^{98}\text{Zr}$	0+	854.1	64.0 ns
$^{98}\text{Mo}$	0+	734.8	21.8 ns
$^{102}\text{Pd}$	0+	1593.2	14.5 ns
$^{236}\text{U}$	(0+)	3434.0	$\leq 20.0$ ns
$^{238}\text{U}$	0+	2557.9	280.0 ns

### A.3 Recoupling coefficients for NEEC–EXI

The following discussion is built on the results obtained with the Flexible Atomic Code (FAC) [177]. This chapter provides examples of the expressions of the recoupling coefficients between the parent and child electronic configurations corresponding to the configurations before and after the electron capture, respectively. Although all these aspects may be well known by atomic and nuclear physicists, I hope this section could be useful to gather all the information in one place and apply them to the case of NEEC. The following books have been invaluable resources for this topic [40, 260–262], as well as Refs. [263, 264], which introduce the computer program NJFORMULA that can be used to perform the symbolic calculations of the recoupling coefficients. For a graphical interpretation of the coupling schemes in terms of a binary tree, please refer to Fig. S1 of Section 2.3, or alternatively, consult the Supplemental Material provided in Ref. [119].

#### A.3.1 $N_{\text{ele}} = 0 \rightarrow N_{\text{ele}} = 1$

If one starts from a completely bare nucleus, the number of electrons in the atomic shell is equal to  $N_{\text{ele}} = 0$  and the charge state  $q = Z$ . Therefore,  $1s^0$  represents the only parent configuration possible for the electronic shell before the electron capture. In contrast, when NEEC took place in a bare nucleus, the resulting electronic configurations have  $N_{\text{ele}} = 1$  and  $q = Z - 1$ . If one considers only capture in K, L, and M shells there are 9 possible child configurations (i.e.,  $1s^1_{1/2}$ ,  $2s^1_{1/2}$ ,  $2p^1_{1/2}$ ,  $2p^1_{3/2}$ ,  $3s^1_{1/2}$ ,  $3p^1_{1/2}$ ,  $3p^1_{3/2}$ ,  $3d^1_{3/2}$ ,  $3d^1_{5/2}$ ) for the single  $1s^0$  parent configuration. All these capture channels are permitted by selection rules.

#### A.3.2 $N_{\text{ele}} = 1 \rightarrow N_{\text{ele}} = 2$

There are 9 parent configurations and 98 child configurations. These result from all the possible combinations of electrons filling different orbitals and their consequent couplings (i.e.,  $1s^1_{1/2}2s^1_{1/2}(J = 0)$  and  $1s^1_{1/2}2s^1_{1/2}(J = 1)$  are two distinct possibilities). Selection rules are satisfied if the spectator electron (the one not involved in the capture) preserves its subshell and the quantum number  $j$  before and after the capture.

#### A.3.3 $N_{\text{ele}} = 2 \rightarrow N_{\text{ele}} = 3$

When moving from 2 to 3 electrons, we pass from 98 parent configurations to 665 child combinations. We need to determine which of these many possibilities are allowed by selection rules. The situation slightly changes: with three electrons there is the possibility that two electrons will fill the same shell, closing it (i.e.,  $s_{1/2}$ ,  $p_{1/2}$ ), and leaving the remaining orbital open. It is important to keep in mind that FAC does not include in the output the electronic configurations that are closed.

Thus, if the NEEC channel is the one that closed the shell, this latter will not be formally found in the child configuration. One has to distinguish thus two cases: (i) capture shell is contained in the child configuration or (ii) not. To indicate parent and

## Appendix

---

child configurations I used the following names: shell-in for the parent configuration and shell-out for the child. As a consequence, the two cases become (i) shell-out  $\neq \emptyset$  or (ii) shell-out =  $\emptyset$ . The reason for this nomenclature is that looking for the name of the capture shell in the child configuration would result in a non-empty or empty set. This situation is depicted in Fig. A.1 for the case  $N_{\text{ele}} = 3 \rightarrow N_{\text{ele}} = 4$ .

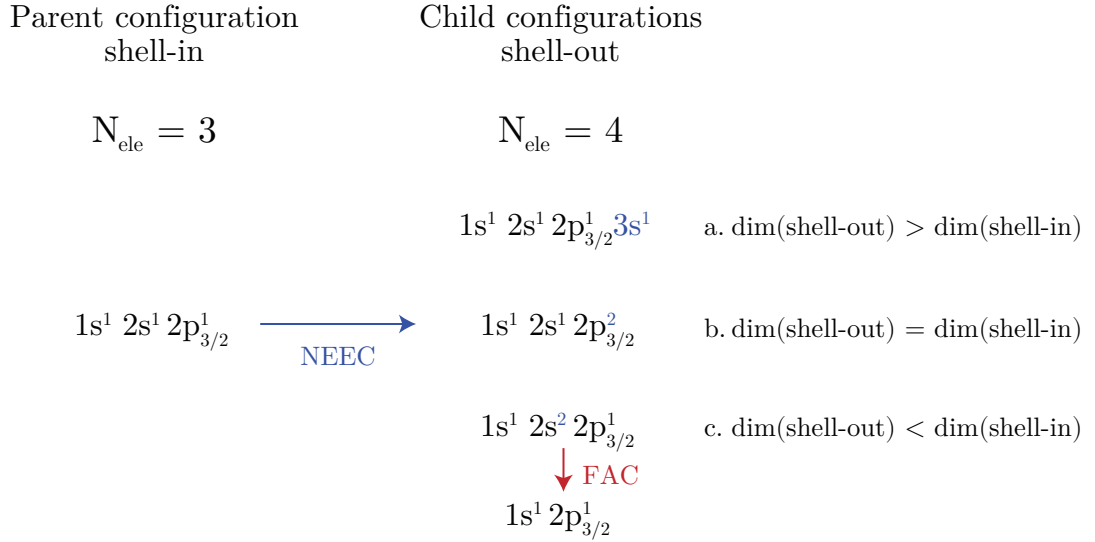


Figure A.1: **Parent and child electronic configurations for  $N_{\text{ele}} = 3 \rightarrow N_{\text{ele}} = 4$ .** When NEEC occurs starting from the parent configuration, three different outcomes are possible depending on the dimension of shell-in and shell-out. The relativistic configuration name of the level provided by FAC includes only open and non-empty shells. This image is an exemplification and does not show all possible variations.

### 1. shell-out $\neq \emptyset$

One has to further distinguish between the cases in which the dimensions of the shell-out and shell-in differ or are equal.

#### 1a. $\dim(\text{shell-out}) > \dim(\text{shell in})$

In this condition, the capture occurs always creating a new shell, that is absent in the parent electronic configuration.

- If capture occurs in the **outer** shell, we must check whether the J of the single coupled shells and the coupling with the other shells are preserved for the spectator electrons. If both are true, the shell can be preserved.
- If  **$\dim(\text{shell-out}) = 3$**  (max possible) and the electron is not captured in the outer shell, it means that the electron capture broke the initial coupling, leading to a recoupling. The child configurations of interest are of the type  $(j_c, j_2)j_3$  or

$(j_1, j_c)j_3$ . Thus the Wigner coefficients differ only in the position of  $j_1$  and  $j_2$ . In the first case we have  $j_c = j_1$  (**Case #1.1**)

$$\left\{ \begin{array}{ccc} j_1 & j_2 & J_{12} \\ j_3 & J & J_{23} \end{array} \right\}, \quad (\text{A.1})$$

while in the second case  $j_c = j_2$  (**Case #1.2**)

$$\left\{ \begin{array}{ccc} j_2 & j_1 & J_{12} \\ j_3 & J & J_{13} \end{array} \right\}, \quad (\text{A.2})$$

where  $J$  is the total angular momentum of the child configuration.

- If  $\dim(\text{shell-out}) = 2$  we have two possibilities (blue highlighting indicates the captured electron):

- **Case #1.3:**  $3d_{5/2}^2 \rightarrow 2p_{1/2}^1 3d_{5/2}^2$
- **Case #1.4:**  $2p_{3/2}^2 \rightarrow 2p_{3/2}^2 3d_{1/2}^1$ .

**Case #1.4** is already considered as capture in the outer shell. For **Case #1.3:** we have two spectator electrons and a captured one. We have to check that those two electrons have the same coupled  $J$  before and after the capture. Basically we are considering the two state vectors  $|j_1(j_2j_3)J_{23}; J\rangle$  and  $|(j_2j_3)J_{23}, j_1; J\rangle$ . Thus, we need to verify that the two  $J_{23}$  are the same.

1b.  $\dim(\text{shell-out}) = \dim(\text{shell-in})$

If we are in this condition, it means that the shell-out configuration might be of the type  $2p_{3/2}^2$  and  $2p_{3/2}^3$ : the capture occurs in a shell that already includes an electron. This means that in any case, the captured electron will couple first with the electron in the same shell and then with the third one. We can distinguish three different cases:

- **Case #2.1** is  $2p_{3/2}^2 \rightarrow 2p_{3/2}^3$
- **Case #2.2** is  $2p_{1/2}^1 2p_{3/2}^1 \rightarrow 2p_{1/2}^1 2p_{3/2}^2$
- **Case #2.3** is  $2p_{3/2}^1 3d_{3/2}^1 \rightarrow 2p_{3/2}^2 3d_{3/2}^1$

**Case #2.1** is a recoupling between the three electrons. In the case of  $2p_{3/2}^3$ ,  $J$  can have only the value  $3/2$ . Anyway, since the three electrons are indistinguishable, the channel is taken into account as happens for conventional NEEC-GSA.

**Case #2.2** Here  $j_2$  and  $j_3$  couple first and then they couple with  $j_1$ . The recoupling coefficient is given by  $\langle(12)3|(23)1\rangle$ , where  $\langle\mathbf{f}|\mathbf{i}\rangle$  denotes the initial and final state vector configurations [261]. The definition of initial and final states is irrelevant as recoupling coefficients enable the passage from one scheme to another, i.e.  $\langle\mathbf{i}|\mathbf{f}\rangle \equiv \langle\mathbf{f}|\mathbf{i}\rangle$  [263]. The

## Appendix

---

recoupling coefficient will be related to the state vectors  $\langle (j_1 j_2) J_{12}, j_3; J | (j_2 j_3) J_{23}, j_1; J \rangle$ , hence the Wigner coefficient is the same as that of Eq. A.1:

$$\left\{ \begin{array}{ccc} j_1 & j_2 & J_{12} \\ j_3 & J & J_{23} \end{array} \right\} \quad (\text{A.3})$$

This case is distinguished from the following one by the position in which the electron is captured.

**Case #2.3** Here  $j_1$  and  $j_2$  couple first and then  $j_3$ . For this reason, the coefficient is the one given in Eq. A.2, but since the two electrons ( $j_1$  and  $j_2$ ) belong to the same shell, they also have the same  $j$ . Therefore, the two expressions in Eq. A.1 and Eq. A.2 are equivalent. The recoupling coefficient is given by  $\langle (12)3 | (13)2 \rangle$ :

$$\left\{ \begin{array}{ccc} j_2 & j_1 & J_{12} \\ j_3 & J & J_{13} \end{array} \right\} \quad (\text{A.4})$$

*c. dim(shell-out) < dim(shell-in)*

This scenario corresponds to the case in which one shell has been closed due to the capture of a free electron. Specifically, given the presence of three electrons, it is possible that either the  $s$ ,  $p_{1/2}$ , or  $d_{3/2}$  shell could have been closed. By construction, FAC will not include this shell in the output file. Nonetheless, the search result did not give an empty set. When searching for the capture channel, I use the notation of the LS coupling (i.e.,  $2p$  or  $3d$ ). Having shell-out  $\neq \emptyset$  suggests, for example, the closure of the  $2p_{1/2}$  subshell while the other electron is in the  $2p_{3/2}$  orbital. Having a closed subshell, we have additional information on the coupled momentum of the two electrons ( $J_{ij} = 0$ ). There is only one case (equivalent to the one involving the  $d$  shell)

- **Case #3.1** is  $2p_{1/2}^1 2p_{3/2}^1 \rightarrow 2p_{1/2}^2 2p_{3/2}^1$

**Case #3.1** Here, we have something analogous to Eq. A.4,  $\langle (12)3 | (13)2 \rangle$ , with  $J_{13} = 0$  and  $j_1 = j_3$

$$\left\{ \begin{array}{ccc} j_2 & j_1 & J_{12} \\ j_3 & J & 0 \end{array} \right\} \quad (\text{A.5})$$

2. shell-out =  $\emptyset$

The case shell-out =  $\emptyset$  implies that the search of the capture shell in the output electronic configuration did not produce any result. For example, this could occur when searching for capture in the  $2p$  shell, with no  $2p_{1/2}$  or  $2p_{3/2}$  electron found. This means that the capture shell existed in the initial configuration and it was subsequently closed with the capture. Only the case ‘c’ of Fig. A.1 occurs.

*2c. Dimension shell out < shell in.*

We can distinguish two cases:

- **Case #4.1**  $2s_{1/2}^1 2p_{1/2}^1 \rightarrow 2s_{1/2}^2 2p_{1/2}^1$

- **Case #4.2** is  $2s_{1/2}^1 2p_{1/2}^1 \rightarrow 2s_{1/2}^1 2p_{1/2}^2$

**Case #4.1** is identical to Case #3.1:

$$\begin{Bmatrix} j_2 & j_1 & J_{12} \\ j_3 & J & 0 \end{Bmatrix} \quad (\text{A.6})$$

**Case #4.2** is identical to Case #2.2 with  $J_{23} = 0$ :

$$\begin{Bmatrix} j_1 & j_2 & J_f \\ j_3 & J & 0 \end{Bmatrix} \quad (\text{A.7})$$

### A.3.4 $N_{\text{ele}} = 3 \rightarrow N_{\text{ele}} = 4$

Here we pass from 665 parent configurations to 3793 child configurations. As similarly done for the previous cases, it is necessary to differentiate the situation in which the search of the capture shell in the output electronic configuration yielded a non-empty set.

1. shell-out  $\neq \emptyset$

*1a.  $\dim(\text{shell-out}) > \dim(\text{shell-in})$*

In this scenario – regardless of the number of subshells present in the output configuration – the capture results in the creation of a new subshell that was absent in the parent configuration.

- If capture occurs in the **outer** shell, it is necessary to verify that the couplings of the  $J_{ij}$  between the subshells of the spectator electrons have been preserved. This is the case in which the capture of the free electron does not break the initial electron coupling: **Case #5.0**.

If the capture takes place in **inner** shells, this breaks the initial angular momentum coupling. The outcome has to be differentiated based on the size of the output configuration: if  $\mathbf{\dim(\text{shell-out})} = 4$  the four electrons are all in different subshells. Three cases can be distinguished, depending on the position of the capture shell (indicated in blue):

- **Case #5.1**  $\langle [(1, 2), 3], 4 | [(2, 3), 4], 1 \rangle$ . The recoupling coefficient is reported in Eq. A.8.
- **Case #5.2**  $\langle [(1, \mathbf{2}), 3], 4 | [(1, 3), 4], 2 \rangle$ . The recoupling coefficient is reported in Eq. A.9.
- **Case #5.3**  $\langle [(1, 2), \mathbf{3}], 4 | [(1, 2), 4], 3 \rangle$ . The recoupling coefficient is reported in Eq. A.10.

if  $\mathbf{\dim(\text{shell-out})} = 3$  the capture always creates a new shell, while the other two spectator electrons (out of four) are in the same shell. Furthermore, since shell-out  $\neq \emptyset$ ,

## Appendix

---

there are no shells that could have potentially been closed. As a first step, it is important to determine the location of the shell containing two electrons in the final electronic configuration. Two cases are possible:

- Case #5.4:  $2p_{1/2}^1 3d_{5/2}^2$
- Case #5.5:  $2p_{3/2}^2 3d_{5/2}^1$

**Case #5.4** can be further split in

- **Case #5.4.1:**  $2p_{1/2}^1 3d_{5/2}^2 \rightarrow 1s^1 2p_{1/2}^1 3d_{5/2}^2$ . The recoupling coefficient is reported in Eq. A.11.
- **Case #5.4.2:**  $2p_{1/2}^1 3d_{5/2}^2 \rightarrow 2p_{1/2}^1 2p_{3/2}^1 3d_{5/2}^2$ . The recoupling coefficient is reported in Eq. A.12.

**Case #5.5** can be further divided in

- **Case #5.5.1:**  $2p_{3/2}^2 3d_{5/2}^1 \rightarrow 1s^1 2p_{3/2}^2 3d_{5/2}^1$ . Eq. A.13.
- **Case #5.5.2:**  $2p_{3/2}^2 3d_{5/2}^1 \rightarrow 2p_{3/2}^2 3d_{3/2}^1 3d_{5/2}^1$ . Eq. A.14.

if  $\dim(\text{shell-out}) = 2$  there are two cases:

- **Case #5.6:**  $3d_{5/2}^x \rightarrow 1s^1 3d_{5/2}^x$ , where  $x$  can be 1 or 3.
- **Case #5.7**  $2p_{3/2}^x \rightarrow 2p_{3/2}^x 3d_{3/2}^1$ , where  $x$  can be 1 or 3.

The capture in the outer shell (**Case #5.7**) is already considered under Case #5.0. For **Case #5.6**, as discussed for Case #1.3, it is necessary to check that the spectator electrons have preserved their own  $j$ .

*1b.  $\dim(\text{shell-out}) = \dim(\text{shell-in})$*

We can differentiate the following cases based on the size of the output shell (which can have a maximum size of 3 due to the dimension of the parent shell) and the index of the captured shell.

- **Case #6.1** is  $3d_{5/2}^x \rightarrow 3d_{5/2}^{(x+1)}$ , Accepted  $\forall x$ .
- **Case #6.2.1** is  $2p_{3/2}^2 3d_{5/2}^1 \rightarrow 2p_{3/2}^2 3d_{5/2}^2$ , Eq. A.15.
- **Case #6.2.2** is  $2p_{3/2}^2 3d_{5/2}^1 \rightarrow 2p_{3/2}^3 3d_{5/2}^1$  Eq. A.14.
- **Case #6.2.3** is  $2p_{3/2}^1 3d_{5/2}^2 \rightarrow 2p_{3/2}^2 3d_{5/2}^2$  Eq. A.16.
- **Case #6.2.4** is  $2p_{3/2}^1 3d_{5/2}^2 \rightarrow 2p_{3/2}^1 3d_{5/2}^3$  Eq. A.17.
- **Case #6.3.1** is  $1s^1 2p_{3/2}^1 3d_{5/2}^1 \rightarrow 1s^1 2p_{3/2}^1 3d_{5/2}^2$  Eq. A.15.
- **Case #6.3.2** is  $1s^1 2p_{3/2}^1 3d_{5/2}^1 \rightarrow 1s^1 2p_{3/2}^2 3d_{5/2}^1$  Eq. A.18.
- **Case #6.3.3**  $2p_{3/2}^1 3d_{3/2}^1 3d_{5/2}^1 \rightarrow 2p_{3/2}^2 3d_{3/2}^1 3d_{5/2}^1$  Eq. A.19.



1c.  $\dim(\text{shell-out}) < \dim(\text{shell-in})$

We can distinguish different cases depending on the relative position of the closed shell and the size of the input shell. When  $\mathbf{dim}(\text{shell-in}) = \mathbf{3}$ , there are two possibilities to consider (keep in mind that the output will have a closed shell, so  $\mathbf{dim}(\text{shell-out}) = \mathbf{2}$ ):

- **Case # 7.1.1**  $1s^1 2p_{1/2}^1 3d_{3/2}^1 \rightarrow 1s^1 2p_{1/2}^1 3s^2$
- **Case # 7.1.2**  $1s^1 2p_{1/2}^1 3d_{3/2}^1 \rightarrow 1s^1 2p_{1/2}^2 3s^1$
- **Case # 7.1.3**  $1s^1 2p_{1/2}^1 3d_{3/2}^1 \rightarrow 1s^2 2p_{1/2}^1 3s^1$

When  $\mathbf{dim}(\text{shell-in}) = \mathbf{2}$ , there are two possibilities to consider (note that the output will have a closed shell, so  $\mathbf{dim}(\text{shell-out}) = \mathbf{1}$ ):

- **Case # 7.2.1**  $2p_{3/2}^2 3d_{3/2}^1 \rightarrow 2p_{3/2}^2 3d_{3/2}^2$
- **Case # 7.2.2**  $1s^1 2p_{3/2}^2 \rightarrow 1s^2 2p_{3/2}^2$

2.  $\text{shell-out} = \emptyset$

2c.  $\dim(\text{shell-out}) < \dim(\text{shell-in})$

Similar to Sec. A.3.4.

### Complete list of the recoupling terms for $\mathbf{N}_{\text{ele}} = \mathbf{3} \rightarrow \mathbf{N}_{\text{ele}} = \mathbf{4}$

The values of  $\theta$  are irrelevant for our purposes since we are focused on evaluating the probability  $\Lambda = |\langle \mathbf{a} | \mathbf{b} \rangle|^2$ , where  $\mathbf{a}$  and  $\mathbf{b}$  represent the two state vectors describing the coupling.

#### Case #5.1:

$$\begin{aligned} \langle [(j_1, j_2) J_{12}, j_3] J_{123}, j_4; J | [(j_2, j_3) J_{23}, j_4] J_{234}, j_1; J \rangle = \\ = (-1)^{\theta_1} R_1 \begin{Bmatrix} j_1 & j_2 & J_{12} \\ j_3 & J_{123} & J_{23} \end{Bmatrix} \begin{Bmatrix} j_1 & J_{23} & J_{123} \\ j_4 & J & J_{234} \end{Bmatrix}, \end{aligned} \quad (\text{A.8})$$

$$R_1 = \sqrt{(2 \cdot j_{12} + 1)(2 \cdot J_{123} + 1)(2 \cdot J_{23} + 1)(2 \cdot J_{234} + 1)},$$

#### Case #5.2:

$$\begin{aligned} \langle [(j_1, j_2) J_{12}, j_3] J_{123}, j_4; J | [(j_1, j_3) J_{13}, j_4] J_{134}, j_2; J \rangle = \\ = (-1)^{\theta_2} R_2 \begin{Bmatrix} j_2 & j_1 & J_{12} \\ j_3 & J_{123} & J_{13} \end{Bmatrix} \begin{Bmatrix} j_2 & J_{13} & J_{123} \\ j_4 & J & J_{134} \end{Bmatrix}, \end{aligned} \quad (\text{A.9})$$

$$R_2 = \sqrt{(2 \cdot J_{12} + 1)(2 \cdot J_{123} + 1)(2 \cdot J_{13} + 1)(2 \cdot J_{134} + 1)},$$

**Case #5.3:**

$$\begin{aligned} \langle [(j_1, j_2)J_{12}, j_3]J_{123}, j_4; J | [(j_1, j_2)J_{12}, j_4]J_{124}, j_3; J \rangle = \\ (-1)^{\theta_3} R_3 \begin{Bmatrix} j_3 & J_{12} & J_{123} \\ j_4 & J & J_{124} \end{Bmatrix}, \end{aligned} \quad (\text{A.10})$$

$$R_3 = \sqrt{(2 \cdot J_{123} + 1)(2 \cdot J_{124} + 1)},$$

**Case #5.4.1:**  $2p_{1/2}^1 3d_{5/2}^2 \rightarrow 1s^1 2p_{1/2}^1 3d_{5/2}^2$  corresponds to the recoupling coefficient  $\langle ((12), (34)) | ((2), (34)), 1 \rangle$ :

$$\begin{aligned} \langle [(j_1, j_2)J_{12}, (j_3, j_4)J_{34}]; J | [j_2, (j_3, j_4)J_{34}]J_{234}, j_1; J \rangle = \\ (-1)^{\theta_4} R_4 \begin{Bmatrix} j_1 & j_2 & J_{12} \\ J_{34} & J & J_{234} \end{Bmatrix}, \end{aligned} \quad (\text{A.11})$$

$$R_4 = \sqrt{(2 \cdot J_{12} + 1)(2 \cdot J_{234} + 1)},$$

**Case #5.4.2:**  $2p_{1/2}^1 3d_{5/2}^2 \rightarrow 2p_{1/2}^1 2p_{3/2}^1 3d_{5/2}^2$  corresponds to the recoupling coefficient  $\langle ((12), (34)) | ((1), (34)), 2 \rangle$ :

$$\begin{aligned} \langle [(j_1, j_2)J_{12}, (j_3, j_4)J_{34}]; J | [j_1, (j_3, j_4)J_{34}]J_{134}, j_2; J \rangle = \\ (-1)^{\theta_5} R_5 \begin{Bmatrix} j_2 & j_1 & J_{12} \\ J_{34} & J & J_{134} \end{Bmatrix}, \end{aligned} \quad (\text{A.12})$$

$$R_5 = \sqrt{(2 \cdot J_{12} + 1)(2 \cdot J_{134} + 1)},$$

**Case #5.5.1:**  $2p_{3/2}^2 3d_{5/2}^1 \rightarrow 1s^1 2p_{3/2}^2 3d_{5/2}^1$  corresponds to the recoupling coefficient  $\langle((1, (23)), 4)|((23), 4), 1\rangle$ :

$$\begin{aligned} \langle [j_1, (j_2, j_3)J_{23}]J_{123}, j_4; J | [(j_2, j_3)J_{23}, j_4]J_{234}, j_1; J \rangle = \\ (-1)^{\theta_6} R_6 \begin{Bmatrix} j_1 & J_{23} & J_{123} \\ j_4 & J & J_{234} \end{Bmatrix}, \end{aligned} \quad (\text{A.13})$$

$$R_6 = \sqrt{(2 \cdot J_{123} + 1)(2 \cdot J_{234} + 1)},$$

**Case #5.5.2:**  $2p_{3/2}^2 3d_{5/2}^1 \rightarrow 2p_{3/2}^2 3d_{3/2}^1 3d_{5/2}^1$  corresponds to the recoupling coefficient  $\langle(((12), 3), 4)|((12), 4), 3\rangle$ :

$$\begin{aligned} \langle [(j_1, j_2)J_{12}, j_3]J_{123}, j_4; J | [(j_1, j_2)J_{12}, j_4]J_{124}, j_3; J \rangle = \\ (-1)^{\theta_7} R_7 \begin{Bmatrix} j_3 & J_{12} & J_{123} \\ j_4 & J & J_{124} \end{Bmatrix}, \end{aligned} \quad (\text{A.14})$$

$$R_7 = \sqrt{(2 \cdot J_{124} + 1)(2 \cdot J_{123} + 1)},$$

**Case #6.2.1:**  $2p_{3/2}^2 3d_{5/2}^1 \rightarrow 2p_{3/2}^2 3d_{5/2}^2$  corresponds to the recoupling coefficient  $\langle((12), (34))|((12), 3), 4\rangle$ :

$$\begin{aligned} \langle [(j_1, j_2)J_{12}, (j_3, j_4)J_{34}]; J | [(j_1, j_2)J_{12}, j_3]J_{123}, j_4; J \rangle = \\ (-1)^{\theta_8} R_8 \begin{Bmatrix} j_4 & j_3 & J_{34} \\ J_{12} & J & J_{123} \end{Bmatrix}, \end{aligned} \quad (\text{A.15})$$

$$R_8 = \sqrt{(2 \cdot J_{34} + 1)(2 \cdot J_{123} + 1)},$$

**Case #6.2.2** is  $2p_{3/2}^2 3d_{5/2}^1 \rightarrow 2p_{3/2}^3 3d_{5/2}^1$  corresponds to the recoupling coefficient  $\langle(((12), 3)4)|((12), 4), 3\rangle$ , that is identical to the Case #5.5.2.

## Appendix

---

**Case #6.2.3** is  $2p_{3/2}^1 3d_{5/2}^2 \rightarrow 2p_{3/2}^2 3d_{5/2}^2$  corresponds to the recoupling coefficient  $\langle((12), (34))|((1, (34)), 2)\rangle$ :

$$\begin{aligned} \langle[(j_1, j_2)J_{12}, (j_3, j_4)J_{34}]; J|[j_1, (j_3, j_4)J_{34}]J_{134}, j_2; J\rangle = \\ (-1)^{\theta_9} R_9 \left\{ \begin{array}{ccc} j_2 & j_1 & J_{12} \\ J_{34} & J & J_{134} \end{array} \right\}, \end{aligned} \quad (\text{A.16})$$

$$R_9 = \sqrt{(2 \cdot J_{12} + 1)(2 \cdot J_{134} + 1)},$$

**Case #6.2.4** is  $2p_{3/2}^1 3d_{5/2}^2 \rightarrow 2p_{3/2}^1 3d_{5/2}^3$  corresponds to the recoupling coefficient  $\langle(1, ((23), 4))|((1, (23)), 4)\rangle$ :

$$\begin{aligned} \langle j_1, [(j_2, j_3)J_{23}, j_4]J_{234}; J|[j_1, (j_2, j_3)J_{23}]J_{123}, j_4; J\rangle = \\ (-1)^{\theta_{10}} R_{10} \left\{ \begin{array}{ccc} j_4 & J_{23} & J_{234} \\ j_1 & J & J_{123} \end{array} \right\}, \end{aligned} \quad (\text{A.17})$$

$$R_{10} = \sqrt{(2 \cdot J_{234} + 1)(2 \cdot J_{123} + 1)},$$

**Case #6.3.1:**  $1s^1 2p_{3/2}^1 3d_{5/2}^1 \rightarrow 1s^1 2p_{3/2}^1 3d_{5/2}^2$  corresponds to the recoupling coefficient  $\langle((12), (34))|(((12), 3), 4)\rangle$ , that is identical to Eq. A.15.

**Case #6.3.2:**  $1s^1 2p_{3/2}^1 3d_{5/2}^1 \rightarrow 1s^1 2p_{3/2}^2 3d_{5/2}^1$  corresponds to the recoupling coefficient  $\langle((1, (23)), 4)|(((12), 4), 3)\rangle$ :

$$\begin{aligned} \langle[j_1, (j_2, j_3)J_{23}]J_{123}, j_4; J|[j_1, j_2)J_{12}, j_4]J_{124}, j_3; J\rangle = \\ (-1)^{\theta_{11}} R_{11} \left\{ \begin{array}{ccc} j_3 & j_2 & J_{23} \\ j_1 & J_{123} & J_{12} \end{array} \right\} \left\{ \begin{array}{ccc} j_3 & J_{12} & J_{123} \\ j_4 & J & J_{124} \end{array} \right\}, \end{aligned} \quad (\text{A.18})$$

$$R_{11} = \sqrt{(2 \cdot J_{23} + 1)(2 \cdot J_{123} + 1)(2 \cdot J_{12} + 1)(2 \cdot J_{124} + 1)},$$

**Case #6.3.3**  $2p_{3/2}^1 3d_{3/2}^1 3d_{5/2}^1 \rightarrow 2p_{3/2}^2 3d_{3/2}^1 3d_{5/2}^1$  corresponds to the recoupling coefficient  $\langle((12), 3), 4|((13), 4), 2\rangle$ :

$$\begin{aligned} \langle[(j_1, j_2)J_{12}, j_3]J_{123}, j_4; J|[(j_1, j_3)J_{13}, j_4]J_{134}, j_2; J\rangle = \\ (-1)^{\theta_{12}} R_{12} \begin{Bmatrix} j_2 & j_1 & J_{12} \\ j_3 & J_{123} & J_{13} \end{Bmatrix} \begin{Bmatrix} j_2 & J_{13} & J_{123} \\ j_4 & J & J_{134} \end{Bmatrix}, \end{aligned} \quad (\text{A.19})$$

$$R_{12} = \sqrt{(2 \cdot J_{12} + 1)(2 \cdot J_{123} + 1)(2 \cdot J_{13} + 1)(2 \cdot J_{134} + 1)},$$

**Case # 7.1.1**  $1s^1 2p_{1/2}^1 3d_{3/2}^1 \rightarrow 1s^1 2p_{1/2}^1 3d_{3/2}^2$  corresponds to the recoupling coefficient  $\langle((12), (34))|((12), 3), 4\rangle$ , where  $J_{34} = 0$ :

$$\begin{aligned} \langle[(j_1, j_2)J_{12}, (j_3, j_4)J_{34}]; J|[(j_1, j_2)J_{12}, j_3]J_{123}, j_4; J\rangle = \\ (-1)^{\theta_{13}} R_{13} \begin{Bmatrix} j_4 & j_3 & J_{34} \\ J_{12} & J & J_{123} \end{Bmatrix} \propto \begin{Bmatrix} j_4 & j_3 & 0 \\ J_{12} & J & J_{123} \end{Bmatrix}, \end{aligned} \quad (\text{A.20})$$

$$R_{13} = \sqrt{(2 \cdot J_{34} + 1)(2 \cdot J_{123} + 1)} = \sqrt{(2 \cdot J_{123} + 1)}$$

**Case # 7.1.2**  $1s^1 2p_{1/2}^1 3d_{3/2}^1 \rightarrow 1s^1 2p_{1/2}^2 3d_{3/2}^1$  corresponds to the recoupling coefficient  $\langle((1, (23)), 4)|((12), 4), 3\rangle$ , where  $J_{23} = 0$ :

$$\begin{aligned} \langle[j_1, (j_2, j_3)J_{23}]J_{123}, j_4; J|[(j_1, j_2)J_{12}, j_4]J_{124}, j_3; J\rangle = \\ (-1)^{\theta_{14}} R_{14} \begin{Bmatrix} j_3 & j_2 & \cancel{J_{23}^0} \\ j_1 & J_{123} & J_{12} \end{Bmatrix} \begin{Bmatrix} j_3 & J_{12} & J_{123} \\ j_4 & J & J_{124} \end{Bmatrix}, \end{aligned} \quad (\text{A.21})$$

$$\begin{aligned} R_{14} &= \sqrt{(2 \cdot J_{23} + 1)(2 \cdot J_{123} + 1)(2 \cdot J_{12} + 1)(2 \cdot J_{124} + 1)} \\ &= \sqrt{(2 \cdot J_{123} + 1)(2 \cdot J_{12} + 1)(2 \cdot J_{124} + 1)}, \end{aligned}$$

## Appendix

---

**Case # 7.1.3**  $1s^1 2p_{1/2}^1 3d_{3/2}^1 \rightarrow 1s^2 2p_{1/2}^1 3d_{3/2}^1$  corresponds to the recoupling coefficient  $\langle(((12), 3), 4)|((13), 4), 2)\rangle$ , where  $J_{12} = 0$ :

$$\begin{aligned} & \langle[(j_1, j_2)J_{12}, j_3]J_{123}, j_4; J|[(j_1, j_3)J_{13}, j_4]J_{134}, j_2; J\rangle = \\ & (-1)^{\theta_{15}} R_{15} \begin{Bmatrix} j_2 & j_1 & \cancel{J_{12}^0} \\ j_3 & J_{123} & J_{13} \end{Bmatrix} \begin{Bmatrix} j_2 & J_{13} & J_{123} \\ j_4 & J & J_{134} \end{Bmatrix}, \end{aligned} \quad (\text{A.22})$$

$$\begin{aligned} R_{15} &= \sqrt{(2 \cdot J_{12} + 1)(2 \cdot J_{123} + 1)(2 \cdot J_{13} + 1)(2 \cdot J_{134} + 1)} \\ &= \sqrt{(2 \cdot J_{123} + 1)(2 \cdot J_{13} + 1)(2 \cdot J_{134} + 1)}, \end{aligned}$$

**Case # 7.2.1**  $2p_{3/2}^2 3s^1 \rightarrow 2p_{3/2}^2 3s^2$  corresponds to the  $\langle((12), (34))|((12), 3), 4)\rangle$  recoupling coefficient, where  $J_{34} = 0$ . It is equivalent to Case #7.1.1 or #6.2.1.

**Case # 7.2.2**  $1s^1 2p_{3/2}^2 \rightarrow 1s^2 2p_{3/2}^2$  corresponds to the  $\langle((12), (34))|(1, (34)), 2)\rangle$  recoupling coefficient, where  $J_{12} = 0$ . It is equivalent to Case #6.2.3:

$$\begin{aligned} & \langle[(j_1, j_2)J_{12}, (j_3, j_4)J_{34}]; J|[(j_1, (j_3, j_4)J_{34})J_{134}, j_2; J\rangle = \\ & (-1)^{\theta_{15}} R_{15} \begin{Bmatrix} j_2 & j_1 & \cancel{J_{12}^0} \\ J_{34} & J & J_{134} \end{Bmatrix}, \end{aligned} \quad (\text{A.23})$$

$$R_{15} = \sqrt{(2 \cdot J_{134} + 1)}.$$

## A.4 Additional Figures

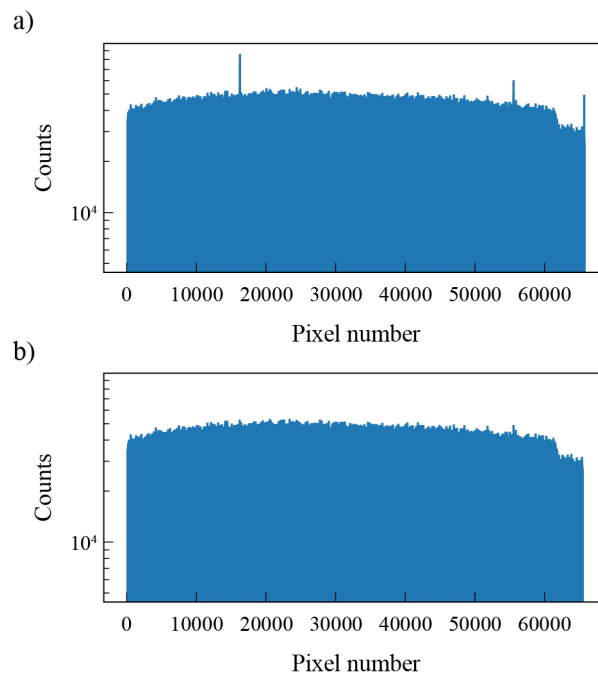


Figure A.2: **Histograms illustrating the detected event distribution as a function of pixel number, both before (a) and after (b) removing outlier pixels.** Pixels are numerated from 0 to 65535. Pixels that exhibit significant deviations from the surrounding are removed before proceeding with the analysis. The slightly lower counts observed for higher pixel numbers may be attributed to the detector inclination with respect to the sample, as this feature disappears when the detector is mounted vertically and pointed directly at the sample. The analysis was alternatively conducted without including the pixels exhibiting lower count rates, but no appreciable difference was observed. To handle the large amount of data, the analysis is performed on smaller subsets of the dataset.

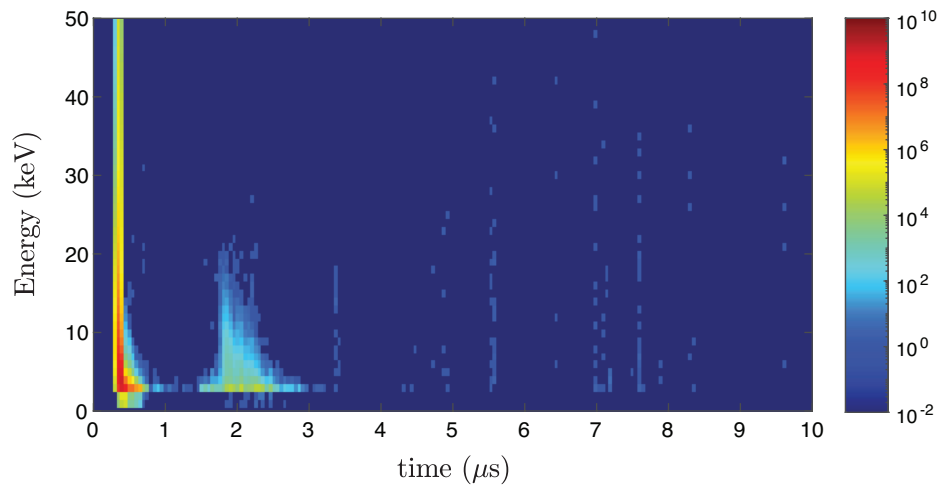


Figure A.3: **Optical-laser generated plasma experiment: 2D energy-time map.** This image replicates Fig. 4.22 using a different colormap (jet) and a color axis with different limits (starting from  $10^{-2}$  instead of  $10^0$ ). As a result, even a single counts are now clearly visible.

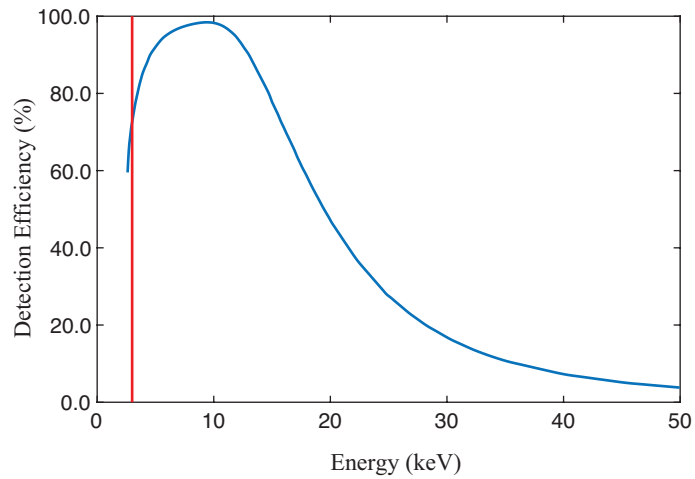


Figure A.4: **Detection efficiency of the AdvaPIX TPX3.** Detection efficiency is represented in blue, while the  $D_{th} = 3$  keV threshold is indicated by the vertical red line.



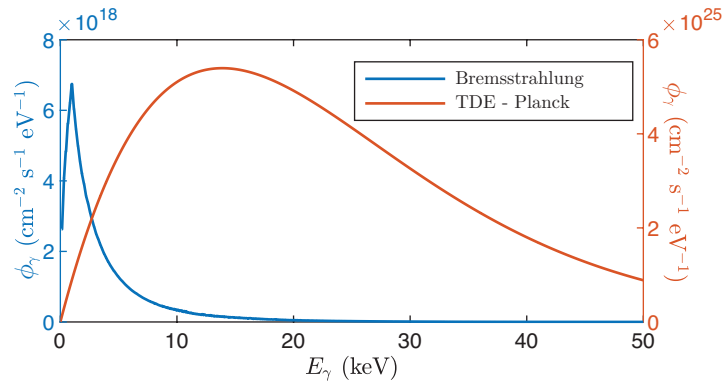


Figure A.5: **Comparison of bremsstrahlung and TDE photon flux models in a laser-generated plasma scenario.** In (a), the photon fluxes  $\phi_\gamma$  are determined using Eqs. 4.7 and 4.8 based on the conditions outlined by SL1. For Eq. 4.7, the value  $\epsilon = 2.7 \times 10^{-6}$  is determined imposing the energy balance between the photon and electron gases.

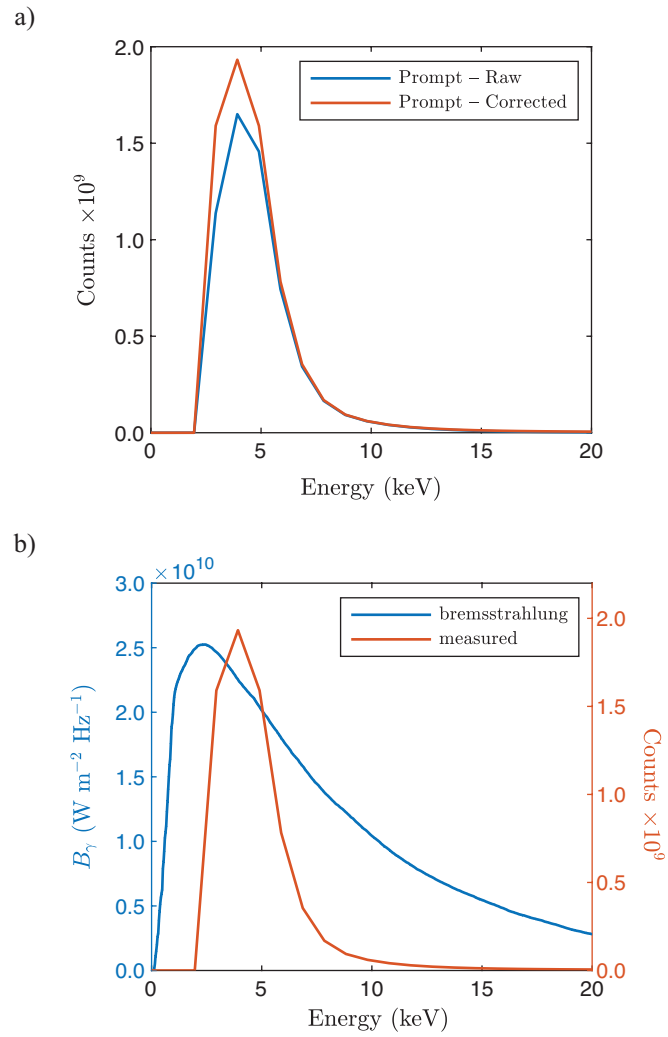


Figure A.6: **Prompt spectrum corrected by the energy-dependent detection efficiency (a) and comparison of the measured spectrum with the bremsstrahlung photon distribution (b).** In (a), the prompt raw spectrum ‘P1’ is corrected with the detection efficiency of the AdvaPIX TPX3. In (b), the corrected spectrum is compared with the bremsstrahlung photon distribution, obtained from Eq. 4.8 as  $B_\nu^B = (hE/4\pi)\phi_\gamma^B$  [232].

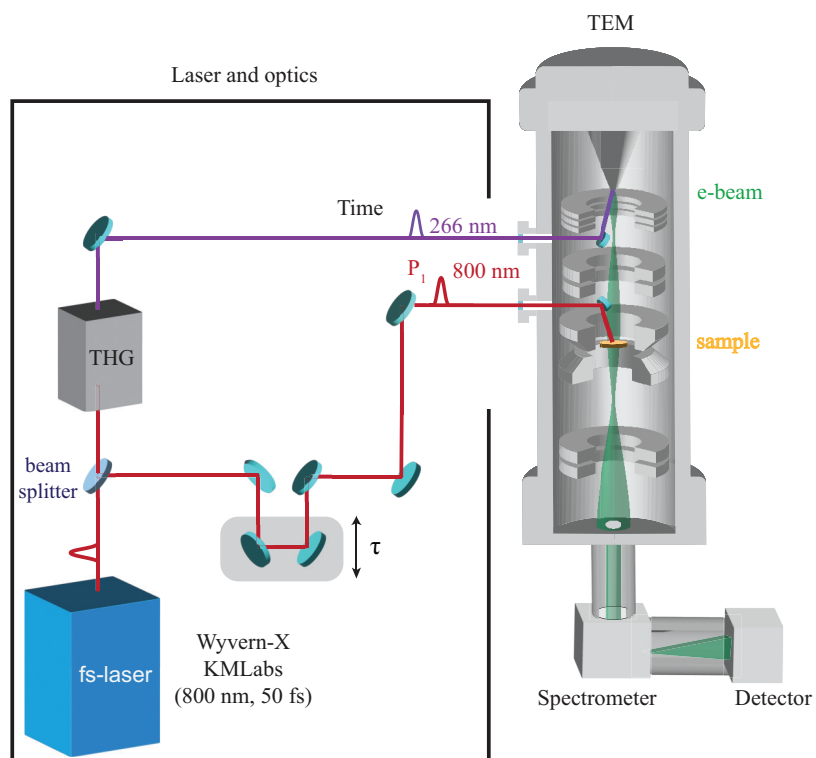


Figure A.7: **The ultrafast transmission electron microscope (UTEM)**. Courtesy of Alexey Sapozhnik.



## Bibliography

1. Peterson, J. B. *Maps of meaning: The architecture of belief* (Routledge, 2002).
2. Hansen, J. *et al.* Target Atmospheric CO<sub>2</sub>: 'Where Should Humanity Aim?' *The Open Atmospheric Science Journal*, *arXiv preprint arXiv:0804.1126* (2008).
3. UNFCCC. *The Paris Agreement (UNFCCC, 2015)* <https://unfccc.int/process-and-meetings/the-paris-agreement/the-paris-agreement>.
4. Meinshausen, M. *et al.* Realization of Paris Agreement pledges may limit warming just below 2° C. *Nature* **604**, 304–309 (2022).
5. The Intergovernmental Panel on Climate Change, [Online]. Available: <https://www.ipcc.ch/sr15/chapter/spm/>. 2023.
6. Ritchie, H., Roser, M. & Rosado, P. CO<sub>2</sub> and Greenhouse Gas Emissions. *Our World in Data*. <https://ourworldindata.org/co2-and-greenhouse-gas-emissions> (2020).
7. Vaclav, S. *Energy myths and realities: Bringing science to the energy policy debate/-Vaclav smil* (American Enterprise Institute for Public Policy Research, Washington, 2010).
8. Our World in Data: <https://ourworldindata.org/energy-key-charts#electricity-mix>. 2023.
9. Gates, B. *How to avoid a climate disaster: the solutions we have and the breakthroughs we need* (Vintage, 2021).
10. Sepulveda, N. A., Jenkins, J. D., de Sisternes, F. J. & Lester, R. K. The role of firm low-carbon electricity resources in deep decarbonization of power generation. *Joule* **2**, 2403–2420 (2018).
11. Sepulveda, N. A., Jenkins, J. D., Edington, A., Mallapragada, D. S. & Lester, R. K. The design space for long-duration energy storage in decarbonized power systems. *Nature Energy* **6**, 506–516 (2021).
12. Alighieri, D. *The divine comedy* (1321).
13. Koningstein, R. & Fork, D. Energy's creative destruction. *Ieee Spectrum* **51**, 30–35 (2014).

14. Koningstein, R. & Fork, D. K. What it would really take to reverse climate change (2014).
15. Fork, D. & Koningstein, R. How Engineers Can Disrupt Climate Change. *IEEE Spectrum* **58**, 24–29 (2021).
16. Jain, A. K., Maheshwari, B. & Goel, A. *Nuclear Isomers: A Primer* (Springer Nature, 2021).
17. Hahn, O. Über eine neue radioaktive Substanz im Uran. *Berichte der deutschen chemischen Gesellschaft (A and B Series)* **54**, 1131–1142 (1921).
18. Fajans, K. & Morris, D. F. Discovery and naming of the isotopes of element 91. *Nature* **244**, 137–138 (1973).
19. Shea, W. R. *Otto Hahn and the rise of nuclear physics* (Springer Science & Business Media, 1983).
20. Walker, P. & Podolyák, Z. 100 years of nuclear isomers—then and now. *Physica Scripta* **95**, 044004 (2020).
21. Gamow, G. Negative protons and nuclear structure. *Physical Review* **45**, 728 (1934).
22. Audi, G., Bersillon, O., Blachot, J. & Wapstra, A. The NUBASE evaluation of nuclear and decay properties. *Nuclear Physics A* **624**, 1–124 (1997).
23. Audi, G., Bersillon, O., Blachot, J. & Wapstra, A. H. The NUBASE evaluation of nuclear and decay properties. *Nuclear physics A* **729**, 3–128 (2003).
24. Kondev, F., Wang, M., Huang, W., Naimi, S. & Audi, G. The NUBASE2020 evaluation of nuclear physics properties. *Chinese Physics C* **45**, 030001 (2021).
25. Garg, S. *et al.* Atlas of nuclear isomers—Second edition. *Atomic Data and Nuclear Data Tables*, 101546 (2022).
26. *LiveChart of Nuclides (IAEA, Nuclear Data Section)* Dec. 2022. <https://nds.iaea.org/livechart>.
27. Feenberg, E. & Hammack, K. C. Nuclear shell structure. *Physical Review* **75**, 1877 (1949).
28. Feenberg, E. & Feld, B. T. *Shell theory of the nucleus* (Princeton University Press, 1955).
29. Mayer, M. G. & Jensen, J. H. D. *Elementary theory of nuclear shell structure* (Wiley, 1960).
30. Woods, R. D. & Saxon, D. S. Diffuse surface optical model for nucleon-nuclei scattering. *Physical Review* **95**, 577 (1954).
31. Takigawa, N. & Washiyama, K. *Fundamentals of nuclear physics* (Springer, 2017).
32. Lehnert, B., Hult, M., Lutter, G. & Zuber, K. Search for the decay of nature’s rarest isotope Ta<sup>180m</sup>. *Physical Review C* **95**, 044306 (2017).

## BIBLIOGRAPHY

---

33. *Internal Conversion Processes* (ed Hamilton, J.) (Academic Press, 1966).
34. Hofmann, C., Reinhardt, J., Greiner, W., Schlüter, P. & Soff, G. Angular correlation of electrons and positrons in internal pair conversion. *Physical Review C* **42**, 2632 (1990).
35. Löbner, K. Systematics of absolute transition probabilities of K-forbidden gamma-ray transitions. *Physics Letters B* **26**, 369–370 (1968).
36. Weisskopf, V. Radiative transition probabilities in nuclei. *Physical Review* **83**, 1073 (1951).
37. Blatt, J. M. & Weisskopf, V. F. *Theoretical nuclear physics* (Courier Corporation, 1991).
38. Ring, P. & Schuck, P. *The nuclear many-body problem* (Springer Science & Business Media, 2004).
39. Wong, S. S. *Introductory nuclear physics* (John Wiley & Sons, 2008).
40. Edmonds, A. R. *Angular momentum in quantum mechanics* (Princeton university press, 1957).
41. Krane, K. S. *Introductory nuclear physics* (John Wiley & Sons, 1991).
42. Kramp, J. *et al.* Nuclear two-photon decay in  $0^+ \rightarrow 0^+$  transitions. *Nuclear Physics A* **474**, 412–450 (1987).
43. Henderson, J. *et al.* Upper Limit on the Two-Photon Emission Branch for the  $0_2^+ \rightarrow 0_1^+$  Transition in  $^{98}\text{Mo}$ . *Physical Review C* **89**, 064307 (2014).
44. De Vries, H., De Jager, C. & De Vries, C. Nuclear charge-density-distribution parameters from elastic electron scattering. *Atomic data and nuclear data tables* **36**, 495–536 (1987).
45. Tiesinga, E., Mohr, P. J., Newell, D. B. & Taylor, B. N. CODATA recommended values of the fundamental physical constants: 2018. *Journal of Physical and Chemical Reference Data* **50**, 033105 (2021).
46. Walker, P. & Dracoulis, G. Energy traps in atomic nuclei. *Nature* **399**, 35–40 (1999).
47. Segre, E. *Nuclei and particles: an introduction to nuclear and subnuclear physics* (WA Benjamin, 1965).
48. V. Weizsäcker, C. Metastabile Zustände der Atomkerne. *Naturwissenschaften* **24**, 813–814 (1936).
49. Racah, G. Nuclear levels and Casimir operator. *L. Farkas memorial volume, edited by A. Farkas and EP Wigner (Research Council of Israel, Jerusalem, 1952)*, 294–304 (1952).
50. Flowers, B. Studies in jj-coupling. I. Classification of nuclear and atomic states. *Proceedings of the Royal Society of London. Series A. Mathematical and Physical Sciences* **212**, 248–263 (1952).

51. Black, J., McHarris, W. C. & Kelly, W. E6 and M5 Transitions Observed in Fe<sup>53m</sup> Decay. *Physical Review Letters* **26**, 451 (1971).
52. Palazzo, T. *et al.* Direct Measurement of Hexacontatetrapole, E6  $\gamma$  Decay from Fe<sup>53m</sup>. *Physical Review Letters* **130**, 122503 (2023).
53. Alaga, G., Alder, K., Bohr, A. & Mottelson, B. R. Intensity rules for beta and gamma transitions to nuclear rotational states (1955).
54. Deutsch, M. & Bauer, R. W. Spins of the isomeric states of Hf<sup>178</sup> and Hf<sup>180</sup>. *Nuclear Physics* **21**, 128–132 (1960).
55. Burson, S., Blair, K., Keller, H. & Wexler, S. The radiations from hafnium. *Physical Review* **83**, 62 (1951).
56. Bohr, A. & Mottelson, B. R. Rotational states in even-even nuclei. *Physical Review* **90**, 717 (1953).
57. Dracoulis, G. Isomers, nuclear structure and spectroscopy. *Physica Scripta* **2013**, 014015 (2013).
58. *Evaluated Nuclear Structure Data File (NNDC, National Nuclear Data Center)* Dec. 2022. <https://www.nndc.bnl.gov/ensdf/> (2022).
59. Walker, P. & Xu, F. High-K isomerism in rotational nuclei. *Physica Scripta* **91**, 013010 (2015).
60. Helmer, R. & Reich, C. Half-life of <sup>178m2</sup>Hf and its neutron capture production. *Nuclear Physics A* **211**, 1–6 (1973).
61. Smith, M. *et al.*  $\gamma$  rays emitted in the decay of 31-yr <sup>178</sup>Hf<sup>m2</sup>. *Physical Review C* **68**, 031302 (2003).
62. Walker, P. M. & Dracoulis, G. Exotic isomers in deformed atomic nuclei. *Hyperfine Interactions* **135**, 83–107 (2001).
63. Eisenberg, J. M. & Greiner, W. *Nuclear Theory: Nuclear Models* (North-Holland, 1975).
64. Baldwin, G. & Klaiber, G. Photo-fission in heavy elements. *Physical Review* **71**, 3 (1947).
65. Bohr, A. *The coupling of nuclear surface oscillations to the motion of individual nucleons* (Munksgaard, 1952).
66. Hill, D. L. & Wheeler, J. A. Nuclear constitution and the interpretation of fission phenomena. *Physical Review* **89**, 1102 (1953).
67. Meitner, L. & Frisch, O. R. Disintegration of uranium by neutrons: a new type of nuclear reaction. *Nature* **143**, 239–240 (1939).
68. Hahn, O. & Strassmann, F. Concerning the existence of alkaline earth metals resulting from neutron irradiation of uranium. *Naturwissenschaften* **27** (1939).

## BIBLIOGRAPHY

---

69. Polikanov, S. *et al.* Spontaneous fission with an anomalously short period. *Soviet Physics JETP* **15**, 1016–1021 (1962).
70. Andreyev, A. *et al.* A triplet of differently shaped spin-zero states in the atomic nucleus  $^{186}\text{Pb}$ . *Nature* **405**, 430–433 (2000).
71. Runkle, R., Champagne, A. & Engel, J. Thermal equilibration of  $^{26}\text{Al}$ . *The Astrophysical Journal* **556**, 970 (2001).
72. Belic, D. *et al.* Photoactivation of  $^{180}\text{Ta}^m$  and Its Implications for the Nucleosynthesis of Nature’s Rarest Naturally Occurring Isotope. *Physical review letters* **83**, 5242 (1999).
73. Baldwin, G. C. & Solem, J. C. Recoilless gamma-ray lasers. *Reviews of Modern Physics* **69**, 1085 (1997).
74. Beeks, K. *et al.* The thorium-229 low-energy isomer and the nuclear clock. *Nature Reviews Physics* **3**, 238–248 (2021).
75. Pospelov, M., Rajendran, S. & Ramani, H. Metastable nuclear isomers as dark matter accelerators. *Physical Review D* **101**, 055001 (2020).
76. Walker, P. M. & Carroll, J. J. Ups and downs of nuclear isomers. *Physics Today* **58** (2005).
77. Dracoulis, G., Walker, P. & Kondev, F. Review of metastable states in heavy nuclei. *Reports on Progress in Physics* **79**, 076301 (2016).
78. Aprahamian, A. & Sun, Y. Long live isomer research. *Nature Physics* **1**, 81–82 (2005).
79. Carroll, J., Karamian, S., Rivlin, L. A. & Zadernovsky, A. X-ray-driven gamma emission. *Hyperfine Interactions* **135**, 3–50 (2001).
80. Carroll, J. J. Nuclear structure and the search for induced energy release from isomers. *Nuclear Instruments and Methods in Physics Research Section B: Beam Interactions with Materials and Atoms* **261**, 960–964 (2007).
81. Walker, P. M. & Carroll, J. J. Nuclear isomers: Recipes from the Past and Ingredients for the Future. *Nuclear Physics News* **17**, 11–15 (2007).
82. Belic, D. *et al.* Photo-induced depopulation of the  $^{180}\text{Ta}^m$  isomer via low-lying intermediate states: Structure and astrophysical implications. *Physical Review C* **65**, 035801 (2002).
83. Dracoulis, G. *On the question of connections between high-K and low-K states in  $^{180}\text{Ta}$  and  $^{176}\text{Lu}$*  in *AIP Conference Proceedings* **1269** (2010), 295–302.
84. Schlegel, C. *et al.* Depopulation of  $\text{Ta}^{m180}$  by Coulomb excitation and possible astrophysical consequences. *Physical Review C* **50**, 2198 (1994).
85. Mohr, P., Käppeler, F. & Gallino, R. Survival of nature’s rarest isotope  $\text{Ta}^{180}$  under stellar conditions. *Physical Review C* **75**, 012802 (2007).



86. Carroll, J. An experimental perspective on triggered gamma emission from nuclear isomers. *Laser Physics Letters* **1**, 275 (2004).
87. Collins, C. *et al.* Accelerated emission of gamma rays from the 31-yr isomer of  $^{178}\text{Hf}$  induced by X-Ray irradiation. *Physical review letters* **82**, 695 (1999).
88. Ahmad, I. *et al.* Search for X-Ray Induced Acceleration of the Decay of the 31-Yr Isomer of  $^{178}\text{Hf}$  Using Synchrotron Radiation. *Physical Review Letters* **87**, 072503 (2001).
89. Ahmad, I. *et al.* Search for x-ray induced decay of the 31-yr isomer of 178 Hf at low x-ray energies. *Physical Review C* **67**, 041305 (2003).
90. Carroll, J. *et al.* Search for low-energy induced depletion of  $^{178}\text{Hf}^{m2}$  at the SPring-8 synchrotron. *Physics Letters B* **679**, 203–208 (2009).
91. Hayes, A. *et al.* Breakdown of K Selection in  $\text{Hf}^{178}$ . *Physical review letters* **96**, 042505 (2006).
92. Roberts, H. The importance of stimulated gamma release from isomers. *Hyperfine interactions* **107**, 91–97 (1997).
93. Ohtsuki, T., Yuki, H., Muto, M., Kasagi, J. & Ohno, K. Enhanced Electron-Capture Decay Rate of  $^7\text{Be}$  Encapsulated in  $\text{C}_{60}$  Cages. *Physical review letters* **93**, 112501 (2004).
94. Cohen, R., Miller, G. & West, K. Nuclear resonance excitation by synchrotron radiation. *Physical Review Letters* **41**, 381 (1978).
95. Pieper, G. & Heydenburg, N. Coulomb excitation of iron-57. *Physical Review* **107**, 1300 (1957).
96. Petrov, Y. V. Possibility of investigating the levels of the compound nucleus produced by interaction between slow neutrons and isomers. *Sov. Phys. JETP* **10**, 833–834 (1960).
97. Roig, O. *et al.* Direct evidence for inelastic neutron “acceleration” by  $\text{Lu}^{177m}$ . *Physical Review C* **83**, 064617 (2011).
98. Karamian, S. & Carroll, J. Cross section for inelastic neutron “acceleration” by  $^{178}\text{Hf}^{m2}$ . *Physical Review C* **83**, 024604 (2011).
99. Goldanskii and Namiot. Excitation of isomeric nuclear levels by laser radiation via the mechanism of inverse interval electron conversion. *Pis'ma Zh. Eksp. Teor. Fiz.* **23**, 495. <http://adsabs.harvard.edu/abs/1976JETPL..23..451G> (1976).
100. Gol'danskii, V. & Namiot, V. Excitation of isomeric nuclear levels by laser radiation via the mechanism of inverse internal electron conversion. *JETP Lett. (USSR) (Engl. Transl.); (United States)* **23** (1976).
101. Dzyublik, A. Y. General theory of nuclear excitation by electron transitions. *Physical Review C* **88**, 054616 (2013).

## BIBLIOGRAPHY

---

102. Carreyre, T. a. *et al.* First direct proof of internal conversion between bound states. *Physical Review C* **62**, 024311 (2000).
103. Karpeshin, F. & Trzhaskovskaya, M. Bound internal conversion versus nuclear excitation by electron transition: Revision of the theory of optical pumping of the Th<sup>229m</sup> isomer. *Physical Review C* **95**, 034310 (2017).
104. Tkalya, E. V. Probability of L-shell nuclear excitation by electronic transitions in <sup>178</sup>Hf<sup>m2</sup>. *Physical Review C* **68**, 064611 (2003).
105. Tkalya, E. V. Induced decay of Hf<sup>178m2</sup>: Theoretical analysis of experimental results. *Physical Review C* **71**, 024606 (2005).
106. Dzyublik, A. Y. Triggering of <sup>178</sup>Hf<sup>m2</sup> by photoinduced electron transition., 11–17 (2013).
107. Kishimoto, S. a. *et al.* Observation of nuclear excitation by electron transition in <sup>197</sup>Au with synchrotron X rays and an avalanche photodiode. *Physical Review Letters* **85**, 1831 (2000).
108. Krutov, V. & Fomenko, V. Influence of electronic shell on gamma radiation of atomic nuclei. *Annalen der Physik* **476**, 291–302 (1968).
109. Crasemann, B. Some aspects of atomic effects in nuclear transitions (1973).
110. Ljubicic, A. Rare nuclear processes-investigations with radioisotope sources. *Journal of Physics G: Nuclear and Particle Physics* **17**, S101 (1991).
111. Berengut, J. Resonant Electronic-Bridge Excitation of the U<sup>235</sup> Nuclear Transition in Ions with Chaotic Spectra. *Physical Review Letters* **121**, 253002 (2018).
112. Volotka, A. *et al.* Nuclear excitation by two-photon electron transition. *Physical Review Letters* **117**, 243001 (2016).
113. Müller, R. A., Volotka, A. V. & Surzhykov, A. Excitation of the Th<sup>229</sup> nucleus via a two-photon electronic transition. *Physical Review A* **99**, 042517 (2019).
114. Krutov, V. Internal conversion in the field of an "electronic bridge". *Soviet Journal of Experimental and Theoretical Physics Letters* **52**, 584 (1990).
115. Krutov, V. & Knyazkov, O. Higher Approximation Effects in Internal Conversion Processes. *Annalen der Physik* **480**, 10–23 (1970).
116. Wilet, L. Excitation of Nuclear Rotational States In  $\mu$ -Mesonic Atoms. *Dan: Mat. Fys . Medd.* **29** (1954).
117. Jacobsohn, B. A. Nuclear Fine Structure in the  $\mu$ -Mesonic Atom. *Physical Review* **96**, 1637 (1954).
118. Gargiulo, S., Gu, M. F., Carbone, F. & Madan, I. Nuclear Excitation by Free Muon Capture. *Physical Review Letters* **129**, 142501 (2022).
119. Gargiulo, S., Madan, I. & Carbone, F. Nuclear excitation by electron capture in excited ions. *Physical Review Letters* **128**, 212502 (2022).

120. Wu, Y., Gargiulo, S., Carbone, F., Keitel, C. H. & Pálffy, A. Dynamical control of nuclear isomer depletion via electron vortex beams. *Physical Review Letters* **128**, 162501 (2022).
121. Zadernovsky, A. Excitation of nuclei by photon beams carrying orbital angular momentum. *Laser physics* **16**, 571–575 (2006).
122. Larocque, H., Kaminer, I., Grillo, V., Boyd, R. W. & Karimi, E. Twisting neutrons may reveal their internal structure. *Nature Physics* **14**, 1–2 (2018).
123. Madan, I., Vanacore, G. M., Gargiulo, S., LaGrange, T. & Carbone, F. The quantum future of microscopy: Wave function engineering of electrons, ions, and nuclei. *Applied Physics Letters* **116**, 230502 (2020).
124. Zhao, P., Ivanov, I. P. & Zhang, P. Decay of the vortex muon. *Physical Review D* **104**, 036003 (2021).
125. Luski, A. *et al.* Vortex beams of atoms and molecules. *Science* **373**, 1105–1109 (2021).
126. Ivanov, I. P. Promises and challenges of high-energy vortex states collisions. *Progress in Particle and Nuclear Physics*, 103987 (2022).
127. Harston, M. & Chemin, J. Mechanisms of nuclear excitation in plasmas. *Physical Review C* **59**, 2462 (1999).
128. Doolen, G. Nuclear excitation rate. *Physical Review Letters* **40**, 1695 (1978).
129. Doolen, G. The nuclear excitation rate for low-lying excited states in  $U^{237}$  and  $U^{238}$ . *Physical Review C* **18**, 2547 (1978).
130. Izawa, Y. & Yamanaka, C. Production of  $^{235}U^m$  by nuclear excitation by electron transition in a laser produced uranium plasma. *Physics Letters B* **88**, 59–61 (1979).
131. Gol'danskii, V. & Namiot, V. Excitation of nuclear isomeric levels in a hot plasma by inverse internal electron conversion. *Sov. J. Nucl. Phys.(Engl. Transl.);(United States)* **33** (1981).
132. Cue, N., Poizat, J.-C. & Remillieux, J. Exciting the nucleus by target electron capture into atomic orbitals. *EPL (Europhysics Letters)* **8**, 19 (1989).
133. Cue, N. Nuclear excitation by target electron capture. *Nuclear Instruments and Methods in Physics Research Section B: Beam Interactions with Materials and Atoms* **40**, 25–27 (1989).
134. Tanis, J. *et al.* Simultaneous electron capture and excitation in S + Ar Collisions. *Physical Review Letters* **47**, 828 (1981).
135. Brandt, D. Resonant transfer and excitation in ion-atom collisions. *Physical Review A* **27**, 1314 (1983).
136. Mokler, P. & Reusch, S. Comments on correlated electron capture in relativistic, highly charged, heavy ions. *Zeitschrift für Physik D Atoms, Molecules and Clusters* **8**, 393–395 (1988).

## BIBLIOGRAPHY

---

137. Arutyunyan, R. *et al.* Cross section for excitation of the isomer  $^{235m}\text{U}$  in the plasma produced by an electron beam. *Soviet Journal of Nuclear Physics (English Translation)* **53**, 23–26 (1991).
138. Mukoyama, T. *Nuclear Excitation involving Inner-Shell Electrons in AIP Conference Proceedings* **652** (2003), 281–290.
139. Pálffy, A. *Theory of nuclear excitation by electron capture for heavy ions* PhD thesis (Justus-Liebig-Universität, 2006). arXiv: 0701206 [physics]. <https://core.ac.uk/download/pdf/56343138.pdf>.
140. Pálffy, A., Scheid, W. & Harman, Z. Theory of nuclear excitation by electron capture for heavy ions. *Physical Review A* **73**, 012715 (2006).
141. Zadernovsky, A. & Carroll, J. Non-radiative triggering of long-lived nuclear isomers. *Hyperfine interactions* **143**, 153–174 (2002).
142. Dauvergne, D. *Expériences interdisciplinaires d'interaction particule-matière* PhD thesis (2006).
143. Morel, P., Daugas, J. M., Gosselin, G. & Gogny, D. Nuclear Excitation by Electronic Processes : NEEC and NEET Effects Plasma at Local, 1085–1088 (2005).
144. Gosselin, G. & Morel, P. Enhanced nuclear level decay in hot dense plasmas. *Physical Review C* **70**, 064603 (2004).
145. Gosselin, G., Méot, V. & Morel, P. Modified nuclear level lifetime in hot dense plasmas. *Physical Review C* **76**, 044611 (2007).
146. Karamian, S. & Carroll, J. Calculated yield of isomer depletion due to NEEC for  $^{93m}\text{Mo}$  recoils. *Physics of Atomic Nuclei* **75**, 1362–1367 (2012).
147. Polasik, M. *et al.* Resonance conditions for Mo 93 m isomer depletion via nuclear excitation by electron capture in a beam-based scenario. *Physical Review C* **95**, 034312 (2017).
148. Chiara, C. *et al.* Isomer depletion as experimental evidence of nuclear excitation by electron capture. *Nature* **554**, 216–218 (2018).
149. Wu, Y., Gunst, J., Keitel, C. H. & Pálffy, A. Tailoring laser-generated plasmas for efficient nuclear excitation by electron capture. *Physical review letters* **120**, 052504 (2018).
150. Gunst, J., Wu, Y., Keitel, C. H. & Pálffy, A. Nuclear excitation by electron capture in optical-laser-generated plasmas. *Physical Review E* **97**, 063205 (2018).
151. Wu, Y., Keitel, C. H. & Pálffy, A. X-ray-assisted nuclear excitation by electron capture in optical laser-generated plasmas. *Physical Review A* **100**, 063420 (2019).
152. Borisjuk, P. *et al.* Excitation of  $^{229}\text{Th}$  nuclei in laser plasma: the energy and half-life of the low-lying isomeric state. *arXiv preprint arXiv:1804.00299* (2018).

153. Thiroff, P., Seiferle, B. & Von der Wense, L. The 229-thorium isomer: doorway to the road from the atomic clock to the nuclear clock. *Journal of Physics B: Atomic, Molecular and Optical Physics* **52**, 203001 (2019).
154. Wu, Y., Keitel, C. H. & Pálffy, A. Mo<sup>93m</sup> Isomer Depletion via Beam-Based Nuclear Excitation by Electron Capture. *Physical review letters* **122**, 212501 (2019).
155. Rzadkiewicz, J., Polasik, M., Słabkowska, K., Carroll, J., Chiara, C., *et al.* Novel Approach to Mo<sup>93m</sup> Isomer Depletion: Nuclear Excitation by Electron Capture in Resonant Transfer Process. *Physical Review Letters* **127**, 042501 (2021).
156. Biggs, F., Mendelsohn, L. & Mann, J. Hartree-Fock Compton profiles for the elements. *Atomic data and nuclear data tables* **16**, 201–309 (1975).
157. Guo, S., Fang, Y., Zhou, X. & Petrache, C. Possible overestimation of isomer depletion due to contamination. *Nature* **594**, E1–E2 (2021).
158. Chiara, C. *et al.* Reply to: Possible overestimation of isomer depletion due to contamination. *Nature* **594**, E3–E4 (2021).
159. Guo, S. *et al.* Probing Mo<sup>93m</sup> Isomer Depletion with an Isomer Beam. *Physical Review Letters* **128**, 242502 (2022).
160. Sun, Z., Zhan, W.-L., Guo, Z.-Y., Xiao, G. & Li, J.-X. RIBLL, the radioactive ion beam line in Lanzhou. *Nuclear Instruments and Methods in Physics Research Section A: Accelerators, Spectrometers, Detectors and Associated Equipment* **503**, 496–503 (2003).
161. Lee, I.-Y. The gammasphere. *Nuclear Physics A* **520**, c641–c655 (1990).
162. Vanacore, G. M. *et al.* Ultrafast generation and control of an electron vortex beam via chiral plasmonic near fields. *Nature materials* **18**, 573–579 (2019).
163. Rotunno, E. *et al.* One-dimensional ghost imaging with an electron microscope: a route towards ghost imaging with inelastically scattered electrons. *arXiv preprint arXiv:2106.08955* (2021).
164. Bliokh, K. Y. *et al.* Theory and applications of free-electron vortex states. *Physics Reports* **690**, 1–70 (2017).
165. Lembessis, V., Ellinas, D., Babiker, M. & Al-Dossary, O. Atom vortex beams. *Physical Review A* **89**, 053616 (2014).
166. Lembessis, V. E. Atomic Ferris wheel beams. *Physical Review A* **96**, 013622 (2017).
167. Pohl, D. *et al.* Atom size electron vortex beams with selectable orbital angular momentum. *Scientific Reports* **7**, 934 (2017).
168. Leopardi, G. *La Ginestra* (1836). Available with parallel italian and english texts on [http://www.tclt.org.uk/leopardi/Canti\\_2011.pdf](http://www.tclt.org.uk/leopardi/Canti_2011.pdf), page 212.
169. Csikszentmihalyi, M., Nakamura, J. & Csikszentmihalyi, M. The Concept of Flow. *Flow and the foundations of positive psychology: The collected works of Mihaly Csikszentmihalyi*, 239–263 (2014).

## BIBLIOGRAPHY

---

170. Zagrebelsky, G. Liberi servi. *Il Grande Inquisitore e l'enigma del potere*, Torino: Einaudi (2015).
171. Devons, S. & Duerdoth, I. Muonic atoms. *Advances in Nuclear Physics: Volume 2*, 295–423 (1969).
172. Borie, E. & Rinker, G. The energy levels of muonic atoms. *Reviews of Modern Physics* **54**, 67 (1982).
173. Nagamine, K. *Introductory muon science* (Cambridge University Press, 2003).
174. Nikiforov, A. F., Novikov, V. G., Uvarov, V. B. & Uvarov, V. *Quantum-Statistical Models of Hot Dense Matter: Methods for Computation Opacity and Equation of State* (Springer Science & Business Media, 2005).
175. Grant, I. P. *Relativistic quantum theory of atoms and molecules: theory and computation* (Springer, 2007).
176. Jönsson, P., Gaigalas, G., Bieroń, J., Fischer, C. F. & Grant, I. New version: Grasp2K relativistic atomic structure package. *Computer Physics Communications* **184**, 2197–2203 (2013).
177. Gu, M. F. The flexible atomic code. *Canadian Journal of Physics* **86**, 675–689 (2008).
178. Michel, N., Oreshkina, N. S. & Keitel, C. H. Theoretical prediction of the fine and hyperfine structure of heavy muonic atoms. *Physical Review A* **96**, 032510 (2017).
179. Oberacker, V. *et al.* Muon-induced fission: A probe for nuclear dissipation and fission dynamics. *Physical Review C* **48**, 1297 (1993).
180. Wheeler, J. A. Some consequences of the electromagnetic interaction between  $\mu$ -mesons and nuclei. *Reviews of Modern Physics* **21**, 133 (1949).
181. Zaretski, D. & Novikov, V. Theory of nuclear excitations by muons in heavy mesic atoms. *Nuclear Physics* **28**, 177–191 (1961).
182. Goulard, B. & Primakoff, H. Nuclear muon-capture sum rules and mean nuclear excitation energies. *Physical Review C* **10**, 2034 (1974).
183. Schröder, W. *et al.* Evidence for Atomic Muon Capture by Fragments from Prompt Fission of Muonic Np<sup>237</sup>, Pu<sup>239</sup>, and Pu<sup>242</sup>. *Physical Review Letters* **43**, 672 (1979).
184. Belovitskii, G. *et al.* On the mechanism of uranium fission induced by slow negative muons. *Soviet Physics JETP* **11**, 296–299 (1960).
185. Ahmad, S. *et al.* Fission yields and lifetimes for muon induced fission in <sup>235</sup>U and <sup>238</sup>U. *Physics Letters B* **92**, 83–86 (1980).
186. Johansson, T. *et al.* Muon induced quadrupole photofission. *Phys. Lett. B* **97**, 29–32 (1980).
187. Hänscheid, H. *et al.* Nuclear excitation and prompt fission in muonic <sup>238</sup>U. *Zeitschrift für Physik A Hadrons and Nuclei* **342**, 111–120 (1992).

188. Oberacker, V. E., Umar, A. S. & Karpeshin, F. F. Prompt muon-induced fission: a sensitive probe for nuclear energy dissipation and fission dynamics. *arXiv preprint nucl-th/0403087* (2004).
189. Greub, C., Wyler, D., Brodsky, S. & Munger, C. Atomic alchemy: Weak decays of muonic and pionic atoms into other atoms. *Physical Review D* **52**, 4028 (1995).
190. Aslam, M. J., Czarnecki, A., Zhang, G. & Morozova, A. Decay of a bound muon into a bound electron. *Physical Review D* **102**, 073001 (2020).
191. Kaufmann, W. & Pilkuhn, H. Nuclear excitation via free-bound muon atomic transitions. *Zeitschrift für Physik A Atoms and Nuclei* **280**, 283–285 (1977).
192. Measday, D. F. The nuclear physics of muon capture. *Physics Reports* **354**, 243–409 (2001).
193. Hughes, V. *Muon Physics: Electromagnetic Interactions* (Elsevier, 2012).
194. Shahbaz, A. Muonic atoms in super-intense laser fields (2009).
195. Shahbaz, A., Müller, C., Bürvenich, T. J. & Keitel, C. H. Laser-induced nonresonant nuclear excitation in muonic atoms. *Nuclear Physics A* **821**, 106–117 (2009).
196. Warren, J. R. & Marshall, B. Unidentified curved bacilli on gastric epithelium in active chronic gastritis. *The lancet* **321**, 1273–1275 (1983).
197. Marshall, B. & Warren, J. R. Unidentified curved bacilli in the stomach of patients with gastritis and peptic ulceration. *The lancet* **323**, 1311–1315 (1984).
198. Egan, B. J. & O’Morain, C. A. A historical perspective of Helicobacter gastro-duodenitis and its complications. *Best Practice & Research Clinical Gastroenterology* **21**, 335–346 (2007).
199. Nietzsche, F. *Thus spoke Zarathustra: A book for everyone and nobody* (Oxford University Press, 2008).
200. Matinyan, S. Lasers as a bridge between atomic and nuclear physics. *Physics reports* **298**, 199–249 (1998).
201. Feng, J. *et al.* Femtosecond pumping of nuclear isomeric states by the Coulomb collision of ions with quivering electrons. *Physical Review Letters* **128**, 052501 (2022).
202. Gibbon, P. & Förster, E. Short-pulse laser-plasma interactions. *Plasma physics and controlled fusion* **38**, 769 (1996).
203. Krainov, V. P. & Smirnov, M. B. Cluster beams in the super-intense femtosecond laser pulse. *Physics reports* **370**, 237–331 (2002).
204. López-Claros, M., Vadillo, J. M. & Laserna, J. J. Determination of plasma ignition threshold fluence during femtosecond single-shot laser ablation on metallic samples detected by optical emission spectroscopy. *Journal of Analytical Atomic Spectrometry* **30**, 1730–1735 (2015).

## BIBLIOGRAPHY

---

205. Schmidt, V., Husinsky, W. & Betz, G. Dynamics of laser desorption and ablation of metals at the threshold on the femtosecond time scale. *Physical review letters* **85**, 3516 (2000).
206. Comet, M. *et al.* Nuclear excitation by electron transition rate confidence interval in a Hg 201 local thermodynamic equilibrium plasma. *Physical Review C* **92**, 054609 (2015).
207. Tkalya, E., Akhrameev, E., Arutyunyan, R., Bol'Shov, L. & Kondratenko, P. Excitation of atomic nuclei in hot plasma through resonance inverse electron bridge. *Physical Review C* **90**, 034614 (2014).
208. Tkalya, E., Akhrameev, E., Arutyunayn, R., Bol'Shov, L. & Kondratenko, P. Cross sections of electron excitation of atomic nuclei in plasma. *Physical Review C* **85**, 044612 (2012).
209. Gobet, F., Dzyublik, A. Y., Gosselin, G., Méot, V. & Versteegen, M. Expected yields of Ta 181 (e, e) Ta\* 181 in the multi-keV range with a plasma-cathode electron beam. *Physical Review C* **105**, 014608 (2022).
210. Carroll, J., Anderson, J., Glesener, J., Eberhard, C. & Collins, C. Accelerated decay of  $^{180}\text{Ta}^m$  and  $^{176}\text{Lu}$  in stellar interiors through gamma, gamma-prime reactions. *The Astrophysical Journal* **344**, 454–459 (1989).
211. Schumann, M., Käppeler, F., Böttger, R. & Schölermann, H. Coulomb excitation of 180 Ta. *Physical Review C* **58**, 1790 (1998).
212. Helmrich, S. *Nuclear Excitation by Electron Capture in Stellar Environments* PhD thesis (Ruprecht-Karls-Universität Heidelberg, Germany, 2011).
213. Letokhov, V. Pumping of nuclear levels by x-ray radiation of a laser plasma. *Soviet Journal of Quantum Electronics* **3**, 360 (1974).
214. Andreev, A. *et al.* Excitation of tantalum-181 nuclei in a high-temperature femtosecond laser plasma. *Journal of Experimental and Theoretical Physics Letters* **69**, 371–376 (1999).
215. Andreev, A. V. *et al.* Excitation of low-lying nuclear levels in a nonrelativistic hot dense laser-produced plasma. *Quantum electronics* **29**, 55 (1999).
216. Arber, T. *et al.* Contemporary particle-in-cell approach to laser-plasma modelling. *Plasma Physics and Controlled Fusion* **57**, 113001 (2015).
217. Pukhov, A. Three-dimensional electromagnetic relativistic particle-in-cell code VLPL (Virtual Laser Plasma Lab). *Journal of plasma physics* **61**, 425–433 (1999).
218. Chung, H.-K., Chen, M., Morgan, W., Ralchenko, Y. & Lee, R. FLYCHK: Generalized population kinetics and spectral model for rapid spectroscopic analysis for all elements. *High energy density physics* **1**, 3–12 (2005).



- 
219. Kibedi, T., Burrows, T., Trzhaskovskaya, M. B., Davidson, P. M. & Nestor Jr, C. W. Evaluation of theoretical conversion coefficients using BrIcc. *Nuclear Instruments and Methods in Physics Research Section A: Accelerators, Spectrometers, Detectors and Associated Equipment* **589**, 202–229 (2008).
220. Poikela, T. *et al.* Timepix3: a 65K channel hybrid pixel readout chip with simultaneous ToA/ToT and sparse readout. *Journal of instrumentation* **9**, C05013 (2014).
221. Harilal, S., Bindhu, C., Tillack, M., Najmabadi, F. & Gaeris, A. Internal structure and expansion dynamics of laser ablation plumes into ambient gases. *Journal of applied physics* **93**, 2380–2388 (2003).
222. *RAEA Next-Generation Ultrafast Ti:sapphire Amplifier* <https://www.kmlabs.com/raea-ultrafast-amplifier>. Accessed on 15.01.2020.
223. Eliezer, S. *The interaction of high-power lasers with plasmas* (CRC press, 2002).
224. Mulser, P. & Bauer, D. *High power laser-matter interaction* (Springer, 2010).
225. Kruer, W. *The physics of laser plasma interactions* (crc Press, 2019).
226. Denisov, N. On a singularity of the field of an electromagnetic wave propagated in an inhomogeneous plasma. *Soviet Physics JETP* **4**, 544–553 (1957).
227. Godwin, R., Sachsenmaier, R. & Sigel, R. Angle-dependent reflectance of laser-produced plasmas. *Physical Review Letters* **39**, 1198 (1977).
228. Brunel, F. Not-so-resonant, resonant absorption. *Physical review letters* **59**, 52 (1987).
229. Bonnaud, G., Gibbon, P., Kindel, J. & Williams, E. Laser interaction with a sharp-edged overdense plasma. *Laser and Particle Beams* **9**, 339–354 (1991).
230. Gibbon, P. & Bell, A. Collisionless absorption in sharp-edged plasmas. *Physical review letters* **68**, 1535 (1992).
231. Ping, Y. *et al.* Absorption of short laser pulses on solid targets in the ultrarelativistic regime. *Physical review letters* **100**, 085004 (2008).
232. Oxenius, J. *Kinetic theory of particles and photons. Theoretical foundations of Non-LTE plasma spectroscopy* (Springer Science & Business Media, 1986).
233. Pratt, R. *et al.* Bremsstrahlung energy spectra from electrons of kinetic energy  $1 \text{ keV} \leq T_1 \leq 2000 \text{ keV}$  incident on neutral atoms  $2 \leq Z \leq 92$ . *Atomic Data and Nuclear Data Tables* **20**, 175–209 (1977).
234. Rybicki, G. B. & Lightman, A. P. *Radiative processes in astrophysics* (John Wiley & Sons, 1991).
235. Ghisellini, G. *Radiative processes in high energy astrophysics* (Springer, 2013).
236. Blumberg, H., Hager, R. & Seltzer, E. The internal conversion of the 6 keV transition in  $^{181}\text{Ta}$ . *Nuclear Physics A* **136**, 624–630 (1969).

## BIBLIOGRAPHY

---

237. Dragoun, O. & Blumberg, H. Anomalous internal conversion of E1 transitions in outer atomic shells. *Czechoslovak Journal of Physics B* **21**, 785–793 (1971).
238. Karpeshin, F., Band, I. & Trzhaskovskaya, M. 3.5-eV isomer of  $^{229m}\text{Th}$ : how it can be produced. *Nuclear Physics A* **654**, 579–596 (1999).
239. Cengel, Y. *Heat Transfer: A Practical Approach* (McGraw-Hill New York, 2002).
240. AdvPix TPX3, [Online]. Available: <https://advacam.com/ca> [2022, October 27]. 2022.
241. Jakubek, J. Energy-sensitive X-ray radiography and charge sharing effect in pixelated detector. *Nuclear Instruments and Methods in Physics Research Section A: Accelerators, Spectrometers, Detectors and Associated Equipment* **607**, 192–195 (2009).
242. Willmott, P. & Huber, J. Pulsed laser vaporization and deposition. *Reviews of Modern Physics* **72**, 315 (2000).
243. Born, M. & Wolf, E. *Principles of optics: electromagnetic theory of propagation, interference and diffraction of light* (Elsevier, 2013).
244. Savel'ev, A., Chefonov, O., Ovchinnikov, A., Agranat, M. & Spohr, K. Direct detection of delayed high energy electrons from the  $^{181}\text{Ta}$  target irradiated by a moderate intensity femtosecond laser pulse. *Plasma Physics and Controlled Fusion* **59**, 035004 (2017).
245. A. Kramida, Yu. Ralchenko, J. Reader & and NIST ASD Team. NIST Atomic Spectra Database (ver. 5.10), [Online]. Available: <https://physics.nist.gov/asd> [2023, March]. National Institute of Standards and Technology, Gaithersburg, MD. 2022.
246. Perelman, C. & Olbrechts-Tyteca, L. *Traité de l'argumentation. La nouvelle rhétorique* (1971).
247. Amossy, R. *Apologie de la polémique* (Presses universitaires de France Paris, 2014).
248. Park, M., Leahey, E. & Funk, R. J. Papers and patents are becoming less disruptive over time. *Nature* **613**, 138–144 (2023).
249. De La Boétie, E., Tournon, L. & Audegean, P. *Discours de la servitude volontaire* (Vrin, 2002).
250. Zewail, A. H. & Thomas, J. M. *4D electron microscopy: imaging in space and time* (World Scientific, 2009).
251. Yannai, M. *et al.* Ultrafast Electron Microscopy of Nanoscale Charge Dynamics in Semiconductors. *ACS Nano* **17**. PMID: 36736033, 3645–3656. eprint: <https://doi.org/10.1021/acsnano.2c10481>. <https://doi.org/10.1021/acsnano.2c10481> (2023).
252. Riffe, D. M. *et al.* Femtosecond thermionic emission from metals in the space-charge-limited regime. *JOSA B* **10**, 1424–1435 (1993).

- 
253. Girardeau-Montaut, J. & Girardeau-Montaut, C. Theory of ultrashort nonlinear multiphoton photoelectric emission from metals. *Physical Review B* **51**, 13560 (1995).
254. Wendelen, W., Autrique, D. & Bogaerts, A. Space charge limited electron emission from a Cu surface under ultrashort pulsed laser irradiation. *Applied Physics Letters* **96**, 051121 (2010).
255. Gargiulo, S. *et al.* Charge Dynamics Electron Microscopy in 2021 Conference on Lasers and Electro-Optics (CLEO) (2021), 1–2.
256. Madan, I. *et al.* Charge Dynamics Electron Microscopy: Nanoscale Imaging of Femtosecond Plasma Dynamics. *ACS Nano* **17**. PMID: 36780289, 3657–3665. eprint: <https://doi.org/10.1021/acsnano.2c10482>. <https://doi.org/10.1021/acsnano.2c10482> (2023).
257. Recchia, F. *et al.* Configuration mixing and relative transition rates between low-spin states in  $^{68}\text{Ni}$ . *Physical Review C* **88**, 041302 (2013).
258. Chiara, C. *et al.* Low-spin states and the non-observation of a proposed 2202-keV, 0+ isomer in  $^{68}\text{Ni}$ . *Physical Review C* **86**, 041304 (2012).
259. Rimskii-Korsakov, A., Koltsov, V. & Karasev, V. Scheme of the  $\beta$ -decay of  $^{234}\text{Th}$ . *Bulletin of the Russian Academy of Sciences: Physics* **80**, 880–883 (2016).
260. Messiah, A. *Quantum mechanics* (Courier Corporation, 2014).
261. Biedenharn, L. C. & Louck, J. D. *The Racah-Wigner algebra in quantum theory* (Addison-Wesley, Advanced Book Program, 1981).
262. Varshalovich, D. A., Moskalev, A. N. & Khersonskii, V. K. *Quantum theory of angular momentum* (World Scientific, 1988).
263. Fack, V., Pitre, S. & Van der Jeugt, J. New efficient programs to calculate general recoupling coefficients. Part II: Evaluation of a summation formula. *Computer physics communications* **86**, 105–122 (1995).
264. Fack, V., Lievens, S. & Van der Jeugt, J. On rotation distance between binary coupling trees and applications for 3nj-coefficients. *Computer physics communications* **119**, 99–114 (1999).

Simone Gargiulo – CURRICULUM VITÆ

Nationality: Italian  
Birth: April 10<sup>th</sup> 1992, Torre del Greco, Napoli, Italy  
E-mail: [simone.gargiulo@epfl.ch](mailto:simone.gargiulo@epfl.ch)  
[simonegargiulo2@gmail.com](mailto:simonegargiulo2@gmail.com)



## Education

---

- April 2023 **Ph.D., Physics** École Polytechnique Fédérale de Lausanne, Switzerland  
Topics: nuclear isomers, nuclear excitation by electron capture (NEEC), laser-plasma physics, ultrafast electron microscopy, plasmonics.  
Title: *Electromagnetic processes of nuclear excitation: from direct photoabsorption to free electron and muon capture.*  
Group: Laboratory for ultrafast microscopy and electron scattering (LUMES).  
Thesis supervisor: Fabrizio Carbone.
- Sept. 2018 **M.Sc., Electronic Engineering** Università degli Studi di Napoli Federico II, Italy  
Topics: crystal-assisted collimation in particle accelerators, X-ray diffraction from bent crystals.  
Title: *Modelling for metrological analysis of an X-ray diffractometer for bent crystals characterization in crystal-assisted collimation.*  
Final mark: 110/110 cum laude, GPA: 4.0/4.0
- Dec. 2014 **B.Sc., Electronic Engineering** Università degli Studi di Napoli Federico II, Italy  
Topic: drug delivery systems.  
Title: *Microgel Photonics.*  
Final mark: 110/110 cum laude, GPA: 3.86/4.0
- Sept. 2010 **High School** Istituto Tecnico Industriale Antonio Pacinotti, Scafati, Italy  
Final mark: 96/100

## Professional Experience

---

Mar. 2019 – **Researcher** Swiss Federal Institute of Technology (EPFL),  
Apr. 2023 Lausanne, Switzerland

- Seeking innovative solutions to address the climate crisis, Google Inc. sponsored my doctoral research, which focused on exploring groundbreaking energy harvesting or storing tools.
- Developed numerical and simulation tools for theoretical calculations related to nuclear excitation processes.
- Designed and implemented a tabletop experimental setup to investigate the excitation of nuclear levels in a neutral plasma, generated by a femtosecond laser pulse.
- Developed finite element method (FEM) models using COMSOL and LUMERICAL, covering various fields of physics, including picosecond thermal dynamics, plasmonics, and electromagnetic wave propagation.
- Particle-in-cell simulations using EPOCH and VLPL for laser-plasma interactions.

Sept. 2017 – **Electronic Engineer** European Organization for Nuclear Re-  
Oct. 2018 search (CERN), Geneva, Switzerland

- Designed and commissioned high-precision instrumentation for the characterization of crystal collimators in the Large Hadron Collider (LHC).
- Developed theoretical frameworks and simulation tools for predicting experimental outcomes, accounting for real-world conditions and uncertainties.
- Developed numerical tools using COMSOL, integrating aspects of ray optics and mechanical stress-induced deformations to analyze the performance of bent crystals used as collimators in the LHC.

*continued on next page*

Jan. 2012 – **Technical Education Teacher** High School Maria  
Feb. 2012 Montessori-L. Da Vinci, Porretta Terme, Italy

- Delivered theoretical lectures and mentored students in the experimental design of electronic circuits.
- Assessed student progress to evaluate the effectiveness and impact of teaching methods and assigned projects.
- Supervised four classes consisting of 20 students each.

### Research projects (selected)

---

March 2019 – **Processes of Nuclear Excitation** EPFL  
April 2023

Theoretical investigation of nuclear excitation processes, including direct excitation through photon absorption, free electron (NEEC) and muon capture (NE $\mu$ C), and Coulomb excitation (inelastic scattering). Experimental design of a table-top setup aiming at the observation of nuclear excitations in laser-plasma scenarios.

June 2019 – **Charge Dynamics Electron Microscopy** EPFL  
Jan. 2023

Imaging of the spatiotemporal evolution of emitted electron clouds from metallic structures upon laser irradiation using an ultrafast transmission electron microscope (UTEM). Imaging the femtosecond dynamics of charge carriers in solids through the interaction between terahertz (THz) near fields and free-electron pulses in UTEM.

June 2021 – **Imaging and control of magnetic Skyrmion** EPFL  
April 2022

Accomplished coherent control of skyrmion crystal rotation in discrete steps at substantially higher speeds compared to prior observations, using circularly polarized femtosecond laser pulses. I contributed to this project by developing thermal simulations to determine sample heating upon laser irradiation on a picosecond timescale using Comsol.

June 2019 – **Metal-insulator transition in VO<sub>2</sub> using photon-induced near-field electron microscopy (PINEM)** EPFL  
Nov. 2020 Employed two-color near-field ultrafast electron microscopy to visualize the photo-induced insulator-to-metal transition in an individual VO<sub>2</sub> nanowire through the related electronic dynamics.

## Publications and Conferences

---

### Peer-Reviewed Publications

1. **S. Gargiulo**, I. Madan, and F. Carbone. Nuclear Excitation by Electron Capture in Excited Ions, in *Physical Review Letters*, vol. 128, n. 21, 212502, 2022.
2. **S. Gargiulo**, M. F. Gu, F. Carbone, I. Madan. Nuclear Excitation by Free Muon Capture, in *Physical Review Letters*, vol. 129, n. 14, 142501, 2022.
3. Y. Wu, **S. Gargiulo**, F. Carbone, C. H. Keitel, A. Pálffy. Dynamical control of nuclear isomer depletion via electron vortex beams, in *Physical Review Letters*, vol. 128, n. 16, 162501, 2022.
4. I. Madan\*, Eduardo JC Dias\*, **S. Gargiulo\***, F. Barantani\*, M. Yannai, G. Berruto, T. LaGrange, L. Piazza, T. T. Lummen, R. Dahan, I. Kaminer, G. M. Vanacore, F. J. García de Abajo, and Fabrizio Carbone. Charge dynamics electron microscopy: nanoscale imaging of femtosecond plasma dynamics, in *ACS Nano*, vol. 17, n. 4, p. 3657-3665, 2023.
5. X. Fu\*, F. Barantani\*, **S. Gargiulo\***, I. Madan, G. Berruto, T. LaGrange, L. Jin, J. Wu, G. M. Vanacore, and F. Carbone. Nanoscale-femtosecond dielectric response of Mott insulators captured by two-color near-field ultrafast electron microscopy, in *Nature Communications*, vol. 11, n. 1, p. 1-11, 2020.
6. I. Madan, G. M. Vanacore, **S. Gargiulo**, T. LaGrange, and F. Carbone. The quantum future of microscopy: Wave function engineering of electrons, ions, and nuclei, in *Applied Physics Letters*, vol. 116, n. 23, 230502, 2020.
7. P. Tengdin, B. Truc, A. Sapozhnik, L. Kong, N. del Ser, **S. Gargiulo**, I. Madan, T. Schönenberger, P. R. Baral, P. Che, A. Magrez, D. Grundler, H. M. Rønnow, T. Lagrange, J. Zang, A. Rosch, and F. Carbone. Imaging the ultrafast coherent control of a skyrmion crystal, in *Physical Review X*, vol. 12, n. 4, 041030, 2022.

8. M. Yannai, R. Dahan, A. Gorlach, Y. Adiv, K. Wang, I. Madan, **S. Gargiulo**, F. Barantani, E. J.C. Dias, G. M. Vanacore, N. Rivera, F. Carbone, F. J. García de Abajo, and I. Kaminer. Ultrafast Electron Microscopy of Nanoscale Charge Dynamics in Semiconductors, in *ACS Nano*, vol. 17, n. 4, p. 3645–3656, 2023.
9. I. Madan, V. Leccese, A. Mazur, F. Barantani, T. LaGrange, A. Sapozhnik, P. M. Tengdin, **S. Gargiulo**, E. Rotunno, J.-C. Olaya, I. Kaminer, V. Grillo, F. Javier García de Abajo, F. Carbone, and G. M. Vanacore. Ultrafast transverse modulation of free electrons by interaction with shaped optical fields, in *ACS photonics*, vol. 9, n. 10, p. 3215-3224, 2022.

### Articles Under Review

10. E. Rotunno\*, **S. Gargiulo**\*, G. M. Vanacore, C. Mechel, A. Tavabi, R. E. Dunin Borkowski, F. Carbone, I. Madan, M. Zanfrognini, S. Frabboni, T. Guner, E. Karimi, I. Kaminer, and V. Grillo. One-dimensional ghost imaging with an electron microscope: a route towards ghost imaging with inelastically scattered electrons, *arXiv:2106.08955*.
11. K. Akbari, **S. Gargiulo**, F. Carbone, and F. J. García de Abajo. Coherent Smith-Purcell  $\gamma$ -Ray Emission, *arXiv:2203.05990*.
12. A. A. Sapozhnik, B. Truc, P. Tengdin, E. Viñas Boström, T. Schönenberger, **S. Gargiulo**, I. Madan, T. LaGrange, A. Magrez, C. Verdozzi, A. Rubio, H. M. Rønnow, and F. Carbone. Observation of a new light-induced skyrmion phase in the Mott insulator  $\text{Cu}_2\text{OSeO}_3$ , *arXiv:2212.07878*.
13. E. J. C. Dias, I. Madan, **S. Gargiulo**, F. Barantani, M. Yannai, G. M. Vanacore, I. Kaminer, F. Carbone, and F. J. García de Abajo. Generation and control of localized terahertz fields in photoemitted electron plasmas, *arXiv:2303.06451*.

### Articles in Preparation

14. **S. Gargiulo**, I. Madan, B. Truc, P. Usai, K. Beeks, V. Leccese, G. M. Vanacore, and F. Carbone. Revisiting the process of direct photoexcitation of the  $^{181\text{m}}\text{Ta}$  isomer in optical laser-generated plasma.
15. V. Leccese, M. Caldara, S. Bisi, M. Pagano, **S. Gargiulo**, C. Trigila, A. Bertsch, A. Mapelli, F. Carbone. Microstructured plastic scintillators for high resolution and high frame rate ion beam profiling.

\* Equally contributing authors.

### Seminars

- Contributed talk at the 75th SUSSP and 20th STFC Summer School in Nuclear Physics and its Applications, Scotland, UK, August 2019.



- Contributed talk at the CLEO Conference, San Jose, USA [virtual], May 2020 .
- Contributed talk at the DNP Fall Meeting, Boston, USA [virtual], October 2021.
- Contributed talk at the APS April Meeting, New York, USA, March April 2022.
- Contributed talk at the MRS Spring Meeting, Honolulu, USA, May 2022.
- Invited talk at the Army Research Laboratory, Adelphi, USA, April 2022.
- Invited talk at TRIUMF, Vancouver, Canada [virtual], July 2022.

#### Posters (selected)

- “Stimulating nuclear excitation in laser-plasma scenario”, Time domain control of atomic shell for nuclear excitation, Lerici, Italy, October 2019.
- “Nuclear Excitations by Electron Capture in Excited Ions”, MUST Annual Meeting, Grindelwald, CH, August 2021.
- “Nuclear Excitations by Electron Capture in Excited Ions”, Joint Annual Meeting of ÖPG and the Swiss Physical Society (SPS), Innsbruck, Austria, September 2021.
- “Nuclear Excitations by Electron Capture in Excited Ions”, 100 Years of Nuclear Isomers, Berlin, Germany, May 2022.
- “Nuclear Excitations by Free Muon Capture”, LISA Winter School – Structure of Complex Atoms, Bagnoles de l’Orne, France, September 2022.
- “Electromagnetic and atomic processes for nuclear isomer excitation in optical laser-generated plasma ”, Atomic Processes in Plasma held at the International Atomic Energy Agency (IAEA), Vienna, Austria, May 2023.

#### Schools

- 75th SUSSP and 20th STFC Summer School in Nuclear Physics and its Applications, Scotland, UK, August 2019.
- Quantum Computing Hard- and Software Summer School, Lausanne, CH, June 2022.
- Structure of Complex Atoms, Bagnoles de l’Orne, France, September 2022.

#### Other conferences attended (selected)

- International Online Workshop “Electrons, Photons and Plasmons-2021”, March 2021, virtual.
- 3rd International Conference on Nuclear Photonics (NP2020), June 2021, virtual.

## Events on Cross-Disciplinary Topics

- 72h VersusVirus Hackathon, top 6 – Economics and Policy **Info** (link).
- Global Young Scientists Summit (GYSS) 2023, Singapore, January 2023.
- Innosuisse Lausanne Business Concept, Lausanne, CH, February-June 2023.

## Peer-Review Activities

---

- Physical Review Letters

## Public Outreach

---

Designed and produced multimedia content, including illustrations, video editing, and animations, to successfully convey the nuclear physics projects carried out by the LUMES group at EPFL. Spearheaded the creation of captivating comic art, images, and informative video, all of which were showcased on the LUMES group's official webpage:

- Google funds EPFL research on nuclear phenomena – **Cover Image** (link).
- The quantum future of electron microscopy – **Comic Art** (link).
- Nuclear Excitation by Free Muon Capture – **Video** (link).

Created a BLENDER animation illustrating the interaction of a laser pulse with a metallic structure, leading to the generation of a photoemitted electron cloud.

- Charge Dynamics Electron Microscopy – **Cover Image** (link).

## Teaching

---

### Teaching assistant for courses

- Physique Générale (General Physics), 1<sup>st</sup> year B.Sc. Géosciences, UNIL.  
Lecturers: Fabrizio Carbone.  
Language: French.
- General Physics I, 1<sup>st</sup> year B.Sc. Physics, EPFL.  
Lecturers: Suliana Manley.  
Language: English.

## Awards and Honors

---

- APS Award, Feb. 2022.
- Special Prize from Hübner & Kennedy Foundation, Sep. 2022.

## Certifications

---

- NI LabVIEW CORE 1 – National Instrument LabVIEW Core 1.
- COMSOL – Geometry, CAD import and Meshing.
- COMSOL – Solvers and Solution Strategies.
- AgilePM Foundation – Project Management.

## Grants

---

- Co-authored a successful grant proposal with Prof. Fabrizio Carbone, securing funding from Lockheed Martin for a nuclear physics research project.

## Languages

---

<b>Neapolitan:</b>	native speaker.	<b>Italian:</b>	bilingual.
<b>English:</b>	full professional proficiency.	<b>French:</b>	intermediate level.